Control of topologically non-trivial spin excitations

Dissertation

zur Erlangung des

Doktorgrades der Naturwissenschaften

(Dr. rer. nat.)

der Naturwissenschaftlichen Fakultät II

Chemie, Physik, Mathematik

der Martin-Luther-Universität Halle-Wittenberg

vorgelegt von Herrn

ALEXANDER FREDERIC SCHÄFFER

geboren am 03.10.1991 in Hannover

PREAMBLE

This is a cumulative thesis. The individual chapters introduce the topic and summarize the results of the appended, selected publications.

ABSTRACT

This thesis presents results on the control of spin excitations with a non-trivial real space topology in magnetic solids. In particular, magnetic skyrmions and related non-collinear magnetic configurations are discussed. Skyrmions are localized whirl-like quasiparticles that can either emerge as isolated objects in a homogeneously magnetized background or form skyrmion crystals. Due to their high mobility and stability, skyrmions are promising candidates for information storage devices. Theoretical concepts and numerical simulations are presented for creating, annihilating, and displacing magnetic quasiparticles.

In the second part of this thesis, the existence of twisted magnons is predicted, which are excitations in extended ferro- or antiferromagnetic systems that carry orbital angular momentum in addition to their spin. Combining analytical and numerical methods, the stability of twisted magnons and the robustness of the associated topological charge against damping and stray field perturbations are demonstrated. Creation and control mechanisms of twisted magnons, transport effects related to spin-pumping, and the transfer of orbital angular momentum between waveguides are elaborated.

The new concepts presented in the thesis are of direct relevance to applications in data storage and information transfer with the potential for improving future technology in terms of speed and energy efficiency.

KURZBESCHREIBUNG

In der vorliegenden kumulativen Dissertation werden verschiedene Aspekte der Manipulation von Spinanregungen mit einer nicht-trivialen Realraumtopologie in magnetischen Festkörpern untersucht. Thema der ersten Hälfte der Arbeit sind magnetische Skyrmionen und verwandte nicht-kollineare magnetische Konfigurationen. Skyrmionen sind wirbelartige Quasiteilchen, die entweder als isolierte Objekte inmitten eines homogen magnetisierten Hintergrundes auftreten oder Skyrmionkristalle bilden können. Aufgrund ihrer hohen Mobilität und Stabilität sind Skyrmionen vielversprechende Kandidaten zur Anwendung in Speichermedien. Diese Dissertation präsentiert theoretische Konzepte und numerische Simulationen zur Erzeugung, Vernichtung und Verschiebung von magnetischen Quasiteilchen.

Die Vorhersage der Existenz von *twisted magnons* (dt. gewundene Magnonen) ist Thema der zweiten Hälfte der vorliegenden Arbeit. *Twisted magnons* sind Spinwellenmoden in ausgedehnten ferro- oder antiferromagnetischen Materialien, die einen Bahndrehimpuls zusätzlich zu ihrem Spin tragen. Durch die Kombination von analytischen und numerischen Methoden wird die Stabilität dieser Spinwellenmoden und die Robustheit ihrer topologischen Ladung gegenüber Dämpfung und Streufeldern demonstriert. Erzeugungs- und Kontrollmechanismen, Transporteffekte und der Transfer des Bahndrehimpulses zwischen Wellenleitern werden ausgearbeitet.

Aufgrund der möglichen Verbesserungen hinsichtlich Geschwindigkeit und Energieeffizienz, sind die präsentierten Konzepte von direkter Relevanz für Anwendungen in der Datenspeicherung und Informationsübertragung.

CONTENTS

CHAPTER 1

INTRODUCTION

Over the past decades, the demand for high-density and low power consuming electronic devices has drastically increased. Already in 2018, the sector of information and communications technology (ICT) accounted for about 10 % of the world's total electricity demand [51]. After an era of miniaturizing complementary metal-oxide-semiconductor (CMOS) technology and storage devices, physical boundaries are within reach. The doubling of transistors in a dense integrated circuit every two years may no longer hold [65], which calls for concepts for the next generation of ICT.

Two main technological challenges concern storing and transferring information. Ideally, once written information should be non-volatile, meaning no energy is necessary to preserve a memory state. This is the main motivation for using magnetic skyrmions as a logical bit. Skyrmions have long lifetimes due to their non-trivial real space topology, a fact referred to as *topological protection*. In the presented works (chapter 3), different creation mechanisms and characteristic temperature-dependent features for such magnetic quasiparticles are investigated.

Concerning the exchange and transfer of data, large bandwidths at high speeds are desirable. In the publications discussed in chapter 4, twisted spin waves are studied as information carriers. The concept of using spin waves with helical wavefronts corresponding to a finite winding number and orbital angular momentum (OAM) could drastically increase the bandwidth for on-chip data transfer similar to optical-based multiplex data transfer.

In fig. 1.1 key aspects discussed in this thesis are highlighted. In addition to the technological relevance (e.g., regarding non-volatile memory, stochastic computing, all solid-state communication and wave-based logic computing), the investigations deal with the aspects of the role of topology, symmetry and geometry in the dynamics of quasiparticle excitations.

The work is structured as follows: Chapter 2 introduces the physics of non-collinear
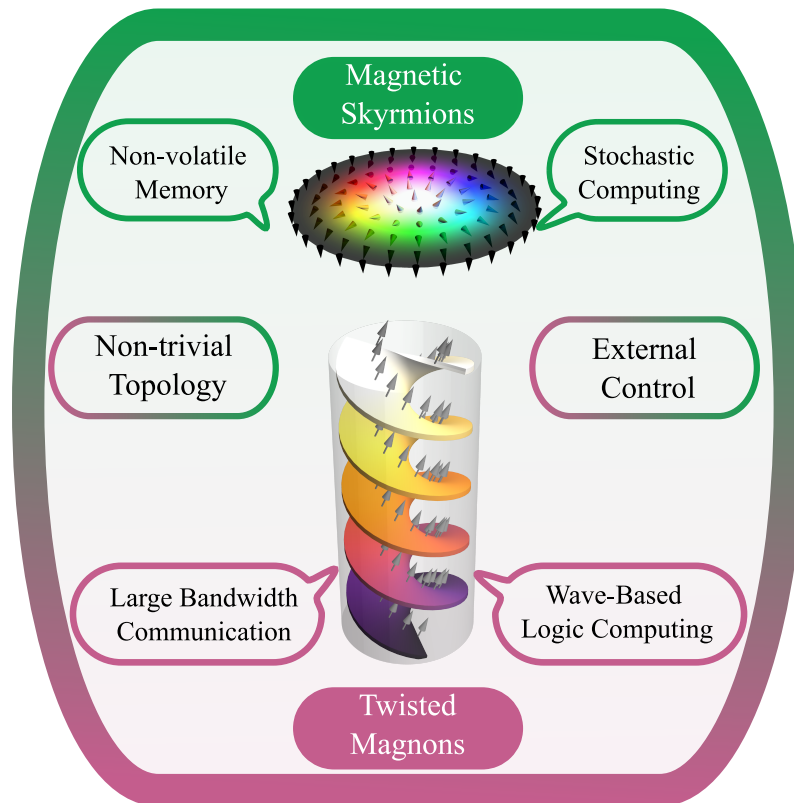
Figure 1.1: Schematic overview, indicating the main scope of skyrmion and twisted magnon related research presented in this thesis.

magnetism, starting from the fundamental quantum mechanical effect of the exchange interaction between two spins. In the following, the basics of magnetization dynamics are established, and an overview over topology-related phenomena in magnetism is given. Chapter 3 discusses the results on skyrmion-related phenomena. Chapter 4 presents the findings on the topic of twisted spin waves. Finally, the contributions are summarized, and an outlook into future projects is presented in chapter 5.

CHAPTER 2

PHYSICAL BACKGROUND

2.1 NON-COLLINEAR MAGNETISM

What causes non-collinearity? This question will be addressed on two levels related to the two regimes of non-collinearity studied in this thesis: statics and dynamics. In the field of spin dynamics, reasons for a non-uniform ordering of the magnetization vector field can be imagined in analogy to waves in fluids. In contrast to the collective uniform ferromagnetic resonance (FMR), magnetic excitations can be characterized by both a frequency and a wave vector $|\mathbf{k}| \neq 0$. Like the generation of water waves by dropping a stone into a pond, propagating spin waves can be excited by a space- and time-dependent effective magnetic field. The origins for such magnetic fields are manifold and range from micrometer-sized antennas over Oersted fields associated with focused electron beams to THz radiation. Below, further techniques and tools which are appropriate for exciting the magnetic systems of interest are discussed.

The sources of static non-collinear magnetic order are less intuitive. They will be discussed in section 2.1.2 in detail.

For clarity, first, the spin interaction and excitations are introduced from a quantum mechanical point of view, followed by the transition to the classical regime (2.1.1).

2.1.1 FROM QUANTUM MAGNETISM TO MICROMAGNETICS

Historically, the discovery of quantum physics and associated with that also quantum magnetism took place centuries after studying classical magnetism. This chapter illustrates the path backward from quantum to semiclassical theory and elucidates why a classical description is suitable to treat modern challenges in physics.

2.1.1.1   Exchange interaction: From quantum mechanics to the Heisenberg model

As outlined in various textbooks [59, 73], a system of two indistinguishable electrons with spin operators $\mathbf{s}_i$ can be described by the Hamiltonian

$$\hat{\mathcal{H}} = \frac{\hat{\mathbf{p}}_1^2}{2m_\mathrm{e}} + \frac{\hat{\mathbf{p}}_2^2}{2m_\mathrm{e}} + V(\mathbf{r}_1, \mathbf{r}_2) \,, \tag{2.1}$$

where $\hat{\mathbf{p}}_i$ denotes the momentum operator of electron i, m_e is the electron's mass and V is the interaction potential of the electrons. Though this Hamiltonian is independent of the electrons' spins, the Pauli exclusion principle demands that two electrons can not have the same quantum numbers, the eigenfunction of 2.1 $\psi(\mathbf{r}_1, \mathbf{r}_2)$ is only the orbital part of the two-electron wavefunction which has to be antisymmetric with respect to exchange of the electrons with spin quantum numbers s_i

$$\Psi(\mathbf{r}_1, \mathbf{r}_2; s_1, s_2) = -\Psi(\mathbf{r}_2, \mathbf{r}_1; s_2, s_1) \,. \tag{2.2}$$

In the absence of spin-orbit coupling, the wave function can be separated into a spatial ψ and a spin-dependent part χ:

$$\Psi(\mathbf{r}_1, \mathbf{r}_2; s_1, s_2) = \psi(\mathbf{r}_1, \mathbf{r}_2)\chi(s_1, s_2) \,. \tag{2.3}$$

For the system of two electrons, the total spin quantum number is $S = 0, 1$ which can be expressed in Dirac's "bra-ket" notation as the singlet state ($S = 0, S_z = 0$)

$$\chi_{(0;0)} = \frac{1}{\sqrt{2}} \left(|\uparrow\downarrow\rangle - |\downarrow\uparrow\rangle \right) \tag{2.4}$$

and the three triplet states ($S = 1, S_z = 1, 0, -1$)

$$\begin{aligned} \chi_{(1;1)} &= |\uparrow\uparrow\rangle \\ \chi_{(1;0)} &= \frac{1}{\sqrt{2}} \left(|\uparrow\downarrow\rangle + |\downarrow\uparrow\rangle \right) \\ \chi_{(1;-1)} &= |\downarrow\downarrow\rangle \,, \end{aligned} \tag{2.5}$$

giving

$$\begin{aligned} \Psi_\mathrm{s}(\mathbf{r}_1, \mathbf{r}_2; s_1, s_2) &= \psi_\mathrm{s}(\mathbf{r}_1, \mathbf{r}_2)\chi_{(0;0)} \\ \Psi_\mathrm{t}(\mathbf{r}_1, \mathbf{r}_2; s_1, s_2) &= \psi_\mathrm{t}(\mathbf{r}_1, \mathbf{r}_2)\chi_{(1;S_z)} \,. \end{aligned} \tag{2.6}$$

The singlet state is antisymmetric under particle exchange, whereas the triplet states are symmetric. Consequently, the spatial parts satisfy

$$|\psi_{\mathrm{s}}\rangle\,(\mathbf{r}_1,\mathbf{r}_2) = |\psi_{\mathrm{s}}\rangle\,(\mathbf{r}_2,\mathbf{r}_1)\ , \tag{2.7}$$

$$|\psi_{\mathrm{t}}\rangle\,(\mathbf{r}_1,\mathbf{r}_2) = -\,|\psi_{\mathrm{t}}\rangle\,(\mathbf{r}_2,\mathbf{r}_1)\ . \tag{2.8}$$

The Schrödinger equations read

$$\hat{\mathcal{H}}\Psi_{\mathrm{s}} = E_{\mathrm{s}}\Psi_{\mathrm{s}}\ , \tag{2.9}$$

$$\hat{\mathcal{H}}\Psi_{\mathrm{t}} = E_{\mathrm{t}}\Psi_{\mathrm{t}}\ , \tag{2.10}$$

meaning that though the Hamilton operator itself is not spin-dependent, the ground state may depend on S_z if the eigenenergies of the singlet and triplet state differ from each other: $E_{\mathrm{s}} \neq E_{\mathrm{t}}$. As the spatial and spin part of the wavefunction are correlated, it is possible to define a new Hamilton operator coupling $\mathbf{s}_1$ and $\mathbf{s}_2$ in spin space in contrast to $\hat{\mathcal{H}}$, which is restricted to the real space part of the wave function. By using the relations for the single electron's spin and the total spin

$$\hat{\mathbf{s}}_i^2 = \hbar^2 s_i(s_i+1) \overset{s_i=1/2}{=} \hbar^2\frac{3}{4} \tag{2.11}$$

$$\hat{\mathbf{S}}^2 = \hbar^2 S(S+1) \overset{!}{=} \hat{\mathbf{s}}_1^2 + \hat{\mathbf{s}}_2^2 + 2\hat{\mathbf{s}}_1\hat{\mathbf{s}}_2 \tag{2.12}$$

$$= \frac{3}{2}\hbar^2 + 2\hat{\mathbf{s}}_1\hat{\mathbf{s}}_2\ , \tag{2.13}$$

the scalar product results in

$$\hat{\mathbf{s}}_1 \cdot \hat{\mathbf{s}}_2 = \frac{\hbar^2}{2}S(S+1) - \frac{3\hbar^2}{4} \tag{2.14}$$

$$= \begin{cases} -\frac{3\hbar^2}{4} & ,\text{if } S=0 \\ \frac{\hbar^2}{4} & ,\text{if } S=1 \end{cases}. \tag{2.15}$$

The spin space Hamilton operator

$$\hat{\mathcal{H}}_\chi = \underbrace{\frac{1}{4}\left(E_{\mathrm{s}} + 3E_{\mathrm{t}}\right)}_{J_0} - \underbrace{\frac{1}{\hbar^2}\left(E_{\mathrm{s}} - E_{\mathrm{t}}\right)\hat{\mathbf{s}}_1 \cdot \hat{\mathbf{s}}_2}_{J_{12}} \tag{2.16}$$

can be constructed which results in the equations

$$\hat{\mathcal{H}}_\chi\Psi_{\mathrm{s}} = \psi_{\mathrm{s}}\hat{\mathcal{H}}_\chi\chi_{(0;0)} = E_{\mathrm{s}}\Psi_{\mathrm{s}}\ , \tag{2.17}$$

$$\hat{\mathcal{H}}_\chi\Psi_{\mathrm{t}} = \psi_{\mathrm{t}}\hat{\mathcal{H}}_\chi\chi_{(1;S_z)} = E_{\mathrm{t}}\Psi_{\mathrm{t}}\ . \tag{2.18}$$

The above Hamiltonian is also called the molecular Heisenberg model $\hat{\mathcal{H}}_\chi = J_0 - J_{12}\hat{\mathbf{s}}_1 \cdot \hat{\mathbf{s}}_2$. The sign of the exchange constant J_{12} defines whether a parallel ($J_{12} > 0$) or antiparallel ($J_{12} < 0$) ordering of the two spins is energetically favorable. This procedure can be extended to any number of electrons on a discrete lattice, which delivers the Heisenberg model for localized spins after dropping the constant energy terms J_0

$$\hat{\mathcal{H}} = -\sum_{\langle ij \rangle} \hat{\mathbf{s}}_i^\mathsf{T} \bar{J} \hat{\mathbf{s}}_j \ . \tag{2.19}$$

Here, the exchange integral $\bar{J}$, which is calculated over all neighboring pairs of electrons, is denoted as a 3×3 matrix. In the most simple cases of materials, which include isotropic (anti-)ferromagnetic ordering, a scalar J is typically sufficient and can be computed as $J = \frac{1}{3}\text{tr}(\bar{J})$. For an isotropic system, all directions are degenerate $J = J_{ii}$. In contrast, systems with broken isotropy (e.g., due to strain, surfaces, etc.) can exhibit different exchange parameters for the spin components: $J_{xx} \neq J_{yy} \neq J_{zz}$. Still, the diagonal elements of the exchange matrix either favor a parallel or an antiparallel orientation of the spin components – no non-collinear spin configurations are implied. Formally, this limitation dissolves with the inclusion of the off-diagonal terms, which can be grouped into the symmetric $\bar{J}^s = \frac{1}{2}\left(\bar{J} + \bar{J}^\mathsf{T}\right) - J\bar{I}$ and antisymmetric part $\bar{J}^a = \frac{1}{2}\left(\bar{J} - \bar{J}^\mathsf{T}\right)$

$$\bar{J} = J\bar{I} + \bar{J}^s + \bar{J}^a \ . \tag{2.20}$$

The symmetric off-diagonal contribution is also called biquadratic interaction. Details can be found in [73]. The evaluation of the term

$$\hat{\mathbf{s}}_i^\mathsf{T} \bar{J}^a \hat{\mathbf{s}}_j = \hat{\mathbf{s}}_i^\mathsf{T} \begin{pmatrix} 0 & J_{xy} - J_{yx} & J_{xz} - J_{zx} \\ J_{yx} - J_{xy} & 0 & J_{yz} - J_{zy} \\ J_{zx} - J_{xz} & J_{zy} - J_{yz} & 0 \end{pmatrix} \hat{\mathbf{s}}_j \tag{2.21}$$

$$= \frac{1}{2} \begin{pmatrix} J_{yz} - J_{zy} \\ J_{xz} - J_{zx} \\ J_{xy} - J_{yx} \end{pmatrix} \cdot \begin{pmatrix} \hat{s}_i^y \hat{s}_j^z - \hat{s}_i^z \hat{s}_j^y \\ \hat{s}_i^z \hat{s}_j^x - \hat{s}_i^x \hat{s}_j^z \\ \hat{s}_i^x \hat{s}_j^y - \hat{s}_i^y \hat{s}_j^x \end{pmatrix} \tag{2.22}$$

$$= \mathbf{D} \cdot \left(\hat{\mathbf{s}}_i \times \hat{\mathbf{s}}_j\right) \ , \tag{2.23}$$

leads to the introduction of the so-called Dzyaloshinskii-Moriya (DM) [28, 67] vector $\mathbf{D}$ and the Hamiltonian

$$\mathcal{H} = -\sum_{\langle ij \rangle} J\hat{\mathbf{s}}_i \cdot \hat{\mathbf{s}}_j - \sum_{\langle ij \rangle} \mathbf{D} \cdot (\hat{\mathbf{s}}_i \times \hat{\mathbf{s}}_j) - \sum_{\langle ij \rangle} \hat{\mathbf{s}}_i \bar{J}^s \hat{\mathbf{s}}_j \ . \tag{2.24}$$

Details on the characteristics and physical origin of the DM interaction (DMI) will be discussed in 2.1.2.5, but for now, it is sufficient to point out that the DMI is chiral in its nature and therefore inherently promotes a non-collinear magnetic ordering.

Until now, starting from the quantum mechanical Hamiltonian of indistinguishable electrons, it was shown that although the Hamiltonian itself is not spin-dependent, the resulting eigenenergies are, and the effective spin-spin interaction was expanded to arbitrary numbers of spins on a lattice, leading to the Heisenberg model (eq. (2.19)). Additionally, it was elaborated that the generalized formulation of the Heisenberg model (eq. (2.24)) allows for both symmetric and antisymmetric spin-spin interactions, which favor collinear or non-collinear spin configurations, respectively. In the framework of the semiclassical Heisenberg model, the different elements of the exchange tensor $\bar{J}$ have to be calculated from first principles like density functional theory (DFT) [41]. Eq. (2.24) is expressed in terms of the expectation values of the atoms' magnetic moments instead of the spin operators. In addition to neglecting quantum fluctuations, a limitation of this toolbox is the lack of scalability. As long as the length scale of magnetic textures (domain walls, skyrmions, spin spirals, spin waves) measures several units of the crystal's lattice constant, the computational effort is reasonable. For larger objects, the theory of *micromagnetism* serves as an optimized environment and will be explained in the next section.

2.1.1.2 EXCHANGE INTERACTION: MICROMAGNETICS

Micromagnetics [16] is the continuum version of the semiclassical Heisenberg model. The question is how the gap between a lattice-based theory and a model that exclusively treats the physical system in terms of continuous (vector) fields can be bridged.

The idea of micromagnetics is similar to *continuum mechanics*. There, physical quantities of distinct objects, e.g., the mass and charge of particles, are "smeared" out to mass and charge *densities*. Due to this transition, the information about every single particle is lost. However, physical problems can be transferred from a large number of coupled equations into partial differential equations of the introduced density fields. This procedure will be illustrated with the example of isotropic exchange interaction (first term in 2.24).

First, the spin operators $\hat{\mathbf{s}}_i$ are substituted with $S\mathbf{m}_i$, where S is the spin quantum

number and $\mathbf{m}_i$ is a classical unit vector pointing in the direction of $\langle \hat{\mathbf{s}}_i \rangle$. Also the former Hamiltonian now becomes a classical potential energy

$$E_{\mathrm{ex}} = -\sum_{\langle ij \rangle} JS^2 \mathbf{m}_i \cdot \mathbf{m}_j \ . \tag{2.25}$$

One of the main assumptions in micromagnetics is that the angle θ_{ij} between adjacent magnetic moments $\mathbf{m}_i = \mathbf{m}(\mathbf{r}_i)$ and $\mathbf{m}_j = \mathbf{m}(\mathbf{r}_j)$ is small, allowing us to expand $\mathbf{m}$ around the position $\mathbf{r}_i$ in a Taylor series:

$$\begin{aligned}
\mathbf{m}(\mathbf{r}_i + \mathbf{a}) = \ &\mathbf{m}(\mathbf{r}_i) \\
&+ \left(a_x \partial_x \mathbf{m}(\mathbf{r}) + a_y \partial_y \mathbf{m}(\mathbf{r}) + a_z \partial_z \mathbf{m}(\mathbf{r}) \right)|_{\mathbf{r}=\mathbf{r}_i} \\
&+ \frac{1}{2} \left(a_x^2 \partial_x^2 \mathbf{m}(\mathbf{r}) + a_y^2 \partial_y^2 \mathbf{m}(\mathbf{r}) + a_z^2 \partial_z^2 \mathbf{m}(\mathbf{r}) \right)|_{\mathbf{r}=\mathbf{r}_i} + \dots
\end{aligned} \tag{2.26}$$

For simplicity, a simple cubic crystal structure shall be assumed so that the sum over the nearest neighbors of $\mathbf{r}_i$ with the six displacement vectors $\mathbf{a}_{1,2} = \pm a\mathbf{e}_x$, $\mathbf{a}_{3,4} = \pm a\mathbf{e}_y$, $\mathbf{a}_{5,6} = \pm a\mathbf{e}_z$ can be calculated, where a is the lattice constant. Because each displacement vector has a complementary vector pointing in he opposite direction, the linear terms cancel out each other when substituting $\mathbf{m}_j$ in 2.26 with the expansion. Also, the constant contribution of the terms $\mathbf{m} \cdot \mathbf{m} = 1$ is neglected, giving

$$E_{\mathrm{ex}} = -\frac{JS^2}{2} \sum_i a^2 \mathbf{m}_i \cdot \left(\partial_x^2 \mathbf{m}_i + \partial_y^2 \mathbf{m}_i + \partial_z^2 \mathbf{m}_i \right) \ . \tag{2.27}$$

The term can further be simplified by using the normalization of $\mathbf{m}$

$$1 = \mathbf{m} \cdot \mathbf{m} \qquad\qquad\qquad\qquad | \, \partial_x^2 \tag{2.28}$$

$$0 = 2(\partial_x \mathbf{m})^2 + 2\mathbf{m} \cdot \partial_x^2 \mathbf{m} \tag{2.29}$$

$$\Leftrightarrow \mathbf{m} \cdot \partial_x^2 \mathbf{m} = -(\partial_x \mathbf{m})^2 \tag{2.30}$$

$$\Rightarrow E_{\mathrm{ex}} = \frac{JS^2}{2a} \sum_i a^3 \left[(\partial_x \mathbf{m}_i)^2 + (\partial_y \mathbf{m}_i)^2 + (\partial_z \mathbf{m}_i)^2 \right] \ . \tag{2.31}$$

So far, 2.31 includes a sum over all unit cells of the system, each occupying a volume $V = a^3$. By transitioning to the continuum limit and using the nabla operator ∇, the micromagnetic expression of the exchange energy is obtained

$$E_{\mathrm{ex}} = \int_V A \left[(\nabla m_x(\mathbf{r}))^2 + (\nabla m_y(\mathbf{r}))^2 + (\nabla m_z(\mathbf{r}))^2 \right] \mathrm{d}V \ . \tag{2.32}$$

Here the exchange stiffness $A = \frac{JS^2}{2a} n$ is introduced, where n denotes the number of

magnetic atoms in the unit cell.

Further contributions to the micromagnetic energy will be discussed in 2.1.2. The big advantages of 2.32 compared to 2.24 are two-fold. Firstly, the exchange energy can now be minimized by optimizing a vector field in contrast to a set of magnetization vectors $\mathbf{m}_i$, which allows for analytical solutions for simple cases. Secondly, the ability to treat large systems is obtained. It is not mandatory to solve each unit cell of the crystal's lattice anymore. This comes at the cost of the inability to study effects that are relevant on the scale of the lattice constant. Also, 2.32 was derived using a Taylor-expansion up to the second order in $\mathbf{m}$, assuming small deviations between adjacent m. This limits the theory of micromagnetism to magnetic textures that have spatial extensions considerably larger than the lattice constant of the crystal.

2.1.2 MAGNETOSTATICS

The approach of micromagnetics is to treat a magnetic system as the vector field $\mathbf{m}(\mathbf{r})$ spanning a length scale up to hundreds of μm. In the absence of time-dependent external fields, classical magnetic order can be described by pure magnetostatic equations. The free energy functional $\mathcal{F}[\mathbf{m}]$ completely defines a magnetic system. It consists of multiple contributions, for example,

$$\mathcal{F}[\mathbf{m}] = \mathcal{F}_{\mathrm{z}} + \mathcal{F}_{\mathrm{a}} + \mathcal{F}_{\mathrm{ex}} + \mathcal{F}_{\mathrm{dm}} + \mathcal{F}_{\mathrm{d}} + \dots , \tag{2.33}$$

the Zeeman energy $\mathcal{F}_{\mathrm{z}}$, anisotropy $\mathcal{F}_{\mathrm{a}}$, exchange interaction $\mathcal{F}_{\mathrm{ex}}$, Dzyaloshinskii-Moriya interaction $\mathcal{F}_{\mathrm{dm}}$ and demagnetizing energy $\mathcal{F}_{\mathrm{d}}$. Further contributions account for magnetoelastic [15] or magnetoelectric [34] coupling mechanisms. Usually, the free energy is calculated from the free energy density f

$$\mathcal{F}[\mathbf{m}] = \int f[\mathbf{m}(\mathbf{r})]\mathrm{d}V . \tag{2.34}$$

Different energy contributions are separated into *local*, *non-local* and *global* constituents.

2.1.2.1 LOCAL ENERGY CONTRIBUTIONS

Local (L) in this context means that only the magnetization field itself and no derivatives of it nor non-local interactions $\mathbf{m}(\mathbf{r}) \leftrightarrow \mathbf{m}(\mathbf{r}')$ are relevant. All local contributions to the free energy density can be expressed as a function of $\mathbf{m}$ at position $\mathbf{r}$ and local fields, summarized as $\mathbf{X}$,

$$f_{\mathrm{L}}[\mathbf{m}](\mathbf{r}, \mathbf{X}(\mathbf{r})) = f_{\mathrm{L}}(\mathbf{m}(\mathbf{r}), \mathbf{X}(\mathbf{r})) . \tag{2.35}$$

The most intuitive candidate for such a contribution is the Zeeman energy, which reflects the energy of a magnetic dipole moment $\boldsymbol{\mu}$ exposed to a magnetic field $\mathbf{H}_{\mathrm{ext}}$

$$E_{\mathrm{z}} = -\mu_0 \boldsymbol{\mu} \cdot \mathbf{H} \,. \tag{2.36}$$

The Zeeman energy in minimal when a parallel orientation $\boldsymbol{\mu}\|\mathbf{B}$ is realized. As for the exchange interaction, the transition to a continuum description is straightforward

$$E_{\mathrm{z}} = -\mu_0 \sum_i \boldsymbol{\mu}_i \cdot \mathbf{H}_{\mathrm{ext}} \tag{2.37}$$

$$\Rightarrow \quad \begin{aligned} \mathcal{F}_{\mathrm{z}} &= -\mu_0 \int M_{\mathrm{s}} \mathbf{m} \cdot \mathbf{H}_{\mathrm{ext}} \mathrm{d}V \\ f_{\mathrm{z}} &= -\mu_0 M_{\mathrm{s}} \mathbf{m} \cdot \mathbf{H}_{\mathrm{ext}}. \end{aligned} \tag{2.38}$$

A second contribution that depends on the local orientation of the magnetization only is the anisotropy f_{a}, e.g.:

$$f_{\mathrm{a}} = \begin{cases} -K_{\mathrm{u}1} \left(\mathbf{m} \cdot \mathbf{e}_{\mathrm{u}}\right)^2 - K_{\mathrm{u}2} \left(\mathbf{m} \cdot \mathbf{e}_{\mathrm{u}}\right)^4 \,, \text{ uniaxial} \\ -K_{\mathrm{c}1} \left(m_x^2 m_y^2 + m_y^2 m_z^2 + m_z^2 m_x^2\right) - K_{\mathrm{c}2} \left(m_x m_y m_z\right)^2 \,, \text{ cubic} \end{cases} \tag{2.39}$$

$K_{\mathrm{u}1,\mathrm{u}2}$ are the first and second-order uniaxial anisotropy-energy parameters with the corresponding anisotropy direction $\mathbf{e}_{\mathrm{u}}$. Other common anisotropy terms are of cubic or hexagonal symmetry. For simplicity, the cubic anisotropy symmetry axes in eq. (2.39) coincide with the Cartesian coordinate directions xyz; $K_{\mathrm{c}1,\mathrm{c}2}$ indicate cubic anisotropy constants of the first and second order. The most prominent origin of anisotropic energy contributions is the so-called magnetocrystalline anisotropy, resulting from the spin-orbit interaction [38, 23]. In a crystal, electron orbitals are connected to the crystal structure. Due to the spin-orbit coupling, the electrons' spins are also influenced by the crystal's characteristics. Hence the spin aligns preferably along well-defined crystallographic axes in bulk materials as denoted in eq. (2.39), which can be obtained from density functional calculations [41, 58, 48, 11] or measured experimentally [91, 18].

Mechanical stress deforming the crystal lattice can change the spin-orbit interaction strength between electron orbitals and the lattice electric fields. This affects the anisotropy constants. The inverse phenomenon, deforming a magnetic sample by changing its magnetization direction, is known as magnetostriction [20]. Secondly, surfaces or interfaces naturally break the crystal symmetry. Due to the asymmetric environment of surface atoms, their magnetic properties differ from the bulk atoms. The impact of surface effects increases for thin films, which can even change the energetically favorable magnetization from in-plane to out-of-plane for ultrathin films [24]. Shape anisotropy is a further

contribution. In contrast to the surface anisotropy, the shape anisotropy incorporates the sample's whole geometry in terms of the dipole-dipole interactions of all magnetic moments. Since this mathematical formulation is highly non-local, this contribution will be discussed in section 2.1.2.3.

2.1.2.2 NON-LOCAL ENERGY CONTRIBUTIONS

Non-local (NL) contributions to the free energy density allow for the local change of the magnetization

$$f_{\mathrm{NL}}[\mathbf{m}](\mathbf{r}, \mathbf{X}(\mathbf{r})) = f_{\mathrm{NL}}(\mathbf{m}(\mathbf{r}), \partial_i^j \mathbf{m}(\mathbf{r}), \mathbf{X}(\mathbf{r})) \ . \tag{2.40}$$

One contribution, including the local change of the magnetization, is the exchange interaction, which was already discussed in detail in 2.1.1

$$f_{\mathrm{ex}}(\mathbf{r}) = A \left[(\nabla m_x(\mathbf{r}))^2 + (\nabla m_y(\mathbf{r}))^2 + (\nabla m_z(\mathbf{r}))^2 \right] \ . \tag{2.41}$$

Another example is the DMI, also known as antisymmetric exchange, which can be separated into bulk and interfacial DMI

$$f_{\mathrm{dm}}^{\mathrm{bulk}}(\mathbf{r}) = D\mathbf{m}(\mathbf{r}) \cdot (\nabla \times \mathbf{m}(\mathbf{r})) \tag{2.42}$$

$$f_{\mathrm{dm}}^{\mathrm{int}}(\mathbf{r}) = D\mathbf{m}(\mathbf{r}) \cdot (\partial_x \mathbf{m}(\mathbf{r}) \times \mathbf{e}_x - \partial_y \mathbf{m}(\mathbf{r}) \times \mathbf{e}_y) \ , \tag{2.43}$$

where D is the DMI coupling constant. The origins and consequences of the chiral DMI for both bulk and interfacial systems will be discussed in more detail in section 2.1.2.5.

A third representative stems from the emergent electric polarization of non-collinear magnetic textures [68], which in turn couples to external electric fields $\mathcal{F}_{me} \propto \mathbf{P} \cdot \mathbf{E}$ [108]. In the continuum limit, the magnetically induced electric polarization reads

$$\mathbf{P} = \xi_{\mathrm{me}} \left[(\mathbf{m} \cdot \nabla)\mathbf{m} - \mathbf{m}(\nabla \cdot \mathbf{m}) \right] \ , \tag{2.44}$$

with the magnetoelectric coupling constant ξ_{me}.

2.1.2.3 LONG-RANGE INTERACTIONS

All terms discussed so far solely require evaluating the magnetization and its derivative at the coordinate vector **r** and a subsequent integration over the whole space to calculate the total free energy. A much more demanding task is to consider the magnetization's dipolar self-interaction, which generates the so-called *demagnetizing field*. The demagnetizing

field depends on the full magnetization vector field

$$f_{\mathrm{d}}(\mathbf{r}) = f_{\mathrm{d}}(\mathbf{m}(\mathbf{r}), \mathbf{H}_{\mathrm{d}}[\mathbf{m}](\mathbf{r})) \tag{2.45}$$

$$= -\frac{1}{2}\mu_0 M_{\mathrm{s}}\mathbf{m}(\mathbf{r}) \cdot \mathbf{H}_{\mathrm{d}}[\mathbf{m}](\mathbf{r}) \ . \tag{2.46}$$

For deriving the demagnetizing field, one can start from the basics of electrostatics: Maxwell's equations. More precisely, Ampère's circuital law in the absence of electric currents and Gauss's law for magnetism, following [47](chapter 2), and [1]

$$\nabla \times \mathbf{H} = 0 \tag{2.47}$$

$$\nabla \cdot \mathbf{B} = 0 \ . \tag{2.48}$$

As the curl of the magnetic field $\mathbf{H}$ vanishes, it can be defined as the gradient of a magnetic scalar potential ϕ

$$\mathbf{H} = -\nabla\phi \ . \tag{2.49}$$

The magnetic flux density $\mathbf{B}$ includes both the magnetic field and the magnetization $\mathbf{M}$

$$\mathbf{B} = \mu_0 \left(\mathbf{H} + \mathbf{M} \right) \tag{2.50}$$

$$0 \stackrel{\text{eq. (2.48)}}{=} \frac{1}{\mu_0}\nabla \cdot \mathbf{B} = \nabla \cdot (-\nabla\phi) + \nabla \cdot \mathbf{M} \tag{2.51}$$

$$\Delta\phi = \nabla \cdot \mathbf{M} \tag{2.52}$$

Finite physical systems demand a vanishing scalar potential $\lim\limits_{r\to\infty} \phi = 0$. The Poisson equation eq. (2.52) can be solved using the Green's function of the Laplace operator

$$\phi(\mathbf{r}) = \frac{1}{4\pi}\int \mathcal{G}(\mathbf{r}, \mathbf{r}')\nabla' \cdot \mathbf{M}'\mathrm{d}V' \tag{2.53}$$

$$= \frac{1}{4\pi}\int \frac{1}{|\mathbf{r} - \mathbf{r}'|}\nabla' \cdot \mathbf{M}(\mathbf{r}')\mathrm{d}V' \ . \tag{2.54}$$

Integration by parts and exploiting that $\mathbf{M}$ vanishes outside the sample results in

$$= \frac{1}{4\pi}\int \mathbf{M}(\mathbf{r}') \cdot \nabla'\frac{1}{|\mathbf{r} - \mathbf{r}'|}\mathrm{d}V' \ . \tag{2.55}$$

For uniformly magnetized, ellipsoidal samples, eq. (2.55) can be solved analytically and results in a uniform demagnetizing field $\mathbf{H}_{\mathrm{d}}$ [23] (pp. 35). In these cases, $\mathbf{H}_{\mathrm{d}}$ is defined by the macroscopic magnetization $\mathbf{M}$ and the demagnetizing matrix, represented by a 3×3,

symmetric, unit trace matrix $\bar{\mathcal{N}}$

$$\mathbf{H}_{\mathrm{d}} = -\bar{\mathcal{N}}\mathbf{M} \, . \tag{2.56}$$

Even for geometries that are strongly deviating from the ellipsoidal system, approximate fields can be estimated, e.g., by calculating the limit of the tensor for a vanishing length of one of the principal axes of the ellipsoid, which leads to the case of a magnetic thin film [74]. Still, this procedure is limited to uniform magnetic states, which is not sufficient for the non-collinear magnetic textures studied throughout this work. Therefore, numerical methods for efficiently solving eq. (2.55) are inevitable. One widely used approach is to extend the above-mentioned demagnetizing matrix to a space-dependent demagnetizing tensor field, which projects the microscopic magnetic configuration onto the field $\mathbf{H}_{\mathrm{d}}$. Eqs. (2.49) and (2.55) deliver

$$\mathbf{H}_{\mathrm{d}} = -\frac{1}{4\pi}\nabla\int \mathbf{M}(\mathbf{r}') \cdot \nabla'\frac{1}{|\mathbf{r}-\mathbf{r}'|}\mathrm{d}V' \tag{2.57}$$

$$= \int \bar{\mathcal{N}}(\mathbf{r}-\mathbf{r}')\mathbf{M}(\mathbf{r}')\mathrm{d}\mathbf{r}' \, . \tag{2.58}$$

The demagnetizing tensor field can be evaluated efficiently on a discretized lattice with cuboid cells occupying a volume of V_i, in which a homogeneous magnetization in each of the cells is assumed

$$\bar{\mathcal{N}}(\mathbf{r}_i - \mathbf{r}_j) = \frac{1}{4\pi V_i}\int_{V_i}\mathrm{d}\mathbf{r}\nabla\int_{V_j}\nabla'\frac{1}{|\mathbf{r}-\mathbf{r}'|}\mathrm{d}\mathbf{r}' \, . \tag{2.59}$$

The discrete convolution integral, resulting from eq. (2.58), can be simplified using the convolution theorem for two functions f, g

$$F\{f * g\} = F\{f\} \cdot F\{g\} \qquad\qquad |F^{-1} \tag{2.60}$$

$$f * g = F^{-1}\{F\{f\} \cdot F\{g\}\} \tag{2.61}$$

$$\mathbf{H}_{\mathrm{d}}(\mathbf{r}_i) = -\sum_j \bar{\mathcal{N}}(\mathbf{r}_i - \mathbf{r}_j)\mathbf{M}(\mathbf{r}_j) \tag{2.62}$$

$$= -F^{-1}\{F\{\bar{\mathcal{N}}\} \cdot F\{\mathbf{M}\}\} \, , \tag{2.63}$$

where "·" represents the point-wise multiplication of the fields $\bar{\mathcal{N}}$ and $\mathbf{M}$. This procedure allows replacing the full convolution integral by a tensor vector multiplication in Fourier

space and subsequent inverse Fourier transformation. The benefit of this operation is that the demagnetizing tensor has to be calculated only once for calculating the demagnetizing fields, as the Fourier transform separates the geometrical contribution from the actual magnetization field configuration. Because of this reduction of computational effort and the advanced computational methods for calculating discrete Fourier transformations, this technique is applied in widely used micromagnetic simulation codes like `mumax` [99] and `OOMMF` [25].

2.1.2.4 NON-COLLINEAR MAGNETIC ORDERING

What ingredients are necessary to achieve a non-collinear magnetic ground state?

The local contributions exclusively are not sufficient to stabilize a non-collinear state (as long as there is no external, space-dependent field applied). The energy surface $f_{\mathrm{L}}(\mathbf{m}(\mathbf{r}, \mathbf{X}))$ at every position vector $\mathbf{r}$ is identical; hence the local energy minima are isotropic.

Every higher-order term may lead to competing interaction mechanisms. An example is the competition of exchange and demagnetizing energy, which requires a magnetic material in a finite geometry. Exemplary results are shown in fig. 2.1 for a $1 \times 1 \times 0.02 \mu \mathrm{m}^3$ Py (permalloy) model system. Panels (a-c) are obtained from minimizing the energy for an initial configuration pointing in the (111)-direction, where (a) is a relaxed state without demagnetizing field, hence favoring a uniform alignment no matter in which direction. (b) includes $\mathbf{H}_{\mathrm{d}}$, but periodic boundary conditions in the in-plane directions are applied, resulting in an in-plane uniform state. (c) shows the effect of open boundaries, leading to a non-collinear state. Instead, the magnetization favors an orientation along the surface of the boundaries minimizing the stray fields at the expense of the exchange energy. For this particular example, the configuration shown in (c) is only a metastable state. The ground state is represented by a vortex-like state, as shown in fig. 2.1(d). Here, four regions preferably pointing along the sample edge are separated by 90° domain walls, the vortex core points in $\pm z$ direction, which results in a four times degenerate state ground state with the rotational sense of the vortex as a second free parameter. Already from this simple model system, it can be seen that non-collinearity is induced when boundaries are included. Examples are domain walls and magnetic vortices [10, 86, 102, 76, 85].

A different approach is followed in the field of magnetic heterostructures, where different materials are grown on top of each other. In the case of the so-called "exchange-spring magnet" [55], hard and weak magnetic layers, meaning a large and small magnetocrystalline anisotropy, are combined. Because of this combination, hysteresis curves show multiple transition points instead of just a single switching event for pure materials. At first, the soft magnet switches, but due to the exchange-coupled interface region, the
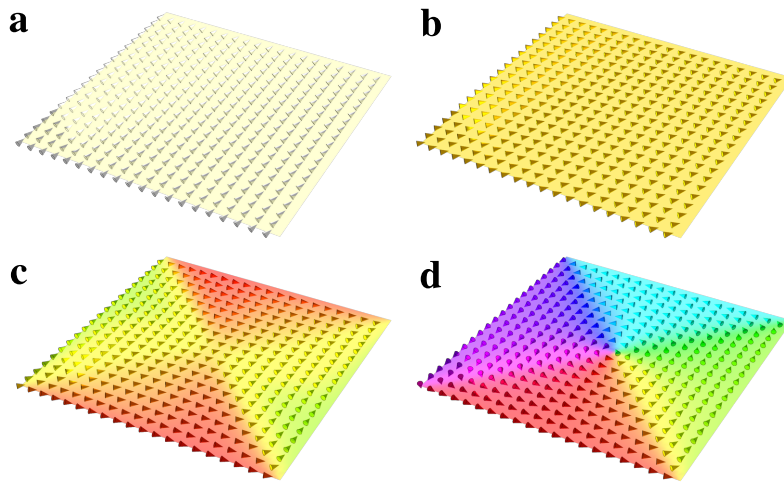
Figure 2.1: Relaxed magnetic states of a $1 \times 1 \times 0.02\mu\text{m}^3$ Py sample. For (a) only the exchange energy has been considered, (b)-(d) also include the demagnetizing fields. In (b) periodic boundary conditions are applied, leading to a randomly oriented in-plane state, whereas (c) and (d) show results for open boundary conditions. Several metastable states can be adopted.

magnetization is canted. The competition of interlayer interaction and intralayer interaction that are both symmetric leads to non-collinear ordering. A similar setup is studied in [AFS3], where antiferromagnetically coupled oxide layers are studied. In Fig. 6 of the publication, the canting of the magnetization close to the interface is visualized.

Today, systems that host a non-collinear ordering are of high interest. One of the most discussed driving mechanisms of non-collinearity is the antisymmetric Dzyaloshinskii-Moriya interaction. It competes with the Heisenberg exchange and the magnetocrystalline anisotropy and is also chirality sensitive. Details on the DMI are discussed in the next section.

2.1.2.5 DZYALOSHINSKII-MORIYA INTERACTION

The theoretical foundation of the DMI is based on the works of Moriya [67] and Dzyaloshinskii [28], in which they disclose the spin-orbit coupling between spins and the crystal lattice as the origin of the previously discovered *weak ferromagnetism*. Eq. 2.24 demonstrates that the DMI vector $\mathbf{D}_{ij}$, coupling two spins $\hat{\mathbf{s}}_i$ and $\hat{\mathbf{s}}_j$ or two classical magnetic moments $\mathbf{M}_i$ and $\mathbf{M}_j$ has to be antisymmetric $\mathbf{D}_{ij} = -\mathbf{D}_{ji}$. Moriya defined the so-called Moriya rules [67], with which the orientation of the DMI vectors can be obtained from symmetry arguments. For the rules, the midpoint position vector between i and j, $\mathbf{r}_m = \frac{\mathbf{r}_i + \mathbf{r}_j}{2}$ and the connecting vector $\mathbf{r}_{ij} = \mathbf{r}_j - \mathbf{r}_i$ are defined. The rules read:

1. If $\mathbf{r}_m$ is a center of inversion symmetry, then $\mathbf{D}_{ij} = \mathbf{0}$.

2. If a mirror plane $P : \mathbf{r}_{ij} \cdot (\mathbf{r} - \mathbf{r}_m) = 0$ exists, then $\mathbf{D}_{ij} \perp \mathbf{r}_{ij}$.

3. If a mirror plane $P : \mathbf{n} \cdot (\mathbf{r} - \mathbf{r}_i) = 0$, with $\mathbf{n} \perp \mathbf{r}_{ij}$, exists, then $\mathbf{D}_{ij} \parallel \mathbf{n}$.

4. If a two-fold rotation symmetry axis $\mathbf{a}$ passes through $\mathbf{r}_m$, then $\mathbf{D}_{ij} \perp \mathbf{a}$.

5. If there exists an n-fold symmetry axis $\mathbf{a} \parallel \mathbf{r}_{ij}$, then $\mathbf{D}_{ij} \parallel \mathbf{r}_{ij}$.

In essence, one can state that finite DMI vectors arise when a crystal lacks bulk inversion symmetry.

However, when the bulk crystal is symmetric under space inversion, finite DMI can occur when surface effects become important, as they explicitly break inversion symmetry. This is the reason why DMI related phenomena are distinguished between *bulk* and *interfacial* DMI. Throughout this work, especially chapter 3, only the interfacial type of DMI is relevant.

In 1980 [33], Lévy and Fert derived an analytic formula of the DMI of two magnetic atoms based on the scattering of conduction electrons at a third (non-magnetic) impurity atom. In this context, impurity does not necessarily mean that atoms contaminate a crystal, but it can also be the combination of different layers, where the atomic positions enable the application of one or more of the Moriya rules. The simplest case is given when the impurity atom k is located in a mirror plane, bisecting the distance of spin i and j ($\mathbf{n} \parallel \mathbf{r}_{ij}$), but is displaced with respect to the straight connection $\mathbf{r}_{ij}$ such that it is also an element of the mirror plane with $\mathbf{n} \parallel (\mathbf{r}_i - \mathbf{r}_k) \times (\mathbf{r}_j - \mathbf{r}_k) \perp \mathbf{r}_{ij}$. In this case, both the inversion and rotational symmetry are broken, and the Moriya rules dictate the orientation of the DMI vector

$$\mathbf{D}_{ijk} \parallel \mathbf{r}_{ik} \times \mathbf{r}_{jk} \,. \tag{2.64}$$

Note that if there exists another impurity atom ℓ that is placed at the position $\mathbf{r}_k$ mirrored at the $\mathbf{D}_{ijk}$-$\mathbf{r}_{ij}$ plane, $\mathbf{D}_{ijk}$ and $\mathbf{D}_{ij\ell}$ cancel out each other. This is why a surface is needed to enable this symmetry-based interaction mechanism. Fig. 2.2 shows the geometric arrangement of the magnetic atoms at positions $\mathbf{r}_{i,j}$, the non-magnetic impurity atom at $\mathbf{r}_k$ and the resulting DMI vector $\mathbf{D}_{ijk} \parallel \mathbf{r}_{ik} \times \mathbf{r}_{jk}$. In [33], a quantitative formula for calculating the DMI vector is given by

$$\mathbf{D}_{ijk} = -V_1 \frac{\sin \left[\kappa_F \left(|\mathbf{r}_{jk}| + |\mathbf{r}_{ki}| + |\mathbf{r}_{ij}| \right) + \pi Z_d / 10 \right]}{|\mathbf{r}_{jk}|^3 |\mathbf{r}_{ki}|^3 |\mathbf{r}_{ij}|} \left(\mathbf{r}_{ik} \cdot \mathbf{r}_{jk} \right) \left(\mathbf{r}_{ik} \times \mathbf{r}_{jk} \right) \tag{2.65}$$

$$V_1 = \frac{135\pi}{32} \frac{\lambda_d \Gamma^2}{E_F^2 \kappa_F^3} \sin \left[\frac{\pi}{10} Z_d \right] \tag{2.66}$$

where κ_F, E_F are the Fermi wave vector and Fermi energy, λ_d is the spin-orbit interaction parameter of the impurity atom, Γ quantifies the interaction between localized spins
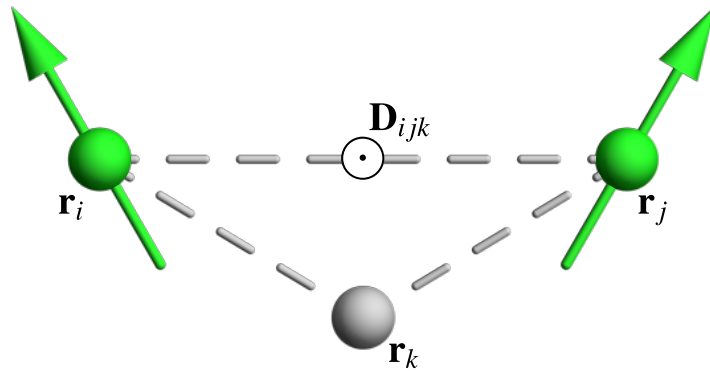
Figure 2.2: Dzyaloshinskii-Moriya vector $\mathbf{D}_{ijk}$ resulting from the positions of the atomic spins $\mathbf{r}_{i,j}$ and the non-magnetic impurity at $\mathbf{r}_k$.

and the conduction electrons and Z_d is the number of d electrons of the considered transition metal impurity atoms. From this result, strong effects of the interfacial DMI can be expected for systems in which a non-magnetic material with a large spin-orbit coupling is involved. For constant distances of i, j, and k, the term $(\mathbf{r}_{ik} \cdot \mathbf{r}_{jk})(\mathbf{r}_{ik} \times \mathbf{r}_{jk})$ is maximized for an angle $\angle IKJ = n\pi/4, n \in \{1, 3, 5, 7\}$.

In summary, as discussed in the case of atomistic spins (eq. (2.24) and section 2.1.2.5) and according to that in the application to the micromagnetic formalism (eqs. (2.42) and (2.43)), the DMI inherently favors non-collinear spin structures. This energy contribution becomes especially important when dealing with topologically non-trivial magnetic states (section 2.3), as non-triviality fundamentally demands non-collinearity.

2.2 MAGNETIZATION DYNAMICS

2.2.1 LANDAU-LIFSHITZ-GILBERT EQUATION

Though eq. (2.33) is perfectly suited for finding magnetic ground states, it does not include information on the equation of motion of the magnetization. The dynamic behavior of magnetic systems constitutes the main scope of this work and can be well described by the Landau-Lifshitz-Gilbert equation for a wide range of applications. In this section, the equation of motion for the magnetization will be derived. Before discussing dissipative terms, an energy-conserving system is assumed, meaning

$$E = -\mathbf{M} \cdot \mathbf{B}_{\text{eff}} = \text{const} , \tag{2.67}$$

where the effective magnetic field $\mathbf{B}_{\text{eff}}$ represents the intensive parameter acting on the magnetic moment $\mathbf{M}$ defined as

$$\mathbf{B}_{\text{eff}} = -\nabla_{\mathbf{M}}\mathcal{F} \ . \tag{2.68}$$

For a quantum mechanical spin operator $\hat{\mathbf{s}}$, the time propagation for each of the vector's components can be computed via the Heisenberg equation of motion

$$\partial_t \hat{s}_j = -\frac{\mathrm{i}}{\hbar}[\hat{s}_j, \hat{\mathcal{H}}] \ . \tag{2.69}$$

In general, the Hamiltonian $\hat{\mathcal{H}}$ depends on the spin; hence it can be expanded in terms of the spin operator [37]

$$\hat{\mathcal{H}} = \sum_{k=x,y,z} \hat{s}_k \partial_{\hat{s}_k} \hat{\mathcal{H}} + \mathcal{O}(\hat{s}_k^2) \tag{2.70}$$

$$\Rightarrow [\hat{s}_j, \hat{\mathcal{H}}] = \left[\hat{s}_j, \sum_{k=x,y,z} \hat{s}_k \partial_{\hat{s}_k} \hat{\mathcal{H}} + \mathcal{O}(\hat{s}_k^2) \right] \ . \tag{2.71}$$

The commutator of the spins is

$$[\hat{s}_j, \hat{s}_k] = \mathrm{i}\hbar\epsilon_{jk\ell}\hat{s}_\ell \tag{2.72}$$

$$\Rightarrow [\hat{s}_j, \hat{\mathcal{H}}] = \mathrm{i}\hbar \sum_{k=x,y,z} \epsilon_{jk\ell}\partial_{\hat{s}_k}\hat{\mathcal{H}}\hat{s}_\ell + \mathcal{O}(s_k^2) \tag{2.73}$$

$$\Rightarrow [\hat{\mathbf{s}}, \hat{\mathcal{H}}] = \mathrm{i}\hbar \left(\nabla_{\hat{\mathbf{s}}}\hat{\mathcal{H}} \times \hat{\mathbf{s}} \right) + \mathcal{O}(\hat{\mathbf{s}}^2) \tag{2.74}$$

so that the Heisenberg equation of motion eq. (2.69) results in

$$\partial_t \hat{\mathbf{s}} = -\hat{\mathbf{s}} \times \nabla_{\hat{\mathbf{s}}}\hat{\mathcal{H}} \tag{2.75}$$

in the linear response regime.

Following the Ehrenfest theorem [29], in the classical limit, the quantum mechanical operators of the spin ($\hat{\mathbf{s}}$) and energy ($\hat{\mathcal{H}}$) can be substituted by their expectation values

$$\hat{\mathbf{s}} \to \langle \hat{\mathbf{s}} \rangle = \mathbf{s} = -\frac{\mathbf{M}}{\gamma} \tag{2.76}$$

$$\hat{H} \to \mathcal{F}[\mathbf{M}] \ , \tag{2.77}$$

where $\gamma = g\mu_{\text{B}}/\hbar$ is the gyromagnetic ratio and g is the Landé factor. This substitution

results in

$$\partial_t \mathbf{M} = -\gamma \mathbf{M} \times \mathbf{B}_{\text{eff}} \ , \tag{2.78}$$

describing the precessional motion of the magnetization around the axis of the effective magnetic field. eq. (2.78) is symmetric under time inversion; hence no alignment between effective magnetic fields and the magnetization can be achieved, which contradicts the observations, for instance, achieved from hysteresis measurements. Because of this lack of agreement, an additional damping term was introduced to eq. (2.78) by Landau and Lifshitz in 1935 [60], which was later refined by Gilbert [40]. The structure of the damping term was chosen such that the corresponding damping torque $\mathbf{T}_{\text{damp}}$ points perpendicular to the motion of the magnetization vector

$$\mathbf{T}_{\text{damp}} \propto \mathbf{M} \times \partial_t \mathbf{M} \ . \tag{2.79}$$

Therefore the magnetization orientation converges to the direction of the effective field without affecting the fundamental Larmor frequency of the precession. This addition leads to the Landau-Lifshitz equation

$$\partial_t \mathbf{M} = -\gamma \mathbf{M} \times \mathbf{B}_{\text{eff}} + \frac{\alpha}{M_{\text{s}}} \mathbf{M} \times \partial_t \mathbf{M} \ , \tag{2.80}$$

where α is the phenomenological, dimensionless Gilbert damping parameter. Gilbert refined the equation using an improved formulation of damping effects and the unit vectors $\mathbf{m} = \mathbf{M}/M_{\text{s}}$ [40]

$$\partial_t \mathbf{m} = -\frac{\gamma}{1 + \alpha^2} \left[\mathbf{m} \times \mathbf{B}_{\text{eff}} + \alpha \mathbf{m} \times (\mathbf{m} \times \mathbf{B}_{\text{eff}}) \right] \ . \tag{2.81}$$

For finite values of α, the motion of $\mathbf{m}$ describes a spiral trajectory, eventually aligning with $\mathbf{B}_{\text{eff}}$, as shown in fig. 2.3. The origins for effective damping are manifold [39], including mechanisms such as spin-lattice interaction, which leads to an energy transfer from magnetic into phononic excitation or radiation damping due to the field emitted by the oscillating magnetic dipoles. A third main dissipation path is the spin-charge interaction, which leads to long lifetimes of magnetic excitations in insulating materials such as yttrium iron garnet (YIG).
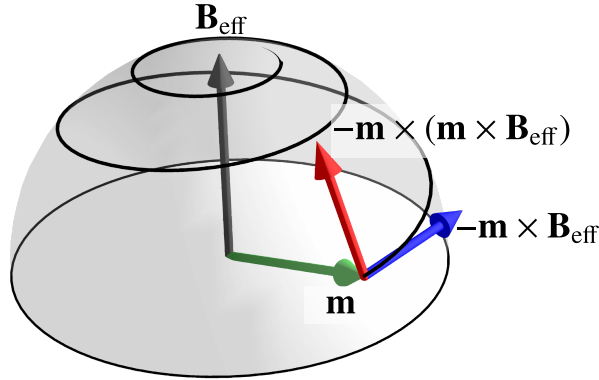
Figure 2.3: Magnetization dynamics following the LLG. The magnetic moment (green arrow) in the presence of a magnetic field (gray arrow) follows a spiral trajectory, resulting from the precessional torque (blue arrow) and the Gilbert damping torque (red arrow). Eventually, the magnetization aligns with the magnetic field.-

2.2.2   DRIVING MAGNETIZATION DYNAMICS

For driving a magnetic system out of its equilibrium state, a plethora of tools is available. External magnetic fields can be tailored spatially and temporally for matching the properties of the excitations of interest. Approaches utilize nanostructured samples [63], over the ultrafast control of electronic states accompanied by localized magnetic fields in atoms and molecules [113, 104], and macroscopic electromagnetic waves as used for ferromagnetic resonance experiments [54, 31].

Two control mechanisms fundamentally different from applying a tailored external magnetic field are spin currents and thermal effects, which will be discussed next.

2.2.2.1   SPIN-TRANSFER AND SPIN-ORBIT TORQUE

So far, localized magnetic moments have been discussed exclusively. Moreover, localized moments interact with the spin of delocalized electrons as they occur, for example, in metals or in the conduction bands of semiconductors. If there is a preferential orientation of the electrons' spins, it is called a spin-polarized current with spin polarization $\mathbf{s}$. Different approaches for estimating the degree of spin polarization can be used. The Stoner model is one of these, assuming a relative energy shift Δ between majority and minority bands of a free electron dispersion $\epsilon(\mathbf{k})$ [92]

$$\epsilon(\mathbf{k}) = \frac{\hbar^2}{2m^*}k^2 + \frac{\Delta}{2}\sigma_z \, . \tag{2.82}$$

A second simplified model is the so-called *s-d interaction* [53, 61], where *s* represents the delocalized electrons, and *d* stands for the localized electronic states of the magnetic atoms. Along the lines of the Heisenberg exchange interaction, the s-d interaction can be written as

$$E_{\mathrm{sd}} = -J_{\mathrm{sd}}\mathbf{s} \cdot \mathbf{M} \, , \tag{2.83}$$

where $J_{\mathrm{sd}}\mathbf{s}$ acts as an additional effective magnetic field on the local magnetization $\mathbf{M}$ (cf. eq. (2.67)) and vice versa, the electric current becomes polarized by the magnetization of the localized atoms. From eq. (2.81), it is clear that only the fraction of the spin that is normal to the magnetization impacts the dynamics given by the LLG.

Generally, spin torques arise whenever the flow of spin angular momentum is non-uniform, meaning sources and sinks of the spin current are present [80]. This can occur for different reasons; the two main situations of current mediated spin torques are as follows: First, as discussed, an electrical current is polarized when flowing through a magnetic material. This process can be understood as spin filtering since the orientation of the magnetization dictates a preferential spin direction. If this spin-polarized current subsequently enters a region with a deviating orientation of the magnetization, it is reoriented. Consequently, the opposite torque acts on the magnetic system. Effectively, the torque is transferred from one magnetic region to another one. Hence, it is called *spin-transfer torque* (STT). Second, a spin current can be generated in a non-magnetic layer grown on top of a magnetic material. Typically, heavy metal materials are used for this endeavor, as this material class is accompanied by a large spin-orbit coupling (SOC). When an electrical current is applied in-plane, a pure out-of-plane spin current is resulting from the spin Hall effect [26, 27](fig. 2.4). This leads to a spin accumulation/depletion at the interface, eventually exciting the magnetic system. The origin of this kind of spin torque lies in the heavy metal SOC, and hence it is called *spin-orbit torque* (SOT). The spin-current $\bar{j}_{\mathrm{s}}$ itself is a tensor quantity that includes the flow of all spin components in an arbitrary direction

$$\bar{j}_{\mathrm{s}} = \mathbf{v} \otimes \mathbf{s} \, , \tag{2.84}$$

though, for cases where an external voltage is applied, the direction of the spin current is defined by the crystal symmetry and the orientation of the electric current. A more detailed discussion of the fast-growing field of spin-torque-related phenomena can be found in review articles by Ralph and Stiles [80] and Song et al. [90].

Both the STT and SOT can be included into the micromagnetic framework. In the case of the software package `mumax3` [99], which will be mostly used in the rest of this thesis, the implementation is based on the seminal publications of Zhang and Li [112] and
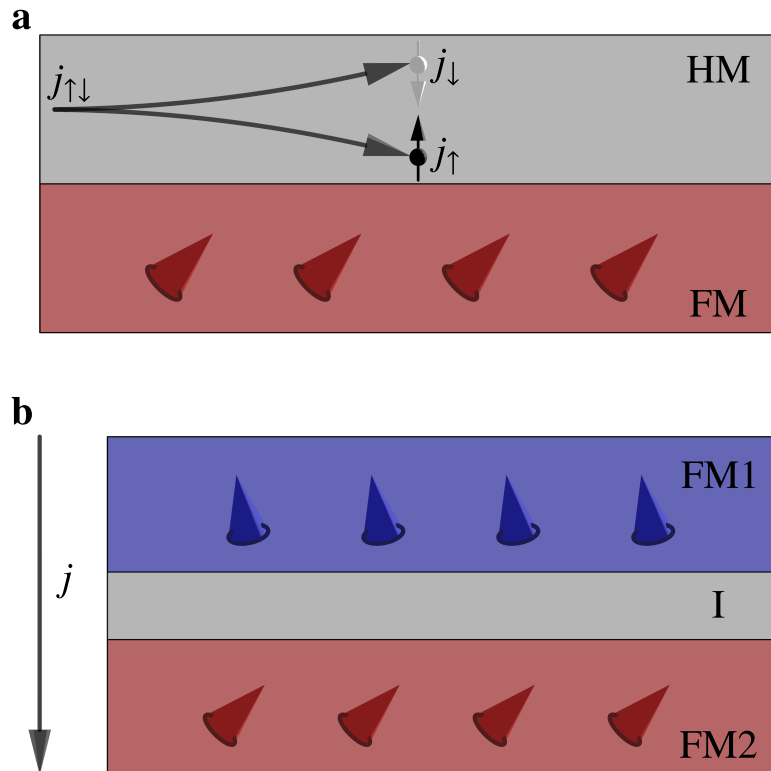
Figure 2.4: Schematic representation of SOT (a) and STT(b). In (a), an electric current j is flowing in a heavy metal layer (HM). The spin-orbit coupling within the HM leads to a separation of electrons with opposite spin. The resulting spin accumulation at the interface affects the ferromagnetic layer (FM) in form of the SOT. In (b), an electric current flows through two ferromagnetic regions, FM1 and FM2, with different magnetization directions and an optional intermediate non-magnetic layer (I). The STT results from the change of polarization of the conduction electrons $\mathbf{s} \parallel \mathbf{m}_{FM1} \Rightarrow \mathbf{s} \parallel \mathbf{m}_{FM2}$.

Slonczewski et al. [89]. The torque equations read

$$\mathbf{T}_{\text{ZL}} = \frac{1}{1 + \alpha^2} \left\{ (1 + \xi\alpha)\, \mathbf{m} \times [\mathbf{m} \times (\mathbf{u} \cdot \nabla)\, \mathbf{m}] + (\xi - \alpha)\, \mathbf{m} \times (\mathbf{u} \cdot \nabla)\, \mathbf{m} \right\} \quad (2.85)$$

$$\mathbf{u} = \frac{\mu_{\text{B}}}{2eM_{\text{s}}\left(1 + \xi^2\right)} \mathbf{j} \,, \quad (2.86)$$

where ξ is the degree of non-adiabaticity of the spin-transfer torque. The Zhang-Li term represents the STT for a non-uniform magnetization, including magnetic multilayers and non-collinear magnetic textures. The Slonczewski term assumes a fixed magnetic layer with orientation $\mathbf{m}_{\text{F}}$ on top (z-direction) of the system of interest

$$\mathbf{T}_{\text{SL}} = \beta \frac{\epsilon - \alpha\epsilon'}{1 + \alpha^2} [\mathbf{m} \times (\mathbf{m}_{\text{F}} \times \mathbf{m})] - \beta \frac{\epsilon' - \alpha\epsilon}{1 + \alpha^2} \mathbf{m} \times \mathbf{m}_{\text{F}} \quad (2.87)$$

$$\beta = \frac{\gamma j_z \hbar}{M_{\text{s}} ed} \quad (2.88)$$

$$\epsilon = \frac{P(\mathbf{r}, t)\Lambda^2}{(\Lambda^2 + 1) + (\Lambda^2 - 1)(\mathbf{m} \cdot \mathbf{m}_{\text{F}})} \,, \quad (2.89)$$

where d defines the thickness of the spacer layer separating the fixed layer and the free layer, which is characterized further by the Slonczewski Λ parameter. ϵ' denotes the secondary spin torque parameter and P is the spin polarization in the direction of $\mathbf{m}_{\text{F}}$. As the above definition does not explicitly consider the stray field of the fixed layer but only the generated spin current, this method is as well suited to describe SOT phenomena.

The question now is, for which purpose the STT or SOT can be used. The first approach to move non-collinear magnetic textures by currents was accomplished by Berger in 1978 [6]. He theoretically studied the effects of electric currents passing through a domain wall, including magnetoresistance and the drag of domain walls. Magnetoresistance effects in antiferromagnetically coupled multilayers became significant after discovering the giant magnetoresistance (GMR) by the groups of Grünberg, and Fert [4, 9], who have both been awarded the Nobel Prize in 2007. The most important application of the GMR is in magnetic field sensors as reading heads of hard disk drives. Details on both the fundamental and applied side can be found in a recent textbook by Reig, de Freitas, and Mukhopadhyay [81]. The second main observation of Berger [6] - the drag of domain walls - inspired researchers as well, for example, in the idea of the so-called *racetrack memory*. Parkin et al. [75, 76] proposed to use a sequence of magnetic domains as a carrier of information in ferromagnetic tracks. The key feature of this concept is the possibility to shift this domain wall train back and forth by electrical currents, whereby an information bit can be moved to a reading head. This does not only avoid physically moving objects like in the spinning hard disk, but it also enables the extension of storage devices into the third dimension, as only a small area of the racetrack is required to

be in contact with the reading heads at the device's surface. Even though sample preparation techniques improved drastically since 1978, several technical obstacles hindered racetrack devices from entering mass production. One main issue is the large current densities needed for displacing domain wall trains along the track. Fert, Cros, and Sampaio proposed a possible solution [32] by discussing the utilization of magnetic skyrmions instead of domain walls. Details on these magnetic quasiparticles are given in section 2.3.2, based on which our works in chapter 3 are carried out.

2.2.2.2   THERMAL EFFECTS

Elevated temperatures result in thermal noise [17], the spin Seebeck effect due to temperature gradients [96], and a complete demagnetization above the Curie temperature. For low temperatures with respect to the Curie temperature, an additional stochastic field can be added into the LLG as [17, 99]

$$\mathbf{B}_{\mathrm{T}} = \boldsymbol{\eta}\sqrt{\frac{2\alpha k_{\mathrm{B}} T}{M_{\mathrm{s}}\gamma\Delta V\Delta t}}\,, \tag{2.90}$$

where T is the temperature and η is a randomly oriented vector from a normal distribution evaluated for each simulation step. By this method, the skyrmion diffusion is modeled in [AFS5].

An approach that bridges the gap between the stochastic LLG eqs. (2.81) and (2.90) and the Ginzburg-Landau theory of phase transitions is the Landau-Lifshitz-Bloch equation (LLB) [36, 30]. The LLB allows not only for a transverse perturbation of the magnetization but also for a longitudinal excitation and relaxation characterized by the corresponding damping parameters $\alpha_{\parallel,\perp}$.

2.2.3   SPIN WAVES

The LLG is suited to treat magnetic excitations far from the equilibrium states by mapping all effective interactions onto the space-dependent effective magnetic field. In the low-energy limit, *magnons* are the fundamental quantized excitations of an ordered magnetic state. Let us assume a Heisenberg ferromagnetic chain ($J > 0$) of N spins with the exchange energy

$$\mathcal{H} = -\sum_i J\mathbf{s}_i \cdot \mathbf{s}_{i+1}\,. \tag{2.91}$$

The ground state is completely uniform, whereas an excited state can be modeled as a single reduced spin

$$|\psi_0\rangle = |s \ldots s\rangle \tag{2.92}$$

$$|\psi_1\rangle = |s \ldots s, s-1, s \ldots s\rangle \ , \tag{2.93}$$

which entails a dramatic energy rise of Js. In the following, low-energy excitations will be derived following Reference [59]. Let us start with a spin $\mathbf{s}_i$ considering exchange and external fields and derive the Heisenberg equation of motion as in section 2.2.1

$$\mathcal{H} = -\frac{1}{2}\sum_{\langle ij\rangle} J\mathbf{s}_i \cdot \mathbf{s}_j - g\mu_B B \sum_i s_i^z \tag{2.94}$$

$$\frac{\mathrm{d}\mathbf{s}_i}{\mathrm{d}t} = \frac{\mathrm{i}}{\hbar}[\mathcal{H}, \mathbf{s}_i] \ . \tag{2.95}$$

Eq. 2.95 can again be simplified by applying the commutator relations of spins, leading to

$$\frac{\mathrm{d}\mathbf{s}_i}{\mathrm{d}t} = -\frac{1}{\hbar}\left(\sum_j J\mathbf{s}_j + g\mu_B B\mathbf{e}_z\right) \times \mathbf{s}_i \ , \tag{2.96}$$

or written out for the different components

$$\hbar\frac{\mathrm{d}s_i^x}{\mathrm{d}t} = -\sum_j J(s_j^y s_i^z - s_j^z s_i^y) + g\mu_B B s_i^y \tag{2.97}$$

$$\hbar\frac{\mathrm{d}s_i^y}{\mathrm{d}t} = -\sum_j J(s_j^z s_i^x - s_j^x s_i^z) - g\mu_B B s_i^x \tag{2.98}$$

$$\hbar\frac{\mathrm{d}s_i^z}{\mathrm{d}t} = -\sum_j J(s_j^x s_i^y - s_j^y s_i^x) \ . \tag{2.99}$$

As low-energy excitations of the ordered state are in the center of interest, $s_i^z \approx s$ can be assumed, which leads to a vanishing time derivative in eq. (2.99), and to two coupled equations for the x and y component of the spin

$$\hbar\frac{\mathrm{d}s_i^x}{\mathrm{d}t} = -s\sum_j J(s_j^y - s_i^y) + g\mu_B B s_i^y \tag{2.100}$$

$$\hbar\frac{\mathrm{d}s_i^y}{\mathrm{d}t} = -s\sum_j J(s_i^x - s_j^x) - g\mu_B B s_i^x \ . \tag{2.101}$$

Those can be separated by introducing the ladder operators

$$s_i^\pm = s_i^x \pm \mathrm{i} s_i^y \tag{2.102}$$

$$\Rightarrow \hbar\frac{\mathrm{d}s_i^\pm}{\mathrm{d}t} = \mp\mathrm{i}\left[s\sum_j J\left(s_i^\pm - s_j^\pm\right) + g\mu_\mathrm{B}Bs_i^\pm\right] , \tag{2.103}$$

where still the coupled elements at sites i and j (and corresponding positions $\mathbf{R}_i$, $\mathbf{R}_j$) have to be dealt with . A simplification can be achieved when rewriting the equation in the momentum space

$$s_\mathbf{k}^\pm = \frac{1}{\sqrt{N}}\sum_{\mathbf{R}_i} s_i^\pm \mathrm{e}^{-i\mathbf{k}\cdot\mathbf{R}_i} \tag{2.104}$$

$$J(\mathbf{k}) = \sum_{\Delta\mathbf{R}} J_{\Delta\mathbf{R}}\mathrm{e}^{-i\mathbf{k}\cdot\Delta\mathbf{R}} \tag{2.105}$$

$$\hbar\frac{\mathrm{d}s_\mathbf{k}^\pm}{\mathrm{d}t} = \mp\mathrm{i}\left\{s[J(\mathbf{0}) - J(\mathbf{k})] + ig\mu_\mathrm{B}B\right\}s_\mathbf{k}^\pm , \tag{2.106}$$

resulting in complete separation of the wave vectors $\mathbf{k}$, which can be solved by

$$s_\mathbf{k}^\pm = M_\mathbf{k}\mathrm{e}^{\mp\mathrm{i}\omega_\mathbf{k}t+\mathrm{i}\alpha_\mathbf{k}} \tag{2.107}$$

$$\hbar\omega_\mathbf{k} = s[J(\mathbf{0}) - J(\mathbf{k})] + g\mu_\mathrm{B}B , \tag{2.108}$$

including a random phase $\alpha_\mathbf{k}$. If only a single mode $s_\mathbf{k}^-$ is excited with the amplitude $M_\mathbf{k}$, the physical components in real space can be obtained,

$$s_i^-(t) = \frac{1}{\sqrt{N}}\mathrm{e}^{\mathrm{i}\mathbf{k}\cdot\mathbf{R}_i}s_\mathbf{k}^- \tag{2.109}$$

$$= \frac{M_\mathbf{k}}{\sqrt{N}}\mathrm{e}^{\mathrm{i}(\mathbf{k}\cdot\mathbf{R}_i+\omega_\mathbf{k}t+\alpha_\mathbf{k})} \tag{2.110}$$

$$s_i^x(t) = \frac{M_\mathbf{k}}{\sqrt{N}}\cos\left(\mathbf{k}\cdot\mathbf{R}_i + \omega_\mathbf{k} + \alpha_\mathbf{k}\right)$$

$$s_i^y(t) = \frac{M_\mathbf{k}}{\sqrt{N}}\sin\left(\mathbf{k}\cdot\mathbf{R}_i + \omega_\mathbf{k} + \alpha_\mathbf{k}\right) \tag{2.111}$$

$$s_i^z(t) \simeq s$$

which is the classical expression for a plane wave. Hence a spin wave with the dispersion relation as shown eq. (2.108) is received. For a given crystal structure and relevant exchange interaction strengths (nearest neighbor, next-nearest neighbor, . . .), the Fourier transform of $J(\mathbf{k})$ can be evaluated.

Let us take a simple cubic lattice with the lattice constant a, involving nearest neighbor

interaction constant J

$$J(\mathbf{k}) = \sum_{\Delta \mathbf{R}} J \mathrm{e}^{-\mathrm{i}\mathbf{k}\cdot\Delta\mathbf{R}} \tag{2.112}$$

$$= 2J \left[\cos(k_x a) + \cos(k_y a) + \cos(k_z a)\right] \tag{2.113}$$

$$\Rightarrow \omega_{\mathbf{k}} = \frac{2Js}{\hbar} \left(3 - \cos k_x a + \cos k_y a + \cos k_z a\right) . \tag{2.114}$$

By expanding the resulting dispersion relation for small $k_i a$, the well known quadratic relation for ferromagnets

$$\omega_{\mathbf{k}} \approx \frac{Js}{\hbar} \sum_i k_i^2 a^2 , \tag{2.115}$$

is obtained.

2.3 TOPOLOGY IN MAGNETISM

2.3.1 OVERVIEW

During the last 50 years, adapting concepts from the mathematical field of *topology* led to seminal results. A prominent example of the significant influence of topology on physics is the Nobel prize from 2016, which was awarded to Kosterlitz, Thouless, and Haldane *for theoretical discoveries of topological phase transitions and topological phases of matter*. Their works include topology-based models for phase transitions in two-dimensional magnets [57] and for the (fractional) quantized electric Hall effect [94, 42, 43]. Another milestone was accomplished by Berry, whose work on geometrical phases in quantum mechanics [7] was a key foundation for the subsequent research in the field of topological electronic matter, including the theoretical prediction [52, 35] and experimental discovery [56, 46, 66] of topological insulators. All these and more effects in electronic matter utilize topological invariants calculated from the electronic band-structure; hence they are governed by reciprocal space characteristics of a material. Another branch of topology-inspired solid-state physics deals with the real space topology of spin structures. The most prominent example of such a spin structure is the *magnetic skyrmion*, which will be discussed in more detail in the next section.

2.3.2 MAGNETIC SKYRMIONS

The term *skyrmion* is based on the British physicist Tony H. R. Skyrme. He worked in the field of nuclear physics in the early 1960s, especially on non-collinear configurations

of baryonic fields [87, 88]. The corresponding quasiparticle-like excitations were later named skyrmions. Almost 30 years after his seminal papers, Bogdanov and Yablonskii transferred this concept to topologically non-trivial excitations in magnetic crystals [14]. While they initially analyzed special crystal symmetries that stabilize skyrmion crystals in the spin texture, the existence and stability of isolated magnetic skyrmions (in the following just called skyrmions) was predicted a few years later [12] and analyzed for a different kind of stabilization mechanisms [13]. The first skyrmion lattice was observed experimentally in bulk MnSi crystals [69] utilizing neutron scattering techniques. By manipulating an external bias field's strength and the temperature, they revealed a rich magnetic phase diagram. In this diagram, they spotted an area where the magnetic texture shows a sixfold structure, which can be identified as a two-dimensional skyrmion crystal. Shortly after, this result was affirmed by real space Lorentz transmission electron microscopy (TEM) [109]. Subsequently, aside from the bulk crystals of the B20 material class, another system that can host magnetic skyrmions was discovered: ultrathin Fe layers grown on Ir(111) [45]. This material shows that not only the non-reciprocity of B20 materials breaks the chirality degeneration of spin-textures, but also the broken inversion symmetry due to an interface in combination with the large SOC of the heavy metal Ir, as discussed in section 2.1.2.5. As it could be expected from the different mathematical shapes of bulk and interfacial DMI (sections 2.1.2.2 and 2.1.2.5), the resulting skyrmion textures differ and are characterized as Bloch and Néel skyrmions in analogy to magnetic domain walls (fig. 2.5). Following these seminal publications, research efforts in the field of skyrmions grew enormously. One reason for the wide interest is the predicted topological protection of skyrmions in contrast to topologically non-trivial states, like conventional domain walls. To make use of this protection, it is important to distinguish topologically trivial from non-trivial states. Though it is easy to distinguish a single-domain state from a two-domain configuration and quantify this, e.g., by measuring a reduced net magnetization, this task becomes more challenging, for instance, when differentiating between a magnetic skyrmion and a magnetic domain wall. For the latter, the concept of topological charges was adopted from the mathematical field of topology. By introducing this charge, also called topological number or winding number, magnetic configurations can be classified into topologically trivial and topologically non-trivial states. In compact, topological protection means that there exists no continuous transformation from a non-trivial vector field to a trivial one. The topological charge N_T for a normalized magnetization field $\mathbf{m}(\mathbf{r})$ is defined by

$$N_\mathrm{T} = \frac{1}{4\pi} \int n_\mathrm{T}(x,y)\mathrm{d}x\mathrm{d}y \tag{2.116}$$

$$n_\mathrm{T} = \mathbf{m} \cdot (\partial_x\mathbf{m} \times \partial_y\mathbf{m}) \ , \tag{2.117}$$

where n_T is the topological charge density. For an infinite system, the N_T can only take integer values, where $N_\mathrm{T} = 0$ corresponds to the trivial state, as, e.g. a homogeneous magnetization leads to a vanishing integrand.

Ideally, the energy barrier separating topologically distinct states is infinite. This contradicts the experimental achievements of creating and annihilating skyrmions, which has been achieved, e.g., by using STM tips [82], in-plane currents that "blow" skyrmions through geometric constrictions similar to soap bubbles [49], or by locally applying SOT [19]. Until today, no manipulation mechanism is universally superior to the other techniques, as multiple requirements such as speed, reliability, and low energy consumption have to be fulfilled.

In the course of exploiting not only the topological stability but also the mobility of magnetic skyrmions, e.g., for realizing racetrack storage devices, the second important operation is displace skyrmions precisely. This operation can effectively be implemented by applying electric currents that can either generate SOT or STT to displace the magnetic quasiparticles (cf. section 2.2.2.1). One crucial effect hindering the linear movement of topologically non-trivial objects is the *skyrmion Hall effect* [50], which describes the transversal deflection of a skyrmion when driving it with an electric current. This phenomenon is similar to the movement of a charged particle in the presence of an external magnetic field in the classical Hall effect [44] and originates from the real space topological properties of skyrmions [110, 71]. The quasiparticle's movement can efficiently be described by the Thiele equation [93], which considers current-driven motion as well as effective damping and topology-dependent transversal deflection. Details can be found in [AFS4] along with an approach on how to avoid the unfavorable skyrmion Hall effect by employing skyrmioniums instead of conventional skyrmions.

2.3.3 TOPOLOGICAL ELECTROMAGNETIC WAVES

The second example of excitations for which topological features can be identified in reciprocal and real space are spin waves. An excellent overview of band-structure-based topological magnons can be found in [64]. Our approach towards topological effects of spin wave transport properties is based on the real space structure, more precisely, the
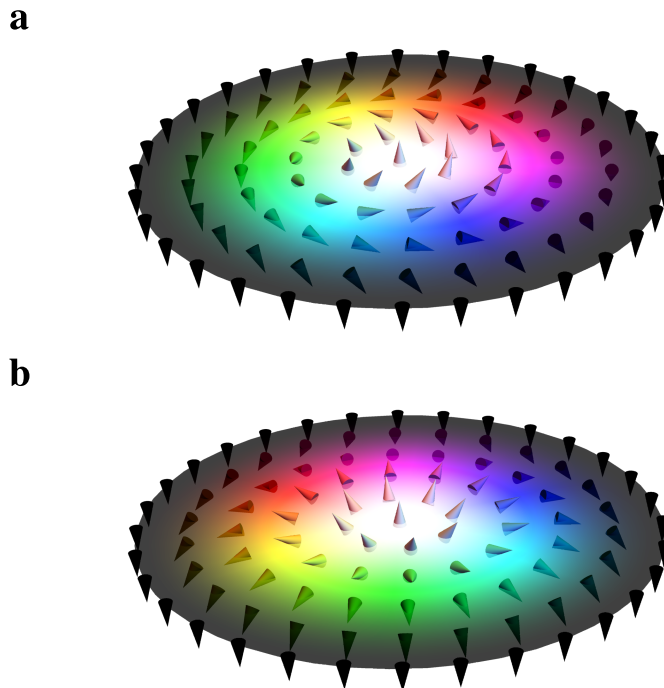
a

b

Figure 2.5: Magnetic configuration of a Bloch (a) and a Néel (b) skyrmion.

geometry of the spin waves' wavefronts. The works discussed in chapter 4 are derived in
analogy to the so-called *twisted light*, also known as optical vortices, representing light
that carries a finite OAM. Today, a whole family of beams carrying OAM is well es-
tablished in physics, including twisted electrons [97, 101], neutrons [22] and foremost
photons [3, 106]. The main motivations for applying twisted beams instead of conven-
tional signals are two-fold. First, the OAM is an additional degree of freedom on top
of a wave's frequency and spin angular momentum (SAM). Second, as the OAM can, in
principle, take arbitrary integer values, it enables a drastic increase in the bandwidth of
communication devices. A proof-of-principle experiment on a photonic chip has been
realized by Chen et al. in Ref. [21]. Secondly, the OAM carried by the beam can be
transferred, for example, to drive electron dynamics in quantum rings [79], semiconduc-
tors [103] or molecules [104]. Subsequently, it was shown how such optically excited
electromagnetic fields could be utilized to drive the local magnetization dynamics in the
vicinity of a target C_{60} molecule [AFS1].

Mathematically, twisted beams can be described in cylindrical coordinates as

$$\boldsymbol{\psi}(\rho, \varphi, z, t) = \mathbf{e}f(\rho, z)g(t)\mathrm{e}^{i\ell\varphi} , \qquad (2.118)$$

where $\mathbf{e}$ is the polarization vector, $g(t)$ is the temporal profile and $f(\rho, z)$ defines the cylindrically symmetric part of the beam's spatial structure. The interesting topological features arise due to the additional angular-dependent phase $\ell\varphi$. Dictated by the periodic angular dependence

$$\boldsymbol{\psi}(\rho, \varphi, z, t) = \boldsymbol{\psi}(\rho, \varphi + 2\pi, z, t) , \qquad (2.119)$$

the topological charge ℓ has to take integer values. This phase factor results in a helical wavefront, as sketched in fig. 2.6. Another direct consequence of this term is a phase singularity at the optical axis $\rho = 0$, which demands a vanishing intensity of the twisted fields for $\ell \neq 0$. Common approaches for such spatial profiles involve Bessel- or Laguerre-Gaussian functions [3, 106]. In chapter 4, our results on extending the family of twisted beams by twisted spin wave modes are discussed.
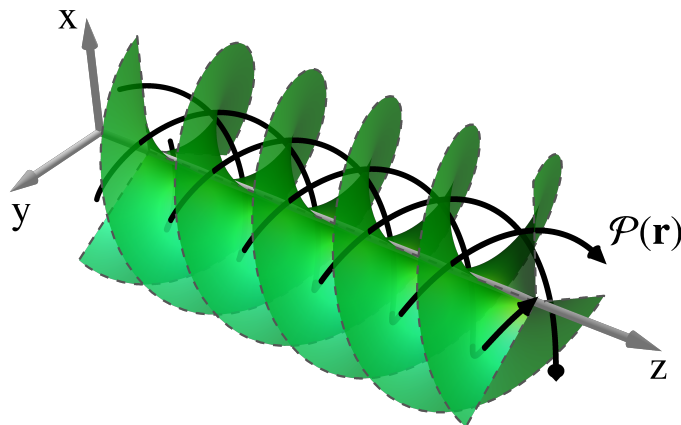
Figure 2.6: Helical wavefront (green) and local Poynting vector $\mathcal{P}(\mathbf{r})$ (black) of a twisted field with $\ell = 3$ propagating in z-direction.

CHAPTER 3

RESULTS A: CONTROL OF MAGNETIC QUASIPARTICLES

In this chapter, different mechanisms for manipulating magnetic quasiparticles are presented. In contrast to displacing objects like skyrmions, which can be realized, for example, by in-plane electric currents, their creation and annihilation are fundamentally more challenging. This increased difficulty partially arises due to the topologically non-trivial spin structure leading to their topological protection. In short, if one tries to deform a skyrmion into a uniformly magnetized state continuously, one naturally ends at a point where a spin-flip is necessary, which is associated with large activation energy. Here, four examples of controlling magnetic textures are presented, each focusing on a different aspect of controlling particle-like spin textures.

The first work, *Ultrafast imprinting of topologically protected magnetic textures via pulsed electrons* [AFS2] [1] investigates the ultrafast speed limit of such processes, which can be achieved by the concept of precessional switching [95]. The idea is that magnetic moments can be accelerated with maximum action when the applied field points orthogonal to the magnetization vector. The electromagnetic fields generated by strongly accelerated electron bunches are utilized according to the experimental capabilities of linear accelerator facilities. As a result, it was shown that chiral magnetic configurations can be manipulated deterministically on the time scale of a few picoseconds.

The second publication, *Electrical writing, deleting, reading, and moving of magnetic skyrmioniums in a racetrack device* [AFS4] [2] utilizes a different kind of magnetic object,

---

[1]Reprinted from (A. F. Schäffer, H. A. Dürr, J. Berakdar, Ultrafast imprinting of topologically protected magnetic textures via pulsed electrons, *Appl. Phys. Lett.* **111**, 3, 032403 (2017); Ref. AFS2), with the permission of AIP Publishing.

[2] Reprinted from (B. Göbel, A. F. Schäffer, J. Berakdar, I. Mertig, S. S. P. Parkin, Electrical writing, deleting, reading, and moving of magnetic skyrmioniums in a racetrack device, *Sci. Rep.* **9**, 12119 (2019); Ref. AFS4). Published by Springer Nature under the terms of the Creative Commons Attribution 4.0 license.

the so-called 2π-skyrmion or skyrmionium [5, 114, 111]. This quasiparticle can be understood as a skyrmion located in the center of a second skyrmion with opposite polarity, characterized by a vanishing topological charge. Because of this, the usually unfavorable skyrmion-Hall effect[50] fades away as well. For the endeavor of proposing a skyrmionium based racetrack memory concept, all four constituents of an operating device are simulated: writing, moving, reading, and deleting. For the creation and annihilation process, an optoelectrical approach exciting localized ultra-short current pulses for generating a spatiotemporally tailored SOT was adopted [105]. Regarding the quasiparticle detection, the topological Hall effect [72, 107, 62] was utilized. Though the net topological charge vanishes, electrodes on the length scale of the skyrmionium's size can measure the local change of the topological Hall conductivity.

In the third publication, *Rotating edge-field driven processing of chiral spin textures in racetrack devices* [AFS9] [3] , another point of action of magnetic skyrmions was exploited. This is the lowered energy barrier for creation/annihilation at the sample boundary [70, 8, 98]. Similar to Ref. [100], magnetic objects are created locally from the rim of the sample by local rotating magnetic fields. On top of that, once skyrmions or domain walls are created, they are repelled from the creation point and actuated by subsequent field rotations at the sample rim. In a well-defined regime of quasiparticle densities, the magnetic objects can be injected and extracted reproducibly.

Summarizing works [AFS2],[AFS4], and [AFS9], different approaches were pursued to manipulate isolated skyrmionic excitations. All three techniques share the achieved deterministic switching ability, which is the fundamental requirement for storage devices. However, each procedure involves several advantages (e.g., speed, efficiency) and disadvantages (e.g., complex nanostructures, high field densities) that have to be gauged carefully before application.

The fourth work, titled *Stochastic dynamics and pattern formation of geometrically confined skyrmions* [AFS5] [4] deals with a different control parameter of skyrmions – an elevated temperature. Usually, thermal magnetization fluctuations can destabilize magnetically stored information in hard disk drives [84]. Similarly, also skyrmions can collapse because of strong thermal effective fields [83]. In this publication, the diffusion characteristics of skyrmions in confined geometries like magnetic nanoislands were investigated. The stochastic skyrmions' dynamics leads to a time-dependent pattern formation of the

---

[3]Reprinted from (A. F. Schäffer, P. Siegl, M. Stier, T. Posske, J. Berakdar, M. Thorwart, R. Wiesendanger, E. Y. Vedmedenko, Rotating edge-field driven processing of chiral spin textures in racetrack devices, *Sci. Rep.* **10**, 20400 (2020); Ref. AFS9). Published by Springer Nature under the terms of the Creative Commons Attribution 4.0 license.

[4]Reprinted from (A. F. Schäffer, L. Rózsa, J. Berakdar, E. Y. Vedmedenko, R. Wiesendanger, Stochastic dynamics and pattern formation of geometrically confined skyrmions, *Commun. Phys.* **2**, 1, 72 (2019); Ref. AFS5). Published by Springer Nature under the terms of the Creative Commons Attribution 4.0 license.

skyrmion density, involving two distinct time regimes. The results point out possible challenges for storage applications, as the (relative) positions of skyrmions are vaguely defined and the topological number is hard to determine with time-integrated measurements. However, this obstacle can be fruitfully utilized developing new skyrmion-based computing concepts like probabilistic or reservoir computing [77, 78], where the stochastic but manipulable motion is beneficial.

Ultrafast imprinting of topologically protected magnetic textures via pulsed electrons

A. F. Schäffer,[1] H. A. Dürr,[2] and J. Berakdar[1]

[1]*Institut für Physik, Martin-Luther-Universität Halle-Wittenberg, 06099 Halle (Saale), Germany*
[2]*Stanford Institute for Materials and Energy Sciences, SLAC National Accelerator Laboratory, 2575 Sand Hill Road, Menlo Park, California 94025, USA*

Short electron pulses are demonstrated to trigger and control magnetic excitations, even at low electron current densities. We show that the tangential magnetic field surrounding a picosecond electron pulse can imprint topologically protected magnetic textures such as skyrmions in a sample with a residual Dzyaloshinskii-Moriya spin-orbital coupling. Characteristics of the created excitations such as the topological charge can be steered via the duration and the strength of the electron pulses. The study points to a possible way for a spatiotemporally controlled generation of skyrmionic excitations. *Published by AIP Publishing.* [http://dx.doi.org/10.1063/1.4991521]

Tremendous progress has been made towards the realization of spatiotemporally controlled electron sources for probing the material local structural, electronic, and magnetic dynamics.[1–4] Working schemes rely on the electron emission from a laser-irradiated nanoscale apex[5–22] with the electron pulse duration being controllable with the laser pulse duration. The laser intensity dictates the electron number in the bunch. Electron pulse acceleration and control are achievable by intense THz fields.[23–25] Here, we explore the potential of very fast, relativistic electron bunches for a possible control of the magnetic dynamics in a thin film which is traversed by the electrons. Our focus is on the sample spin dynamics triggered by the electric and magnetic fields associated with the electron bunch.[26] In fact, a pioneering experiment[27] explored the ultimate speed limit for precessional magnetic dynamics of a CoCrPt film driven by the magnetic field $\mathbf{B}(\mathbf{r}, t)$ of short relativistic electron pulses (with a duration of $\delta = 2.3$ ps) passing a 14 nm thin film of granular CoCrPt ferromagentic samples with grain sizes of 20.6 ± 4 nm. The main experimental results are shown along with our simulations in Fig. 1. Prior to the electron-pulse, the sample was magnetized homogeneously in the z direction. The pulse induced ring pattern of the magnetic domains pointing either up or down (with respect to the easy direction of the magnetic films) is well captured by our micromagnetic simulations and can be interpreted by the analytical model enclosed in the supplementary material. As pointed out in Ref. 27, the critical precessional angle $\phi \geq \pi/2$ is determined by the local strength of the magnetic field and indicates the achieved angular velocity ω. The pulse duration δ plays a crucial role.[28] As discussed in Ref. 28, an appropriate sequence of ps pulses allows for an optimal control scheme, achieving a ballistic magnetic switching, even in the presence of high thermal fluctuations. Longer pulses might drive the system back to the initial state.[28] So, the critical precessional angle and δ are the two key parameters[27] for the established final precessional angle $\phi = \omega\delta$. Note that the demagnetization fields are also relevant, as inferred from Fig. 1, but they do not change the main picture (further details are in the supplementary material). Having substantiated our methods against the experiment, we turn to the main focus of

our study, namely, the generation of topologically protected magnetic excitations such as skyrmions via the electron pulses. We consider that samples exhibiting Dzyaloshinskii-Moriya (DM) spin-orbital coupling are appropriate. A recent work[29] evidences that ultrathin nanodiscs of materials such as $Co_{70.5}Fe_{4.5}Si_{15}B_{10}$ (Ref. 30) sandwiched between Pt and Ru/Ta are well suited for our purpose. The magnetization's
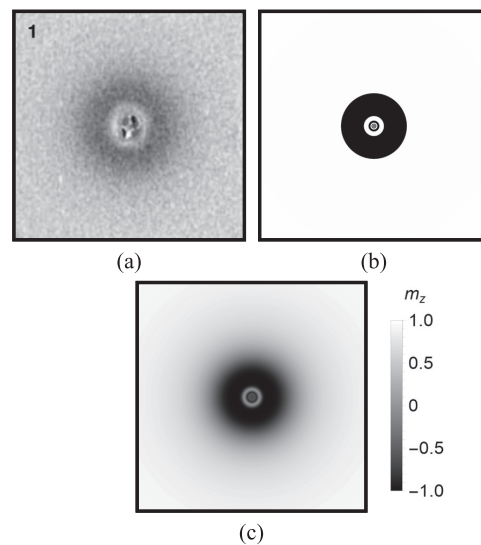

FIG. 1. Comparison between experimental (a)[27] and numerical results (b) and (c). Both numerical simulations and the experimental data cover an area of $150 \times 150\,\mu m^2$. In contrast to panel (b), in (c), the demagnetizing fields are included in simulations. The grey shading signals the magnetization's z-component with white color meaning $m_z = +\hat{e}_z$ and black $m_z = -\hat{e}_z$. The electrons in the beam impinging normal to the sample have an energy of 28 GeV. The pulse's time-envelope is taken as a Gaussian with a pulse duration of $\sigma_t = 2.3$ ps, which translates to a number of $n_e \approx 10^{10}$ electrons and an equivalent time-dependence of the generated Oersted field whose radial ρ dependence away from the beam axis derives to $B(\rho) = 54.7$ T$\mu m\,/(\rho + \epsilon)$ (at the peak electron bunch intensity). The cut-off distance $\epsilon = 40$ nm is included in order to avoid a divergent behavior at the origin and can be understood as a rough approximation of the beam width.

structure may nucleate spontaneously into skyrmionic configurations. We adapted the experimentally verified parameters for this sample and present here the result for the magnetic dynamics triggered by short electron beam pulses. Taking a nanodisc of a variable size, the ground state with a topological number $|N| = 1$ is realized after propagating an initially homogeneous magnetization in the $\pm z$ direction according to the Landau-Lifshitz-Gilbert equation (LLG) including DM interactions.[35–38] The two possible ground states, depending on the initial magnetization's direction, are shown in Fig. 2 along with the material's parameters.

Our main focus is on how to efficiently and swiftly create skyrmions, an issue of relevance when it comes to practical applications. Previous theoretical predictions (e.g., Ref. 31) utilize a spin-polarized current for the skyrmion generation. However, large current densities and a finite spin polarization of injected currents are needed. Thus, it is of interest to investigate the creation and annihilation of skyrmions with current pulses similar to those discussed above using the surrounding magnetic field. Of interest is the skyrmion generation and modification via a nano-focussed relativistic electron pulse. While currently such pulses can be generated with micron size beam dimensions,[32] future sources are expected to reach ficus sizes down to the few nm range.[33] In principle, the possibility of beam damage occurring in the beam focus as in the case of the experiment in Ref. 27 is present. However, ongoing experiments with relativistic

(a)   (b)

φ
2π

π

0

(c)

FIG. 2. Magnetic ground states for a nanodisc with a diameter of 300 nm and a thickness of 1.5 nm. The material parameters are $M_{sat} = 450 \times 10^3$ A/m, $A_{ex} = 10$ pJ/m, $\alpha = 0.01$, $K_u = 1.2 \times 10^5$ J/m^3 (out-of plane anisotropy), and the interfacial DMI-constant $D_{ind} = 0.31 \times 10^{-3}$ mJ/m^2. (a) corresponds to $N = 1$, whereas (b) possesses $N = -1$, and both skyrmions are of the Néel type. The bottom panel illustrates pictorially the influence of the magnetic field associated with the electron bunch. The cones correspond to the initial magnetic configuration as in (a) and (b), whereas the golden arrows show the induced magnetic field. The resulting torque points perpendicular to the magnetization, affecting the magnetic configuration accordingly.

electron beams[32] indicate that the use of ultrathin freestanding films may alleviate damage concerns.

Topologically protected magnetic configurations, such as magnetic skyrmions, are well-defined quasiparticles. They can be characterized mathematically by the topological or winding number $N = \frac{1}{4\pi} \int \mathbf{m} \cdot \left(\frac{\partial \mathbf{m}}{\partial x} \times \frac{\partial \mathbf{m}}{\partial y} \right) dxdy$ (Ref. 34), which counts simply how often the unit vector of the magnetization wraps the unit sphere when integrated over the two-dimensional sample. Therefore, skyrmions are typically a quasiparticle in thin (mono)layers. The topological number adopts integer values, indicating the magnetic configuration to be skyrmionic ($N = \pm 1$) or skyrmion multiplexes ($|N| > 1$). If the topological number is not an integer, the topological protection is lifted and the magnetic texture is unstable upon small perturbations. The topological stability of skyrmionic states stem from the necessity of flipping at least one single magnetic moment by $180°$, to overcome the barrier and transfer the state into a "trivial" state, like a single domain or vortex state. In the following, we will attempt to overcome this energy barrier with the previous methods so that the magnetization will be converted into a state with a different topological invariant. Advantageous is the spatial structure of the magnetic field curling around the beam's center, which gives a good point of action in order to manipulate topologically protected configurations.[35–38]

Using the short electron pulses, one may overcome the topological energy barrier with a magnetic "kick" and the magnetization relaxes afterwards, possessing a different winding number. In contrast to the mesoscopic system studied in Fig. 1, in the following, not only the far field but also the near magnetic field of the Gaussian pulses will be treated. To do this, the Biot-Savart law is solved numerically and fitted with a model function. For magnetic systems, a minimum time of exposure is necessary, whereas the spatial focus of the beam is limited. To overcome this conflict, the pulse duration is fixed at 2.3 ps as before, when nothing different is mentioned. Details on the resulting magnetic field can be seen in the supplementary material. Starting from such an electron beam, two main parameters can be adjusted to achieve the favored reaction of the nanodiscs. Those are the pulse width and the number of electrons, which will be treated independently. In Fig. 3, the final topological charges after a single Gaussian electron pulse irradiating a nanodisc are plotted as a function of the number of electrons and the width of the Gaussian distributed electrons. The results do not show the transient time evolution of the sample but only the final steady-state values of the winding number. They are obtained by applying an electron pulse, propagating the magnetization during the pulse, and then relaxing the magnetic configuration as to approach a local minimum of the free energy's hypersurface.

We note the strong correlation between the change of the topological charge and the number of electrons or accordingly the beam width. Relatively large intervals of both parameters lead to the same final values for N. We note that not only the variation of these control parameters but also of the duration of the pulse is experimentally accessible, particularly in a nanoapex ultrafast transmission electron microscope. It is noteworthy that the graphs for opposite
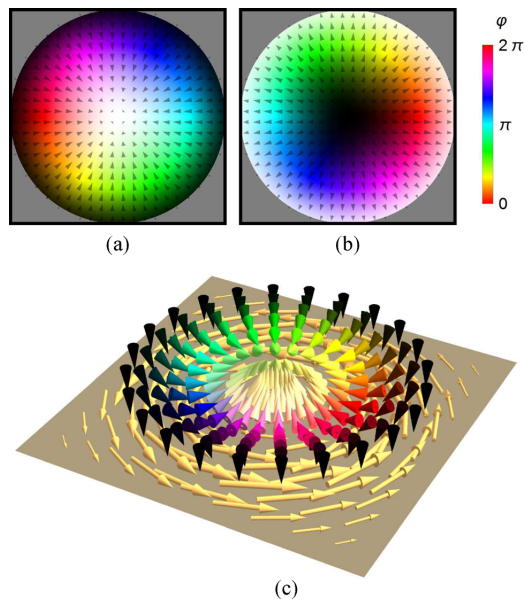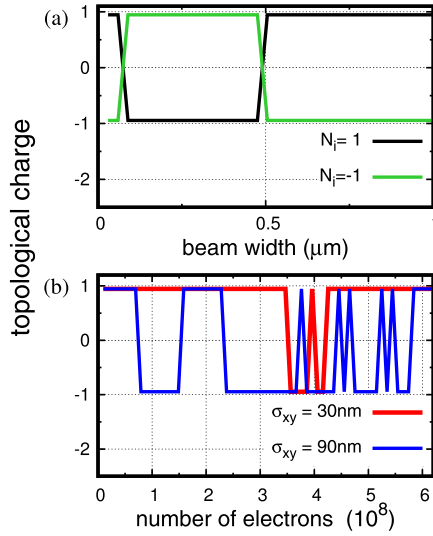
FIG. 3. Varying the number of electrons per pulse or the spatial enlargement of the pulse, the imprinted topological charge can be tuned. The pulse duration is set to 2.3 ps. Black and green curves correspond to starting with a magnetic ordering having $+1$ or -1 topological charge, respectively, as shown in Fig. 2 for different pulse widths. Both the blue and red curves start from $N_i = +1$. The sample is a magnetic disc (diameter $d = 300$ nm), which is irradiated with a Gaussian beam pulse with $\sigma_{xy} = 30$ nm (and 90 nm) in the case of the bottom graph. The upper graphs' beam has a constant number of $n_e = 10^8$ electrons.

initial configurations [see Fig. 3(a)] are axially symmetric with respect to the x axis. This can be explained by the coinciding symmetry centers of the pulse and the skyrmionic structure. This symmetric and robust behavior can be exploited to switch between accessible different values for the topological charges which are quite close to the ideal integer values that would be realized in an infinitely small discretization.

Interestingly, the switching between the two stable states occurs repetitively for an increase in the number of electrons, whereas the spatial manipulation of the beam leads to one regime only in which the fields are sufficient to switch the topological number. The first observation can be explained with the schematics shown in Fig. 2(c). Depending on the strength of the pulse, the magnetic moments are forced to rotate multiple times around the $\hat{e}_\varphi$ vector in a collective manner, as each moment of equal distance to the center experiences the same torque. The final position of the surrounding moments couples backwards to the center and determines the new topological charge. The electron number linearly translates to the peak magnetic field, whereas the beam width has a more complicated influence. When the width is increased, the spatial profile in the xy-plane is manipulated, as the maximum magnetic field is shifted towards the disc's rim and beyond. How the system reacts on this change depends crucially on the exact profile of the beam, especially on the point of maximum magnetic field strength, as can be seen in Fig. 3(a). This leads to the question of the optimum parameter regime, to manipulate the system reliably, which cannot be finally answered as it strongly

depends on the experimentally available capabilities. Hence, this work focuses on an exemplary study on the effect.

The same switching phenomenon as discussed before can also be observed for different setups. Weaker pulses, as long as they are able to overcome the internal fields to excite the system, can be used as well, but obviously, the field's amplitude translates to the strength of the resulting torque. This implies a longer radiation time needed for pulses of lower intensity to be capable of switching the system. In the case of different materials or geometries, the accessible topological states have to be investigated, before they can be utilized. Otherwise undesired, interstitial states might be achieved by accident, and the switching is not deterministic anymore.

Aside from the manipulation of the topological charge of a given nanodisc system, the creation of skyrmions on extended thin layers is an open challenge. To treat this, we start from a quadratic region with a size of (800×800) nm^2 and periodic boundary conditions in x and y directions to avoid finite size effects. To overcome the homogeneously magnetized state, the peak intensity has to be increased further, as well as a focussing down to the scale of the desired skyrmion. The Gaussian profile in the xy-plane has a standard deviation of 30 nm, whereas the pulse duration is reduced to 500 fs and a single pulse includes 10^8 electrons. Even though this is experimentally challenging, it is necessary to create skyrmions on an extended film. If the beam size is too large, only trivial domain rings are built up. On the other hand, the duration has to be long enough to allow the magnetic texture to react to the pulse. A well-known characteristic of magnetic skyrmions is a tendency to have a blow-up behavior to minimize the exchange energy, when no external stabilization is present. In nanodiscs, the stabilizing factor is the geometric confinement. Several experimental works incorporate an additional external magnetic field perpendicular to the surface to amplify the uniaxial anisotropy in an attempt to block the blow-up effect. As we are mainly interested in the generation of topological defects, we focus on this aspect keeping in mind that a stabilization of the induced skyrmions is necessary to maintain their localized structure. As can be seen in Fig. 4, the irradiation by the electron beam leads to the injection of a topological charge. The used pulse has the peak intensity at $5\sigma_t = 2.5$ ps to account for its finite rising time. After short oscillations, the system relaxes to a skyrmionic state. On the time scale of the electron pulse, the state's topological nature is perfectly stable, but the excitations tend to expand when no further stabilizations are present. Therefore, the diameter of the skyrmion increases, the type changes from Néel to Bloch, and the topological charge is still conserved. The situation changes markedly for longer pulses ($\sigma_t \gtrsim 20$ ps). Just like before the pulse leads to topological excitations. On top of this, a domain-wall ring similar to the results presented above is induced, which shields the included skyrmions in two different ways (see Fig. 5). The blow-up behavior is blocked due to the domain wall. The spin waves reflected from the open boundaries are absorbed by the domain ring so that the inside is not affected. In the supplementary animation "(Multimedia view)," the formation of the structure shown in Fig. 5 can be seen. In the first 220 ps, the time step
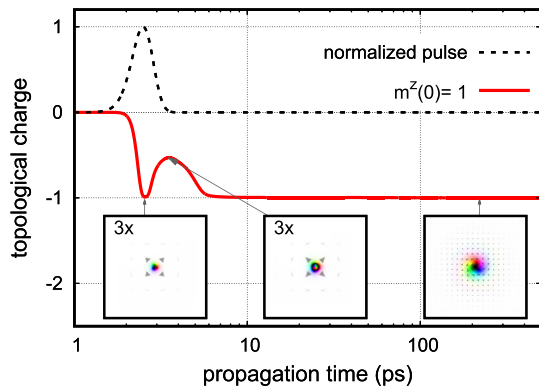
FIG. 4. Evolution of the topological charge after a single Gaussian beam with $n_e = 10^8$ electrons, $\sigma_{xy} = 30$ nm, and $\sigma_t = 0.5$ ps. The initial magnetization points homogeneously in the z direction. The system size is (800×800) nm^2 with periodic boundary conditions. On the bottom, we present a few snap-shots corresponding to the red curve at time moments depicted on each snapshot. The first and second pictures are scaled with a factor of three in order to make the development clearer.
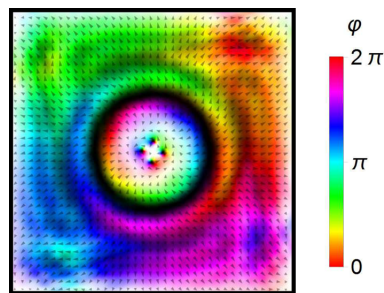
FIG. 5. Magnetization configuration 1 ns after a pulse with a duration of 22 ps and correspondingly 10^{11} electrons focused on $\sigma_{xy} = 10$ nm. Four skyrmions in the inside of a domain-wall ring are protected against fluctuations outside the ring. The sample covers an area of 800×800 nm^2. (Multimedia view) [URL: http://dx.doi.org/10.1063/1.4991521.1]

between the single frames is 4.4 ps. Then, the movie is accelerated to 22 ps/frame which can be easily recognized by the arising spin-waves outside the domain ring. Applying another pulse, the ring structure can be opened and the topological charge changed with the same process.

Summarizing, we demonstrated the usefulness of ultrashort electron pulses for generating and steering the magnetization dynamics due to the electromagnetic fields associated with the electron pulses. In particular, topologically protected magnetic textures such as skyrmions can be imprinted and manipulated in a controllable spatiotemporal way.

See supplementary material for the information on the analytical macrospin approach towards the results shown in Fig. 1, further details on the numerical calculations, and the magnetic fields induced by ultrafast electron pulses.

[1]A. Paarmann, M. Gulde, M. Müller, S. Schäfer, S. Schweda, C. Maiti, C. Xu, T. Hohage, F. Schenk, C. Ropers, and R. Ernstorfer, J. Appl. Phys. **112**, 113109 (2012).
[2]J. Hoffrogge, J. Paul Stein, M. Krüger, M. Förster, J. Hammer, D. Ehberger, P. Baum, and P. Hommelhoff, J. Appl. Phys. **115**, 094506 (2014).
[3]A. Feist, K. E. Echternkamp, J. Schauss, S. V. Yalunin, S. Schäfer, and C. Ropers, Nature **521**, 200 (2015).
[4]M. Gulde, S. Schweda, G. Storeck, M. Maiti, H. K. Yu, A. M. Wodtke, S. Schäfer, and C. Ropers, Science **345**, 200 (2014).
[5]C. Ropers, D. R. Solli, C. P. Schulz, C. Lienau, and T. Elsaesser, Phys. Rev. Lett. **98**, 043907 (2007).
[6]B. Barwick, C. Corder, J. Strohaber, N. Chandler-Smith, C. Uiterwaal, and H. Batelaan, New J. Phys. **9**, 142 (2007).
[7]P. Hommelhoff, C. Kealhofer, and M. A. Kasevich, Phys. Rev. Lett. **97**, 247402 (2006).
[8]P. Hommelhoff, Y. Sortais, A. Aghajani-Talesh, and M. A. Kasevich, Phys. Rev. Lett. **96**, 077401 (2006).
[9]C. Ropers, T. Elsaesser, G. Cerullo, M. Zavelani-Rossi, and C. Lienau, New J. Phys. **9**, 397 (2007).
[10]H. Yanagisawa, C. Hafner, P. Dona, M. Klöckner, D. Leuenberger, T. Greber, M. Hengsberger, and J. Osterwalder, Phys. Rev. Lett. **103**, 257603 (2009).
[11]H. Yanagisawa, C. Hafner, P. Dona, M. Klöckner, D. Leuenberger, T. Greber, J. Osterwalder, and M. Hengsberger, Phys. Rev. B **81**, 115429 (2010).
[12]M. Schenk, M. Krüger, and P. Hommelhoff, Phys. Rev. Lett. **105**, 257601 (2010).
[13]R. Bormann, M. Gulde, A. Weismann, S. V. Yalunin, and C. Ropers, Phys. Rev. Lett. **105**, 147601 (2010).
[14]M. Krüger, M. Schenk, P. Hommelhoff, and M. Kruger, Nature **475**, 78 (2011).
[15]D. J. Park, B. Piglosiewicz, S. Schmidt, H. Kollmann, M. Mascheck, and C. Lienau, Phys. Rev. Lett. **109**, 244803 (2012).
[16]G. Herink, D. R. Solli, M. Gulde, and C. Ropers, Nature **483**, 190 (2012).
[17]L. Wimmer, G. Herink, D. R. Solli, S. V. Yalunin, K. E. Echternkamp, and C. Ropers, Nat. Phys. **10**, 432 (2014).
[18]H. Yanagisawa, M. Hengsberger, D. Leuenberger, M. Klöckner, C. Hafner, T. Greber, and J. Osterwalder, Phys. Rev. Lett. **107**, 087601 (2011).
[19]A. R. Bainbridge and W. A. Bryan, New J. Phys. **16**, 103031 (2014).
[20]R. J. D. Miller, Annu. Rev. Phys. Chem. **65**, 583 (2014).
[21]D. J. Flannigan and A. H. Zewail, Acc. Chem. Res. **45**, 1828 (2012).
[22]J. S. Kim, T. LaGrange, B. W. Reed, M. L. Taheri, M. R. Armstrong, W. E. King, N. D. Browning, and G. H. Campbell, Science **321**, 1472 (2008).
[23]T. L. Cocker, V. Jelic, M. Gupta, S. J. Molesky, J. A. J. Burgess, G. De Los Reyes, L. V. Titova, Y. Y. Tsui, M. R. Freeman, and F. A. Hegmann, Nat. Photonics **7**, 620 (2013).
[24]T. Kampfrath, K. Tanaka, and K. A. Nelson, Nat. Photonics **7**, 680–690 (2013).
[25]T. L. Cocker, D. Peller, P. Yu, J. Repp, and R. Huber, Nature **539**, 263–267 (2016).
[26]J. D. Jackson, *Classical Electrodynamics*, 3rd ed. (Wiley, 1998), ISBN 0-471-30932-X).
[27]I. Tudosa, C. Stamm, A. B. Kashuba, F. King, H. C. Siegmann, J. Stöhr, G. Ju, B. Lu, and D. Weller, Nature **428**, 831 (2004).
[28]A. Sukhov and J. Berakdar, Phys. Rev. Lett. **102**, 057204 (2009); Phys. Rev. B **79**, 134433 (2009); Appl. Phys. A **98**, 837 (2010).
[29]A. G. Kolesnikov, A. S. Samardak, M. E. Stebliy, A. V. Ognev, L. A. Chebotkevich, A. V. Sadovnikov, S. A. Nikitov, Y. J. Kim, I. H. Cha, and Y. K. Kim, J. Magn. Magn. Mater. **429**, 221 (2017).
[30]B. S. Chun, S. D. Kim, Y. S. Kim, J. Y. Hwang, S. S. Kim, J. R. Rhee, T. W. Kim, J. P. Hong, M. H. Jung, and Y. K. Kim, Acta Mater. **58**, 2836–2842 (2010).
[31]N. Romming, C. Hanneken, M. Menzel, J. E. Bickel, B. Wolter, K. von Bergmann, A. Kubetzka, and R. Wiesendanger, Science **341**(6146), 636–639 (2013).
[32]S. Weathersby, G. Brown, M. Centurion, T. Chase, R. Coffee, J. Corbett, J. Eichner, J. Frisch, A. Fry, M. Guehr, N. Hartmann, C. Hast, R. Hettel,

K. Jobe, E. Jongewaard, J. Lewandowski, R. Li, A. Lindenberg, I. Makasyuk, J. May, D. McCormick, M. Nguyen, A. Reid, X. Shen, K. Sokolowski-Tinten, T. Vecchione, S. Vetter, J. Wu, J. Yang, H. Durr, and X. Wang, Rev. Sci. Instrum. **86**, 073702 (2015).
[33]Y. Zhu and H. Dürr, Phys. Today **68**(4), 32 (2015).
[34]N. Nagaosa and Y. Tokura, Nat. Nanotechnol. **8**, 899–911 (2013).
[35]L. D. Landau and E. M. Lifshitz, Phys. Z. Sowjetunion **8**, 135 (1935).
[36]T. L. Gilbert, Phys. Rev. **100**, 1243 (1955).
[37]A. Sukhov, P. P. Horley, J. Berakdar, A. Terwey, R. Meckenstock, and M. Farle, IEEE Trans. Magn. **50**(12), 1 (2014).
[38]A. Vansteenkiste, J. Leliaert, M. Dvornik, M. Helsen, F. Garcia-Sanchez, and B. Van Waeyenberge, AIP Adv. **4**, 107133 (2014).

SCIENTIFIC REPORTS

natureresearch

OPEN

Electrical writing, deleting, reading, and moving of magnetic skyrmioniums in a racetrack device

Börge Göbel [1], Alexander F. Schäffer [2], Jamal Berakdar [2], Ingrid Mertig[1,2] & Stuart S. P. Parkin[1]

A magnetic skyrmionium (also called 2π-skyrmion) can be understood as a skyrmion—a topologically nontrivial magnetic whirl—which is situated in the center of a second skyrmion with reversed magnetization. Here, we propose a new optoelectrical writing and deleting mechanism for skyrmioniums in thin films, as well as a reading mechanism based on the topological Hall voltage. Furthermore, we point out advantages for utilizing skyrmioniums as carriers of information in comparison to skyrmions with respect to the current-driven motion. We simulate all four constituents of an operating skyrmionium-based racetrack storage device: creation, motion, detection and deletion of bits. The existence of a skyrmionium is thereby interpreted as a '1' and its absence as a '0' bit.

Magnetic skyrmions[1–3] are whirl-like quasiparticles that are under consideration as carriers of information in modern data storages: Sampaio *et al.*[4] proposed to write and move skyrmions in thin film nanowires what constitutes a derivative of a racetrack storage device, initially proposed for domain walls in a ferromagnetic thin films[5–7]. The low driving current, small size and high stability of skyrmions, combined with the stackability of these tracks into three dimensions may lead to the development of highly efficient magnetic memory-storage devices with capacities that rival those of magnetic hard-disk drives, satisfying the ever-growing demand for data storage.

Since the initial discovery of skyrmions in the form of periodic lattices in bulk single crystals of MnSi[2], scientific effort has led to promising advances towards the utilization of isolated skyrmions as information carriers[4,8–13]. Still, one major issue for driving skyrmions on a racetrack is the skyrmion Hall effect[3,11,14,15] originating from the real-space topological properties of skyrmions. A skyrmion carries a topological charge of $N_{\mathrm{Sk}} \pm 1$, defined as the integral over the topological charge density

$$n_{\mathrm{Sk}}(\boldsymbol{r}) = \frac{1}{4\pi}\boldsymbol{m}(\boldsymbol{r}) \cdot \left[\frac{\partial \boldsymbol{m}(\boldsymbol{r})}{\partial x} \times \frac{\partial \boldsymbol{m}(\boldsymbol{r})}{\partial y} \right], \tag{1}$$

where $\boldsymbol{m}(\boldsymbol{r})$ is the unit vector magnetization field. Skyrmions driven by spin-polarized electrical currents are not propelled parallel to the racetrack. They experience a transverse deflection towards the edge of the racetrack where they may be confined. This effect is detrimental for racetrack applications.

Theoretical suggestions for suppressing the skyrmion Hall effect are to manipulate the driving torque orientation[16–19] or to use antiferromagnetic skyrmions with a vanishing topological charge[20–23] instead of skyrmions. However, both approaches have not yet been realized experimentally.

Here, we utilize another type of magnetic quasi-particle (Fig. 1a) with a zero topological charge: the skyrmionium (also called a 2π-skyrmion)[24–34]. The skyrmionium has been observed experimentally created by laser pulses[27], as target skyrmionium in nanodiscs[28] and very recently in a thin ferromagnetic film on top of a topological insulator[29]. A magnetic skyrmionium (Fig. 1b) can be described as a skyrmion, with a second skyrmion situated in the center. The inner skyrmion has a reversed polarity and deforms the outer skyrmion to a ring.

Here, we show that skyrmioniums can be used as carriers of information in a racetrack storage device (Fig. 1a): the existence of a skyrmionium is interpreted as a '1' bit, while its absence is a '0' bit. Based on recent progresses in optically generated current pulses[35] we propose a way to write and delete magnetic skyrmioniums on the

[1]Max-Planck-Institut für Mikrostrukturphysik, D-06120, Halle, Saale, Germany. [2]Institut für Physik, Martin-Luther-Universität Halle-Wittenberg, D-06099, Halle, Saale, Germany. Börge Göbel and Alexander F. Schäffer contributed equally. Correspondence and requests for materials should be addressed to B.G. (email: bgoebel@mpi-halle.mpg.de) or A.F.S. (email: alexander.schaeffer@physik.uni-halle.de)
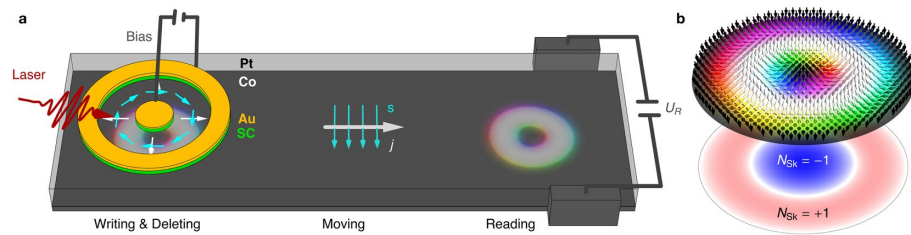
Figure 1. Skyrmionium-based racetrack storage device. (**a**) Schematic presentation of the proposed device including the four constituents: writing, deleting, moving and reading. A skyrmionium, the circular object in the Co layer (gray), is written or deleted by a photosensitive switch built from gold (Au) and a semi-conductor (SC). A radial current (white) is triggered upon illuminating the antenna with a fs-laser pulse due to the applied bias voltage. The current mainly flows in the Pt layer (transparent) where the SHE injects spins (cyan) into the Co layer that are oriented perpendicularly to the plane normal and current directions. Depending on the polarity of the gate voltage, the sign of the optically activated current pulse and the orientation of the polarization are determined, so that a skyrmionium can be written or deleted. To move the skyrmionium a uniform current density j is applied along the track, again generating spins s that exert a SOT onto the skyrmionium. When a skyrmionium is located near the two leads on the right, a Hall voltage U_R can be measured, allowing for a distinct detection of a skyrmionium bit. (**b**) (top) Magnetic texture of a skyrmionium, and (bottom) topological charge density n_{Sk} with opposite signs for the inner skyrmion and the outer ring.

picosecond timescale, so that the current-induced skyrmionium flow–without the detrimental skyrmion Hall effect–can remain steady while writing. Also we show that skyrmioniums can be detected electrically by their topological Hall signal, that arises from the local topological charge density (Fig. 1b bottom), even though the global topological charge vanishes.

Results

Skyrmionium racetrack.   In the following, we simulate and analyze point by point the four essential constituents to operate a racetrack-storage device based on magnetic skyrmioniums. First, we show via micromagnetic simulations how skyrmioniums can be written and deleted by optically excited localized current pulses. Thereafter, we present advantages in the current-driven motion of skyrmioniums compared to that of conventional skyrmions; we explain the simulated results by an effective description using the Thiele equation. Ultimately, we show via Landauer-Büttiker calculations that the local separation of the two subskyrmions of a skyrmionium can be exploited to electrically detect skyrmioniums even though they exhibit no topological Hall voltage when integrated over the whole sample.

For the device (Fig. 1a) we consider a magnetic layer on a heavy metal: here we exemplarily select Co (gray) on Pt (transparent), as in refs[4,26]. In this setup an applied charge current density j (white) within the Pt layer is translated into a spin current by the considerable spin Hall effect that has been observed in Pt. The spin current flows perpendicularly to the plane into the Co potentially hosting skyrmioniums. The spin polarization s (cyan) is perpendicular to j and the plane normal, thereby leading to a spin-orbit torque[36] (SOT) that can propel a skyrmionium.

On top of the basic racetrack that is formed from the Pt/Co bilayer a photosensitive switch[37] is fabricated that can switch the magnetization as experimentally shown in ref.[35]. A circular gold disk inside a gold ring is isolated from the metallic racetrack by an underlying semiconducting layer (green) so that a bias voltage can be applied between the inner and outer gold electrodes (Corbino geometry). The semiconductor is electrically activated by fs-laser pulses which generate a radially symmetric current pulse profile $j = j_{write} \frac{r_0}{r} \hat{e}_r$ (white) in the Pt-layer. By analogy with the explanation given above, this leads to a toroidal spin polarization profile $s(r) || \pm \hat{e}_\phi$ (cyan) of the spin currents (parallel to $\hat{e}_z$) that diffuse into the Co layer to create or delete the skyrmionium. To model the skyrmionium generation, deletion and motion we use a micromagnetic framework based on the Landau-Lifshitz-Gilbert (LLG) equation[36,38,39]. For details and simulation parameters see Methods.

For the reading process we utilize the local topological properties of a skyrmionium. The non-zero topological charge density n_{Sk} leads to a deflection of electrons into a transverse direction. A Hall voltage U_R builds up that can be measured by attaching two small leads (gray) to the sides of the device.

Optoelectrical writing of skyrmioniums.   Several mechanisms for writing skyrmions have been proposed, such as the application of spin-polarized currents[40], laser beams[27] and electron beams[41,42]. These mechanisms can potentially be adapted to generate also skyrmioniums. It has been predicted that skyrmioniums can be generated by alternating the out-of-plane orientation of an external magnetic field[30] or by the perpedicular injection of spin currents[26,31].

We propose a faster writing mechanism, where spins are injected from the perpendicular direction for an ultrashort duration. We consider a SOT-driven approach based on a nanostructured skyrmionium manipulation unit as sketched in Fig. 1a. Optically excited radially symmetric charge currents (white) in the Pt-layer lead to out-of-plane spin currents with a controllable toroidal spin polarization configuration (cyan): For opposite signs of the applied bias-voltage opposite spin polarizations are achieved ($\pm \hat{e}_\varphi$). According to Yang *et al.*[35] current den-
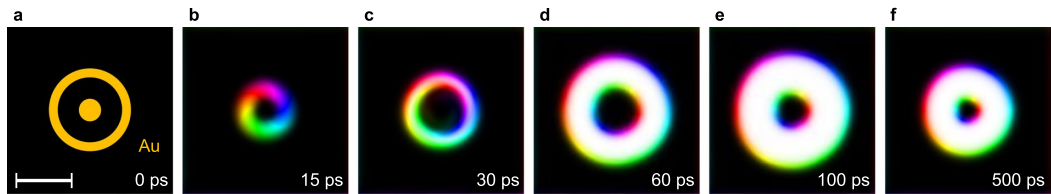
Figure 2. Writing skyrmioniums by optically excited current pulses. (**a**) The starting point is a ferromagnet magnetized along $-z$. The orange areas indicate the gold nanostructures that generate a current pulse of 9 ps duration (FWHM) with $j_{max}(t = 15\,ps) = 2 \times 10^{13} A/m^2$ at the disk. (**b**) After the spin current has induced a skyrmionium-shaped excitation the quasiparticle relaxes in (**c**–**f**). The color code is the same as in Fig. 1. An animated version is accessible in Supplementary Video 1. For sample and beam parameters see text and Methods. The scale bar corresponds to 50 nm.
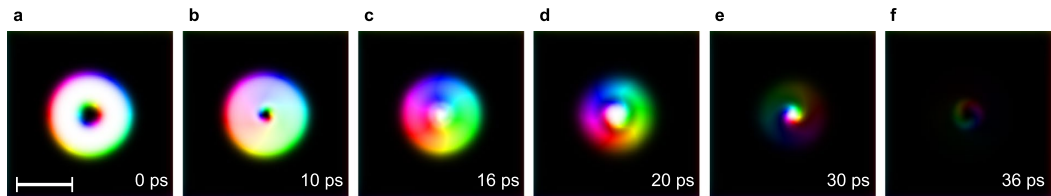
Figure 3. Deleting skyrmioniums by optically excited current pulses. (**a**) We start from the skyrmionium stabilized in Fig. 2 and generate a spin current with opposite polarization ($\hat{e}_\varphi$) compared to the writing process achieved by switching the sign of the bias voltage. (**b**,**c**) The domain wall unwinds the inner skyrmion leading to its collapse. (**d**–**f**) Subsequently, the skyrmion-like configuration contracts and dissolves. An animated version is accessible in Supplementary Video 2. The scale bar corresponds to 50 nm.

sities on the order of $j_{max} = 2 \times 10^{13} A/m^2$ could be created for a pulse duration of 9 ps full width at half maximum (FWHM). These values were adapted in our proposed optoelectrical writing and deleting process of a single skyrmionium. They cannot be reached by a conventional perpendicular spin current injection. The diameter of the inner disk of the photosensitive switch is 20 nm and the outer ring's inner diameter is 60 nm in order to match the skyrmionium's dimension. These dimensions are at the limit of what is possible today using conventional lithographic processes.

Starting from an initially uniform magnetization pointing into the $-z$ direction (Fig. 2a), the system is excited by an out-of-plane spin current with toroidal polarization. Because of the ultrashort current pulses of 9 ps (FWHM) the excitation itself is non-adiabatic and the magnetic texture will relax on a longer time scale.

During the current-pulse (Fig. 2b, maximum current at 15 ps) the magnetization in the excited ring-shaped region begins to align with the spin current's polarization, i.e. along $-\hat{e}_\varphi$. The amplitude of the current as well as its location needs to be tuned in such a way, that it will effectively switch a ring-shaped domain of a suitable size (Fig. 2c). Subsequently not only spin waves propagate radially, but also the central circular region remaining in its initial orientation starts to pulsate (Fig. 2c–f). Associated with this, the domain wall between the central $-z$ region and the intermediate $+z$ region is rotating such that a central Néel-skyrmion is generated, thereby, in total, constituting a skyrmionium. The slowest relaxation is the adjustment of the skyrmionium's size, taking place after the central fluctuations decay. The shrinking towards the final diameter (around 80 nm) lasts for ~500 ps (Fig. 2e,f).

Optoelectrical deleting of skyrmioniums. Deleting a non-collinear magnetic texture means turning it into a ferromagnetic state. Since no stabilizing external magnetic field is applied to the racetrack, the magnetization can in principle point into both out-of-plane directions. The uncontrolled annihilation of a skyrmionium can therefore easily lead to a local reversal of the magnetization direction, i. e., the formation of a domain. Therefore '1' bits need to be turned into '0' bits in a controlled way; no ferromagnetic domains must form. An efficient way is to invert the writing mechanism by reversing the bias voltage, which goes along with a change of the spin current's polarization from $-\hat{e}_\varphi$ to $+\hat{e}_\varphi$.

The annihilation process is shown in Fig. 3. The generated spin current effectively unwinds the skyrmionium structure step by step. First, the rotation of the domain wall leads to the dissolving of the central $-z$ domain (Fig. 3a–c). Second, the remaining skyrmion-like configuration contracts (Fig. 3d,e) until it collapses (Fig. 3f). The system relaxes towards the ferromagnetic state in less than 40 ps.

Current-driven motion of skyrmioniums. Skyrmions and skyrmioniums can be driven by spin torques. As discussed above, we use a two-layer setup that utilizes SOT, which means $s || -y$ for $j||x$. This mechanism has
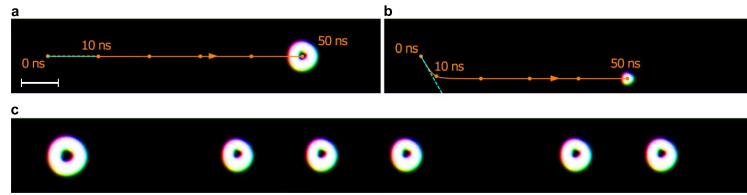
Figure 4. Current-driven motion of skyrmioniums. (**a**) A skyrmionium in a racetrack is driven by SOT: applied current density $j_x\Theta_{SH} = 0.6\,\text{MA/cm}^2$, injected spins are oriented along $-y$. (**b**) The motion of a skyrmion is shown for comparison. In both cases the image is taken after 50 ns of propagation time. The orange curve shows the trajectory of the quasiparticles' centers (starting point is indicated by 0 ns). The blue line indicates the motion direction under the skyrmion Hall angle, calculated from the Thiele equation (see text). (**c**) The results of a 'writing-under-current' simulation are shown after 35 ns propagation time in a racetrack with a doubled length. Due to the stronger current ($j_x\Theta_{SH} = 2.0\,\text{MA/cm}^2$) the skyrmioniums are slightly deformed. Skyrmioniums are written after 0 ns, 5 ns, 15 ns, 20 ns, 25 ns, and 35 ns. The last skyrmion is not yet fully relaxed. An animated version of the skyrmionium-sequence generation is accessible in the Supplementary Video 3. The scale bar corresponds to 100 nm.

been proven to be far more efficient compared to propagation induced by spin-polarized currents applied within the ferromagnetic layer (spin-transfer torque)[4,26].

In our simulations (Fig. 4a,b) a reference skyrmion (Fig. 4b) first moves to the edge partially along the $-y$ direction of the racetrack for about 10 ns and then moves at a steady velocity along the confining edge along the $+x$ direction. The skyrmionium (Fig. 4a) on the other hand is propelled almost instantly to the steady state velocity and moves in the middle of the racetrack along $+x$.

The results of micromagnetic simulations can most easily be understood by an effective center-of-mass description of magnetic quasiparticles (velocity $\boldsymbol{v}$): the Thiele equation (in units of force)[4,19,26,43]

$$b\,\boldsymbol{G} \times \boldsymbol{v} - b\underline{D}\alpha\boldsymbol{v} + Bj\underline{I}\boldsymbol{s} = \nabla U(y). \tag{2}$$

The properties of the respective quasiparticle are condensed into the gyromagnetic coupling vector $\boldsymbol{G} = Ge_z$ with $G = -4\pi N_{Sk}$, and the dissipative tensor $\underline{D}$ determined by $D_{ij} = \int \partial_i \boldsymbol{m}(\boldsymbol{r}) \cdot \partial_j \boldsymbol{m}(\boldsymbol{r})\,\mathrm{d}^2 r$. Only D_{xx} and D_{yy} are nonzero. The tensor $\underline{I}$ is calculated from $I_{ij} = \int [\partial_i \boldsymbol{m}(\boldsymbol{r}) \times \boldsymbol{m}(\boldsymbol{r})]_j\,\mathrm{d}^2 r$ and has only nonzero xy and yx elements for the stabilized Néel skyrmion (the type of skyrmion is determined by the Dzyaloshinskii-Moriya interaction (DMI)[44,45] arising at the interface between the Pt and Co layers) and skyrmionium. This tensor describes the interaction of injected spins $\boldsymbol{s}$ and the magnetic texture. The constants are $b = M_s d_z/\gamma_e$ and $B = \hbar/(2e)\Theta_{SH}$.

While neglecting the racetrack potential U (minimum in the middle of the racetrack), both textures experience a skyrmion Hall angle of $\theta_{Sk} = \arctan(G/D_{xx}\alpha)$, which gives an angle of $-60.5°$ for the skyrmion and $0°$ for the skyrmionium with respect to the $+x$ direction, in agreement with the first period of the simulation (blue dashed lines in Fig. 4a,b). The magnetic quasiparticles move at a velocity of

$$v_x = \frac{B}{b}\frac{I_{xy}}{D_{xx}}\frac{1}{\alpha}j_x - \tan\theta_{Sk}v_y \tag{3}$$

along the racetrack. If the current density j_x is small enough, a skyrmion moves to the edge of the racetrack due to its topological charge, until the gradient potential of the racetrack edge compensates the transverse force. In this case the longitudinal velocity is increased, because the second term vanishes. Due to $\theta_{Sk} = 0$ a skyrmionium on the other hand moves instantly at a constant velocity, which is given by the first term of Eq. 3.

In agreement with ref.[26] we find a slightly increased skyrmionium velocity ($|v_x^{st}| = 13.8\,\text{m/s}$) compared to the skyrmion velocity ($|v_x^{st}| = 13.2\,\text{m/s}$) even in the steady state, which is explained by $v_x \propto I_{xy}/D_{xx}$ in Eq. 3. In infinitely wide racetracks this ratio is equal for skyrmions and skyrmioniums. In finite tracks however, the confining potential deforms the magnetic quasiparticles slightly, altering the above ratio. Since skyrmioniums are larger than skyrmions, they experience a stronger deformation which manifests itself in a slightly increased I_{xy}/D_{xx} ratio.

The striking advantage of skyrmioniums as carriers of information compared to skyrmions becomes apparent in the first 10 ns of their motion after a current pulse is applied. During this period of time the skyrmionium already moves at maximum speed in the middle of the track, thereby allowing the writing of several skyrmioniums in sequence while the driving current is still applied (Fig. 4c).

Similarly to the skyrmion-skyrmion interaction[46], also the interaction between skyrmioniums is decreasing exponentially with the distance between them (see Supplementary Fig. S1). A repulsion of the quasiparticles is mainly limited to the case of a spatial overlap of the spin textures, therefore leaving the inter-skyrmionium distance in Fig. 4c constant during the considered time period.

In Fig. 4c we apply a current density of $j\Theta_{SH} = 2.0\,\text{MA/cm}^2$. The skyrmionium moving at 46.28 m/s is no longer rotationally symmetric: Its inner part is pushed to the top while the outer ring is dragged to the bottom of the racetrack, in accordance with the opposite skyrmion Hall effects that originate in the opposite partial topological charges of the two skyrmionium parts.
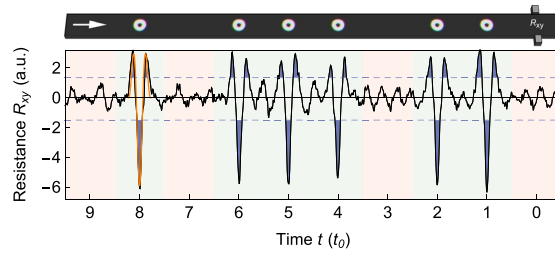
Figure 5. Electrical reading of skyrmioniums. The black curve shows the calculated transverse resistance signal when the skyrmionium sequence (top panel) passes the leads. In the presence of a skyrmionium between the leads (green background) a distinct pattern is found that exceeds two thresholds (dashed lines) three times. In good approximation the signal is proportional to the integrated topological charge density between the leads (orange). If no skyrmionium is present (red) the curve fluctuates around zero. Parameters: skyrmionium radius: 40 sites, track width: 120×2000 sites, bit width: 240 sites, lead width: 29 sites, $m/t = 5$, $E_\mathrm{F} = -8.5\,t$.

The maximal current density that can be applied to skyrmions and skyrmioniums is limited to around the same value. When the driving current is too large skyrmioniums self destruct because the forces pushing the two parts of the skyrmionium in opposite directions become too large[26] (For an analysis of the current dependence of the skyrmionium velocity and stability see Supplementary Fig. S2). On the other hand skyrmions are annihilated at the edge. For skyrmioniums the steady state velocity can be increased up to around 140 m/s. Alternatively, skyrmioniums can also be driven by spin waves[32,33].

Electrical reading of skyrmioniums. Due to its distinct magnetization a skyrmionium can easily be detected by out-of-plane measurements. However, electrical in-plane measurement can be included in the racetrack geometry more easily. For this reason we consider detection of skyrmioniums via the Hall voltage as has been done experimentally for conventional skyrmions[9].

When a small reading current I is applied along the track, the Hall resistivity is given by anomalous Hall and topological Hall contributions. The anomalous contribution is proportional to the net magnetization of the texture between the two detecting leads. For this reason every non-collinear magnetic texture is easily detected by the anomalous Hall effect. However, the signal is rather similar for different textures. Skyrmioniums cannot unambiguously be distinguished from skyrmions or even domain walls. This problem is resolved by the additional topological contribution to the Hall effect.

The topological Hall effect[3,9,10,47–52] is a hallmark of the skyrmion phase: Traversing electrons are deflected into a transverse direction, since their spins (partially) align with the non-collinear texture and a Berry phase is accumulated. The topological charge density acts like a fictitious magnetic field, called an emergent field[3]. We show that even though a skyrmionium has a zero topological charge it exhibits a distinct topological Hall signal that allows for a failsafe detection of skyrmioniums as '1' bits in comparison to other non-collinear textures that may appear as defects in imperfect racetracks.

We calculate the Hall resistance for skyrmioniums in a racetrack by means of the Landauer-Büttiker formalism[53,54], by analogy with refs[10,52] where skyrmions have been considered (see Methods for details). To model the interaction of electrons with the magnetic texture we considered a tight-binding model, which features nearest-neighbor hopping (amplitude t; creation and annihilation operator $c_i^\dagger$, c_i) and a Hund's coupling term (amplitude m, vector of Pauli matrices $\boldsymbol{\sigma}$)

$$H = \sum_{\langle i,j \rangle} t\, c_i^\dagger c_j + m \sum_i \boldsymbol{m}_i \cdot (c_i^\dagger \boldsymbol{\sigma} c_i).$$

(4)

Without the presence of skyrmioniums the Hamiltonian for the ferromagnet gives the energy bands $E = 2t[\cos(k_x a) + \cos(k_y a)] \pm m$. Since skyrmions are detected most easily for low carrier concentrations[10], we set the Fermi energy of the system close to the lower band edge, where the electrons behave like free electrons ($E_\mathrm{F} = -8.5\,t$ for $m = 5\,t$).

Since $N_\mathrm{Sk} = 0$ the topological Hall effect vanishes globally: The inner part of the skyrmion deflects electrons to the bottom, while the outer ring redirects electrons into the opposite direction. Fortunately, this spatial separation of the two opposing contributions leads to a non-zero signal in a local measurement (Fig. 5). The topological Hall resistance $R_{xy} = (U_\mathrm{up} - U_\mathrm{down})/I$ is determined by the difference in voltage U at the two leads normalized by the reading current.

Whenever a skyrmionium approaches the contacts, at first only electrons deflected by the outer ring are detected. Later, when the skyrmionium is right between the leads, the inner part dominates the electron deflection and the effective charge accumulation is reversed. Finally, upon leaving the vicinity of the contacts, only the outer ring contributes to the signal. This leads to a characteristic curve that is well approximated (orange) by the topological charge density between the leads for a skyrmionium at position x

$$R_{xy}(x) \propto \int_y \int_{-x_0}^{x_0} n_\mathrm{Sk}(x - x', y')\, \mathrm{d}x' \mathrm{d}y'.$$

(5)

Electrons that traverse the spin texture are deflected by the locally nonzero emergent field of the skyrmionium $\boldsymbol{B}_{em} \propto n_{Sk}\boldsymbol{e}_z$ to the leads (voltage U_{up} and U_{down}) of finite width ranging from $x = -x_0$ to $+x_0$. Note, that for $x_0 \to \infty$ the result of zero global resistivity is recovered, independent of the position of the skyrmionium.

Discussion

In this Paper we simulated the four fundamental constituents of a racetrack storage device utilizing magnetic skyrmioniums as carriers of information.

For the writing and deleting mechanism we proposed a new method that utilizes the optoelectrical control of localized spin currents and their polarizations. Based on previous experimental advances we designed a nanostructured geometry enabling the writing or deleting of single skyrmionium bits, depending on the sign of the bias voltage. Since the writing process is ultrafast, skyrmioniums can be written while the driving current is applied even at the maximal velocity of the bits along the track of around 140 m/s (Fig. 4c). The reliability of this deterministic method is emphasized by the result, that an excitation with the 'wrong' gate voltage cannot change an existing bit (see Supplementary Videos 4 and 5). In that case the spin current's associated chirality is not suited to wind or unwind the present configuration, respectively. Furthermore, even when room temperature fluctuations (see Methods for details) are accounted for, the proposed manipulation technique still works (see Supplementary Fig. S3 and Videos 6 and 7) what makes the presented mechanism highly attractive over other proposals. Also, we checked the range of parameters characterizing the optoelectrical writing mechanism that allow for a controlled generation of skyrmioniums (cf. Supplementary Fig. S4).

We analyzed the motion of skyrmioniums under application of electrical currents in the Pt layer where a spin current is injected perpendicularly into the Co layer (SOT). Due to their vanishing topological charge, skyrmioniums move in the middle of the racetrack and reach a steady state of motion almost instantly.

Reading magnetic skyrmioniums is possible via measurements of the Hall voltage. A local drop in the net magnetization leads to the emergence of an anomalous Hall effect and the segregation of the two skyrmionic subsystems even allows for the detection of a topological contribution: While the outer ring deflects electrons into one transverse direction, the inner ring redirects electrons into the other direction. Since the detecting leads are of finite size, one observes an oscillating Hall signal when the skyrmionium moves through them allowing for a highly reliable reading process.

Compared to skyrmions the main advantages of utilizing skyrmioniums as bits of information are (a) the slightly higher velocity (effect increases for narrower racetracks), (b) the absence of an acceleration phase (v_x is instantly proportional to j_x; this effect is more prominent for a wider track), and (c) the skyrmionium moves always in the middle of the track. Advantages (b) and (c) are essential for an effective reading process, allow for changes in the moving direction and–combined with the ultrafast writing speed of the presented optoelectrical approach–allow for a convenient 'writing-while-moving' as well as 'deleting-while-moving' functionality of a skyrmionium racetrack (cf. Fig. 4c).

In conclusion, writing and reading of magnetic skyrmioniums in thin films can be exploited to allow for the operation of an efficient skyrmionium-based racetrack storage device. In contrast to other magnetic quasiparticles, that are predicted to move without a skyrmion Hall effect, skyrmioniums have already been detected in experiments. Our proposals will expedite the development of a working data storage device based on magnetic quasiparticles.

Methods

Micromagnetic simulations. We use the GPU-accelerated micromagnetic software package Mumax3[55,56] to solve the LLG equation with the SOT term for every magnetic moment $\boldsymbol{m}_i$ of the discretized magnetization[36,38,39]

$$\dot{\boldsymbol{m}}_i = -\gamma_e \boldsymbol{m}_i \times \boldsymbol{B}_{i,\text{eff}} + \alpha \boldsymbol{m}_i \times \dot{\boldsymbol{m}}_i + \gamma_e \epsilon \beta [(\boldsymbol{m}_i \times \boldsymbol{s}) \times \boldsymbol{m}_i]. \tag{6}$$

Here, $\gamma_e = 1.760 \times 10^{11}\,\text{T}^{-1}\,\text{s}^{-1}$ is the gyromagnetic ratio of an electron. The in-plane torque coefficient is $\varepsilon\beta = \frac{\hbar j \Theta_{SH}}{2 e d_z M_s}$; the out-of-plane torque parameter is set zero as it is small and does not drive the quasiparticles. The space- and time-dependent effective magnetic field

$$\boldsymbol{B}_{\text{eff}}^i = -\frac{\delta F[\boldsymbol{m}]}{M_s \delta \boldsymbol{m}_i} \tag{7}$$

is derived from the system's total free energy density F, given as the sum of exchange interaction, magnetocrystalline anisotropy, the demagnetization field, Zeeman energy, and DMI.

To generate skyrmioniums we use a modified photosensitive switch setup as shown in Fig. 1a, motivated by the experimental results from Yang et al.[35]. As discussed in the main text an optoelectrically induced spin current is superposed on the uniform spin current, which drives the skyrmioniums along the racetrack. For the simulations we assumed a Gaussian envelope in time according to ref.[35].

Additionally, for the room temperature simulations an effective thermal field is included as

$$\boldsymbol{B}_{\text{therm}}^i = \boldsymbol{\eta}\sqrt{\frac{2\alpha\mu_0 k_B T}{M_s \gamma \Delta V \Delta t}}, \tag{8}$$

where $\boldsymbol{\eta}$ is a random vector generated according to a standard normal distribution for each simulation cell and changed after every time step. k_B is Boltzmann's constant, T the temperature, ΔV the simulation cells' size and Δt the time simulation's step. The thermal fluctuations due to the room-temperature ambience lead to deformations of the skyrmionium structure, but the switching mechanism still works successfully.

The system of Co/Pt is described by the following parameters[4,26]: saturation magnetization $M_s = 0.58$ MA/m, exchange stiffness $A = 15$ pJ/m, interfacial DMI $D = 3.5$ mJ/m^2, uniaxial anisotropy in z-direction $K_z = 0.8$ MJ/m^3, Gilbert damping parameter $\alpha = 0.3$ and the spin Hall angle $\Theta_{SH} = 0.4$. We simulate a Co nanowire racetrack of width 150 nm and thickness $d_z = 1$ nm, and discretize the magnetization in cubic cells of size 1 nm^3.

We use these values for comparability with refs[4,26], while noting that the DMI constant[57] and the spin Hall angle[58] are still under debate. For the here presented parameters a skyrmionium is stable for DMI strengths between 3.3 mJ/m^2 and 3.7 mJ/m^2 (cf. Supplementary Fig. S5). In this context we note, that the effective DMI constant can be tuned, for instance as in a Pt/Co/Ir setup presented in ref.[59] or by utilizing a different bilayer system, what is possible since our predictions are generally applicable and not limited to Co/Pt interfaces.

Topological Hall effect calculations. To calculate the topological Hall resistivity we consider the tight-binding Hamiltonian (Eq. 4) on a finite square lattice that forms the racetrack, as in Fig. 5. We apply four leads to the track: to the left and right to inject a small reading current, i. e., $I_l = -I_r = I$ and $V_l = -V_r$, and up and down to detect the voltage due to the transverse deflection and accumulation of the electrons, i. e., $I_u = I_d = 0$ and V_u and V_d. The transverse resistance follows directly from these voltages and currents, see text. To calculate the relationship between the currents and voltages we use a Landauer-Büttiker approach[53,54], by analogy with refs[10,52], where skyrmions have been investigated. For the calculations we use the transport simulation package Kwant[60].

We solve the set of linear equations $\{m, n\} = \{l, r, u, d\}$

$$I_m = \frac{e^2}{h} \sum_n T_{mn} V_n, \tag{9}$$

containing the transition matrix

$$T_{mn} = \mathrm{Tr}(\Gamma_m G_{mn} \Gamma_n G_{mn}^\dagger), \tag{10}$$

for the current I and non-fixed voltages V_u and V_d. Here, the retarded Green's function

$$\boldsymbol{G} = (E - H - \sum \Sigma_i)^{-1} \tag{11}$$

and $\Gamma_i = \mathrm{i}(\Sigma_i - \Sigma_i^\dagger)$ enter (E energy, H tight-binding Hamiltonian). Σ_i is the self energy of the i th lead.

Analyzing the results for different geometric parameters we find that skyrmioniums need to have a minimal size so that the topological charge density is well resembled. The leads should not be too large (optimally below half the skyrmionium radius) since they integrate the locally distinct signal making it broader and ambiguous. The distance between two bits can be small but then their signals begin to overlap, hampering an unambiguous detection. A minimal distance is given by $2(r_0 + x_0)$, which is the width of the predicted signal (orange). In '0' bit regions oscillations of the signal around zero are visible originating from backscattering of electrons from the racetrack edges. This unfavorable effect decreases for wider tracks.

References

1. Bogdanov, A. & Yablonskii, D. Thermodynamically stable vortices in magnetically ordered crystals. the mixed state of magnets. *Zh. Eksp. Teor. Fiz* **95**, 182 (1989).
2. Mühlbauer, S. *et al.* Skyrmion lattice in a chiral magnet. *Science* **323**, 915–919 (2009).
3. Nagaosa, N. & Tokura, Y. Topological properties and dynamics of magnetic skyrmions. *Nature Nanotechnol.* **8**, 899–911 (2013).
4. Sampaio, J., Cros, V., Rohart, S., Thiaville, A. & Fert, A. Nucleation, stability and current-induced motion of isolated magnetic skyrmions in nanostructures. *Nature Nanotechnol.* **8**, 839 (2013).
5. Parkin, S. S. P. Shiftable magnetic shift register and method of using the same. US Patent 6,834,005 (2004).
6. Parkin, S. S. P., Hayashi, M. & Thomas, L. Magnetic domain-wall racetrack memory. *Science* **320**, 190–194 (2008).
7. Parkin, S. S. P. & Yang, S.-H. Memory on the racetrack. *Nature Nanotechnol.* **10**, 195–198 (2015).
8. Romming, N. *et al.* Writing and deleting single magnetic skyrmions. *Science* **341**, 636–639 (2013).
9. Maccariello, D. *et al.* Electrical detection of single magnetic skyrmions in metallic multilayers at room temperature. *Nature Nanotechnol.* **13**, 233–237 (2018).
10. Hamamoto, K., Ezawa, M. & Nagaosa, N. Purely electrical detection of a skyrmion in constricted geometry. *Appl. Phys. Lett.* **108**, 112401 (2016).
11. Jiang, W. *et al.* Direct observation of the skyrmion Hall effect. *Nat. Phys.* **13**, 162–169 (2017).
12. Kang, W., Huang, Y., Zhang, X., Zhou, Y. & Zhao, W. Skyrmionelectronics: An overview and outlook. *Proceedings of the IEEE* **104**, 2040–2061 (2016).
13. Kang, W. *et al.* Voltage controlled magnetic skyrmion motion for racetrack memory. *Sci. Rep.* **6**, 23164 (2016).
14. Zang, J., Mostovoy, M., Han, J. H. & Nagaosa, N. Dynamics of skyrmion crystals in metallic thin films. *Phys. Rev. Lett.* **107**, 136804 (2011).
15. Litzius, K. *et al.* Skyrmion Hall effect revealed by direct timeresolved x-ray microscopy. *Nat. Phys.* **13**, 170–175 (2017).
16. Zhang, X. *et al.* Skyrmion-skyrmion and skyrmion-edge repulsions in skyrmion-based racetrack memory. *Sci. Rep.* **5**, 7643 (2015).
17. Kim, K.-W., Moon, K.-W., Kerber, N., Nothhelfer, J. & Everschor-Sitte, K. Asymmetric skyrmion Hall effect in systems with a hybrid Dzyaloshinskii-Moriya interaction. *Phys. Rev. B* **97**, 224427 (2018).
18. Büttner, F., Lemesh, I. & Beach, G. S. Theory of isolated magnetic skyrmions: From fundamentals to room temperature applications. *Sci. Rep.* **8**, 4464 (2018).
19. Göbel, B., Mook, A., Henk, J. & Mertig, I. Overcoming the speed limit in skyrmion racetrack devices by suppressing the skyrmion Hall effect. *Phys. Rev. B* **99**, 020405(R) (2019).
20. Barker, J. & Tretiakov, O. A. Static and dynamical properties of antiferromagnetic skyrmions in the presence of applied current and temperature. *Phys. Rev. Lett.* **116**, 147203 (2016).
21. Zhang, X., Zhou, Y. & Ezawa, M. Magnetic bilayer-skyrmions without skyrmion Hall effect. *Nature Commun.* **7**, 10293 (2016).
22. Zhang, X., Zhou, Y. & Ezawa, M. Antiferromagnetic skyrmion: stability, creation and manipulation. *Sci. Rep.* **6**, 24795 (2016).
23. Göbel, B., Mook, A., Henk, J. & Mertig, I. Antiferromagnetic skyrmion crystals: Generation, topological Hall, and topological spin Hall effect. *Phys. Rev. B* **96**, 060406(R) (2017).

24. Bogdanov, A. & Hubert, A. The stability of vortex-like structures in uniaxial ferromagnets. *J. Magn. Magn. Mater.* **195**, 182–192 (1999).
25. Beg, M. *et al.* Ground state search, hysteretic behaviour, and reversal mechanism of skyrmionic textures in confined helimagnetic nanostructures. *Sci. Rep.* **5**, 17137 (2015).
26. Zhang, X. *et al.* Control and manipulation of a magnetic skyrmionium in nanostructures. *Phys. Rev. B* **94**, 094420 (2016).
27. Finazzi, M. *et al.* Laser-induced magnetic nanostructures with tunable topological properties. *Phys. Rev. Lett.* **110**, 177205 (2013).
28. Zheng, F. *et al.* Direct imaging of a zero-field target skyrmion and its polarity switch in a chiral magnetic nanodisk. *Phys. Rev. Lett.* **119**, 197205 (2017).
29. Zhang, S., Kronast, F., van der Laan, G. & Hesjedal, T. Real-space observation of skyrmionium in a ferromagnet-magnetic topological insulator heterostructure. *Nano Lett.* **18**, 1057–1063 (2018).
30. Hagemeister, J., Siemens, A., Rózsa, L., Vedmedenko, E. Y. & Wiesendanger, R. Controlled creation and stability of kπ skyrmions on a discrete lattice. *Phys. Rev. B* **97**, 174436 (2018).
31. Kolesnikov, A. G., Stebliy, M. E., Samardak, A. S. & Ognev, A. V. Skyrmionium–high velocity without the skyrmion Hall effect. *Sci. Rep.* **8**, 16966 (2018).
32. Li, S., *et al.* Dynamics of a magnetic skyrmionium driven by spin waves. *Appl. Phys. Lett.* **112**, 142404 (2018).
33. Shen, M., Zhang, Y., Ou-Yang, J., Yang, X. & You, L. Motion of a skyrmionium driven by spin wave. *Appl. Phys. Lett.* **112**, 062403 (2018).
34. Pylypovskyi, O. V. *et al.* Chiral skyrmion and skyrmionium states engineered by the gradient of curvature. *Phys. Rev. Appl.* **10**, 064057 (2018).
35. Yang, Y. *et al.* Ultrafast magnetization reversal by picosecond electrical pulses. *Sci. Adv.* **3**, e1603117 (2017).
36. Slonczewski, J. C. Current-driven excitation of magnetic multilayers. *J. Magn. Magn. Mater.* **159**, L1–L7 (1996).
37. Ketchen, M. *et al.* Generation of subpicosecond electrical pulses on coplanar transmission lines. *Appl. Phys. Lett.* **48**, 751–753 (1986).
38. Landau, L. D. & Lifshitz, E. On the theory of the dispersion of magnetic permeability in ferromagnetic bodies. *Phys. Z. Sowjetunion* **8**, 101–114 (1935).
39. Gilbert, T. A Lagrangian formulation of the gyromagnetic equation of the magnetization field. *Phys. Rev.* **100**, 1243 (1955).
40. Fert, A., Cros, V. & Sampaio, J. Skyrmions on the track. *Nature Nanotechnol.* **8**, 152–156 (2013).
41. Schäffer, A. F., Dürr, H. A. & Berakdar, J. Ultrafast imprinting of topologically protected magnetic textures via pulsed electrons. *Appl. Phys. Lett.* **111**, 032403 (2017).
42. Schäffer, A. F., Dürr, H. A. & Berakdar, J. Ultrafast nanoscale magnetic switching via intense picosecond electron bunches. *In Ultrafast Nonlinear Imaging and Spectroscopy V* **10380**, 103800G (2017).
43. Thiele, A. Steady-state motion of magnetic domains. *Phys. Rev. Lett.* **30**, 230 (1973).
44. Dzyaloshinsky, I. A thermodynamic theory of weak ferromagnetism of antiferromagnetics. *J. Phys. Chem. Sol.* **4**, 241–255 (1958).
45. Moriya, T. Anisotropic superexchange interaction and weak ferromagnetism. *Phys. Rev.* **120**, 91 (1960).
46. Schäffer, A. F., Rózsa, L., Berakdar, J., Vedmedenko, E. Y. & Wiesendanger, R. Stochastic dynamics and pattern formation of geometrically confined skyrmions. *Commun. Phys.* **2**, 72 (2019).
47. Bruno, P., Dugaev, V. & Taillefumier, M. Topological Hall effect and Berry phase in magnetic nanostructures. *Phys. Rev. Lett.* **93**, 096806 (2004).
48. Neubauer, A. *et al.* Topological Hall effect in the a phase of MnSi. *Phys. Rev. Lett.* **102**, 186602 (2009).
49. Hamamoto, K., Ezawa, M. & Nagaosa, N. Quantized topological Hall effect in skyrmion crystal. *Phys. Rev. B* **92**, 115417 (2015).
50. Göbel, B., Mook, A., Henk, J. & Mertig, I. Unconventional topological Hall effect in skyrmion crystals caused by the topology of the lattice. *Phys. Rev. B* **95**, 094413 (2017).
51. Göbel, B., Mook, A., Henk, J. & Mertig, I. Signatures of lattice geometry in quantum and topological Hall effect. *New J. Phys.* **19**, 063042 (2017).
52. Yin, G., Liu, Y., Barlas, Y., Zang, J. & Lake, R. K. Topological spin Hall effect resulting from magnetic skyrmions. *Phys. Rev. B* **92**, 024411 (2015).
53. Landauer, R. Spatial variation of currents and fields due to localized scatterers in metallic conduction. *IBM Journal of Research and Development* **1**, 223–231 (1957).
54. Büttiker, M. Absence of backscattering in the quantum Hall effect in multiprobe conductors. *Phys. Rev. B* **38**, 9375 (1988).
55. Vansteenkiste, A. & Van de Wiele, B. Mumax: a new highperformance micromagnetic simulation tool. *J. Magn. Magn. Mater.* **323**, 2585–2591 (2011).
56. Vansteenkiste, A. *et al.* The design and verification of mumax3. *AIP Adv.* **4**, 107133 (2014).
57. Simon, E., Rózsa, L., Palotás, K. & Szunyogh, L. Magnetism of a co monolayer on pt (111) capped by overlayers of 5 d elements: A spin-model study. *Phys. Rev. B* **97**, 134405 (2018).
58. Tao, X. *et al.* Self-consistent determination of spin Hall angle and spin diffusion length in pt and pd: The role of the interface spin loss. *Science Adv.* **4**, eaat1670 (2018).
59. Moreau-Luchaire, C. *et al.* Additive interfacial chiral interaction in multilayers for stabilization of small individual skyrmions at room temperature. *Nature Nanotechnol.* **11**, 444 (2016).
60. Groth, C. W., Wimmer, M., Akhmerov, A. R. & Waintal, X. Kwant: a software package for quantum transport. *New J. Phys.* **16**, 063065 (2014).

Acknowledgements

Author Contributions

B.G. and A.S. initiated research and planned the project. J.B., I.M. and S.P. supervised the project. B.G. conducted calculations of the topological Hall effect and analyzed the Thiele equation. A.S. did the micromagnetic simulations. B.G. and A.S. wrote the manuscript. All authors discussed the results and commented on the manuscript.

Additional Information

Supplementary information accompanies this paper at https://doi.org/10.1038/s41598-019-48617-z.

Competing Interests: The authors declare no competing interests.

Publisher's note: Springer Nature remains neutral with regard to jurisdictional claims in published maps and institutional affiliations.

scientific reports

OPEN

Rotating edge-field driven processing of chiral spin textures in racetrack devices

Alexander F. Schäffer[1,2 ✉], Pia Siegl[3], Martin Stier[3], Thore Posske[3], Jamal Berakdar[1], Michael Thorwart[3], Roland Wiesendanger[2] & Elena Y. Vedmedenko[2]

Topologically distinct magnetic structures like skyrmions, domain walls, and the uniformly magnetized state have multiple applications in logic devices, sensors, and as bits of information. One of the most promising concepts for applying these bits is the racetrack architecture controlled by electric currents or magnetic driving fields. In state-of-the-art racetracks, these fields or currents are applied to the whole circuit. Here, we employ micromagnetic and atomistic simulations to establish a concept for racetrack memories free of global driving forces. Surprisingly, we realize that mixed sequences of topologically distinct objects can be created and propagated over far distances exclusively by local rotation of magnetization at the sample boundaries. We reveal the dependence between chirality of the rotation and the direction of propagation and define the phase space where the proposed procedure can be realized. The advantages of this approach are the exclusion of high current and field densities as well as its compatibility with an energy-efficient three-dimensional design.

Magnetic logic devices based on magnetic domain walls (DW) were introduced in 2005[1], where DWs were driven by rotating magnetic fields in magnetic stripes. Subsequently, the control of the domain walls by electric currents was proposed in memory devices[2]. Since that time, both driving mechanisms were refined and extended to chiral objects[3–6]. Recently, we have shown theoretically[7] that certain topological magnetic structures can be created without the help of global fields or currents, only by imposing time-dependent boundary conditions. Particularly, stable spirals of classical spins of different winding numbers can be created in antiferromagnetic chains by a local rotation of magnetization at the chain ends. The concept has also been applied to chains of quantum spins recently[8]. This one-dimensional model can be applied to multilayered pillars[9] or atomistic magnetic chains on substrates[10]. An appealing idea is to use such constraints to create metastable topological quasiparticles like domain walls (DWs), solitons, or skyrmions, in two- or three-dimensional racetracks. A significant decrease in energy consumption could be achieved by using similar time-dependent boundary conditions for further transfer and storage of magnetic objects created alongside the racetrack. However, it was not clear up to now whether the one-dimensional concept[7] can be applied to racetracks and whether these magnetic objects—once created—can then be transported and deleted by locally manipulating the boundaries without global currents or fields. Here, we develop theoretical concepts for the processing of topological magnetic objects in racetracks, including their creation, deletion, and transportation using time-dependent boundary conditions only. We especially consider systems with a relevant Dzyaloshinskii-Moriya interaction (DMI), potentially hosting both chiral DWs and skyrmions.

Results
First, we investigate whether local magnetic fields, instead of global effects[11], can be used to create non-collinear topological magnetic quasiparticles as DWs or skyrmions. Several approaches could either directly or effectively realize the necessary control about the edge-fields. (1) In toggle magnetoresistive random access memory (MRAM), a specific timing sequence of currents in independent signal lines smoothly rotates the writing magnetic field in micrometer-sized samples[12]. (2) The utilization of nanostructured magnets for obtaining smoothly rotating magnetic fields with magnitudes on the order of hundreds of mT is demonstrated in ref.[13]. (3) Another possibility to generate strong local effective fields exists in tailoring multilayer systems[14]. Lo Conte et al. stabilize room temperature skyrmions by tuning the interlayer exchange coupling between two magnetic layers. As one

[1]Institute of Physics, Martin-Luther-Universität Halle-Wittenberg, 06120 Halle (Saale), Germany. [2]Department of Physics, Universität Hamburg, 20355 Hamburg, Germany. [3]I. Institute for Theoretical Physics, Universität Hamburg, 20355 Hamburg, Germany. ✉email: alexander.schaeffer@physik.uni-halle.de
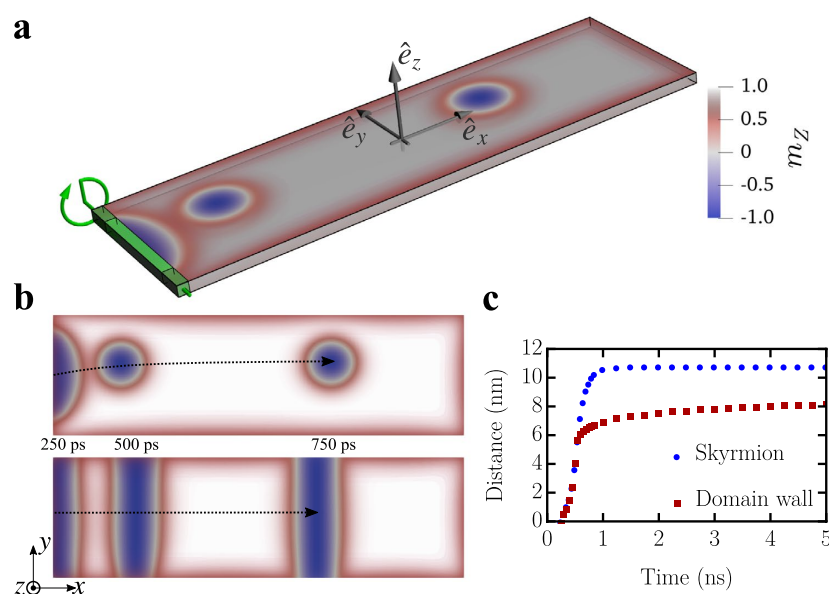
Figure 1. Skyrmion and domain wall creation in a magnetic stripe. (**a**) Schematics of the rotating effective magnetic field applied locally at the edge (green rectangular area) of the system. The time-dependent magnetic field rotates along the green arrow in the xz-plane with angle θ. (**b**) Real-space image of the motion of the skyrmion and DW for different time steps. For the skyrmion, the field is applied to two thirds of the width of the stripe (bright green area in (**a**)), in the case of the DW, the full width is affected by the field. The shown positions correspond to 250 ps (half a rotation), 500 ps (full rotation), and 750 ps (half a period after turning off the time-dependent field). The Gilbert damping parameter is reduced to $\alpha = 0.01$ in order to emphasize the differences in the motions. (**c**) Distance-time-diagram of a single created DW and skyrmion for a standard damping parameter $\alpha = 0.1$. System size: $100 \times 30 \times 1c^3$ with material parameters corresponding to Pd/Fe/Ir(111); $c = 0.233$nm.

of the adjusted parameters is the thickness of a spacer layer between the magnetic layers, this principle could be extended to nanostructuring the spacer. Hence the strength of the interaction could be manipulated spatially. (4) A different procedure uses current-carrying electronic states in atoms[15] or molecules[16]. These states host fully controllable magnetic fields when irradiated by laser fields. In the case of the atomic system, magnetic flux densities up to 47 T are predicted[15]. For both the laser-excited molecular systems and the nanostructured magnetic materials, the effective magnetic fields are strongly localized and hence provide promising approaches for the local creation of nanometer-sized magnetic textures. We simulate similar, smoothly rotating effective magnetic fields locally applied to the edge ($x = 0$) of a thin magnetic stripe in the xy-plane and with dimensions of $100 \times 30 \times 1c^3$ with $c = 0.233$nm, as shown in Fig. 1a, and calculate the spin dynamics in the stripe by micromagnetic simulations and atomistic Landau-Lifshitz-Gilbert (LLG) approaches (details can be found in the Supplementary Material, Sec. A. For the micromagnetic calculations, we conduct simulations using the open-source, GPU-accelerated software package mumax3[17], see "Methods" for details.

The simulations are performed primarily with parameters for the Pd/Fe bilayer on an Ir(111) surface, known for hosting nanometer-sized skyrmions at moderate magnetic bias fields (saturation magnetization $M_{sat} = 1.1$ MA m^{-1}, interfacial DMI constant $D = 3.9$mJ m^{-2}, exchange stiffness $A_{exch} = 2$pJ m^{-1}, uniaxial anisotropy constant $K_u = 2.5$MJ m^{-3} and Gilbert damping parameter $\alpha = 0.1$)[18]. The second model system we consider is a Co/Pt multilayer with weaker DMI. The local edge-field rotates in the xz-plane (cf. Fig 1a). Additionally, a static background field of $B_z^{stat} = 1.5$T was applied to ensure a spin-polarized ground state and the stability of both DWs and skyrmions in our calculations. We apply a local edge-field with an amplitude of $|\mathbf{B}(t)| = B = 10$ T, rotating once within 500 ps ($\nu = 2$GHz) and then being deactivated, meaning

$$\mathbf{B}(t < \nu^{-1}) = B\sin(2\pi\nu t)\hat{\mathbf{e}}_x + \left[B_z^{stat} + B\cos(2\pi\nu t)\right]\hat{\mathbf{e}}_z,$$
$$\mathbf{B}(t \geq \nu^{-1}) = B_z^{stat}\hat{\mathbf{e}}_z. \tag{1}$$

Figure 1b,c show how stable non-collinear magnetic objects are successfully inscribed for matching rotational senses of both the field and the intrinsic magnetic chirality determined by the DMI. Chiral DWs and skyrmions can be induced by a field applied either to the complete edge (DW) or only to its central two thirds (skyrmion), respectively (Fig. 1b,c, cf. lighter and darker green area in Fig. 1a). Once generated, the spin arrangements move along the racetrack until they slow down and come to rest at a finite distance from the point of creation. In order
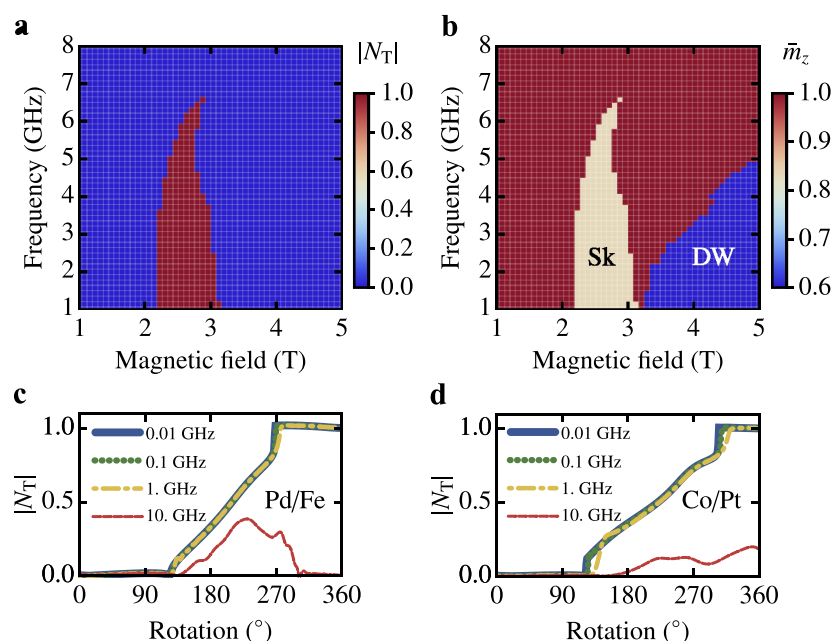
Figure 2. Quasiparticle creation due to a single rotation of a magnetic field localized at the sample edge. (**a,b**) Parameter space diagrams for a single field rotation and subsequent system relaxation. Shown is the absolute value of the topological charge $|N_T|$ (**a**), and the vertical magnetization averaged over the sample (**b**) as a function of the frequency and amplitude of the time-dependent driving field. The excited area at the left boundary is $7\,c \times 24\,c$, and the damping parameter $\alpha = 0.1$. (**c,d**) Absolute value of the topological charge as a function of the rotational phase of the local field for Pd/Fe/Ir(111) (**c**) and Co/Pt (**d**). System size: $60 \times 30 \times 1c^3$ for (**a–c**) and $100 \times 64 \times 1c_{Co}^3$ for (**d**), with material parameters corresponding to Pd/Fe/Ir(111) (**a–c**) and Co/Pt (**d**); $c = 0.233$nm, $c_{Co} = 1$nm.

to emphasize the different dynamics of the DW and the skyrmion, the Gilbert damping parameter in Fig. 1b is chosen to be relatively low ($\alpha = 0.01$), to achieve significant lateral displacements. The positions of both objects are shown after half a rotation of the external edge-field (250 ps), after the full rotation (500 ps), and another half period after turning off the rotating effective field (750 ps). The displacements of the created quasiparticles for $\alpha = 0.1$ are shown in Fig. 1c, an animated version can be found in the Supplementary Video 1. The path-time diagrams demonstrate that the magnetic quasiparticles possess initial momentum and inertia as they continue to move after the field has been switched off. As in ref.[19], the Thiele equation, customarily used to describe the center of mass dynamics of magnetic quasiparticles, may be extended to include higher-order terms like the gyrodamping. This is essential for our creation mechanism, as it involves highly non-linear dynamics. However, the nature of a quasiparticle model lacks the ability to treat the creation of the skyrmion itself. Therefore we employ numerical spin dynamics simulations.

In the following, the control of the magnetic quasiparticles is performed by magnetic fields, localized at an optimized number of simulation cells close to one edge of the sample represented by a rectangular slab. This control includes displacement operations, which usually are achieved by applying global electrical currents. In the first step, we optimized the area where the magnetic field is applied in terms of generating skyrmions or domain walls at low field amplitudes. A detailed description of this parameter optimization and the application of more sophisticated field distributions are discussed in "Methods" and the Supplementary Material, Sec. B. For a fixed area affected by the rotating effective edge-field of 7×24 simulation cells, the rotation speed (frequency ν from 1 to 8 GHz) and the amplitude (B from 1 to 5 T) are varied. Based on the magnetic configurations, resulting from the rotating effective excitation field and subsequent relaxation, the absolute value of the topological charge $|N_T|$ (Fig. 2a) and the out-of-plane component of the magnetization $\bar{m}_z$ averaged over the sample surface (Fig. 2b) are calculated. The topological charge N_T is defined as

$$N_T = \frac{1}{4\pi} \int n_T(x,y)\,dxdy\,, \tag{2}$$

where
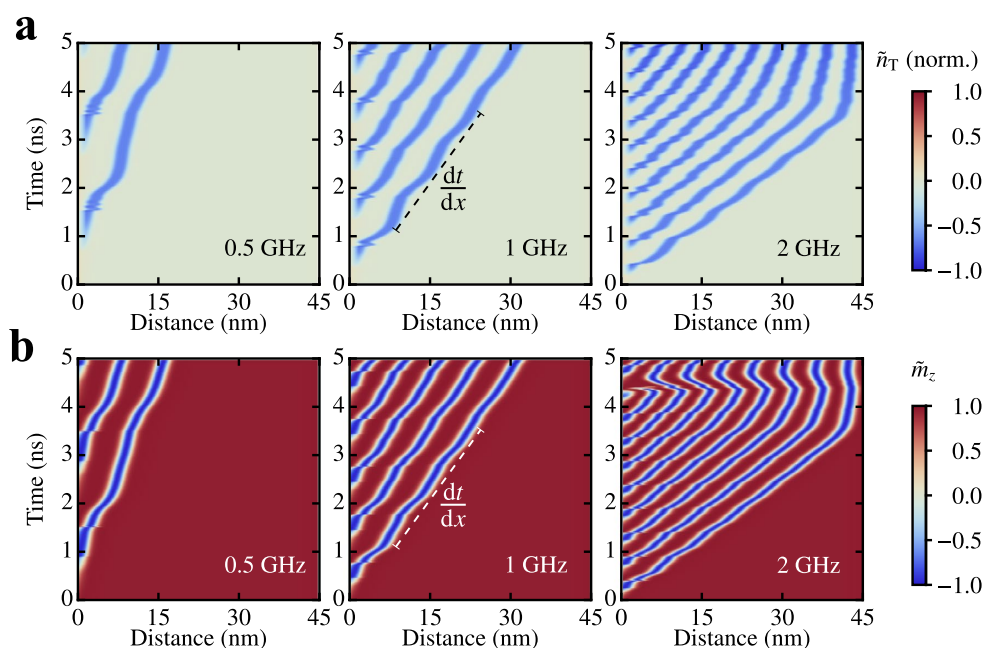
Figure 3. Skyrmion and domain wall steered by a continuously rotating effective magnetic field localized at the sample edge. Path-time diagrams of the skyrmion (**a**) and DW (**b**) propagation for $\nu = 0.5, 1, 2$ GHz, respectively (from left to right). Each horizontal line of pixels shows (**a**) the topological charge density or (**b**) the out-of-plane component of the magnetization, each averaged over cross sections of the nanostripe in ($\tilde{n}_T(x,t), \tilde{m}_z(x,t)$). The inverse mean slopes of the curves give the velocities of the quasiparticles. System size: $200 \times 30 \times 1c^3$, with material parameters corresponding to Pd/Fe/Ir(111); $c = 0.233$nm.

$$n_T = \mathbf{m} \cdot \left(\frac{\partial \mathbf{m}}{\partial x} \times \frac{\partial \mathbf{m}}{\partial y} \right) \qquad (3)$$

is the topological charge density and **m** represents the vector field of the magnetization. As expected[20], we only observe skyrmions and no antiskyrmions[11] in the considered parameter regime. Therefore, the sign of the topological charge only reflects the polarity of the skyrmions, which is fixed by the non-rotating edge magnetization of the sample. To avoid confusion, absolute values $|N_T|$ are shown in Fig. 2a. By combining both maps, two distinct regimes become apparent. For frequencies up to $\nu \approx 6.5$GHz a pocket forms in a regime of moderate field amplitudes in which a well-defined topological charge of $|N_T| = 1$ is measured. This area corresponds to the injection of a single skyrmion. For larger amplitudes or higher frequencies, respectively, no skyrmion can be inscribed into the system. Remarkably, for even higher amplitudes of the field, another distinguished area in the parameter space opens up, where the average magnetization is diminished even more than in the case of the skyrmion. It turns out that this blue area in Fig. 2b represents a single created DW without indication in the total topological charge. Here, the possibility of the individual creation of magnetic objects with distinct topologies opens new technological perspectives. Most interestingly, radially symmetric skyrmions or chiral DWs can be inscribed in the same nanostripe setup by solely changing the amplitude of the local effective rotating edge-field. This is in contrast to Fig. 1b,c, where we assumed different spatial extensions of the magnetic fields.

As a second model system we use Co/Pt multilayers, in which skyrmions have been observed in the absence of global magnetic fields ($M_{sat} = 0.58$ MA m^{-1}, $A_{exch} = 15$ pJ m^{-1}, $D = 3.5$ mJ m^{-2}, $K_u = 0.8$ MJ m^{-3}, $\alpha = 0.3$, system size: $100 \times 64 \times 1$nm^3, cell size: 1 nm^3)[3,21]. In Fig. 2c,d the topological charge is displayed for both materials as a function of the rotation angle θ (cf. Fig. 1a) of the external field. The rotation frequencies span from 10 MHz up to 10 GHz for an amplitude of the localized rotating effective field of $B = 2.5$ T in the case of the Pd/Fe/Ir(111) system. For Co/Pt an area of 7×48 simulation cells is excited with a field amplitude of 1 T (see "Methods" for details on the choice of parameters). Note that due to the non uniform magnetization of the boundary, the topological charge varies smoothly. New quasiparticles are created at rotation angles $\Delta\varphi_{Pd/Fe} \approx 270°$; $\Delta\varphi_{Co/Pt} \approx 300°$ (where $|N_T|$ reaches unity in Fig. 2c,d). Though the material parameters differ significantly and we do not apply a static magnetic field for stabilizing skyrmions in the case of Co/Pt, the quasiparticle creation is still successful in a similar frequency regime up to the GHz range (Fig. 2d). This indicates that our results are not limited to the Pd/Fe/Ir(111) system, but can be applied to various chiral magnets.

In the next step, we investigate whether a created magnetic object can be moved to any position along the racetrack using local effective rotating edge-fields. To achieve this goal, continuously rotating fields of different
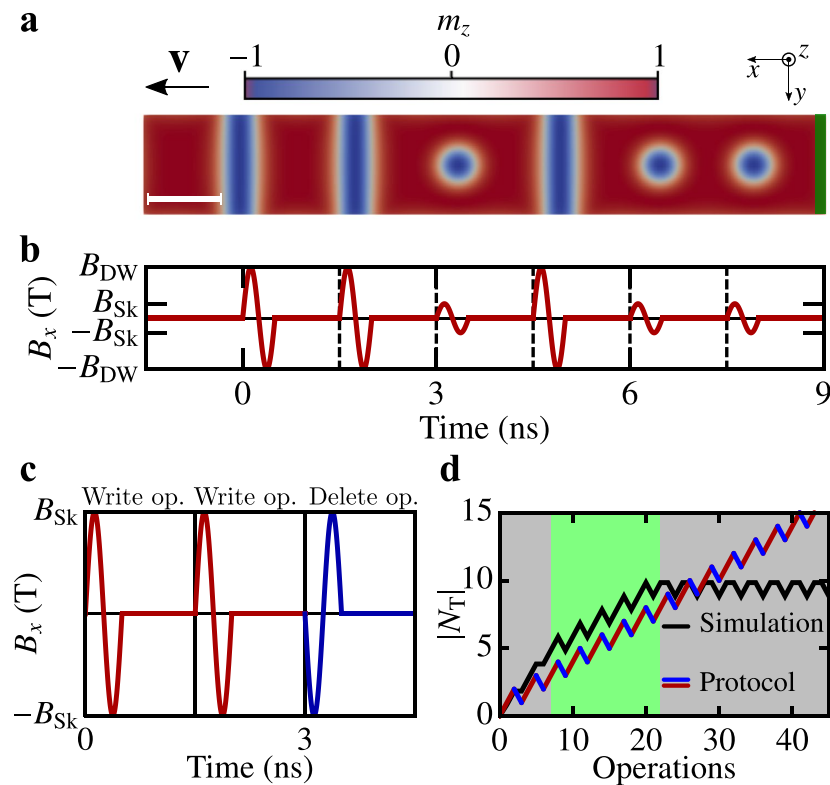
Figure 4. Writing and deleting operations. (**a**) Mixed sequence of three DWs and three skyrmions generated by multiple different field operations in the green area. (**b**) In-plane component of the rotating effective magnetic field with two different amplitudes. (**c**) Field protocol $B_x(t)$ for two writing operations (red) and one deletion operation (blue) with rotational sense opposite to the DMI. (**d**) Simulated total topological charge (black line) as a function of the number of subsequent field operations according to the protocol shown in (**c**). In the bright green area, the simulated topological charge is parallel to the behavior of an ideal system exactly following the protocol (red/blue line), therefore indicating high reproducibility. System size: $200 \times 30 \times 1c^3$, with material parameters corresponding to Pd/Fe/Ir(111).

frequencies are applied to the Pd/Fe/Ir(111) nanostripe edge. Here, the excited area is again 7×24 simulation cells large , whereas the amplitude of the field is set to $B_{Sk} = 2.5T$ or $B_{DW} = 3.5T$ according to Fig. 2b. The path-time diagrams are shown in Fig. 3 for both the topological charge density in the case of the skyrmion creation (Fig. 3a) and the out-of-plane component of the magnetization for DW simulations (Fig. 3b). Both quantities are averaged over one cross-section of the stripe $\tilde{n}_T(x) = \langle n_T(x, y) \rangle_y, \tilde{m}_z(x) = \langle m_z(x, y) \rangle_y$ to track the skyrmions and DWs along the stripe more easily. For sufficiently large DMI, the created magnetic objects are stable and obtain an initial velocity that drives them away from the boundary (see Fig. 3a,b). In contrast to racetrack concepts based on electrical currents[2,22,23], where a single magnetic object is moved along a racetrack, in our setup, trains of quasiparticles are created and moved collectively: at each subsequent 2π rotation of a magnetic field, a new quasiparticle is created, while already existing quasiparticles are moved away due to the repulsive interactions between them (see Fig. 3a,b). Furthermore, the distance traveled by the created quasiparticles during the creation time increases linearly with increasing frequency. This can be seen in the path-time diagrams of Fig. 3a,b, where the inverse of the linear slope gives the mean velocity of the quasiparticle, which reaches $v \approx 12m\,s^{-1}$ at $\nu = 2GHz$. This speed can be further increased by smart combinations of material parameters and frequencies of the rotating effective field. The distances traveled by each of the particles suggests a linear speed-frequency relation. Additionally, the minor delay in the motion of previously and newly created quasiparticles in the stripe implies that the time scale of magnetic interactions is much smaller than that of the driving local edge-field. This limits the validity of the suggested linear speed-frequency relation to sufficiently low frequencies or large damping parameters. The velocity of propagation decreases when the quasiparticles fill the sample (see right panels of Fig. 3a,b for $\nu = 2GHz$). In this regime, the mean distance of skyrmions/DWs is comparable to the interaction range of these objects[24–27]. If the energy barrier given by the repulsion of the quasiparticle from the edge is large enough, the packing density of quasiparticles increases as shown in detail in the Supplementary Video 2. A difference between skyrmion and DW creation starts to appear at high quasiparticle densities, i.e., in

the 2 GHz panel for $t > 4$ns. Here the skyrmion injection persists, whereas a maximal possible density of DWs is reached and excess DWs are repelled out of the sample after a short backaction. This behavior can be related to the smaller feature size of a skyrmion compared to a DW.

So far, we have shown that it is possible to create and move trains of magnetic quasiparticles by local excitations in a controllable way, without currents or global driving fields. Only the local edge-field is necessary for creating an object, the intrinsic interactions result in quasiparticle propagation. Because the DMI has a directional sense and because the quasiparticles repel each other, the creation of an additional object lets the existing quasiparticles move in a given direction with a well-defined velocity. To increase the functionality of the proposed current-free racetrack, we check the possibility of using magnetic quasiparticles of different topology as bits of information based on our findings in Fig. 2a,b. Figure 4 shows results for different combinations of effective rotating edge-fields. Figure 4a is obtained by changing the amplitude of the driving edge-field according to the protocol shown in Fig. 4b for the x component of the magnetization (cf. Eq. (1)). Each operation, separated by a dashed line in the graphic representation, consists of a single rotation of amplitude B_{Sk} or B_{DW} and two periods (in units of ν^{-1}) of relaxation time with $\nu = 2$GHz (see Supplementary Video 3 for an animated version of the resulting magnetization dynamics). Thus, the creation and successful propagation of any mixed sequence of DWs and skyrmions are possible.

Finally, we want to study the dynamics of the created magnetic objects if the rotational sense of the local field is reversed to potentially delete previously created quasiparticles. Figure 4c shows the field operations considered for studying the necessary skyrmion densities to permit reversible creation and annihilation operations. Starting from a field polarized state, two writing attempts and one deletion process with opposite chirality are performed (see Supplementary Video 4 for an animated version of the resulting magnetization dynamics in a small model system). The resulting topological charge of the Pd/Fe stripe after each operation is shown in Fig. 4d along with the ideal response according to the discussed protocol. Above a threshold topological charge of $|N_T| \gtrsim 10$, the skyrmion density is too large to add further quasiparticles successfully. Instead, undesired escapes of skyrmions take place (second gray area in Fig. 4d). In contrast, for low skyrmion densities ($|N_T| \lesssim 5$) the quasiparticles lose contact to the boundary and can not be deleted reliably (first gray area in Fig. 4d). In the bright green region, the field protocol is parallel to the writing-deleting events; hence, this area signifies high operational stability.

Discussion

Global current-free writing, propulsion, and deletion of magnetic quasiparticles with distinct topological properties can be achieved in the same system by local excitations at the boundary of a magnetic racetrack device. The proposed procedure relies on internal magnetic interactions instead of global driving currents, which strongly decreases the required energy consumption and potentially avoids overheating. By attributing a binary zero to one of the two topologically distinct objects, while binary unity to the other, a racetrack memory can be developed in a suitable quasiparticle density regime. The main benefit of utilizing two different kinds of quasiparticles is avoiding relying on a conserved void between objects of a single species. Due to the thermal motion of magnetic quasiparticles[24], they naturally distribute uniformly over samples at finite temperatures. Previously, different approaches have been developed to evade this problem, e.g., by periodically modifying the energy surface[28] such that objects rest at preferential positions. Therefore, the quasiparticles can no longer move isotropically, and, once written, information encoded in occupied and unoccupied positions is conserved. Therefore increased energy is needed to move objects at all and the necessary precise tuning of driving forces to move quasiparticles to the desired positions. These challenges do not apply to the concept presented here, as the placeholder between magnetic objects as bits of information is another magnetic quasiparticle. Additionally, the current-free storage concept proposed here is compatible with a three-dimensional design of magnetic networks, which significantly increases the information storage capacity.

Methods

Micromagnetic simulations. The functional derivative of the free energy density $\mathcal{F}[\mathbf{m}]$ with respect to the unit vector field of the magnetization $\mathbf{m}(\mathbf{r}, t)$ defines the time- and space-dependent effective magnetic field

$$\mathbf{B}_i^{\text{eff}}(t) = \mathbf{B}_i^{\text{ext}}(t) + \mathbf{B}_i^{\text{exch}} + \mathbf{B}_i^{\text{d}} + \mathbf{B}_i^{\text{a}} + \mathbf{B}_i^{\text{dmi}} . \tag{4}$$

It is composed of the external field $\mathbf{B}_i^{\text{ext}}(t)$, including the rotating edge-field; the exchange interaction field $\mathbf{B}_i^{\text{exch}} = 2A_{\text{exch}}/M_{\text{sat}} \Delta \mathbf{m}_i$, with the exchange stiffness A_{exch} and the saturation magnetization M_{sat}, the demagnetizing field $\mathbf{B}_i^{\text{d}} = M_{\text{sat}} \hat{\mathbf{K}}_{ij} * \mathbf{m}_j$, where we refer to ref.[17] for details of the calculation of the demagnetizing kernel $\hat{\mathbf{K}}$, the uniaxial magnetocrystalline anisotropy field $\mathbf{B}_i^{\text{a}} = 2K_u/M_{\text{sat}} m_z \mathbf{e}_z$, with K_u the anisotropy constant, and the field generated by the Dzyaloshinskii-Moriya interaction $\mathbf{B}_i^{\text{dmi}} = 2D/M_{\text{sat}} \left(\partial_x m_z, \partial_y m_z, -\partial_x m_x - \partial_y m_y \right)^T$, with D the strength of the interfacial Dzyaloshinskii-Moriya interaction. The effective magnetic field enters the LLG equation,

$$\dot{\mathbf{m}}_i(t) = -\frac{\gamma}{1 + \alpha^2} \left[\mathbf{m}_i \times \mathbf{B}_i^{\text{eff}} + \alpha \mathbf{m}_i \times \left(\mathbf{m}_i \times \mathbf{B}_i^{\text{eff}} \right) \right] , \tag{5}$$

which is solved for every simulation cell i of the discretized magnetization vector field $\mathbf{m}_i$. The gyromagnetic ratio of an electron is denoted by $\gamma_0 = 1.76 \times 10^{11} (\text{T}^{-1}\text{s}^{-1})$ and α is the Gilbert damping parameter. The integral definition of the topological charge N_T (Eq. 2) is applied to the discrete lattice system.

Optimization of excitation area. To optimize the excitation mechanism for the uniformly distributed magnetic field restricted to a rectangular shaped area, two benchmarks to rate magnetic field sweeps are defined.

First, the possibility of choosing between skyrmion or DW creation by changing the amplitude of the rotating magnetic field should be preserved. Hence we are looking for separate regimes of skyrmion and DW creation. Second, the proposed device should work at minimum field amplitudes to ensure low energy consumption. For Pd/Fe/Ir(111) the excited area is varied between (1×2) and (15×30) simulation cells for a fixed frequency of $\nu = 1\text{GHz}$. From the obtained 240 B-field sweeps, 53 show both features of skyrmions (topological charge $|N_T| = 1$) and DWs (average out-of-plane magnetization $\bar{m}_z < 0.7$). Afterward, the data set with the lowest threshold magnetic field for the DW creation is selected from the filtered data sets. This value is favored over the critical skyrmion creation field, as it is the highest necessary field for operating the mixed skyrmion DW track. The scan through frequency and field amplitude for the chosen area of excitation of (7×24) simulation cells is shown in Fig. 2a,b of the main text.

The same procedure is applied for the Co/Pt system, where the excited area is altered between (1×2) and (52×64) simulation cells. Here 32 out of the 352 data sets show indications for both DWs and skyrmions, and we identified an area of (7×48) simulation cells for optimal functionality.

Data availability
Data that support the findings of this work are available from the corresponding author on request.

Code availability
For obtaining the results, we used the open-source, GPU-accelerated software package `mumax3`[17] for the micromagnetic simulations. The atomistic spin dynamics simulations were executed with a self-developed code. Input files are available from the corresponding author on request.

References

1. Allwood, D. A. *et al.* Magnetic domain wall logic. *Science* **309**, 1688 (2005).
2. Parkin, S. S. P., Hayashi, M. & Thomas, L. Magnetic domain-wall racetrack memory. *Science* **320**, 190 (2008).
3. Sampaio, J., Cros, V., Rohart, S., Thiaville, A. & Fert, A. Nucleation, stability and current-induced motion of isolated magnetic skyrmions in nanostructures. *Nat. Nanotechnol.* **8**, 839 (2013).
4. Fernández-Pacheco, A. *et al.* Three-dimensional nanomagnetism. *Nat. Commun.* **8**, 1–14 (2017).
5. Luo, Z. *et al.* Chirally coupled nanomagnets. *Science* **363**, 1435 (2019).
6. Luo, Z. *et al.* Current-driven magnetic domain-wall logic. *Nature* **579**, 214 (2020).
7. Vedmedenko, E. Y. & Altwein, D. Topologically protected magnetic helix for all-spin-based applications. *Phys. Rev. Lett.* **112**, 017206 (2014).
8. Posske, T. & Thorwart, M. Winding up quantum spin helices: How avoided level crossings exile classical topological protection. *Phys. Rev. Lett.* **122**, 097204 (2019).
9. Lavrijsen, R. *et al.* Magnetic ratchet for three-dimensional spintronic memory and logic. *Nature* **493**, 647 (2013).
10. Menzel, M. *et al.* Information transfer by vector spin chirality in finite magnetic chains. *Phys. Rev. Lett.* **108**, 197204 (2012).
11. Stier, M., Häusler, W., Posske, T., Gurski, G. & Thorwart, M. Skyrmion-anti-skyrmion pair creation by in-plane currents. *Phys. Rev. Lett.* **118**, 267203 (2017).
12. Andre, T. *et al.* A 4-Mb 0.18 μm 1T1MTJ toggle MRAM with balanced three input sensing scheme and locally mirrored unidirectional write drivers. *IEEE J. Solid State Circ.* **40**, 301 (2005).
13. McNeil, R. P. *et al.* Localized magnetic fields in arbitrary directions using patterned nanomagnets. *Nano Lett.* **10**, 1549–1553 (2010).
14. Lo Conte, R. *et al.* Tuning the properties of zero-field room temperature ferromagnetic skyrmions by interlayer exchange coupling. *Nano Lett.* **20**, 4739 (2020).
15. Zhang, X. *et al.* Ultrafast oscillating-magnetic-field generation based on electronic-current dynamics. *Phys. Rev. A* **99**, 013414 (2019).
16. Wätzel, J., Pavlyukh, Y., Schäffer, A. & Berakdar, J. Optical vortex driven charge current loop and optomagnetism in fullerenes. *Carbon* **99**, 439–443 (2016).
17. Vansteenkiste, A. *et al.* The design and verification of mumax3. *AIP Adv.* **4**, 107133 (2014).
18. Romming, N., Kubetzka, A., Hanneken, C., von Bergmann, K. & Wiesendanger, R. Field-dependent size and shape of single magnetic skyrmions. *Phys. Rev. Lett.* **114**, 177203 (2015).
19. Schütte, C., Iwasaki, J., Rosch, A. & Nagaosa, N. Inertia, diffusion, and dynamics of a driven skyrmion. *Phys. Rev. B* **90**, 174434 (2014).
20. Böttcher, M., Heinze, S., Egorov, S., Sinova, J. & Dupé, B. B-T phase diagram of Pd/Fe/Ir (111) computed with parallel tempering Monte Carlo. *New J. Phys.* **20**, 103014 (2018).
21. Zhang, X. *et al.* Control and manipulation of a magnetic skyrmionium in nanostructures. *Phys. Rev. B* **94**, 094420 (2016).
22. Tomasello, R. *et al.* A strategy for the design of skyrmion racetrack memories. *Sci. Rep.* **4**, 6784 (2014).
23. Göbel, B., Schäffer, A. F., Berakdar, J., Mertig, I. & Parkin, S. S. Electrical writing, deleting, reading, and moving of magnetic skyrmioniums in a racetrack device. *Sci. Rep.* **9**, 12119 (2019).
24. Schäffer, A. F., Rózsa, L., Berakdar, J., Vedmedenko, E. Y. & Wiesendanger, R. Stochastic dynamics and pattern formation of geometrically confined skyrmions. *Commun. Phys.* **2**, 72 (2019).
25. Pinna, D. *et al.* Skyrmion gas manipulation for probabilistic computing. *Phys. Rev. Appl.* **9**, 064018 (2018).
26. Lin, S.-Z., Reichhardt, C., Batista, C. D. & Saxena, A. Particle model for skyrmions in metallic chiral magnets: Dynamics, pinning, and creep. *Phys. Rev. B* **87**, 214419 (2013).
27. Reichhardt, C. & Reichhardt, C. Clogging and transport of driven particles in asymmetric funnel arrays. *J. Phys. Condens. Matter* **30**, 244005 (2018).
28. Suess, D., Vogler, C., Bruckner, F., Heistracher, P. & Abert, C. A repulsive skyrmion chain as a guiding track for a racetrack memory. *AIP Adv.* **8**, 115301 (2018).

Acknowledgements

Author contributions

E.Y.V. proposed and developed a general concept of this investigation. A.F.S. contributed to the concept and conducted and analyzed the micromagnetic simulations. P.S., M.S. and E.Y.V. performed the atomistic spin dynamics simulations. A.F.S. and E.Y.V. wrote the manuscript. R.W., M.T., J.B., T.P., M.S. and P.S. discussed the results and contributed to the manuscript.

Funding

Competing interests

The authors declare no competing interests.

Additional information

Supplementary information is available for this paper at https://doi.org/10.1038/s41598-020-77337-y.

Correspondence and requests for materials should be addressed to A.F.S.

Reprints and permissions information is available at www.nature.com/reprints.

Publisher's note Springer Nature remains neutral with regard to jurisdictional claims in published maps and institutional affiliations.

ARTICLE

Stochastic dynamics and pattern formation of geometrically confined skyrmions

Alexander F. Schäffer [1], Levente Rózsa [2], Jamal Berakdar [1], Elena Y. Vedmedenko [2] & Roland Wiesendanger[2]

Ensembles of magnetic skyrmions in confined geometries are shown to exhibit thermally driven motion on two different time scales. The intrinsic fluctuating dynamics ($t \sim 1\,\mathrm{ps}$) are governed by short-range symmetric and antisymmetric exchange interactions, whereas the long-time limit ($t \gtrsim 10\,\mathrm{ns}$) is determined by the coaction of skyrmion–skyrmion-repulsion and the system's geometry. Micromagnetic simulations for realistic island shapes and sizes are performed and analyzed, indicating the special importance of skyrmion dynamics at finite temperatures. We demonstrate how the competition between skyrmion mobility and observation time directly affects the addressability of skyrmionic bits, which is a key challenge on the path of developing skyrmion-based room-temperature applications. The presented quasiparticle Monte Carlo approach offers a computationally efficient description of the diffusive motion of skyrmion ensembles in confined geometries, like racetrack memory setups.

[1] Institut für Physik, Martin-Luther-Universität Halle-Wittenberg, D-06099 Halle, (Saale), Germany. [2] Institut für Nanostruktur- und Festkörperphysik, Universität Hamburg, D-20355 Hamburg, Germany. Correspondence and requests for materials should be addressed to A.F.S. (email: alexander.schaeffer@physik.uni-halle.de)

Magnetic skyrmions[1–3] are quasiparticles that are considered as possible carriers of information for future storage devices. Their specific chirality is determined by the antisymmetric Dzyaloshinskii–Moriya exchange interaction (DMI)[4,5]. The DMI can be induced by a broken inversion symmetry in a crystal itself (e.g., MnSi)[2] or by interfacing a heavy metal layer (e.g., Pt, W, Ir) with a ferromagnetic material (e.g., Fe, Co)[6,7].

Conceptually the utilization of these topologically non-trivial[8] quasiparticles in so-called racetrack setups is of great interest[9–11]. Skyrmions can be manipulated (written and deleted)[12,13] and addressed individually[14–16] on a magnetic stripe, allowing a memory device extension from a pure surface density into the third dimension by pushing the quasiparticle-hole-train back and forth, e.g., by applying electrical currents[17,18]. The low threshold driving current[19] along with the small size and high stability of the skyrmions are key features of this concept.

To connect experimental and theoretical model systems with technological applications, investigating the influence of finite temperatures is of crucial importance. The bits on a racetrack-based memory device need to fulfill two main features, stability against external perturbations and addressability. Both are affected by thermal fluctuations, as shown below.

The stability of skyrmions was examined in several publications over the last years[20–24]. Rózsa et al.[21] investigated theoretically periodic two-dimensional Pd/Fe double-layers on Ir(111) and determined the phase diagram as a function of external field and temperature, which includes field-polarized, skyrmion lattice, spin spiral, fluctuation-disordered, and paramagnetic regions. Skyrmion lifetimes in the fluctuation-disordered regime were calculated. The lifetimes of isolated skyrmions in racetrack geometries for Pd/Fe/Ir(111) and Co/Pt(111) systems were investigated in refs. [22,23], and different mechanisms were revealed for the collapse of a skyrmion inside the track and at the boundary.

The diffusive motion of skyrmions at finite temperature has also attracted significant research attention lately[25–28]. Previous studies concentrated on diffusion in infinite or extended geometries, but a clarification of the role of the sample shape still seems to be missing in the case where the system size becomes comparable to that of the skyrmions. Effects of this kind directly impede the addressability, which is indispensable when using skyrmions for storage technology, e.g., in racetrack memory devices. As the number of skyrmions during the diffusive motion remains constant, quasiparticle models have been developed for their description in this limit[25,26,29,30], which are primarily based on the Thiele equation[31]. The advantage of such a collective-coordinate description over micromagnetic or atomistic spin dynamics simulations is the significantly lower computation cost.

Owing to the finite temporal resolution, imaging techniques on the atomic length scale like spin-polarized scanning tunneling microscopy (SP–STM)[32] or magnetic force microscopy (MFM)[33] cannot access temporally the diffusive motion of the skyrmions. Instead, the time-averaged skyrmion probability distribution is imaged that may well be different from the zero-temperature configuration or a snapshot of a simulation. Here, we discuss the formation, stability, and addressability of diffusive skyrmion configurations. Using micromagnetic simulations, it is shown that the complex interplay of the repulsive interaction between the skyrmions[29,34] along with the confinement effect of the nanoisland and the thermally induced skyrmion diffusion leads to a pattern formation of the skyrmion probability distribution on the nanosecond time scale. A computationally efficient quasiparticle Monte Carlo method is introduced, which is found to yield comparable results to time-averaged micromagnetic simulations regarding the skyrmion probability distribution. The simple implementation and high speed of such a method may make it
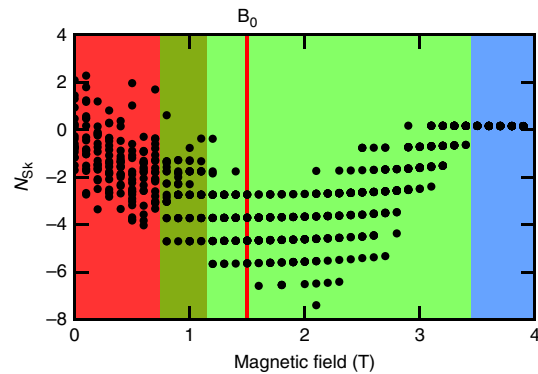

Fig. 1 Field dependence of the total topological charge. Red region: external fields below the strip-out instability leading to spin spiral segments; dark green: transition regime; bright green: ensemble of skyrmions; blue: completely field-polarized island, where skyrmions collapse under the strong external field. Solid red line indicates the magnetic field $B = 1.5$ T used for subsequent calculations. For each step in the vertically applied field 20 randomly magnetized configurations of a 21 nm diameter nanodisk were relaxed towards the nearest metastable state on the energy hypersurface at $T = 0$ K

advantageous over micromagnetic simulations when the actual number of skyrmions has to be determined based on a time-averaged experimental image.

Results

Skyrmion stability. We study metastable skyrmions and their motion and mobility at finite temperatures. At first, the phase space has to be explored with respect to the external magnetic field and temperature. A detailed description of the phase diagram for extended systems of ultrathin biatomic layers of Pd/Fe on an Ir(111) substrate hosting magnetic skyrmions can be found, e.g., in refs. [21,35]. Here, simulations are performed for the same system in the micromagnetic framework, by solving the Landau–Lifshitz–Gilbert equation (LLG)[36], as described in the Methods section.

In Fig. 1 possible equilibrium spin configurations are investigated in a 21-nm-diameter nanodisk of 0.4 nm thickness at zero temperature. For each fixed external magnetic field ($B = B_z$), 20 different randomly generated initial states are considered and relaxed towards the closest local minimum of the total energy hypersurface. Subsequently, the total skyrmion number N_{Sk} of the relaxed states is calculated and plotted against the external magnetic field in Fig. 1 to gain an overview of the possible metastable states. Below the strip-out instability field[37], skyrmions as localized cylindrical spin structures are not stable and the configuration consists of spin spiral segments. For these the topological number is not a well-defined quantity, as spin spiral structures can extend over the whole island, and therefore the boundaries have a significant effect. This is reflected by the continuous distribution of the topological charge values found below 0.75 T in the red regime in Fig. 1, whereas discrete skyrmion numbers correspond to discrete steps in the total topological charge. The upper boundary of this region is reasonably close to the strip-out field of $B = 0.65$ T[37,38] determined for extended systems.

With increasing the external field, individual skyrmions may be stabilized in the system, where they will coexist with spin spiral segments. This corresponds to the darker green area in Fig. 1 ~ $B \approx 1$ T, where besides the continuous distribution also discrete steps can be observed in the topological charge.

In the following bright green region, stronger magnetic fields lead to shrunken skyrmions, which in turn enables the magnetic island to host a larger number of quasiparticles. In this regime the topological charge is always close to an integer, with the small deviation caused by the tilting of the spins at the edge of the sample. Reaching field values above $B \approx 3.5$ T, the system becomes completely field-polarized and skyrmions are not stabilized anymore starting from a random configuration, even at zero temperature. Previous calculations[37–39] indicated that skyrmions on the lattice collapse at around $B = 4.5$ T in the system.

In order to prevent the appearance of spin spiral states and to be able to consider the skyrmions as well-defined quasiparticles, we choose $B = 1.5$ T for the following calculations, unless mentioned otherwise. Figure 1 shows that several metastable configurations associated with different topological charges are accessible starting from randomly generated initial states. However, in this approach not all stable structures are covered, as the included ones are obtained from relaxing random initial configurations. Different configurations may also be generated in a controlled way by adding skyrmions to the field-polarized state one-by-one, and relaxing the state at zero temperature. This is shown in Fig. 2 for the disk-shaped (Fig. 2a) and a triangular (Fig. 2b) geometry for $B = 1.5$ T.

On top of the transitions owing to a variation of the magnetic field, the impact of finite temperature is also of crucial importance. In Fig. 3a temperature effects on the topological charge are displayed. Starting from a relaxed configuration at $T = 1$ mK, the temperature is increased every 500 ps by $\Delta T = 2$ K and the topological charge is averaged over time at each temperature. The results show a first discontinuity at $T_1 \approx 40$ K. Up to this temperature the thermal fluctuations are relatively weak, and the number of well-defined skyrmions inside the sample remains constant. The small standard deviation of the topological number in this regime can be attributed to the thermal motion of the spins at the edge. However, the combination of thermal fluctuations and the repulsion between the skyrmions triggers the escape of a single skyrmion out of the sample at $T_1 \approx 40$ K. Hence, the total topological number is changed from $N_{Sk} \approx -5$ to $N_{Sk} \approx -4$, see Supplementary Movie 1. This change is also shown in the plot of the topological number susceptibility in Fig. 3b, defined as

$$\chi_N = \frac{1}{T} \left(\langle N_{Sk}^2 \rangle - \langle N_{Sk} \rangle^2 \right), \quad (1)$$

with $\langle N_{Sk} \rangle = \frac{1}{t_1 - t_0} \int_{t_0}^{t_1} N_{Sk}(t) \mathrm{d}t$. Only a minor deviation from the otherwise smooth function is visible. This means that the thermal fluctuations are still not strong enough to perturb the quasiparticles drastically.

A first characteristic change in the slope of the topological susceptibility can be seen at $T_2 \approx 50$ K. Comparing Fig. 3a, b it is obvious that the fluctuations of topological number are increasing with temperature, and around this point the lifetime of skyrmions is reduced below the averaging window. The average topological charge continuously approaches zero above this temperature. In this disordered regime, the lifetime of skyrmions is shorter than the observation time, as the fluctuations allow a collapse inside the sample. Hence, this temperature range is not favorable for information storage applications.

Finally, at about $T_3 \approx 100$ K the paramagnetic regime is entered, which is characterized by a completely disordered time-averaged magnetic configuration. Here the average topological charge is very close to zero. This behavior is also indicated by a change of sign in the first derivative $\mathrm{d}\chi_N(T)/\mathrm{d}T|_{T=T_3}$.

In the following, the external parameters are fixed to $T = T_0 = 15$ K and $B = B_0 = 1.5$ T, shown by the solid red lines in Figs. 1 and 3. This ensures that the thermal fluctuations do not lead to a
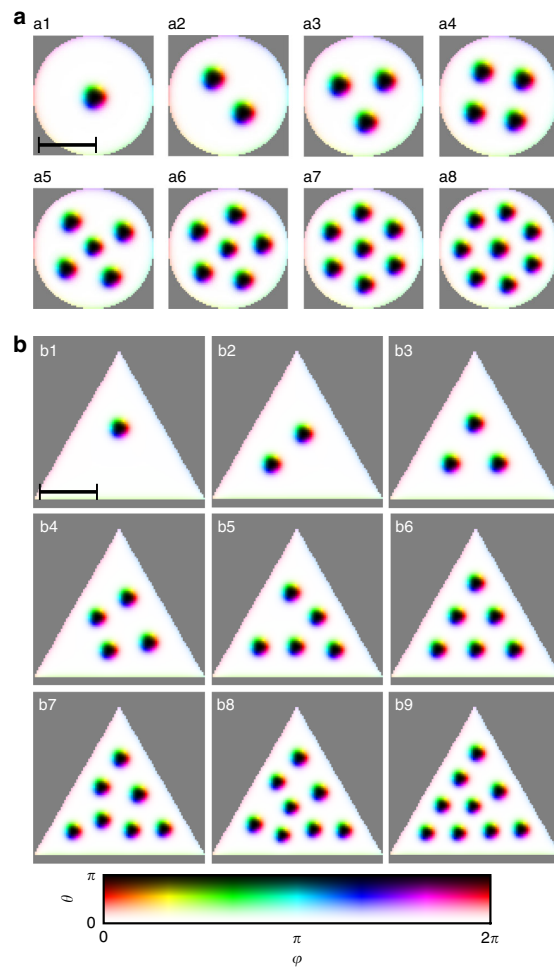

Fig. 2 Relaxed states for different initial skyrmion numbers. Brightness corresponds to the out-of-plane component of the magnetization characterized by the polar angle θ, whereas the color denotes the in-plane orientation described by the azimuthal angle φ, as shown in the color map. $B = 1.5$ T, $T = 0$ K. System size: **a** $21 \times 21 \times 0.4$ nm^3; **b** $30 \times 30 \times 0.4$ nm^3. The saturation magnetization is locally set to zero in the dark gray areas. Scale bar corresponds to 10 nm.

collapse or escape for the skyrmions, only to a diffusive motion, and that the number of particle-like skyrmions will be constant during the simulation time.

Skyrmion diffusion. With these first results, giving information on the segment of the parameter space we deal with, we will focus on the influence of thermal fluctuations on the dynamics of the skyrmions. In Figs. 4a and 5, results for different initial numbers of skyrmions presented in Fig. 2 are shown for the circular and triangular geometries, respectively. The first row shows the magnetic configuration after 20 ps of simulation time and the second row the final state, which means the magnetization state after our total simulation time of 20 ns. Only the out-of-plane z component is shown in grayscale. The magnetic configuration after only 20 ps is qualitatively very similar to the final one, displaying slightly deformed skyrmion configurations owing to the
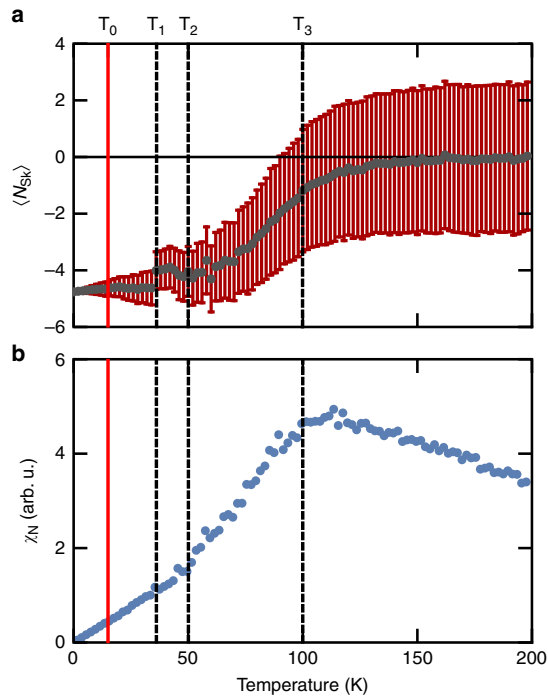
Fig. 3 Temperature dependence of the topological number. Disk-shaped island (21-nm diameter) for $B = 1.5$ T. **a** Total topological number $\langle N_{Sk} \rangle$ averaged over 0.5 ns with error bars indicating the standard deviation. **b** Topological number susceptibility χ_N (Eq. (1)), with the dashed black lines indicating three characteristic temperatures discussed in the main text. Solid red line marks the temperature used for successive simulations

thermal fluctuations compared to the zero-temperature initial states in Fig. 2. This short timescale, on which the short-range Heisenberg and DMI dominate the dynamics and cause shape deformations, is examined more extensively below.

The third row corresponds to the time-averaged z component, calculated over the simulation time divided into 1000 snapshots. In our understanding this result comes as close as possible to real-space scanning-probe measurements, due to the limited time resolution and finite measurement duration in such techniques. According to ref. [37], typical limits of the time resolution in SP–STM are $t_{res} > 5$ ms. With the present simulation parameters, we found that increasing the simulation time further does not lead to a significant change in the time-averaged images, indicating that similar observations may be expected on the much longer experimental time scales as well. The observed two characteristic time scales can be attributed to different interaction types of clearly distinguishable energy scales: local deformations on the picosecond time scale of the magnetic texture are dominated by thermal excitations competing with the short-range symmetric and antisymmetric exchange interactions, whereas the translational motion leading to the complex pattern formation over tens of nanoseconds is caused by the repulsive interactions between pairs of skyrmions and between skyrmions and the boundaries.

In case of the disk, it is extremely challenging to make a clear statement about the number of skyrmions in the system based on the time-averaged images only. As the symmetry of the system is a cylindrical one, also the resulting picture is cylindrically symmetric, consisting of concentric bright and dark circles and
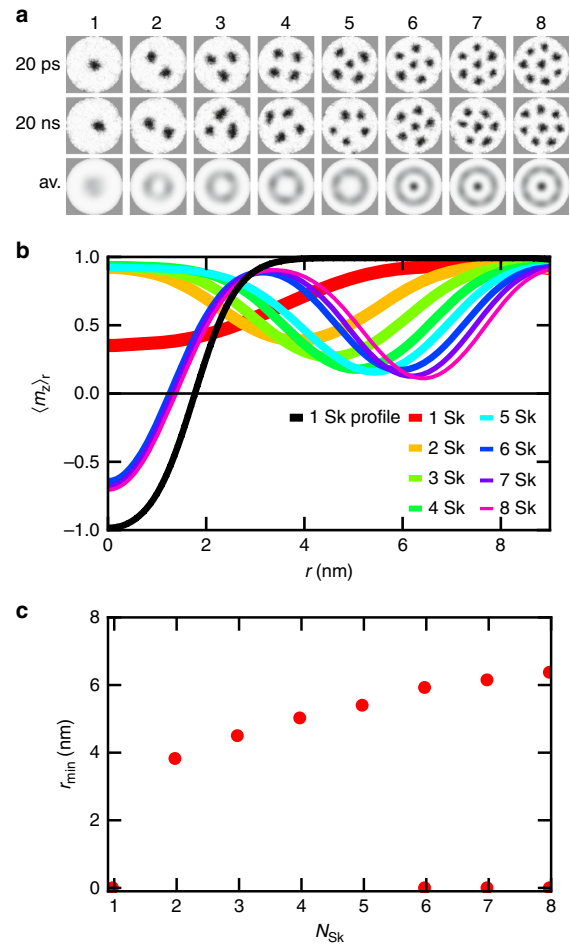
Fig. 4 Diffusive skyrmion motion on a circular island. **a** z component of the magnetization (white $+z$, black $-z$) for an ascending total skyrmion number. First row shows the configuration after 20 ps, the second row after 20 ns of elapsed time, and the third row represents the time average for the total simulation time over 1000 snapshots. **b** Time-averaged signal as a function of the distance from the center of the disk for different skyrmion numbers, averaged over the angular coordinate. Black line shows the static profile of a central single skyrmion. **c** Radii r_{min} corresponding to the local minima of the time-averaged signal in **b**, in dependence on the skyrmion number. Disk system (21 × 21 × 0.4 nm³), $T = 15$ K, $B = 1.5$ T. The saturation magnetization is locally set to zero in the dark gray areas

rings. The small contrast differences along the angular direction within a single diffusive ring-like area (third row in Fig. 4a) arise because of the finite simulation time, but also as an artifact of the finite grid, leading to a deviation from the ideal radial symmetry. For all initial configurations the total skyrmion number is conserved. As the skyrmions repulse each other, the radius of the resulting gray ring increases for higher skyrmion densities, before one of them becomes localized quite strongly in the center. This behavior is analyzed in Fig. 4b, where the out-of-plane magnetization component depending on the distance from the center of the disk is calculated by integration over the angular coordinate. For comparison, the static profile of a single skyrmion in the center of the disk is plotted as well (black curve).
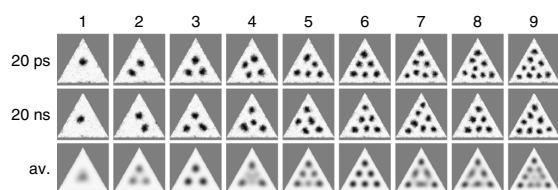
Fig. 5 Diffusive skyrmion motion on a triangular island. z component of the magnetization (white $+z$, black $-z$). First row shows the configuration after 20 ps, the second row after 20 ns of elapsed time, and the third row represents the time average for the total simulation time over 1000 snapshots. Triangular system ($30 \times 30 \times 0.4$ nm³), $T = 15$ K, $B = 1.5$ T. The saturation magnetization is locally set to zero in the dark gray areas

The positions of the local minima of the integrated functions are shown in Fig. 4c. Without performing the averaging over time, the profile of the skyrmion rotates from $m_z = -1$ in the center towards $m_z = 1$ in the field-polarized background. Owing to the diffusive motion of the skyrmions, the time-averaged images show a smaller difference compared with the background magnetization at the approximate positions of the skyrmions, providing a measure for the localized nature of the quasiparticles in the sample. For an increasing number of skyrmions, not only the radius of the resulting ring-shaped pattern increases, but so does the localization of the skyrmions.

For the triangular system in Fig. 5, the lower symmetry of the geometry is reflected in the resulting time-averaged pictures. The symmetry of the spin configuration coincides with that of the sample for one, three, and six skyrmions without thermal fluctuations, as shown in Fig. 2b. In the time-averaged images in the third row of Fig. 5, this results in well-localized skyrmions with a strong dark contrast for these numbers of quasiparticles in the system. Interestingly, also the adjacent configurations show almost the same time-averaged pattern as the highly symmetric configuration, e.g., two or four skyrmions compared with the case of three skyrmions. For the case where one skyrmion is missing from the highly ordered configuration, the remaining skyrmions imitate the absent skyrmion and effectively show up as an additional "phantom skyrmion". In contrast, a surplus skyrmion smears out in the time-averaged picture, so that mostly the high-symmetry points remain observable, even though they can also be slightly broadened— see the 6th and 7th columns in Fig. 5. For an even larger numbers of skyrmions, the repulsive interaction between them in combination with temperature fluctuations is strong enough for the skyrmions to escape at the boundary during the simulation time, as shown in the decreased number of quasiparticles in the second row compared to the first row in the 8th and 9th columns in Fig. 5.

To identify the different time regimes more clearly, the convergence behavior of the time-averaged pictures is investigated. The time-integrated pictures are calculated up to each snapshot time and compared with the averaged image after 20 ns via a matching parameter, where a complete agreement is denoted by a value of 1. The mathematical definition of the matching parameter is given in the Methods. The results are plotted in Fig. 6. Panels a and b show the convergence behavior for different skyrmion occupations for the disk and for the triangular geometry. For the circle, there are no major differences in terms of the convergence speed for different skyrmion numbers. Only the ensembles of three and seven skyrmions exhibit a slightly faster convergence, which is explicable by the resemblance of those states to the close-packed arrangement. As expected, the close-packed array possesses a lower mobility. In the case of the triangle, for three and six skyrmions the value 1 is
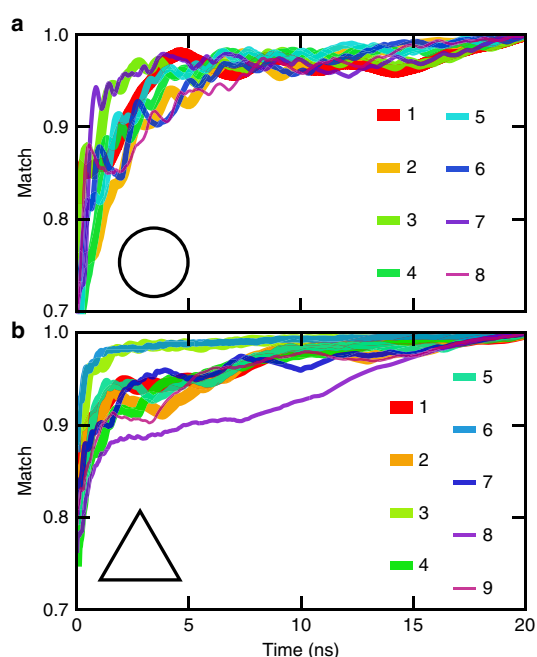

Fig. 6 Convergence behavior of the time-integrated magnetization for different skyrmion numbers. The match between the final time-averaged pattern after 20 ns and the time average taken until time t is defined such that a value of 1 corresponds to perfect agreement, see the Methods for details. **a**, **b** show the convergence of the matching parameter for the disk and triangular setup, respectively, for different skyrmion numbers

reached much faster than for the other configurations. This effect can again be explained by the strong localization of the skyrmions in these cases, preventing an exchange of their positions. A different trend is visible for the eight-skyrmion case (purple line in Fig. 6b), which shows a much slower convergence. This delayed behavior arises due to the non-conserved skyrmion number, which can be seen in Fig. 5. Consequently, after the escape of the skyrmions it takes more time until the averaged picture has adapted to this change.

For exploring the stochastic dynamics on the short time scale, which we suppose to be governed by the skyrmion deformations in contrast to the slow skyrmion displacement, multiple simulations are performed for the same initial configuration, two skyrmions inside the disk relaxed at zero temperature, but with different pseudorandom number seeds. The simulations cover a time of 100 ps each with 50 different initializations. After every 0.5 ps, a snapshot is taken and the positions of the two skyrmions extracted. On the scale of the simulation time no noteworthy displacement of each of the skyrmions takes place, however, a deformation of the magnetic textures is visible. The mean skyrmion radius relative to the zero temperature radius calculated as described in the Methods, is averaged over the different simulations, shown in Fig. 7 for each of the skyrmions (Fig. 7a, b). Here, two features are remarkable. First, the radius increases, approaching an enhancement of ~10% after 100 ps. Second, the radius is oscillating with a high frequency of approximately 60 GHz, estimated from the average time between the peaks. This oscillation can be identified with internal skyrmion modes, like the so-called breathing modes (see ref. [38]: at $T = 0$ K, $B = 1.5$ T and the triangular atomic lattice the
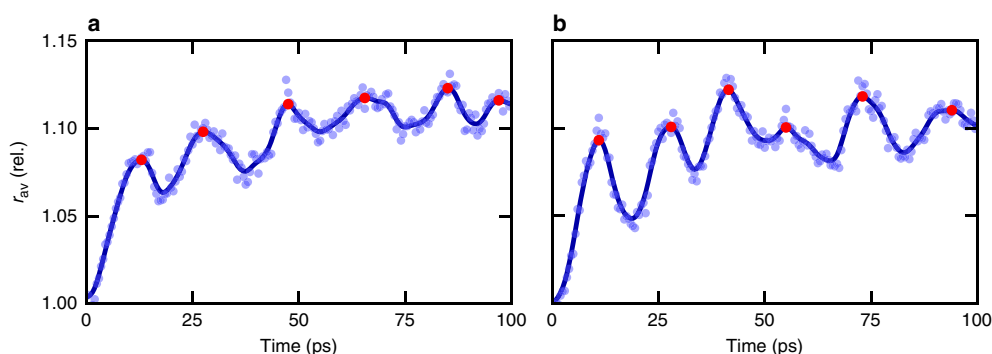
Fig. 7 Fast deformation dynamics of two skyrmions on a disk-shaped island. Two skyrmions on a single disk $(21 \times 21 \times 0.4)$ nm^3 are initialized from a relaxed zero-temperature configuration. Afterward, 50 different seeds for the pseudorandom number generator are used to simulate the skyrmion dynamics over 100 ps, saved every 0.5 ps. The results are analyzed by calculating the centers of the skyrmions, followed by the computation of the average skyrmion radius (see Methods) for each of them as shown in **a** and **b**. Averaging over the different simulations smears out most of the pure stochastic dynamics, yielding an oscillating pattern superposed with a general trend of an increased skyrmion radius compared to the zero-temperature configuration. Bright blue points show data averaged over different simulations, the solid blue line corresponds to data smoothened by a Gaussian filter in order to calculate the peak positions (red dots)

breathing mode frequency is $f = 70.88$ GHz, which is expected to decrease at higher temperature). These findings support the result that in confined geometries, different time scales are important for the skyrmion dynamics. On the short time scale the internal modes and deformations of the skyrmions are dominant, whereas on the longer time scale the interaction leads to a slowly converging pattern formation.

All of the discussed examples show the strong influence of the interaction between skyrmions as well as the role of the geometrical aspects on their mobility, that can vary between delocalization and a strong localization, e.g., in the center of the disk in Fig. 4a. This feature of variable mobility, depending on the geometry and packing density of skyrmions, is of general nature. In real experimental systems, further contributions may affect the mobility, and ultimately the measured position of the skyrmion as well. As an example of such a feature, defects in the grown thin film nanoislands will be discussed. In Fig. 8a, a nanoisland geometry inspired by the experimental results in refs. [7,12] is considered. In addition to the previous simulation parameters, a magnetic defect is inserted in the top-left corner of the island, treated as a simulation cell with the magnetization frozen along the in-plane $+x$ direction. The initial configuration including five skyrmions is evolved in time over a span of 20 ns, as shown in the snapshots in panel a. During the time evolution one skyrmion is pinned at the defect, whereas the others are moving rather freely. The resulting time average of the images reflects this behavior, as only a single spot is visible with a well-defined position in the upper left corner, and the rest of the quasiparticle features form a blurred trace mostly following the geometry of the island. In addition, the profile of the out-of-plane spin component is shown in Fig. 8b along the dashed arrow in the lower right panel of Fig. 8a. In this representation, the discrepancy between the measured profiles of the different skyrmions is even more pronounced. Where the localized skyrmion appears as a sharp dip almost reaching $m_z = -1$, the superposition of the other four skyrmions leads to broader and shallower features, and therefore no clear indication of their positions.

Quasiparticle model. The localization of the quasiparticles discussed above may also be interpreted as the probability density of finding a skyrmion at a selected position over the

complete simulation time. Such a probabilistic interpretation is capable of describing the different contrast levels observed for nominally equivalent skyrmions, and it proves to be valuable in the interpretation of scanning-probe experimental results where the characteristic measurement times are significantly longer than the time scale of the diffusive motion. In this section, a simplified quasiparticle model is introduced, motivated by the time-averaged data of the micromagnetic simulations, offering a time-efficient opportunity in predicting the complex pattern formation of the skyrmion probability distribution discussed above.

For the purpose of using a quasiparticle approach, the repulsive potential between pairs of skyrmions and between the skyrmion and the boundary needs to be quantified. Due to the Neumann boundary condition[40] at the edge of nanoislands, the DMI leads to a noncollinear spin texture, similar to a skyrmion[41]. Therefore, the interaction mechanism is the same between the skyrmions and between a skyrmion and the boundary, as has been studied in previous publications[29]. The exponential model function $E(r) = a \, \exp(-r/b)$ is fitted by the parameters $a = 0.211$ meV, $b = 1.343$ nm for skyrmion–boundary (Sk-Bnd) repulsion and $a = 1.246$ meV, $b = 1.176$ nm for skyrmion–skyrmion (Sk–Sk) interaction utilizing micromagnetic results. For details on the calculation of the potentials see the Supplementary Methods and Supplementary Fig. 1.

Starting from the modeled Sk–Sk and Sk–Bnd potentials quasiparticle simulations are executed, in order to compare the calculated probability densities with the time-averaged configurations obtained from full-fledged micromagnetic simulations. The main assumption for this endeavor is that neither the thermal fluctuations lead to the collapse, creation or escape of skyrmions, nor does a high skyrmion density lead to a merging of the skyrmions on the island as discussed in ref. [39]. A triangular setup containing two quasiparticles serves as the model system. The side of the triangle is chosen to be 30 nm, the same as in the case of the micromagnetic calculations shown in Figs. 2b and 5. The motion of the skyrmions inside the potential is calculated by modeling them as interacting random walkers, using an implementation of a Markov–chain Monte Carlo algorithm with Metropolis transition probabilities to study their diffusion, described in detail in the Methods section. This method offers a fast way of obtaining the cumulative probability density function
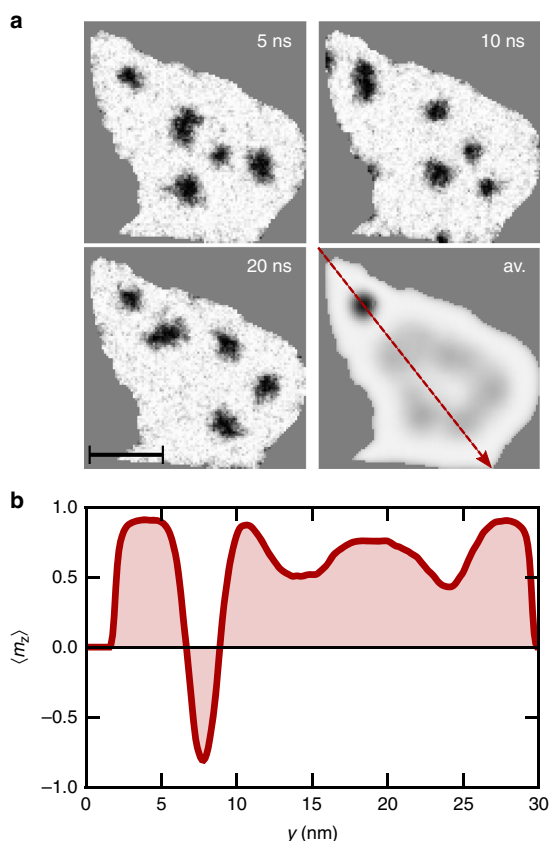
a

b

Fig. 8 Diffusive skyrmion motion on an asymmetric nanoisland including a defect. *z* component of the magnetization (white +*z*, black −*z*) is imaged. In the top-left corner, a defect is modeled by freezing the magnetization direction in a single simulation cell along the +*x* direction. **a** Snapshots of the magnetization at different times, as well as the resulting time-averaged picture (av.). Scale bar corresponds to 10 nm. **b** Time-averaged signal along the dashed arrow shown in the lower right part of **a**. Simulation box: $30 \times 30 \times 0.4$ nm^3, $T = 25$ K, $B = 1.5$ T. The saturation magnetization is locally set to zero in the dark gray areas

Fig. 9 Comparison of the Monte Carlo and micromagnetic simulations. The probability density function for two skyrmions inside a triangular island as obtained from **a**: micromagnetic simulations, and **b**: from calculations following the Monte Carlo algorithm. For the micromagnetic distribution, the coordinates of the skyrmions are extracted from the snapshots taken every 20 ps over 20 ns of simulation time at $T = 15$ K. **b** is generated over 10^5 Monte Carlo steps. Scale bar corresponds to 10 nm

of the positions of the two particles, which in turn can be compared to the time-averaged images in Figs. 4 and 5 obtained from micromagnetic simulations. In the following, a quantitative comparison between full micromagnetic simulations and Monte Carlo calculations will be presented to review the validity of the simplified quasiparticle approach. For this endeavor, we tracked the positions of two skyrmions in the triangular system from the micromagnetic simulation snapshots after every 20 ps and calculated the probability density distribution of the center coordinates. The resulting distribution is shown in Fig. 9a, along with the Monte Carlo result after 10^5 Monte Carlo steps in Fig. 9b. The largest difference between the two results arises because of the substantially less data for the micromagnetic calculation. As the histogram is calculated with only 10^3 snapshots compared with 10^5 Monte Carlo steps, this behavior is expected. Nevertheless, the characteristic features are similar. In both results the three peak densities are not radially symmetric, but are resembling the triangular boundary shape. Hence, this deformation is not an artifact of the Monte Carlo simulation.

In addition, the average distance between the density maxima may serve as a good quantity for comparing both methods. As Fig. 9a lacks the resolution for calculating the peak positions reliably, we start instead from the time-integrated magnetization pictures in Fig. 5. Based on the averaged result for two skyrmions, we extract again the peak positions and calculate subsequently the mean distance. The positions for the Monte Carlo calculations are at $(11.0, 6.5)$ nm, $(15.0, 13.5)$ nm, $(19.0, 6.5)$ nm, the micromagnetic simulations deliver $(11.1, 6.6)$ nm, $(15.0, 13.5)$ nm, $(19.0, 6.5)$ nm. This leads to an average distance of 8.0 nm for both the Monte Carlo calculations and the micromagnetic simulations, supporting the validity of the simplified quasiparticle approach in the investigated parameter space.

The model is capable of predicting the skyrmion distribution in the long-time limit and thereby serves as a method for computationally efficient calculations for larger or more complex systems.

As an example, the probability density functions of the Monte Carlo simulations are shown in Fig. 10 after 10^5 Monte Carlo steps for different temperatures and sample sizes. Owing to the repulsion between the two skyrmions, equilibrium positions are found close to the vertices of the triangle, with energy barriers between these local energy minima. At low temperature ($T = 1$ K) and a small island size (30 nm edge length) in the upper left panel in Fig. 10, no transitions between the minima occur during the duration of the simulation, and two skyrmions may be observed in the obtained probability densities. As the temperature is increased to $T = 15$ K or $T = 30$ K in the first row of Fig. 10, the transition rate between the preferential positions is enhanced, and an additional "phantom skyrmion" appears in the probability density function, in remarkable agreement with the micromagnetic results as analyzed before. By enlarging the size of the island (second and third rows in Fig. 10 for 45 nm and 60 nm edge length), the energy surface becomes flatter, which in turn leads to higher transition probabilities between the energy minima at the same temperature. Therefore, raising the temperature or increasing the size of the system have similar effects on the resulting probability density functions for the skyrmions. Consequently, large island sizes or high temperatures result in completely delocalized skyrmions as indicated in the bottom right panel in Fig. 10.

Discussion

In this paper, we studied the temperature-driven diffusive motion of ensembles of magnetic skyrmions in finite magnetic islands. Based on experimentally determined system parameters for
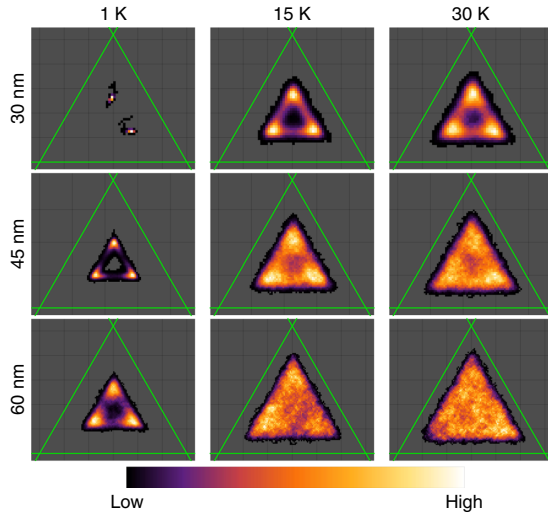
Fig. 10 Probability density function for two skyrmions inside a triangular model potential calculated following a Monte Carlo algorithm. The temperatures are $T = 1$ K, $T = 15$ K, and $T = 30$ K, the edge lengths of the triangle are 30 nm, 45 nm, and 60 nm. Probability distributions for the centers of the two skyrmions are calculated over 10^5 Monte Carlo steps

ultrahin Pd/Fe bilayers on Ir(111), we performed full-fledged micromagnetic simulations for various nanoisland geometries. For moderate temperatures and external magnetic fields, magnetic skyrmions with a long lifetime are present in the system, so that the topological charge is conserved. Our study of this model system showed two different time scales on which the stochastic dynamics of skyrmions takes place. On the short time scale ($t \sim 1$ ps), the fluctuating dynamics governed by the symmetric and antisymmetric exchange interaction is most prominent, which essentially leads to local deformations, exciting internal modes of the skyrmions. In the long-time limit ($t \gtrsim 10$ ns), interactions between pairs of skyrmions, as well as between the quasiparticles and the boundaries, are dominant. These thermally activated mechanisms lead to complicated time-averaged pictures of the skyrmion distribution, where the number of quasiparticles in the system is not immediately apparent. These results can be compared directly to images obtained from time-integrating measurement techniques such as SP–STM or MFM, the time-resolution of which (~ 5 ms[37]) is typically much longer than the time scale of the inherent dynamics of skyrmions. Our findings open an alternative way compared to conventional interpretations of experimental results obtained with scanning-probe methods on mobile arrays of skyrmions, by differentiating between the various time scales of magnetization dynamics.

Furthermore, we proposed and developed a Monte Carlo quasiparticle model, which can be of great use to efficiently calculate the stochastic motion of larger systems of skyrmions in arbitrarily shaped geometries. According to the results, the time-averaged images of the micromagnetic simulations can be qualitatively well reproduced by the probability density distributions obtained from the simple quasiparticle model, as long as it is possible to treat the skyrmions as stable objects with lifetimes significantly longer than the simulation time at the given temperature. This method can be used to describe larger systems containing more skyrmions at various temperatures in a computationally efficient way, including model applications

in storage technology like racetrack memory devices. Here, not only the stability of the information bit is important, but also its addressability, which is immediately affected by the diffusive motion of the skyrmions.

Methods

Micromagnetic simulations. Finite-temperature micromagnetic calculations, using the open-source, GPU-accelerated software package mumax3[40], were performed to solve the LLG equation,

$$\mathbf{\dot{m}}_i(t) = -\frac{\gamma}{1 + \alpha^2}\left[\mathbf{m}_i \times \mathbf{B}_i^{\mathrm{eff}} + \alpha \mathbf{m}_i \times \left(\mathbf{m}_i \times \mathbf{B}_i^{\mathrm{eff}}\right)\right], \quad (2)$$

for every simulation cell $\mathbf{m}_i$ of the discretized magnetization vector field. Here, $\gamma_0 = 1.76 \times 10^{11}(\mathrm{T}^{-1}\,\mathrm{s}^{-1})$ is the gyromagnetic ratio of an electron and α is the Gilbert damping parameter. The time- and space-dependent effective magnetic field,

$$\mathbf{B}_i^{\mathrm{eff}} = \mathbf{B}_i^{\mathrm{ext}} + \mathbf{B}_i^{\mathrm{exch}} + \mathbf{B}_i^{\mathrm{d}} + \mathbf{B}_i^{\mathrm{a}} + \mathbf{B}_i^{\mathrm{dmi}} + \mathbf{B}_i^{\mathrm{th}}, \quad (3)$$

is composed of the external field $\mathbf{B}_i^{\mathrm{ext}}$; exchange interaction field $\mathbf{B}_i^{\mathrm{exch}} = 2A_{\mathrm{exch}}/M_{\mathrm{sat}}\Delta \mathbf{m}_i$, with A_{exch} the exchange stiffness and M_{sat} the saturation magnetization; demagnetizing field $\mathbf{B}_i^{\mathrm{d}} = M_{\mathrm{sat}}\mathbf{K}_{ij} * \mathbf{m}_j$, where details on the calculation of the demagnetizing kernel $\mathbf{K}$ can be found in ref. [40]; uniaxial magnetocrystalline anisotropy field $\mathbf{B}_i^{\mathrm{a}} = 2K_{\mathrm{u}}/M_{\mathrm{sat}}m_z\mathbf{e}_z$, with K_{u} the anisotropy constant; and the field generated by the DMI $\mathbf{B}_i^{\mathrm{dmi}} = 2D/M_{\mathrm{sat}}$ $(\partial m_z/\partial x, \partial m_z/\partial y, -\partial m_x/\partial x - \partial m_y/\partial y)^T$, with D the strength of the interfacial DMI. The simulation parameters were determined experimentally in ref. [7] based on the field dependence of the skyrmion profile: $M_{\mathrm{sat}} = 1.1$ MA m^{-1}, $D = 3.9$ mJ m^{-2}, $A_{\mathrm{exch}} = 2$ pJ m^{-1}, $K_{\mathrm{u}} = 2.5$ MJ m^{-3} and $\alpha = 0.05$.

In addition, an effective thermal field is included in Eq. (3) as

$$\mathbf{B}_i^{\mathrm{th}} = \eta\sqrt{\frac{2\alpha k_{\mathrm{B}}T}{M_{\mathrm{sat}}\gamma_0\Delta V\Delta t}}, \quad (4)$$

where η is a random vector generated according to a standard normal distribution independently for each simulation cell and time step. k_{B} is Boltzmann's constant, T is the temperature, ΔV is the size of the simulation cell and Δt is the time step of simulation.

During the simulations, the cell size was set to $\Delta V = 0.3 \times 0.3 \times 0.4$ nm^3. The linear size of the cell is comparable to the lattice constant $a = 0.271$ nm of the Pd/Fe bilayer on Ir(111). This means that the micromagnetic simulations performed here should closely resemble the results of atomistic simulations where the skyrmions collapse when their size becomes comparable to the lattice constant[37,39], and where the use of temperature-independent model parameters is justified.

The total skyrmion number N_{Sk} in the simulations was calculated via

$$N_{\mathrm{Sk}} = \frac{1}{4\pi}\int \mathbf{m} \cdot \left(\frac{\partial \mathbf{m}}{\partial x} \times \frac{\partial \mathbf{m}}{\partial y}\right)\mathrm{d}x\mathrm{d}y. \quad (5)$$

Processing of the micromagnetic results. For the results shown in Fig. 6, the z component of the magnetization averaged up to time t is stored in grayscale pictures as a matrix, $A_{ij}(t) = (m_z(x_i, y_j, t) + 1)/2$, where x_i and y_j denote the position of the micromagnetic simulation cell. The distance induced by the Frobenius norm between the image averaged up to time t, $A_{ij}(t)$, and the image averaged over the whole simulation length $\tau = 20$ ns, $A_{ij}(\tau)$ is divided by the square root of the number of matrix elements and subtracted from 1, yielding the matching parameter

$$M(t) = 1 - \sqrt{\sum_{i=1}^{N_x}\sum_{j=1}^{N_y}\frac{(A_{ij}(t) - A_{ij}(\tau))^2}{N_x N_y}}. \quad (6)$$

This procedure gives a matching parameter of 1 for a perfect agreement of the compared pictures.

In order to determine the skyrmion radius as a function of time in Fig. 7, first the contour lines where the z component of the magnetization is zero are calculated for the skyrmion at each time step. The contour lines are discretized on N points in space, $\mathbf{L}_i(t) = (x_i(t), y_i(t))$, $i \in (1, ..., N)$. Subsequently, the center of the skyrmion is calculated via

$$\mathbf{c}(t) = \frac{1}{N}\sum_{i=1}^N \mathbf{L}_i(t), \quad (7)$$

which in turn is used to obtain the average skyrmion radius

$$\bar{r}(t) = \frac{1}{N}\sum_{i=1}^N \|\mathbf{L}_i(t) - \mathbf{c}(t)\|. \quad (8)$$

Finally, the radius is normalized with respect to the zero temperature radius r_0 obtained from the relaxed initial configuration of choice.

Quasiparticle simulations. For the calculation of the stochastic motion of skyrmions following the quasiparticle approach, the Metropolis algorithm[42] was utilized. With this method, the probability density function converges to the Boltzmann distribution determined by the energy functional of the system. For the triangular geometry, the potential surface was computed by taking the superposition of the potentials shown in Supplementary Fig. 1 from the three boundaries for every grid point of the chosen finite, rectangular mesh. The cell size was $\Delta V = 0.5 \times 0.5 \times 0.4$ nm. The initial positions of the skyrmions were randomly chosen inside the confined structure, excluding the case in which both quasiparticles start from the same simulation cell. At each time step, a possible adjacent position is selected for each skyrmion simultaneously via pseudorandom numbers. If the energy of the attempted new state, including interaction between the skyrmions, is lower than the energy of the initial one, the skyrmion will move there. If not, the transition into this state happens with a probability of $p(\Delta E) = \exp(-\Delta E / k_B T)$ following the Boltzmann distribution. Here $\Delta T = E_2 - E_1$ is the energy difference between the final and the initial states, k_B is Boltzmann's constant and T is the temperature. Subsequently, new attempted positions are generated and accepted or rejected as before until a fixed number of simulation steps is reached.

Data availability
Data that support the findings of this work are available from the corresponding author on request.

Code availability
For obtaining the results, we used the open-source, GPU-accelerated software package mumax3[40] for the micromagnetic simulations. The quasiparticle simulations were carried out via a Mathematica[43] code developed for this purpose. Input files are available from the corresponding author on request.

References
1. Bogdanov, A. & Yablonskii, D. Thermodynamically stable vortices in magnetically ordered crystals. The mixed state of magnets. *Zh. Eksp. Teor. Fiz.* **95**, 178–182 (1989).
2. Mühlbauer, S. et al. Skyrmion lattice in a chiral magnet. *Science* **323**, 915–919 (2009).
3. Nagaosa, N. & Tokura, Y. Topological properties and dynamics of magnetic skyrmions. *Nat. Nanotechnol.* **8**, 899–911 (2013).
4. Dzyaloshinsky, I. A thermodynamic theory of weak ferromagnetism of antiferromagnetics. *J. Phys. Chem. Sol.* **4**, 241–255 (1958).
5. Moriya, T. Anisotropic superexchange interaction and weak ferromagnetism. *Phys. Rev.* **120**, 91–98 (1960).
6. Heinze, S. et al. Spontaneous atomic-scale magnetic skyrmion lattice in two dimensions. *Nat. Phys.* **7**, 713–718 (2011).
7. Romming, N., Kubetzka, A., Hanneken, C., von Bergmann, K. & Wiesendanger, R. Field-dependent size and shape of single magnetic skyrmions. *Phys. Rev. Lett.* **114**, 177203 (2015).
8. Bogdanov, A. & Hubert, A. The stability of vortex-like structures in uniaxial ferromagnets. *J. Magn. Magn. Mater.* **195**, 182–192 (1999).
9. Parkin, S. S., Hayashi, M. & Thomas, L. Magnetic domain-wall racetrack memory. *Science* **320**, 190–194 (2008).
10. Sampaio, J., Cros, V., Rohart, S., Thiaville, A. & Fert, A. Nucleation, stability and current-induced motion of isolated magnetic skyrmions in nanostructures. *Nat. Nanotechnol.* **8**, 839–844 (2013).
11. Tomasello, R. et al. A strategy for the design of skyrmion racetrack memories. *Sci. Rep.* **4**, 6784 (2014).
12. Romming, N. et al. Writing and deleting single magnetic skyrmions. *Science* **341**, 636–639 (2013).
13. Schäffer, A. F., Dürr, H. A. & Berakdar, J. Ultrafast imprinting of topologically protected magnetic textures via pulsed electrons. *Appl. Phys. Lett.* **111**, 032403 (2017).
14. Hanneken, C. et al. Electrical detection of magnetic skyrmions by non-collinear magnetoresistance. *Nat. Nanotechnol.* **10**, 1039–1042 (2015).
15. Göbel, B., Mook, A., Henk, J. & Mertig, I. Magnetoelectric effect and orbital magnetization in skyrmion crystals: Detection and characterization of skyrmions. *Phys. Rev. B* **99**, 060406 (2019).
16. Maccariello, D. et al. Electrical detection of single magnetic skyrmions in metallic multilayers at room temperature. *Nat. Nanotechnol.* **13**, 233–237 (2018).
17. Slonczewski, J. C. Current-driven excitation of magnetic multilayers. *J. Magn. Magn. Mater.* **159**, L1–L7 (1996).
18. Iwasaki, J., Mochizuki, M. & Nagaosa, N. Universal current-velocity relation of skyrmion motion in chiral magnets. *Nat. Commun.* **4**, 1463 (2013).
19. Jonietz, F. et al. Spin transfer torques in MnSi at ultralow current densities. *Science* **330**, 1648–1651 (2010).
20. Hagemeister, J., Romming, N., von Bergmann, K., Vedmedenko, E. & Wiesendanger, R. Stability of single skyrmionic bits. *Nat. Commun.* **6**, 8455 (2015).
21. Rózsa, L., Simon, E., Palotás, K., Udvardi, L. & Szunyogh, L. Complex magnetic phase diagram and skyrmion lifetime in an ultrathin film from atomistic simulations. *Phys. Rev. B* **93**, 024417 (2016).
22. Lobanov, I. S., Jónsson, H. & Uzdin, V. M. Mechanism and activation energy of magnetic skyrmion annihilation obtained from minimum energy path calculations. *Phys. Rev. B* **94**, 174418 (2016).
23. Bessarab, P. F. et al. Lifetime of racetrack skyrmions. *Sci. Rep.* **8**, 3433 (2018).
24. von Malottki, S., Dupé, B., Bessarab, P., Delin, A. & Heinze, S. Enhanced skyrmion stability due to exchange frustration. *Sci. Rep.* **7**, 12299 (2017).
25. Schütte, C., Iwasaki, J., Rosch, A. & Nagaosa, N. Inertia, diffusion, and dynamics of a driven skyrmion. *Phys. Rev. B* **90**, 174434 (2014).
26. Miltat, J., Rohart, S. & Thiaville, A. Brownian motion of magnetic domain walls and skyrmions, and their diffusion constants. *Phys. Rev. B* **97**, 214426 (2018).
27. Zázvorka, J. et al. Thermal skyrmion diffusion used in a reshuffler device. *Nat. Nanotechnol.* https://doi.org/10.1038/s41565-019-0436-8 (2019).
28. Pinna, D. et al. Skyrmion gas manipulation for probabilistic computing. *Phys. Rev. Appl.* **9**, 064018 (2018).
29. Lin, S.-Z., Reichhardt, C., Batista, C. D. & Saxena, A. Particle model for skyrmions in metallic chiral magnets: dynamics, pinning, and creep. *Phys. Rev. B* **87**, 214419 (2013).
30. Reichhardt, C., Ray, D. & Reichhardt, C. J. O. Collective transport properties of driven skyrmions with random disorder. *Phys. Rev. Lett.* **114**, 217202 (2015).
31. Thiele, A. A. Steady-state motion of magnetic domains. *Phys. Rev. Lett.* **30**, 230–233 (1973).
32. Wiesendanger, R. Spin mapping at the nanoscale and atomic scale. *Rev. Mod. Phys.* **81**, 1495–1550 (2009).
33. Martin, Y. & Wickramasinghe, H. K. Magnetic imaging by force microscopywith 1000 Å resolution. *Appl. Phys. Lett.* **50**, 1455–1457 (1987).
34. Rózsa, L. et al. Skyrmions with attractive interactions in an ultrathin magnetic film. *Phys. Rev. Lett.* **117**, 157205 (2016).
35. Böttcher, M., Heinze, S., Egorov, S., Sinova, J. & Dupé, B. B–T phase diagram of Pd/Fe/Ir (111) computed with parallel tempering Monte Carlo. *New J. Phys.* **20**, 103014 (2018).
36. Gilbert, T. L. A phenomenological theory of damping in ferromagnetic materials. *IEEE Trans. Magn.* **40**, 3443–3449 (2004).
37. Leonov, A. et al. The properties of isolated chiral skyrmions in thin magnetic films. *New J. Phys.* **18**, 065003 (2016).
38. Rózsa, L., Hagemeister, J., Vedmedenko, E. Y. & Wiesendanger, R. Localized spin waves in isolated k π skyrmions. *Phys. Rev. B* **98**, 224426 (2018).
39. Siemens, A., Zhang, Y., Hagemeister, J., Vedmedenko, E. & Wiesendanger, R. Minimal radius of magnetic skyrmions: statics and dynamics. *New J. Phys.* **18**, 045021 (2016).
40. Vansteenkiste, A. et al. The design and verification of MuMax3. *AIP Adv.* **4**, 107133 (2014).
41. Rohart, S. & Thiaville, A. Skyrmion confinement in ultrathin film nanostructures in the presence of Dzyaloshinskii-Moriya interaction. *Phys. Rev. B* **88**, 184422 (2013).
42. Metropolis, N. et al. Equation of state calculations by fast computing machines. *J. Chem. Phys.* **21**, 1087–1092 (1953).
43. Inc., W. R. Mathematica, Version 12.0. (Champaign, IL 2019).

Author contributions
A.F.S. conducted and analyzed the micromagnetic and quasiparticle Monte Carlo simulations. E.Y.V. proposed and developed a general concept of this investigation.

Additional information

Supplementary information accompanies this paper at https://doi.org/10.1038/s42005-019-0176-y.

Competing interests: The authors declare no competing Interests.

Reprints and permission information is available online at http://npg.nature.com/reprintsandpermissions/

Publisher's note: Springer Nature remains neutral with regard to jurisdictional claims in published maps and institutional affiliations.

CHAPTER 4

RESULTS B: TWISTED MAGNONS

In contrast to the previous discussion, this chapter is dedicated to dynamical topologically non-trivial magnetic excitations. Based on theoretical derivations, an unexplored class of spin waves is predicted. These waves are best characterized by their helical wavefronts and their associated orbital angular momentum. In remembrance of the well-studied *twisted* light, electrons, and neutrons (cf. section 2.3.3), these spin wave modes are called twisted magnons.

The investigation starts with a cylindrically symmetric ferromagnetic nanowire that offers a comfortable playground for theoretical considerations. In the work *Twisted magnon beams carrying orbital angular momentum* [AFS6] [1], general features of these spin wave modes are derived, including their dispersion relation, the OAM-tunable magnon Hall effect, and discuss the possible electric field control of the spin wave topology via the Aharonov-Casher effect [2]. One key result regarding multiplex communication applications that rely on the orthogonality of different spin wave modes is the robustness of the topological charge against damping effects. Consequently, information can be transported in magnonic waveguides over long distances in topologically distinct data channels.

Based on these findings, different excitation mechanisms of twisted magnon modes are elaborated. In contrast to the tailored external control parameters presented in [AFS6], in the publication *Twisting and tweezing the spin wave: on vortices, skyrmions, helical waves, and the magnonic spiral phase plate* [AFS7] [2] the possibility of realizing a magnonic spiral phase plate in analogy to optical spiral phase plates [3] is demonstrated. This magnetic heterostructure transforms an incoming plane wave into a helical wave of chosen OAM or vice versa. The materials and spiral height are chosen such that a travers-

---

[1] Reprinted from (C. Jia, D. Ma, A. F. Schäffer, J. Berakdar, Twisted magnon beams carrying orbital angular momentum, *Nat. Commun.* **10**, 2077 (2019); Ref. AFS6). Published by Springer Nature under the terms of the Creative Commons Attribution 4.0 license.

[2] Reprinted from (C. Jia, D. Ma, A. F. Schäffer, J. Berakdar, Twisting and tweezing the spin wave: on vortices, skyrmions, helical waves, and the magnonic spiral phase plate, *J. Opt.* **21**, 124001 (2019); Ref. AFS7). Published by IOP Publishing under the terms of the Creative Commons Attribution 3.0 license.

ing wave accumulates an angular-dependent additional phase $\ell\varphi$. In the shown exemplary simulations, the heterostructure is composed of Py and YIG because of their small Gilbert damping parameters. Remarkably, the formation of the twisted magnon succeeds despite large stray fields at the interfaces of the heterostructures occur due to the unequal saturation magnetization. The resulting partial reflection and scattering of magnons do not harm the imprinting of the topological charge. This effect demonstrates the stability of helical modes and opens up another way to excite a twisted magnon mode of choice.

Additionally, it is reported on the interaction of waveguides hosting twisted magnon modes. In the paper *Generation, electric detection, and orbital-angular momentum tunneling of twisted magnons* [AFS8] [3], results on the dipole-field driven tunneling of OAM between separate magnetic disks are presented. The spin current generated by the twisted spin wave modes via the inverse spin Hall effect (ISHE) is calculated, enabling a distinctive electrical detection in future experimental realizations.

Finally, the concept of twisted magnon modes is extended to antiferromagnetic (AFM) materials in the publication *Chiral Logic Computing with Twisted Antiferromagnetic Magnon Modes* [AFS10] [4] and the potential utilization for swift data communication and wave-based logic computing is demonstrated. In contrast to FM waveguides, AFM systems are composed out of two antiferromagnetically coupled sublattices, which inherently show resonance frequencies in the range of terahertz though the corresponding wavelengths remain on the scale of 10^{-8} m. Hence, information transfer and topology-based chiral logic computing operations can be realized at high operation frequencies. On top of that, the stray fields of both sublattices compensate each other in the AFM ground state, making AFM devices less vulnerable to external field perturbations compared to FMs. Similar to the FM case, an analytical model is derived for a cylindrical AFM waveguide from the equations of motion of the coupled spin system. This procedure leads to the existence of magnonic eigenmodes in AFM waveguides that possess a well-defined topological charge. Based on these results, the control of twisted AFM modes via electrically tunable DMI is studied. Because of the arbitrary spin wave polarization in AFM, logic gate operations (Phase-shift, Hadamard, Pauli-gates) can be realized, but in addition to that, the orthogonality of spin wave modes with distinct topological charges is exploitable. Hence parallel, wave-based, topologically protected logic operations are achievable. To demonstrate the feasibility, spin dynamics simulations are performed for a NiO model system. The propagated (mixed) wave packets are shown to cause character-

---

[3]Reprinted from (M. Chen, A. F. Schäffer, J. Berakdar, C. Jia, Generation, electric detection, and orbital-angular momentum tunneling of twisted magnons, *Appl. Phys. Lett.* **116**, 17, 172403 (2019); Ref. AFS8), with the permission of AIP Publishing.

[4] Reprinted from (C. Jia, M. Chen, A. F. Schäffer, J. Berakdar, Chiral logic computing with twisted antiferromagnetic magnon modes, *npj Comput. Mat.* **7**:101 (2021); Ref. AFS10). Published by Springer Nature under the terms of the Creative Commons Attribution 4.0 license.

istic topology- and chirality-dependent signals in the pumped spin density at a waveguide surface. Hence twisted AFM spin waves are controllable, measurable and can be utilized for parallel logic computing operations.

ARTICLE

Twisted magnon beams carrying orbital angular momentum

Chenglong Jia[1], Decheng Ma[1], Alexander F. Schäffer [2] & Jamal Berakdar [2]

Low-energy eigenmode excitations of ferromagnets are spin waves or magnons that can be triggered and guided in magnonic circuits without Ohmic losses and hence are attractive for communicating and processing information. Here we present new types of spin waves that carry a definite and electrically controllable orbital angular momentum (OAM) constituting twisted magnon beams. We show how twisted beams emerge in magnonic waveguides and how to topologically quantify and steer them. A key finding is that the topological charge associated with OAM of a particular beam is tunable externally and protected against magnetic damping. Coupling to an applied electric field via the Aharanov-Casher effect allows for varying the topological charge. This renders possible OAM-based robust, low-energy consuming multiplex magnonic computing, analogously to using photonic OAM in optical communications, and high OAM-based entanglement studies, but here at shorter wavelengths, lower energy consumption, and ready integration in magnonic circuits.

---

[1] Key Laboratory for Magnetism and Magnetic Materials of the Ministry of Education and Institute of Theoretical Physics, Lanzhou University, 73000 Lanzhou, China. [2] Institut für Physik, Martin-Luther-Universität Halle-Wittenberg, 06099 Halle (Saale), Germany. Correspondence and requests for materials should be addressed to C.J. (email: cljia@lzu.edu.cn) or to J.B. (email: jamal.berakdar@physik.uni-halle.de)

Recently, the spatial structuring of photonic, electronic, or neutron beams has been demonstrated[1–5] enabling to encode additional information in the beam spatial distribution. For instance, a photonic beam can be spatially modulated to have a helical or twisted wavefront embodying a well-defined, internal, meaning origin-independent, orbital angular momentum. The external orbital angular momentum (OAM) is origin dependent and is obtained from the photonic angular momentum density $\mathbf{L}_\gamma = \mathbf{r}_\gamma \times \mathbf{P}_\gamma$, where $\mathbf{r}_\gamma$ is measured with respect to the beam center and $\mathbf{P}_\gamma$ is the linear momentum density[6]. Similar arguments apply to matter fields[3–5]. The intense research on this topic is fueled not only by fundamental interest but also by the new possibilities and functionalities accomplished by structuring the spatial distributions of the waves. For instance, OAM can take very large values that can be exploited for multiplex communications and quantum information based on entangled photons with large OAM[1–5,7–9]. Here we uncover the existence of twisted magnon beams, which are low-energy spin waves that carry a well-defined OAM. We demonstrate how they are triggered in a magnonic waveguide (such as in Fig. 1), and how to quantify their topological nature by an associated topological charge, which is found to be related to the OAM of a particular twisted beam. It is shown that this topological charge is electrically tunable and protected against damping. Hence, twisted magnonic beams are ideal candidates for robust, low-energy cost multiplex magnonic computing using the versatile toolbox for material and spin waves engineering[10–17]. In addition, we find an OAM-dependent magnonic Hall effect that depends on the value of OAM and, hence its value can be steered electrically. We also inspect the nature of thermal magnetic fluctuations around the equilibrium-ordered phase in a magnetic sample supporting twisted modes and find an anisotropic dependence of the correlation length.

Results

Analytical model for twisted magnon beams. What are the requirements for the emergence of OAM-carrying waves in magnetic systems and what is their relevance? In magnetically ordered systems key low-energy carriers of information are spin waves or magnons, which are the quanta of low-energy magnetic excitations. Identifying twisted magnonic beams that carry OAM would open a subfield in magnonics since OAM in principle can have an unbounded value. Thus, let us consider a generic ferromagnetic (FM) cylindrical waveguide modeled by localized magnetic moments at site i described by the magnetic moment operator $\mathbf{M}_i$ or the corresponding (dimensionless) spin operator $\mathbf{S}_i = -\mathbf{M}_i/(\gamma\hbar)$ (γ is the gyromagnetic ratio). The (Heisenberg) Hamiltonian reads $\mathcal{H} = -\frac{1}{2}\sum_{ij} J_{ij}\mathbf{M}_i \cdot \mathbf{M}_j - \frac{K_s}{2}\sum_i (\widehat{\mathbf{e}}_z \cdot \mathbf{M}_i)^2 - \sum_i \mathbf{B} \cdot \mathbf{M}_i$, where $J_{ij} > 0$ is the exchange coupling between nearest-neighbor sites (ij), and $K_s > 0$ is a magnetic anisotropy contribution including the shape anisotropy (the demagnetizing factor tensor D_{ij} at any given direction of the cylindrical nanowire are approximately zero, except for $D_{xx} = D_{yy} \simeq 1/2$[18,19]). $\mathbf{B} = (0, 0, B_z)$ is an external magnetic field along the waveguide (this direction is taken as the z-axis). For magnetically ordered systems longitudinal excitations, meaning changes in the expectation value of $\mathbf{M}_i$, caused for example by changes in J_{ij}, are much higher in energy than transversal ones. The latter correspond to a precession of the unit vector field $\mathbf{m}_i = \mathbf{M}_i/|\mathbf{M}_i|$, while $|\mathbf{M}_i| = M = $ constant and their energy is typically set by K_s, which is much smaller than J_{ij}[20]. Hence, we inspect the transversal spin dynamics governed by the Heisenberg equation of motion $d\mathbf{m}_i/dt = -i/\hbar[\mathbf{m}_i, \mathcal{H}]$. The dynamics of the magnetization unit vector field proceeds as (we introduce the
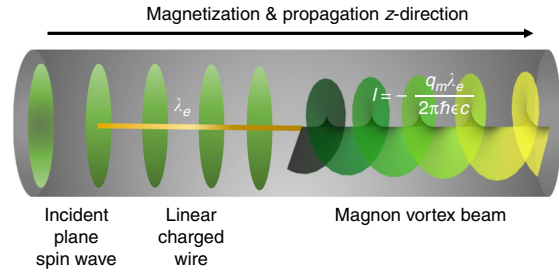

Fig. 1 Proposal for generating a twisted magnon beam exploiting the Aharanov–Casher effect. Incident spin waves (impinging from left) that propagate in a cylindrical magnetic insulator waveguide traverse a region with a linear charge density λ_e (marked yellow). As demonstrated here, a magnonic twisted beam emerges to the right and can be quantified by the topological charge $\ell \propto \lambda_e$, which is associated with a monopole-like vector potential, $\mathbf{A}_e(\mathbf{r}) \sim \frac{\lambda_e}{r}\widehat{\mathbf{e}}_\phi$ that is intimately related to the Dirac phase for magnons

effective field $\mathbf{B}_s := (K_s M_{iz} + B_z)\widehat{\mathbf{e}}_z$)

$$\frac{d\mathbf{m}_i}{dt} = \gamma\left[\mathbf{m}_i \times \mathbf{B}_s - \sum_{j\in i} MJ_{ij}\left(\mathbf{m}_i \times \mathbf{m}_j\right)\right]. \quad (1)$$

We are interested in weak transversal fluctuations around the ordered magnetic phase (weak means slow variation in $\mathbf{m}_i$ within a lattice constant a). Furthermore, we will consider sufficiently large spins where quantum/thermal fluctuations are subsidiary and magnetic reversals are rare. Thus, it is useful to go over to a continuous magnetic texture vector field $\mathbf{m}_i(t) \to \mathbf{m}(\mathbf{r}_i, t)$ and interpret $\mathbf{m}(\mathbf{r}, t)$ as the local, time-dependent expectation value of the field operator $\mathbf{m}(\mathbf{r}, t)$. The exchange contribution in Eq. (1) appears as the divergence of the spin current[21], $\sum_j \gamma MJ_{ij}(\mathbf{m}_i \times \mathbf{m}_j) \to \sum_{\mu\nu} \partial_\mu \mathcal{J}^\mu_{m_\nu}$. Here $\mathcal{J}^\mu_{m_\nu} = \gamma MJa^2\left[\mathbf{m} \times \partial_\mu \mathbf{m}\right]_\nu$ stands for the ν polarized spin current along the μ spatial direction. With this Eq. (1) reads

$$\frac{\partial\mathbf{m}(\mathbf{r}, t)}{\partial t} = \gamma\mathbf{m}(\mathbf{r}, t) \times \mathbf{B}_s - \sum_\mu \partial_\mu \mathcal{J}^\mu_{\mathbf{m}}(\mathbf{r}, t). \quad (2)$$

The uniaxial symmetry of $\mathbf{B}_s$ dictates a conservation of the z-component of magnetization, meaning that $\partial_t m_z + \nabla \cdot \mathcal{J}_{m_z} = 0$. As discussed below, $\mathcal{J}_{m_z}$ is the only spin current with a non-vanishing time average. Within this general setting, we derive the equations governing the dynamics of small transverse deviations around the z-axis unit vector $\widehat{\mathbf{e}}_z$ by writing $\mathbf{m}(\mathbf{r}, t) \approx \widehat{\mathbf{e}}_z + \widetilde{\mathbf{m}}(\mathbf{r}, t)$ with $\widetilde{\mathbf{m}} \perp \widehat{\mathbf{e}}_z$ and $|\widetilde{\mathbf{m}}| \ll 1$. With $\widetilde{\mathbf{m}} = (m_x, m_y, 0)$ and inserting in Eq. (2) we infer the Schrödinger equation

$$i\hbar\partial_t\psi(\mathbf{r}, t) = \mathcal{H}_m\psi(\mathbf{r}, t), \quad (3)$$

where $\psi(\mathbf{r}, t) = m_x(\mathbf{r}, t) - im_y(\mathbf{r}, t)$ and

$$\mathcal{H}_m = \frac{\mathbf{p}^2}{2m_j^\star} + V(r), \quad (4)$$

where $\mathbf{p} = -i\hbar\nabla$ is the momentum operator and $m_j^\star = \hbar/(2\gamma JMa^2)$ is an effective mass. The wave function $\psi(\mathbf{r}, t)$ vanishes outside the waveguide and, otherwise, is subject to the potential $V(\mathbf{r}) = -\hbar\gamma(K_s M + B_z)$. In an extended cylindrical waveguide and in cylindrical coordinates $\mathbf{r} \to (r, \phi, z)$, Eq. (3) admits the non-diffractive Bessel solutions (see for instance

ref. [22])

$$\psi(\mathbf{r}, t) \propto J_\ell(k_\perp r) \exp(i\ell\phi + ik_z z) \exp(-i\omega t), \quad (5)$$

with $J_\ell(x)$ is the Bessel function of the first kind with order ℓ. The total energy is

$$E(\mathbf{k}) = \hbar\omega = \hbar^2(k_z^2 + k_\perp^2)/2m_J^\star + V. \quad (6)$$

Note that similar to optics, conventional (meaning $\ell = 0$ in Eq. (5)) Bessel modes[22,23] also exist, but those do not carry any OAM. A striking consequence is that Bessel beams do not interact with electric fields, in contrast to twisted magnon beams and also do not allow for ℓ-based operations. This fact is decisive when it comes to constructing OAM-sensitive magnonic circuits (similar to ref. [11]) that are controlled by electric fields offering so new functionality, as discussed in ref. [24]. A further important aspect is the difference between our propagating OAM modes and static/driven magnetization vortices[25–27]. The latter are localized topological excitations that are much higher in energy than a magnon wave (cf. Eq. (5)), which extends over the whole waveguide. The much lower energy set by $E(\mathbf{k})$ is tunable by J, $m_J^\star$ and V. Both magnetization vortices and propagating, OAM-carrying magnons have well-defined topological features that can be quantified. To do that in our case, we consider the z-component of the magnon current $\mathcal{J}_{m_z}$, which is nothing but the probability current density coiling around the z-axis

$$\mathcal{J}_{m_z} = \hbar\Re\left[\psi(\mathbf{r}, t)\frac{\mathbf{p}}{m_J^\star}\psi^\star(\mathbf{r}, t)\right] \propto \left(\frac{\ell}{r}\widehat{\mathbf{e}}_\phi + k_z\widehat{e}_z\right)\rho_\ell(r), \quad (7)$$

meaning that the spin waves spiral around the axis of the waveguide, similarly to the case of photon, electron, or neutron twisted beams[1–5]. In fact, the analogy runs deeper: let us introduce pseudo-electric and -magnetic fields as $\widetilde{\mathbf{E}} = \mathbf{m}_x + i\mathbf{m}_y$ and $\widetilde{\mathbf{B}} = i(\mathbf{m}_x - i\mathbf{m}_y)$. Physically, $\widetilde{\mathbf{B}}$ and $\widetilde{\mathbf{E}}$ describe the (paraxial) spin wave modes rotating clockwise and anticlockwise, respectively. The magnon density is $\mathcal{W}_m = \frac{1}{2}(|\widetilde{\mathbf{E}}|^2 + |\widetilde{\mathbf{B}}|^2)$, and the m_z polarized magnon current density $\mathcal{J}_{m_z}$ can be related to the pseudo-Poynting-like vector[28], $\mathcal{P}_\mu := \mathcal{J}_{m_z}^\mu \propto \frac{1}{2}\left[\widetilde{\mathbf{E}}^\star \times (\partial_\mu\widetilde{\mathbf{B}}) + \widetilde{\mathbf{B}}^\star \times (\partial_\mu\widetilde{\mathbf{E}})\right]$. It is straightforward to infer that $\mathcal{P}$ has the proper time and space symmetry of a canonical momentum. Noting that our twisted beam is localized within the waveguide, we can introduce the canonical OAM of the magnon twisted beam as $\mathbf{L} = \mathbf{r} \times \mathcal{P}$, which is extrinsic and dependent on the choice of the coordinate origin. However, the integral orbital angular momentum over the cross-section is indeed intrinsic, amounting to

$$\langle\mathcal{P}\rangle \propto \langle\mathbf{k}\rangle, \quad \langle\mathbf{L}\rangle \propto \ell\langle\mathbf{k}\rangle/k, \quad (8)$$

with $\mathbf{k} \simeq k_z\widehat{e}_z$ being the mean wave vector of the spin wave. We have then $\langle\mathbf{L}\rangle \cdot \langle\mathcal{P}\rangle/\mathcal{P} = \ell$, in full analogy with paraxial optical twisted beams[28]. This ℓ can be identified with the topological charge associated with a particular twisted beam. Generally, our magnons are characterized by the integral momentum $\langle\mathcal{P}\rangle$ and the orbital angular moment $\langle\mathbf{L}\rangle$ as two independent properties, meaning that in addition to the intrinsic spin angular moment $\hbar$ along the $\widehat{e}_z$, the magnon in the cylindrical nanowire may carry a longitudinal and intrinsic orbital angular moment $L_z \sim \hbar\ell$ as well, which formally can take arbitrarily large values and can be utilized in magnonic and spintronics applications.

Undamped topological charge of twisted beams. An important feature of twisted magnons is the robustness of the associated topological charge to magnetic damping. This fact is crucial when it comes to utilization of the OAM of twisted magnons as information carriers, analogously to OAM-based optical

communications[7,8]. Generally, the (Gilbert) damping of magnetization procession[11,17] is governed by a term of the form $\alpha\mathbf{m} \times \partial\mathbf{m}/\partial_t$. In Eq. (3), this amounts to substituting $\partial_t \to (1 + i\alpha)\partial_t$, which leads to the time-decaying magnon density $\rho_\ell(t) = \rho_\ell(t = t_0)\exp(-2\alpha\omega(t - t_0))$ when propagating from time t_0 to t. The magnon OAM ℓ derives, however, by an averaging of $\langle\mathbf{L}\rangle$ over the cross-section of the waveguide S, meaning $\langle\mathbf{L}\rangle = \langle\mathbf{r} \times \mathbf{P}\rangle_S = \widehat{e}_z(\int\ell\rho_\ell(t)\mathrm{d}S)/(\int\rho_\ell(t)\mathrm{d}S) = \ell\widehat{e}_z$. Thus, damping leads to a decaying magnon density (its photon analog is the light intensity), which is however independent of ℓ and hence of OAM. In other words, the OAM (ℓ) is not affected by damping and is conserved during the magnetization evolution. Another point of view is that the damping term would dominate the interfacial spin-pumping current by $\mathbf{m} \times \partial\mathbf{m}/\partial t \propto \Im[\psi(\mathbf{r}, t)\partial_t\psi^\star(\mathbf{r}, t)] = \omega\rho_\ell$, which clearly does not depend on the internal phase structure of the twist excitation (and hence on ℓ). These conclusions are supported by the full-fledge numerical simulations presented below.

Simulating an experimental realization. Having laid down the principle existence of twisted OAM and the robustness of the associated topological charge to perturbations that subsume into damping of the precessional dynamics, the experimental feasibility as well as the role of further magnetic interactions that emerge in a realistic setting, have to be clarified. Therefore, we resort to full-fledge numerical micromagnetic simulations (see Methods) for an experimentally realistic waveguide made of insulating yttrium iron garnet (YIG).

The cylindrical YIG waveguide has a diameter of 0.4 μm and a length of 2.0 μm. The saturation magnetization is $M_s = 1.4 \times 10^5$ A/m, the exchange stiffness constant is $A_{ex} = 3 \times 10^{-12}$ J/m, the uniaxial magnetocrystalline anisotropy along z is $K_u = 5 \times 10^3$ J/m^{-3}, and the Gilbert damping $\alpha = 0.01$[24]. The ground state equilibrium magnetization is oriented along the $+z$-axis, parallel to the main axis of the waveguide. To launch the spin waves, we excite locally at one end $z = 0$ with a twisted magnetic B field (see Methods) that is linearly polarized in the x-direction and having the amplitude $B_{max} = 10$ mT and the frequency $\omega_B = 5$ GHz. Figure 2a shows a snapshot of the x-component of magnetization excitations propagating after 2 ns. More details of excitation mode are gained from slices along the tube in Fig. 2b, which demonstrates the generation of propagating twisted magnon beams. An animated version of m_x at the transversal slice $z = 1$ μm during the magnon propagation is provided as Supplementary Movie 1. The finite damping leads to a decaying magnon density along the YIG tube with the amplitude being normalized with respect to the maximum excitation at $z = 0$. Remarkably, when evaluating the OAM ℓ from the numerically calculated pseudo-Poynting vector, we indeed find that ℓ is independent of the magnon density and is conserved during the spin wave propagation along the tube (cf. Fig. 2c). These full numerical calculations endorse the above formal analysis as well as the experimental feasibility and relevance of twisted magnon beams.

Aharonov–Casher effect and Landau levels. The simulations shown in Fig. 2 as well as our formal analysis evidence that the twisted magnon beams embody a non-vanishing z-polarized spin current density allowing for a coupling to an external electric field $\mathcal{E}$ through the Aharonov–Casher (AC) effect[29]. For magnon-based information transfer, this fact is crucial as it allows to control the flow of OAM-carrying magnons with electric means. In the presence of an electric field, the exchange interaction in the Heisenberg Hamiltonian becomes anisotropic according to $J_{ij}\mathbf{M}_i \cdot \mathbf{M}_j \to \frac{1}{2}J_{ij}\left(M_i^+ M_j^- e^{i\theta_{ij}} + M_i^- M_j^+ e^{-i\theta_{ij}}\right) + J_{ij}M_i^z M_j^z$, where $\theta_{ij} = \frac{g\mu_B}{\hbar c^2}\int_{\mathbf{r}_i}^{\mathbf{r}_j}\mathrm{d}\mathbf{r} \cdot (\mathcal{E} \times \widehat{e}_z)$ is the AC phase. The canonical momentum $\mathbf{p}$ in
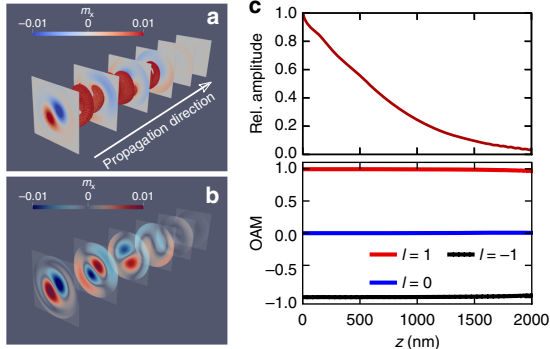
Fig. 2 Spiraling spin wave propagating along a cylindrical micro-scale waveguide of the insulting magnet yttrium iron garnet. **a** Snapshot of the magnon beams after 2 ns for the x-component of the triggered magnetization. **b** Vortex configuration of the excitation modes along the waveguide. **c** The z-resolved amplitude and the orbital angular momentum of the spin waves. In **a–c**, the spin waves are excited locally at one end of the waveguide by a twisted radio frequency (rf) magnetic field having the peak amplitude $B_{max} = 10$ mT, and a frequency $\omega_B = 5$ GHz. For the time evolution of m_x at the transversal slice $z = 1\,\mu$m see Supplementary Movie 1

Eq. (4) has then the kinetic momentum form $\mathfrak{p}_e = \mathbf{p} - q_m \mathbf{A}_e$, where $q_m = g\mu_B/c$ and the electric vector potential $\mathbf{A}_e$ is given by $\mathbf{A}_e(\mathbf{r}) = -\mathcal{E}(\mathbf{r}) \times \widehat{\mathbf{e}}_z/c$. For the electric field $\mathcal{E}(\mathbf{r}) = \mathcal{E}(x/2, y/2, 0)$, one finds the symmetric twist vector potential $\mathbf{A}_e(\mathbf{r}) = \frac{\mathcal{E}}{c}(-y/2, x/2, 0) = \frac{Br}{2}\widehat{\mathbf{e}}_\phi$. Our case is analogous to an electron system in uniform perpendicular magnetic field $\sigma|\mathcal{B}|\widehat{\mathbf{e}}_z$[30], and $\sigma = \text{sign}(\mathcal{E})$ is set by the direction of the applied electric field $\mathcal{E}$. From the gauged Hamiltonian $\mathcal{H}_m = \mathfrak{p}_e^2/2m_I^\star$ follow the well-known quantized Landau states having the form of non-diffracting Laguerre–Gaussian (LG) modes[31-33]

$$\psi_{\ell,n}^L(r,\phi) \propto \left(\frac{\sqrt{2}r}{w_e}\right)^{|\ell|} L_n^{|\ell|}\left(\frac{2r^2}{w_e^2}\right) \exp\left(-\frac{r^2}{w_e^2}\right) e^{i\ell\phi + ik_z z}, \quad (9)$$

where $L_n^{|\ell|}$ are the associated Laguerre polynomials, and $n = 0, 1, 2, \ldots$ is the quantized radial number. The Landau energy levels read

$$E_k^L = \frac{\hbar^2 k_z^2}{2m_I^\star} - \hbar\Omega_e \ell + \hbar|\Omega_e|(2n + |\ell| + 1). \quad (10)$$

Here $w_e = 2\sqrt{\hbar/q_m|\mathcal{B}|}$ is a characteristic width that depends on the amplitude of the applied electric field, $\Omega_e = q_m\sigma|\mathcal{B}|/2m_I^\star$ is the Larmor frequency ($\sigma = \pm 1$ correspond to the clockwise or anticlockwise rotation, respectively). Thus, the electric field $\mathcal{E}$ confines the magnons to form paraxial LG beams with

$$\mathcal{J}_{m_z}^L \propto \left[\frac{1}{r}\left(\ell + \sigma\frac{2r^2}{w_e^2}\right)\widehat{\mathbf{e}}_\phi + k_z\widehat{\mathbf{e}}_z\right]\rho_{\ell,n}^L(r,z). \quad (11)$$

The azimuthal component is directly related to the kinetic orbital angular momentum $\mathcal{L} = \mathbf{r} \times \mathcal{P}_e$ as $\langle\mathcal{L}_z\rangle = -\hbar\langle i\partial_\phi + q_m r A_e\rangle$. Unlike the Bessel beams with uniform rotational direction described by the topological charge ℓ, the direction of $\langle\mathcal{L}_z\rangle$ of the LG beams depends on ℓ and the twist vector potential $\mathbf{A}_e$ as well. Note, the $\langle\mathcal{L}_z\rangle$ radial structure depends strongly on σ, that is, the direction of the applied electric field in terms of the first radial maximum of the LG mode $r_{|\ell|} = w_e\sqrt{|\ell|/2}$: For $\ell\sigma > 0$, we have a uniform, rotationally azimuthal current as usual. However, for

$\ell\sigma < 0$ the currents in the region of $r < r_\ell$ and $r > r_\ell$ are counter-circulating and are dominated by the topological charge ℓ and the twist vector potential $\mathbf{A}_e$, respectively. For an estimate, we take: $JM^2 = 0.1\,\mu$eV, $a = 10$ Å, and $\mathcal{E} = 1$ V/nm, which give $w_e \approx 1.4\,\mu$m and $\hbar|\Omega_e| \approx 0.33\,\mu$eV. Increasing the strength of the applied electric field, higher electric Larmor frequencies Ω_e are achievable but the electric Landau radius w_e is smaller.

OAM-tunable magnon Hall effect. Having clarified the role of an external electric field, one may wonder how the twisted magnon beam is affected by magnetic perturbations. A hallmark of a charge wave-packet propagation in a magnetic field is the transverse deflection, that is, the Hall effect, which in its simplest variant is assigned to the Lorentz force. A similar effect for uncharged particles, such as photons, phonons, or magnons, may thus appear surprising. In our FM case, on the other hand, the Hall effect is also sensitive to the residual magnetization, a phenomenon termed the anomalous Hall effect. Indeed, the Hall effect for magnons has already been observed[34]. Is this effect OAM dependent and can we control it by tuning the OAM? A positive answer would be an important advance, since OAM can be controlled externally, as demonstrated in Fig. 2. To approach this issue, we note that LG modes have well-defined azimuthal and radial wavefront distributions (quantified by ℓ and n, respectively) and they form an orthogonal and complete basis in terms of which an arbitrary function can be represented. So let us consider a magnonic wave packet centered at $(\mathbf{p}_c, \mathbf{r}_c)$ (similar to electronic wave packets[35,36]). From the above, we conclude that the trajectory spirals around the z-axis. Projecting the local coordinate frame along the curved trajectory, we end up with a noncommutative geometry and a covariant derivative in momentum space[37-40]: $D_i = \partial/\partial_{p_i} + \mathcal{A}_i^g(\mathbf{p})$, where $\boldsymbol{\mathcal{A}}^g(\mathbf{p}) = i\langle\psi_{\ell,n}^L|\partial/\partial_\mathbf{p}|\psi_{\ell,n}^L\rangle$ is the Berry connection. The corresponding Berry gauge field (curvature), $\mathcal{B}_g = \partial/\partial_\mathbf{p} \times \mathcal{A}^g(\mathbf{p})$ gives rise to a deflection of the wave packet center. Given that the z-axis is now locally directed along $\mathbf{p}$, the vector $(\widehat{\mathbf{e}}_x + i\widehat{\mathbf{e}}_y)$ is orthogonal to $\mathbf{p}$ and moves on the unit sphere with $\mathbf{p}/p$ under variation of $\mathbf{p}$, which results in a magnetic-monopole-type field[41,42], $\mathcal{B}_g = -\ell\mathbf{p}/p^3$ for the orbital motion of magnons (since $\exp(i\ell\phi) = (\widehat{\mathbf{e}}_x + i\widehat{\mathbf{e}}_y)^\ell$). As a result, we infer the Hamiltonian equations of motion[35,39]

$$\frac{d r_c}{dt} = \frac{\partial H}{\partial p_c} - \hbar\dot{p}_c \times \mathcal{B}_g = \frac{p_c}{m_I^\star} + \hbar\ell\dot{p}_c \times \frac{p_c}{p_c^3}, \quad (12)$$

$$\frac{d p_c}{dt} = -\frac{\partial H}{\partial r_c} = -\frac{\partial V(r)}{\partial r_c} - \frac{q_m}{cm_I^\star}\frac{\partial}{\partial r_c}[\mathbf{p} \cdot (\mathcal{E} \times \widehat{\mathbf{e}}_z)]. \quad (13)$$

The anomalous velocity term $\hbar\ell\dot{p}_c \times p_c/p^3$ is perpendicular to $\mathbf{p}_c$ causing a transversal motion of the wave packet. The corresponding transverse shift $\delta\mathbf{r}_c$ is cast as $\delta\mathbf{r}_c = \hbar\ell\int_L(\mathbf{p}_c \times d\mathbf{p}_c)/p_c^3$ and is determined by the geometry of the contour L in momentum space and ℓ. This is in so far remarkable, as arbitrarily large values of ℓ are possible giving rise to a large deflection at small driving force.

For concreteness, let us consider a weak spatially varying, perpendicular magnetic field B_z, say along the x-direction[43,44]. The driving force is $\mathbf{F}_x = -\partial_x B_z(\mathbf{r})\widehat{\mathbf{e}}_x$ and thus $\dot{\mathbf{p}}_c = \mathbf{F}_x$ and $\delta\dot{\mathbf{r}}_c = \hbar\ell\mathbf{F}_x \times \mathbf{p}_c/p_c^3$. Assuming paraxial magnonic propagation, meaning $\mathbf{p}_c \simeq p_z\widehat{\mathbf{e}}_z$, the transverse deflection reads (an exact but cumbersome analytical expression is available) $\delta\mathbf{r}_c \simeq \delta\mathbf{y} \propto \frac{\hbar\ell F_x z}{p_c^3}\widehat{\mathbf{e}}_y$. Different LG modes with different topological charges ℓ split at the waveguide end (cf. Fig. 3a). Similar to photon[41] and electron[42] twisted beams, we predict a magnonic
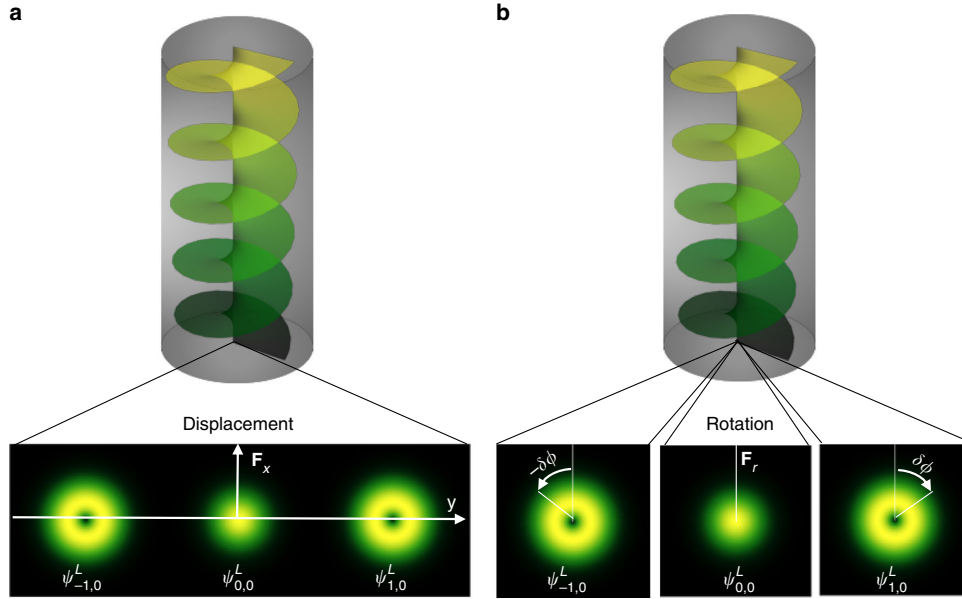
Fig. 3 Demonstration of the orbital angular momentum (OAM)-dependent magnon Hall effect. **a** Transverse displacement by a driving force $\mathbf{F}_x$ along the x-direction and **b** uniform rotation by a r^2-inhomogeneity

OAM-dependent Hall effect, which is qualitatively different from the usual magnon Hall effect[10,34].

For a cylindrically inhomogeneous waveguide, for instance due to inhomogeneity in the demagnetization field[18,19], we may formally write the potential in Eq. (4) as $V(r) = \bar{V} + V_2 r^2 / 2$ with $|V_2| \ll |\bar{V}|$ causing further $\delta \mathbf{r}_c = \delta \boldsymbol{\phi} \propto \frac{\hbar \ell V_2 z}{p_c^3} \widehat{\mathbf{e}}_\phi$. The displacement direction is along $\widehat{\mathbf{e}}_\phi$, meaning that LG modes are rotated uniformly clockwise or anticlockwise depending on ℓ (cf. Fig. 3b), a result in line with the optical Magnus effect[6,45].

Another aspect arises when the waveguide is an FM metallic wire, in which case the electric field vanishes inside the wire. However, we may still have nontrivial magneto-electric effects. Starting from a general symmetrical but inhomogeneous electric potential $V_e(r)$, the energy shift due to the AC effect is given to the first order in the perturbation $V_e(r)$ by $\delta E \simeq \frac{q_m}{m_i^* c} \langle \frac{1}{r} \frac{\partial V_e}{\partial r} [\widehat{\mathbf{e}}_z \cdot (\mathbf{r} \times \mathbf{p})] \rangle = \frac{q_m}{m_i^* c} \langle \frac{L_z}{r} \frac{\partial V_e}{\partial r} \rangle$. For a step-function profile of the wire electric potential $V_e(r) = U\Theta(r - R)$ (here $\Theta(r)$ is the Heaviside function and R is the radius of the metallic wire), we find $\partial V_e / \partial r = U\delta(r - R)$. No electric field is present in the nanowire except for the surface. Nonetheless, the twisted magnon beam acquires an additional phase upon traveling a distance z along the nanowire $\varphi(\ell, z) = U\rho_\ell(R) \frac{q_m}{\hbar c} \frac{\ell}{k_z} \frac{z}{R}$. This phase accumulation may result in an interference between the different LG modes, for example, $(\psi_{-\ell} + \psi_\ell) \propto \cos[|\ell|\phi + \varphi(|\ell|, z)]$.

Anisotropic correlation length of magnetic fluctuations. While the control of twisted magnons via external electromagnetic fields is crucial for applications, one may wonder about the stability of the FM state to twisted excitations. To explore this aspect we have to study the influence of vorticity on the magnetic fluctuations and in particular the correlation length. Both are indicators on how magnetic ordering reacts to excitations[46]. Let us start with the Ginzburg–Landau free energy density of the FM waveguide at temperature T (in unit of $1/M^2$), $\mathcal{F} = \frac{Ja^2}{2} (\boldsymbol{\nabla}\mathbf{m})^2 + (k_B T -$

$\frac{K_s}{2}) m_z^2 + K_4 m^4 - B_z m_z$ (with k_B is Boltzmann constant and $|m_z| \le 1$). The quartic term with $K_4 > 0$ stabilizes the long-range FM ordering below $T_c \approx K_s / 2k_B$. Because of the uniaxial anisotropy and the cylindrical demagnetizing field, the SU(2) spin symmetry is reduced to $SO(2) \times \mathbb{Z}_2$. Low-energy Goldstone modes are due to the continuous SO(2) symmetry.

For $T < T_c$ the saddle point approximation delivers the mean-field value of m_z in the absence of an external magnetic field: $\bar{m}_z(T) = \pm\sqrt{k_B(T_c - T)/2K_4}$ in the FM sector. The stiffness of deformations around the saddle point solution is inferred from the longitudinal (along $\widehat{\mathbf{e}}_z$) and transverse (along $\widehat{\mathbf{e}}_r$ and $\widehat{\mathbf{e}}_\phi$) fluctuations[46], $\mathbf{m} \simeq [\mathcal{R}(\mathbf{r}), \Phi(\mathbf{r}), \bar{m}_z + \mathcal{Z}(\mathbf{r})]$. The fluctuations energy cost, up to second order, is $\delta\mathcal{F} = \frac{Ja^2}{2} [(\boldsymbol{\nabla}\mathcal{R})^2 + (\boldsymbol{\nabla}\Phi)^2 + (\boldsymbol{\nabla}\mathcal{Z})^2] - 2k_B(T - T_c)\mathcal{Z}^2$. For non-diffracting Bessel modes at $T \ll T_c$, we find the anisotropic characteristic length scales, $\frac{1}{\xi_z} \simeq \sqrt{\frac{2K_s}{Ja^2}}$, $\frac{1}{\xi_r^{\ell n}} \approx \frac{\chi_{\ell n}}{R}$ and $\frac{1}{\xi_\phi^\ell} \approx \frac{\ell}{R}$, where $\chi_{\ell n}$ is the nth root of the Bessel prime function $dJ_\ell(r)/dr|_{r=R} = 0$. The definition of $\chi_{00} = 0$ gives $\frac{1}{\xi_r^{00}} = 0$ and $\frac{1}{\xi_\phi^0} = 0$, which implies that the transverse excitations correspond to the Goldstone modes of the SO(2) symmetry.

For the paramagnetic region $T > T_c$, the quartic K_4 term is not relevant and the mean-field equilibrium solution is $\bar{m}_z = B_z / k_B(T - T_c)$. For transverse fluctuations around the saddle point solution $\bar{m}_z$, we write $\mathbf{m} \simeq \sqrt{1 - \rho^2}\widehat{\mathbf{e}}_z + \rho\widehat{\mathbf{e}}_r$, with $0 \le \rho \le 1$. Substituting in $\delta\mathcal{F}$ and neglecting constants and higher order terms in ρ leads to $\delta\mathcal{F}_\rho = \frac{Ja^2}{2}(\boldsymbol{\nabla}\rho)^2 - \alpha(T)\rho^2 + \beta\rho^4$ with $\alpha(T) = [k_B T - (K_s + B_z)/2]$ and $\beta = B_z/8$. Interestingly, transverse fluctuations are most probable not at the boundary $\rho = 0$ but at $\rho_0 = \sqrt{\alpha/2\beta}$, the global minimum of the free energy $\delta\mathcal{F}_\rho$. For cylindrical waveguide the transverse fluctuations are subject to a non-zero restoring force and the correlation length is $\frac{1}{\xi_r} \simeq \sqrt{\frac{4\alpha(T)}{Ja^2}}$. Thus, the transverse scattering density is Lorentzian.
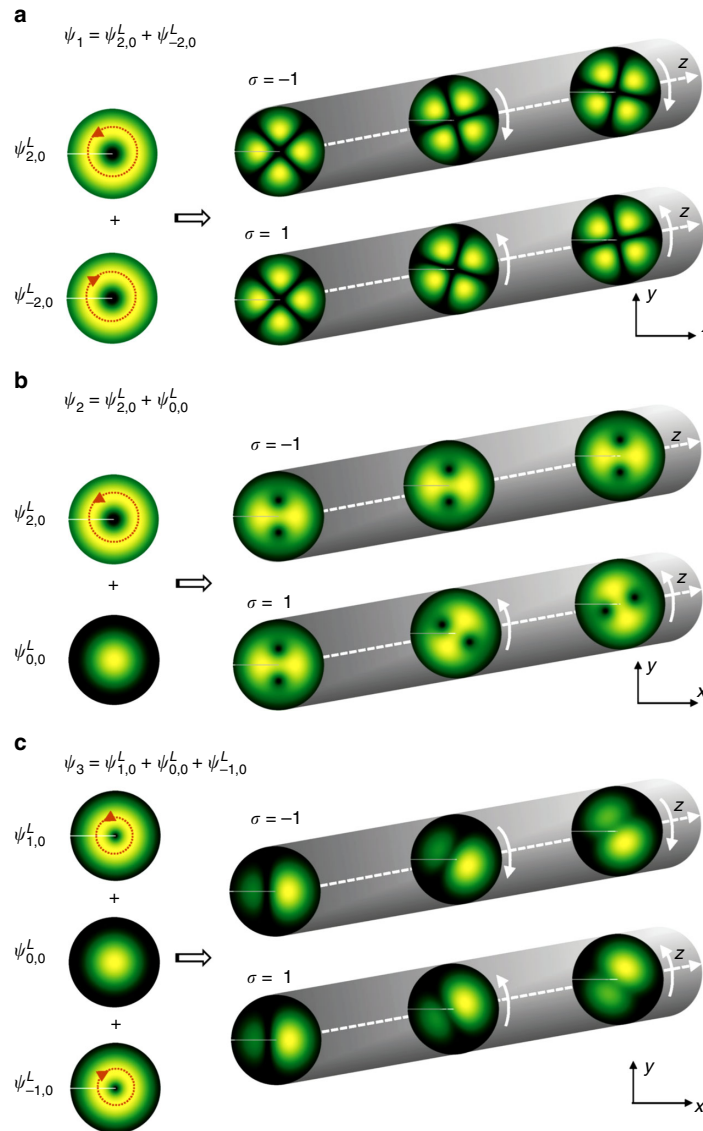
Fig. 4 Propagation of Laguerre–Gaussian (LG) eigenmodes along a magnonic waveguide. **a** orbital angular momentum (OAM)-balanced, **b** OAM-unbalanced, and **c** mixed LG eigenmodes. σ denotes the direction of the applied electric field

Generation of twisted magnon beams. In Fig. 2 we demonstrated how to trigger twisted magnons via magnetic fields. In fact, there are various other ways to accomplish this goal: one may use, for instance, an engineered magnetic spiral phase plate or fabricate a hologram such as a pitch fork for scattering of incoming magnons before entering the waveguide. Another possibility is the following (cf. also Fig. 1): let us consider a uniformly charged thin wire with a linear charge density λ_e located in the region $z \in [d_1, d_2]$ on the axis of a FM cylindrical waveguide. The radial electric field $\mathcal{E}(\mathbf{r}) = \frac{\lambda_e}{2\pi\epsilon r}\widehat{e}_r$ in the FM nanowire within $z \in [d_1, d_2]$ (ϵ is the electric permittivity of the FM). For z-polarized magnons, the interaction of magnons with the radial electric field $\mathcal{E}$ involves the vector potential $\mathbf{A}_e(\mathbf{r}) =$

$-\mathcal{E} \times \widehat{\mathbf{e}}_z/c = \frac{\lambda_e}{2\pi\epsilon cr}\widehat{\mathbf{e}}_\phi$, which is intimately related to the so-called Dirac phase for magnons moving along a contour C, $\Phi_D = -\frac{q_m}{\hbar}\int_C \mathbf{A}_e(\mathbf{r}) \cdot d\mathbf{r}$, producing a phase structure $\exp(i\ell\phi)$ with the quantized number $\ell = -\frac{q_m\lambda_e}{2\pi\hbar\epsilon c}$. Similar to twisted electron beams[47], the twisted magnons can be produced by considering a transition of a conventional magnon with ($\ell = 0$) in the region $z \le d_1$ without any flux ($\lambda_e = 0$) to the region $z \in [d_1, d_2]$ with the non-zero flux ($\lambda_e \ne 0$). For an estimate, we have $\frac{q_m\lambda_e}{2\pi\hbar\epsilon c} \sim 5.6\lambda_e \times 10^{-15}$ with the linear charge density λ_e in unit of e/m. For $\sim 10^{22}$ cm^{-3} carrier density in copper and magnon wavelength (governed by the exchange interaction) $\sim\mu$m, the linear density $\lambda_e \sim 10^{14}$–10^{16} e/m is experimentally feasible.

Demonstration of OAM magnon beams evolution. As evidenced, twisted magnon beams are controlled in numerous ways including external electric and magnetic fields, geometry design and holographic means. For instance, with suitably designed holograms, different superpositions of twisted beams can be created such as the OAM-balanced superposition. This is determined by two LG eigenmodes with the same radial number n but opposite topological charges $\pm\ell$, meaning $\psi_1 = \psi_{-\ell,n}^L + \psi_{\ell,n}^L$. This superposition has zero net canonical OAM $\langle L_z \rangle = 0$ exhibiting a flower-like symmetry pattern: $|\psi_1|^2 \propto \cos^2(\ell\phi)$ at $z = 0$, as shown in Fig. 4a. The OAM-unbalanced superposition consists of two LG eigenmodes with the same radial number n but different topological charge 0 and ℓ means that $\psi_2 = \psi_{0,n}^L + \psi_{\ell,n}^L$. This superposition carries a finite net canonical OAM, $\langle L_z \rangle \propto l$, and is characterized by a pattern with ℓ off-axis vortices (cf. Fig. 4b).

In the paraxial approximation with a relatively small transverse kinetic energy and considering that $\Omega_e \propto \sigma|\mathcal{B}|$, we infer the allowed wave number as $k_z \simeq k + \Delta k_z$, with $\Delta k_z = -[\sigma\ell + (2n + |\ell| + 1)]/z_e$. Here $z_e = w_e \sqrt{E/\hbar|\Omega_e|}$ is a characteristic longitudinal scale. On the propagation distance z, the electric field modifies the longitudinal wave vector resulting in an additional phase $\varphi = \Delta k_z z$, which strongly depends on the direction (σ) of the applied electric field. As for $\ell\sigma > 0$, the induced phase φ shows a linear dependence on the topological charge ℓ. In contrast, for $\ell\sigma < 0$, $\varphi = -(2n + 1)z/z_e$ is independent of ℓ. These phenomena are caused by partial cancellation of counter-circulating azimuthal currents produced by the beam with $\exp(i\ell\phi)$ and by the twist vector potential $\mathbf{A}_e$.

The propagation of twisted magnon beams in the waveguide can give rise to a Faraday effect similar to the case of electron vortex states[32,33]. As for the OAM-balanced superpositions, the induced phases for the modes $\psi_{\pm\ell,n}^L$ reads $\varphi_\pm = \mp\sigma\ell z/z_e$, which results in rotation of the interference pattern by the angle $\Delta\varphi = \sigma z/z_e$, as displayed in Fig. 4a. For the OAM-unbalanced superpositions, the mode $\psi_{\ell,n}^L$ acquires an additional phase $\Delta\varphi = -(\sigma\ell + |\ell|)z/z_e$, as compared to the $\psi_{0,n}^L$ mode. The superposition with $\sigma\ell > 0$ shows a rotation of the interference pattern by the angle $\Delta\varphi = 2\sigma z/z_e$, as demonstrated by the lower panels in Fig. 4b with $\sigma = -1$, whereas the superposition with $\sigma\ell < 0$, has no rotation at all ($\Delta\varphi = 0$, as evidenced by the $\sigma = -1$ panels in Fig. 4b).

All these electric field tunable phases, including the mixed cases with $\psi_3 = \psi_{-\ell,n}^L + \psi_{0,n}^L + \psi_{\ell,n}^L$, as shown in Fig. 4c, indicate rich magneto-electric patterns of the interference intensity, which also may serve as a marker for identifying the twisted magnon beam.

Discussion

Imprinting an orbital angular momentum on a magnon beam puts a new twist on magnonics, as OAM can be functionalized as an independent robust, meaning damping resistant parameter. Together with the fact that OAM can be tuned to very large values, the twisted magnon beams offer new opportunities for reliable multiplex communications. The susceptibilies of the OAM-carrying magnons to electric and magnetic fields are thereby a key advantage, as they offer versatile tools to extract and steer the flow of information. Further immediate consequences of the topological nature of the discovered twisted beams are that the internal global phases, related to OAM, result in a controllable interference pattern when such beams interfere. This we may employ to imprint spatially modulated magnon density on a length scale well below the beam's extensions. The parameters of the twisted beams are directly reflected in the magnon density spatio-temporal pattern. Thus, in addition to the well-established,

energy-saving applications of magnonics and magnon-based spintronics, this new offspring is useful for OAM-based, electrically controlled functionalities in magnonic-based information transfer and processing. Future studies are focused on the scattering of twisted magnon beams from a magnetization vortex core[48] and its possible application in a long distance (at short wavelength[49]) electrically controlled multiplex communication channel between different vortex cores.

Methods

Micromagnetic simulations. We used the open-source, graphical processing unit (GPU)-accelerated software package MuMax3[50] for the micromagnetic simulations. The $(0.4 \times 0.4 \times 2.0)$ μm^3 large system is discretized into $(100 \times 100 \times 500)$ cubic cells with a size of $(4 \text{ nm})^3$. The spatial profile of the excitation field applied at the $z = 0$ layer reads $B_\ell(\rho, \phi, t) = \Re\left\{\hat{e}B_{\max}\left(\frac{\rho}{w_0}\right)^{|\ell|}\exp\left[\frac{|\ell|}{2}\left(1 - \frac{\rho^2}{w_0^2}\right)\right]\exp[-i(t\omega_B + \ell\phi)]\right\}$. The waist parameter w_0 denotes the distance of maximum field strength $B_{\max}$, $\hat{e}$ corresponds to the polarization vector, which is equal to $\hat{e}_x$ in our case, whereas $w_0 = 75$ nm. The time evolution is computed using a Dormand–Prince algorithm with adaptive time-steps. To avoid artifacts due to finite size simulations, we apply open boundary conditions (disregard demagnetizing fields).

Data availability

Figures 1, 3, and 4 have been produced from the equations given in text. Derived data that support the findings of this study are available from the corresponding author upon request.

Code availability

For obtaining the results plotted in Fig. 2 as well as the movie file, we used the open-source, GPU-accelerated software package MuMax3[50] for the micromagnetic simulations. For reproducing the data, one has to use the paramter for YIG, as given in the text and discretize the $(0.4 \times 0.4 \times 2.0)$ μm^3 large cylinder into $(100 \times 100 \times 500)$ cubic cells with a size of $(4 \text{ nm})^3$. Full details on the code are in ref [50].

References

1. Allen, L., Beijersbergen, M. W., Spreeuw, R. J. C. & Woerdman, J. P. Orbital angular momentum of light and the transformation of Laguerre–Gaussian laser modes. *Phys. Rev. A* **45**, 8185 (1992).
2. Yao, A. M. & Padgett, M. J. Orbital angular momentum: origins, behavior and applications. *Adv. Opt. Photon.* **3**, 161 (2011).
3. Uchida, M. & Tonomura, A. Generation of electron beams carrying orbital angular momentum. *Nature* **464**, 737 (2010).
4. Verbeeck, J., Tian, H. & Schattschneider, P. Production and application of electron vortex beams. *Nature* **467**, 301 (2010).
5. Clark, C. W. et al. Controlling neutron orbital angular momentum. *Nature* **525**, 504 (2015).
6. Bliokh, K. Y. & Bliokh, Y. P. Modified geometrical optics of a smoothly inhomogeneous isotropic medium: the anisotropy, Berry phase, and the optical Magnus effect. *Phys. Rev. E* **70**, 263 (2004).
7. Willner, A. E. et al. Optical communications using orbital angular momentum beams. *Adv. Opt. Photon.* **7**, 66 (2015).
8. Bozinovic, N. et al. Terabit-scale orbital angular momentum mode division multiplexing in fibers. *Science* **340**, 1545 (2013).
9. Mair, A., Vaziri, A., Weihs, G. & Zeilinger, A. Entanglement of the orbital angular momentum states of photons. *Nature* **412**, 313–316 (2001).
10. Chumak, A. V., Vasyuchka, V. I., Serga, A. A. & Hillebrands, B. Magnon spintronics. *Nat. Phys.* **11**, 453 (2015).
11. Wang, Q. et al. Reconfigurable nanoscale spin-wave directional coupler. *Sci. Adv.* **4**, e1701517 (2018).
12. Sadovnikov, A. V. et al. Directional multimode coupler for planar magnonics: side-coupled magnetic stripes. *Appl. Phys. Lett.* **107**, 202405 (2015).
13. Sadovnikov, A. V. et al. Toward nonlinear magnonics: iIntensity-dependent spin-wave switching in insulating side-coupled magnetic stripes. *Phys. Rev. B* **96**, 144428 (2017).
14. Sadovnikov, A. V. et al. Magnon straintronics: reconfigurable spin-wave routing in strain-controlled bilateral magnetic stripes. *Phys. Rev. Lett.* **120**, 257203 (2018).
15. Kruglyak, V. V., Demokritov, S. O. & Grundler, D. Magnonics. *J. Phys. D* **43**, 264001 (2010).

16. Vogt, K. et al. Realization of a spin-wave multiplexer. *Nat. Commun.* **5**, 3727 (2014).

17. Chumak, A. V., Serga, A. A. & Hillebrands, B. Magnon transistor for all-magnon data processing. *Nat. Commun.* **5**, 4700 (2014).

18. Osborn, J. A. Demagnetizing factors of the general ellipsoid. *Phys. Rev.* **67**, 351 (1945).

19. Chen, D. X., Brug, J. A. & Goldfarb, R. B. Demagnetizing factors for cylinders. *IEEE Trans. Magn.* **27**, 3601 (1991).

20. Coey, J. M. D. *Magnetism and Magnetic Materials* (Cambridge University Press, Cambridge, 2010).

21. Rückriegel, A. & Kopietz, P. Spin currents, spin torques, and the concept of spin superfluidity. *Phys. Rev. B* **95**, 104436 (2017).

22. McGloin, D. & Dholakia, K. Bessel beams: diffraction in a new light. *Contemp. Phys.* **46**, 15 (2005).

23. Fletcher, P. C. & Kittel, C. Considerations on the propagation and generation of magnetostatic waves and spin waves. *Phys. Rev.* **120**, 2004 (1960).

24. Wang, X. G., Chotorlishvili, L., Guo, G. H. & Berakdar, J. Electric field controlled spin waveguide phase shifter in YIG. *J. Appl. Phys.* **124**, 073903 (2018).

25. Shinjo, T., Okuno, T., Hassdorf, R., Shigeto, K. & Ono, T. Magnetic vortex core observation in circular dots of permalloy. *Science* **289**, 930–932 (2000).

26. Wachowiak, A. et al. Direct observation of internal spin structure of magnetic vortex cores. *Science* **298**, 577–580 (2002).

27. Van Waeyenberge, B. et al. Magnetic vortex core reversal by excitation with short bursts of an alternating field. *Nature* **444**, 461–464 (2006).

28. Bliokh, K. Y. & Nori, F. Transverse and longitudinal angular momenta of light. *Phys. Rep.* **592**, 1 (2015).

29. Aharonov, Y. & Casher, A. Topological quantum effects for neutral particles. *Phys. Rev. Lett.* **53**, 319 (1984).

30. Prange, R. E. & Girvin, S. M. *The Quantum Hall Effect* (Springer, Berlin, 1987).

31. Landau, L. D. & Lifshitz, E. M. *Quantum Mechanics: Non-Relativistic Theory* (Butterworth-Heinemann, Burlington, 1981).

32. Bliokh, K. Y., Schattschneider, P., Verbeeck, J. & Nori, F. Electron vortex beams in a magnetic field: a new twist on Landau levels and Aharonov–Bohm states. *Phys. Rev. X* **2**, 041011 (2012).

33. Greenshields, C., Stamps, R. L. & Franke-Arnold, S. Vacuum Faraday effect for electrons. *N. J. Phys.* **14**, 103040 (2012).

34. Onose, Y. et al. Observation of the Magnon Hall effect. *Science* **329**, 297 (2010).

35. Chang, M.-C. & Niu, Q. Berry phase, hyperorbits, and the Hofstadter spectrum: semiclassical dynamics in magnetic Bloch bands. *Phys. Rev. B* **53**, 7010 (1996).

36. Sundaram, G. & Niu, Q. Wave-packet dynamics in slowly perturbed crystals: gradient corrections and Berry-phase effects. *Phys. Rev. B* **59**, 14915 (1999).

37. Wilczek, F. & Shapere, A. *Geometric Phases in Physics* (World Scientific, Singapore, 1989).

38. Murakami, S., Nagaosa, N. & Zhang, S.-C. Dissipationless quantum spin current at room temperature. *Science* **301**, 1348 (2003).

39. Bliokh, K. Y. & Bliokh, Y. P. Topological spin transport of photons: the optical Magnus effect and Berry phase. *Phys. Lett. A* **333**, 181 (2004).

40. Bliokh, K. Y. Topological spin transport of a relativistic electron. *Europhys. Lett.* **72**, 7 (2007).

41. Onoda, M., Murakami, S. & Nagaosa, N. Hall effect of light. *Phys. Rev. Lett.* **93**, 45 (2004).

42. Bliokh, K. Y., Bliokh, Y. P., Savel'ev, S. & Nori, F. Semiclassical dynamics of electron wave packet states with phase vortices. *Phys. Rev. Lett.* **99**, 190404 (2007).

43. Meier, F. & Loss, D. Magnetization transport and quantized spin conductance. *Phys. Rev. Lett.* **90**, 2371 (2003).

44. Nakata, K., Klinovaja, J. & Loss, D. Magnonic quantum Hall effect and Wiedemann–Franz law. *Phys. Rev. B* **95**, 125429 (2017).

45. Dooghin, A. V., Kundikova, N. D., Liberman, V. S. & Zel'dovich, B. Ya Optical Magnus effect. *Phys. Rev. A* **45**, 8204 (1992).

46. Kardar, M. *Statistical Physics of Fields* (Cambridge University Press, Cambridge, 2007).

47. Bliokh, K. Y. et al. Theory and applications of free-electron vortex states. *Phys. Rep.* **690**, 1 (2017).

48. Wintz, S. et al. Magnetic vortex cores as tunable spin-wave emitters. *Nat. Nanotechnol.* **11**, 948–953 (2016).

49. Liu, C. et al. Long-distance propagation of short-wavelength spin waves. *Nat. Commun.* **9**, 738 (2018).

50. Vansteenkiste, A. et al. The design and verification of MuMax3. *AIP Adv.* **4**, 107133 (2014).

Author contributions

C.J. initiated and performed the analytic modeling, D.M. and A.F.S. performed and analyzed the numerical calculations. C.J. and J.B. supervised the project and wrote the paper. All authors discussed and analyzed the results and contributed to the final version of the paper.

Additional information

Twisting and tweezing the spin wave: on vortices, skyrmions, helical waves, and the magnonic spiral phase plate

Chenglong Jia[1,3] ⬤**, Decheng Ma**[1] ⬤**, Alexander F Schäffer**[2] ⬤ **and Jamal Berakdar**[2,3] ⬤

[1] Key Laboratory for Magnetism and Magnetic Materials of the Ministry of Education & Institute of Theoretical Physics, Lanzhou University, People's Republic of China
[2] Institut für Physik, Martin-Luther-Universität Halle-Wittenberg, 06099 Halle (Saale), Germany

E-mail: cljia@lzu.edu.cn and jamal.berakdar@physik.uni-halle.de

CrossMark

Abstract

Spin waves are the low-energy excitations of magnetically ordered materials. They are key elements in the stability analysis of the ordered phase and have a wealth of technological applications. Recently, we showed that spin waves of a magnetic nanowire may carry a definite amount of orbital angular momentum components along the propagation direction. This helical, in addition to the chiral, character of the spin waves is related to the spatial modulations of the spin-wave phase across the wire. It, however, remains a challenge to generate and control such modes with conventional magnetic fields. Here, we make the first proposal for *magnetic* spiral phase plate by appropriately synthesizing two magnetic materials that have different speeds of spin waves. It is demonstrated with full-numerical micromagnetic simulations that despite the complicated structure of demagnetization fields, a homogeneous spin wave passing through the spiral phase plate attains the required twist and propagates further with the desired orbital angular momentum. While excitations from the ordered phase may have a twist, the magnetization itself can be twisted due to internal fields and forms what is known as a magnetic vortex. We point out the differences between both types of magnetic phenomena and discuss their possible interaction.

Keywords: beams carrying orbital angular momentum, topological magnonics, spin waves, twisted beams, spintronics, magnetic vortices, skyrmions

(Some figures may appear in colour only in the online journal)

1. Introduction

Over the past few decades, it has been established that waves with an appropriate spatial structure of the phase can carry a definite amount of orbital angular momentum (OAM). This has been shown for classical electromagnetic waves, as well as for the quantum dynamics of electrons or neutrons (see [1–6] and references therein). Also acoustic vortices have recently been discussed [7].

Our focus here is on magnetic materials and their excitations that propagate within the material itself. To appreciate the difference to electromagnetic waves carrying OAM, for instance, let us recall that the magnetization $\mathbf{M}$ (the order parameter in this case) enters the Maxwell-equation indirectly through the constitutive equation $\mathbf{B}/\mu_0 = \mathbf{H} + \mathbf{M}$ which is a material-dependent equation ($\mathbf{B}$ is the magnetic flux density, and $\mathbf{H}$ is the magnetic field strength). The question of interest for magnetism is which ground state configuration is attained by $\mathbf{M}$, and what is the structure of the excitation spectrum and

---

[3] Authors to whom any correspondence should be addressed.

the corresponding excited state for a given sample. Obviously, it is imperative to set up the free-energy density of the field-free magnetic system, as well as the equation of motion for **M**. Once established, we may in principle couple the magnetic dynamics of **M** to the Maxwell dynamics of **B** (via the above constitutive equation), which allows investigating the photonic and the optomagnetic properties of the sample, as discussed in the first attempt in [8].

The aim here is to solely study **M** and its excitations in micro-structured magnets. To this end, we start from a free-energy density that accounts for the exchange, the dipolar interactions, the magnetic anisotropies (subsumed in the demagnetization fields) and determine the magnetic configuration as the minimum of this free energy. The dynamics is governed by the Landau-Lifshitz-Gilbert (LLG) equations [9] with the low-energy eigenmode excitations being transverse spin waves and with the quanta of these excitations being magnons. These collective excitations live only in the ferromagnet and have no signature in the (vacuum) far zone. Experiments have established that magnons can be thermally or non-thermally excited, confined, spectrally shaped, and guided via material design and/or microstructuring of the sample [10–17]. Magnonic (spin-wave) currents imply a flow of a *spin* angular momentum and are routinely generated at low (thermal) energy cost. Electronic excitations can be regarded as practically frozen at this low energy scale and hence the spin-wave propagation is not hindered by Ohmic losses, albeit magnetic losses may still be present and are described in our scheme collectively by the Gilbert damping. A further attractive feature of magnonic-based information processing is the possibility of realizing well-controllable magnonic logic circuits [10–17] that can be integrated in (spin-)electronic devices. Generally, ferromagnetic spin waves are always right-handed circular polarized waves. Hence, the use of the polarization state of such waves is somehow restricted. In view of the markedly different structure of the material and sample-specific equations of motion for magnetization, as well as those of the Maxwell or the Schrödinger equations, it is not clear whether spin waves with OAM may exist as eigenmodes in ferromagnets and have similar properties as optical or electronic waves with OAM. Recently, we showed under which conditions twisted (helical) magnon beams, meaning OAM-carrying spin waves, do appear as magnetic eigenmode excitations in a waveguide. The amount of OAM along the propagation direction carried by a propagating spin wave is unbound. Such spin waves interact with an external electric field via the Aharanov-Casher-effect [18], and exhibit an OAM-controllable magnonic Hall effect [19, 20]. Despite the differences between magnon and photonic twisted beams which are discussed in [21], there are several formal analogies that can be drawn which should be of a key role for understanding the interaction between twisted magnon and twisted photons, an issue not discussed in this paper. The purpose here is to discuss how to generate and steer twisted magnonic beams. In [21], we applied at one end of the magnonic waveguide an external

magnetic field that carries OAM. Such fields might be difficult to realize in a general setting. Thus, we inspect here the possibility of realizing a magnonic spiral phase plate (SPP), similar to the one in optics, but now the SPP is molded out of magnetic materials that have different but (for our purpose) appropriate speed of spin waves. This idea is motivated by the similarity of the simplified magnonic wave equation in a wire that we used in [21] and the optical waveguide equation. The analytical approach of [21] does not apply however for magnonic SPP, as demagnetization fields and the local magnetic order are expected to have a strongly anisotropic spatial distribution, as indeed confirmed below. Hence, we have to employ the micromagnetic equations in full generality and resort to numerical simulations of the spin dynamics in SPP that we constructed out of a conducting permalloy (Py) and an insulting yttrium iron garnet (YIG). The results indeed show how a spin wave with a spatially homogeneous phase structure attains OAM when traversing the SPP, and it propagates further as a twisted beam. Our numerical method allows at the same time to calculate in addition to the excitations, the thermodynamically stable magnetic states. Interestingly, if the magnetic waveguide is compressed in length to just a disc, magnetic vortices appear as states of the stable magnetizations. Hence, it is of interest to explore how the geometric confinement-induced magnetic vortices relate to the twisted spin waves when the length of the waveguide becomes extended. This issue is an important first step towards a possible manipulation of magnetic vortices with twisted magnons and is being addressed below.

2. Magnonic spiral phase plate for generating twisted magnon beams

One well-documented method for generating optical vortex fields is to use a spiral phase plate [1]. Thus, the question arises of how to construct a magnonic spiral phase plate. Previously [21], we employed the magnetic component of a spatially structured electromagnetic wave to excite twisted magnon modes in a ferromagnetic waveguide. In contrast, upon traversing a magnonic spiral phase plate, a conventional, spatially homogeneous spin wave is transformed into a twisted magnon beam.

In order to tackle this challenge, it is expedient to start from the fundamentals of magnetization dynamics. A classical magnetic dipole moment **m** exposed to an external magnetic field **H** precesses around the orientation of the field, a dynamic governed by the equation of motion (EOM)

$$\dot{\mathbf{m}} = -\gamma \mu_0 (\mathbf{m} \times \mathbf{H}), \quad (1)$$

where $\gamma_0 = 1.76 \times 10^{11} (\mathrm{T}^{-1} \mathrm{s}^{-1})$ is the gyromagnetic ratio and $\mu_0 = 4\pi \, 10^{-7} \mathrm{VsA}^{-1} \mathrm{m}^{-1}$ is the vacuum permeability. In practice, magnetic losses result in the magnetic moments being eventually aligned along the applied magnetic field. This effect can be introduced in the EOM via a phenomenological (Gilbert) damping parameter α leading to the LLG
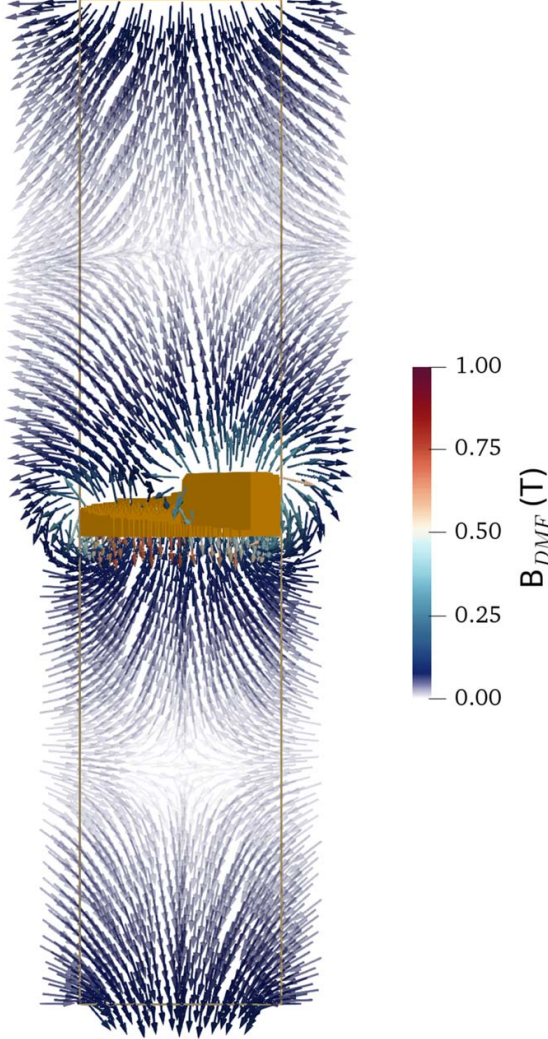
Figure 1. Demagnetizing field of a cylindrical YIG nanowire (lines mark the wire geometric boundaries) equipped with a SPP (orange structure in the center). The color code corresponds to the magnitude of the demagnetizing fields $\mathbf{B}_{DMF}$. SPP height: 120 nm. Cylinder radius: 200 nm, length: 2000 nm.

equation [9]

$$\dot{\mathbf{m}} = -\frac{\gamma\mu_0}{1+\alpha^2}[\mathbf{m} \times \mathbf{H} + \alpha\mathbf{m} \times (\mathbf{m} \times \mathbf{H})]. \quad (2)$$

Due to the newly established damping term, the magnetization dynamics is defined by a non-linear partial differential equation. By proceeding with a system of interacting magnetic moments which also includes dipolar interactions, the equation is not only non-linear but also non-local as every magnetic moment interacts with all others over their dipolar fields. These stray fields are commonly called demagnetizing fields as their contribution to the free energy functional favors vortex like configurations that diminish the net magnetization

of the system. As an example, the demagnetizing field of a YIG cylindrical waveguide including a Py SPP is shown in figure 1.

Magnetization EOM of a magnetic material differs strongly from the Maxwell dynamics for electromagnetic waves. Nevertheless, the complex magnetization dynamics still can host spin waves with helical wave fronts as we showed recently [21]. These twisted spin waves show analogies to the optical case. The question here is, whether it is also possible to transfer the principle of a spiral phase plate to the magnonic world, in spite of the non-local fields and non-linear dynamics.

To assess the feasibility of this basic idea, we set up and conduct micromagnetic simulations using the GPU-accelerated, open-source software package mumax3 [22]. We solved the LLG equation in a discretized waveguide for every simulation cell $\mathbf{m}_i$ of the discrete magnetization vector field. The time- and space-dependent effective magnetic field,

$$\mathbf{B}_i^{EFF}(t) = \mathbf{B}_i^{EXT} + \mathbf{B}_i^{EXCH} + \mathbf{B}_i^{A} + \mathbf{B}_i^{DMF}, \quad (3)$$

includes the conventional external field $\mathbf{B}_i^{EXT}$ that excites spin waves in one end of the waveguide. The exchange interaction field is $\mathbf{B}_i^{EXCH} = 2A_{ex}/M_s \Delta\mathbf{m}_i$, with A_{ex} being the exchange stiffness and M_s the saturation magnetization. The uniaxial magnetocrystalline anisotropy field is $\mathbf{B}_i^{A} = 2K_u/M_s m_z\mathbf{e}_z$, with K_u being the anisotropy constant. The demagnetizing field reads $\mathbf{B}_i^{DMF} = M_{sat}\hat{\mathbf{K}}_{ij} * \mathbf{m}_j$, details on the calculation of the demagnetizing kernel $\hat{\mathbf{K}}$ can be found in [22].

The external magnetic field, which is circularly polarized and is in the radio-frequency range, acts on the bottom end of the ferromagnetic wire. The peak amplitude is set to $B_{max} = 10$ mT, the frequency is $\omega = 2\pi \times 5$ GHz and the polarization is circular right-handed.

Upon switching on the external magnetic field magnonic plane waves are launched. The task is to convert this wave into a magnon OAM. To construct a magnonic spiral phase plate, we use two different materials. As in [21, 23], we use a wire of YIG in which the OAM magnonic wave will propagate. In the middle of the wire, the Py spiral-phase-plate nanostructure is inserted. Both materials are widely used in magnonics and have low damping coefficient. Still, the material parameters differ, which should lead to a thickness dependent phase accumulation when passing through a spiral spatial structure.

As a first approach, we disregard the computationally expensive demagnetizing field and check whether a spiral phase plate leads to the desired effect of thickness-dependent phase accumulation. The resulting wave fronts can be observed in figure 2. For the presented results of the simulations, a system of $100 \times 100 \times 300$ unit cells (u. c.) each of $(4\,\text{nm})^3$ size was initialized as a cylindrical base geometry. The Py phase plate (orange structure in figure 2) has a height of 30 unit cells. The YIG region itself is transparent in the graphical representation to be able to show the equal phase fronts of m_x instead (red: incident plane wave; blue: transformed helical wave after passing through the SPP).

Depending on the rotational sense of the phase plate, the resulting handedness of the helical wave fronts can be tuned, as shown in figures 2(a) (counterclockwise) and (b)
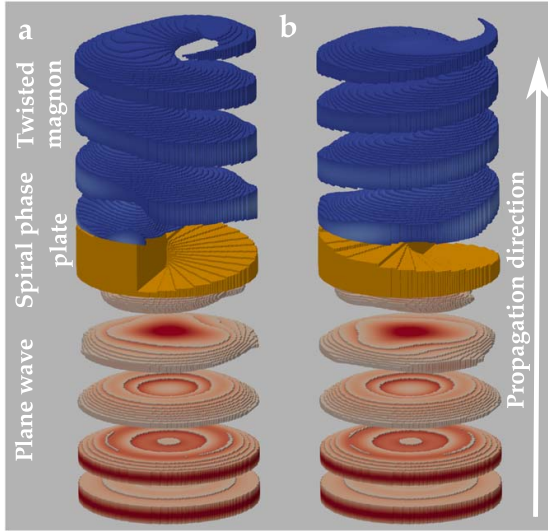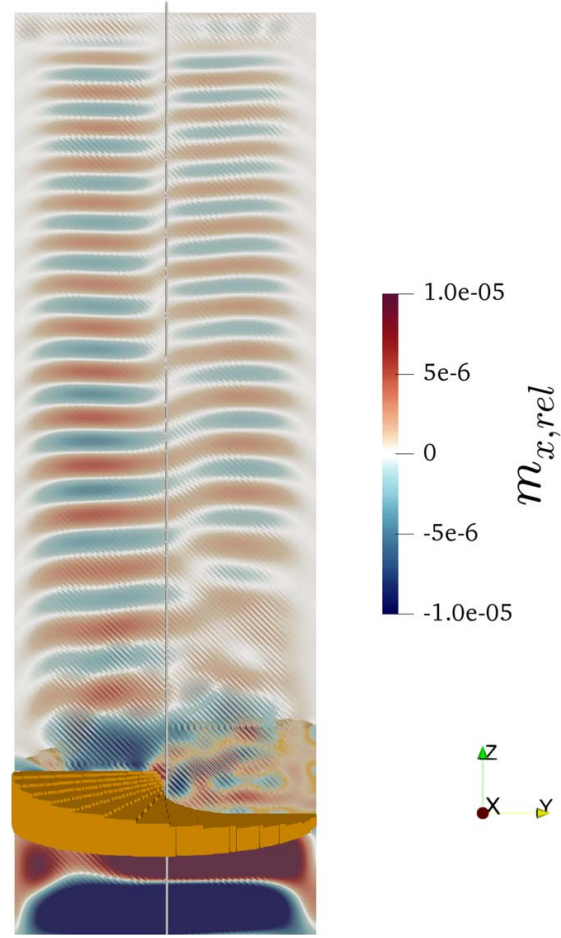
Figure 2. The transformation of an incident magnonic plane wave into twisted magnons by a magnonic spiral phase plate disregarding demagnetizing fields. The blue and red regions show wave fronts of equal phases of the m_x component, clearly demonstrating the change from planar to helical wave fronts. The orange regions show the geometries of the spiral phase plate generating either counter-clockwise **a** or clockwise **b** rotations of the twisted magnons.

(clockwise). Still, for both cases, the polarization of each magnetic moment is right-handed, which is the only possible rotational sense in ferromagnetic materials. It is remarkable that even though the nanostructured SPP is limited by the simulation grid's resolution and hence far from a perfectly smooth phase plate, the resulting twisted magnon wave shows the characteristics of the theoretically proposed OAM carrying magnon beam.

In addition to the described basic geometry, the system outer boundaries are modeled to absorb most of the incoming magnons by introducing an exponentially increasing damping parameter in a tube shell with a 20 u. c. thickness. This helps to avoid reflection effects. The used material parameters for the YIG wire are: $M_s = 1.4 \times 10^5$ A m^{-1}, $A_{ex} = 3 \times 10^{-12}$ J m^{-1}, $K_u = 5 \times 10^3$ J m^{-3}, $\alpha = 0.01$ [24]. In the case of Py, we assume: $M_s = 8.3 \times 10^5$ A m^{-1}, $A_{ex} = 10 \times 10^{-12}$ J m^{-1}, $K_u = -1 \times 10^3$ J m^{-3}, $\alpha = 0.02$ [25].

When dealing with ferromagnetic systems on the micrometer scale, usually stray fields play an important role. This also holds for the cylindrical wires, where not only do the outer surfaces of the structure lead to strong demagnetizing fields but also the boundary between SPP and YIG nanowire will have an impact, mainly due to the large difference in the saturation magnetization of both materials. For a correct interpretation of the simulation results, one has to keep in mind that because of the demagnetizing field, the magnetization is not homogeneously aligned anymore but shows a canting close to the surface. Therefore, the excitation of the magnetization in figure 3 is calculated relative to the relaxed magnetization before applying an external field.

Figure 3. The transformation of an incident magnonic plane wave into a twisted magnon by a magnonic spiral phase plate considering demagnetizing fields. The color code corresponds to the excitation of the magnetization in the *yz* plane relative to the initial relaxed state (see figure 1). The blue and red regions show wave fronts of equal phases of the m_x component, demonstrating the change from planar to helical wave fronts. The orange regions show the geometry of the spiral phase plate.

Figure 3 shows the *x* component of the relative excitation after a $\omega = 2\pi \times 10$ GHz plane wave has passed the SPP (orange). In addition to the time dependent magnetic field, a 1T static magnetic field was applied along the *z* direction to reduce the magnon wavelength and therefore check the propagation after more periods in the same geometry as before. A few observations are striking. First, we can identify the region after the SPP with a helical magnon beam, as some singularity in the excitation is present, separating different phases of the wave in its cross-section. Second, it is obvious that the region directly adjacent to the SPP shows some rather chaotic patterns for the magnetization excitation. This partially arises due to the limited resolution of the SPP but also is a footprint of the demagnetizing fields hindering the passage of spin waves (see field distribution in figure 1). Third, there is a

transition region where the center of the twisted beam is not coinciding with the center of the waveguide for similar reasons. However, these two symmetry axes align with each other after some distance.

Summarizing this section, we showed that in spite of the fundamental differences between the nature of magnetization dynamics—*non-linear*, *non-local*—and electromagnetic waves in free space, the concept of the SPP for the transformation of plane waves to helical waves holds for the field of magnonics. The long-range dipolar interaction does not necessarily endanger the spatial structure of magnon beams carrying orbital angular momentum but will have an even stronger influence as in the presented example for less symmetric geometries like cuboid-shaped waveguides, which has to be addressed in future studies.

3. Magnetic vortex versus twisted magnons

Magnonic twisted beams are in essence small transverse deviations from the collinearly ordered phase. Hence, they are qualitatively different from other well-known twisted magnetic states, for instance, magnetic vortices which are intrinsically non-collinear in their stable configuration [26–28]. It has been shown theoretically and experimentally that for thin ferromagnetic disks and other-shaped elements of micrometer size and below, the magnetic vortex is energetically favored. As one kind of topological magnetic excitations, magnetic vortices are driven by a subtle competition between geometrical balance of exchange interaction and the demagnetizing field (i.e. the shape anisotropy): the magnetization tends to align parallel to the surface in order to minimize the surface charge, however, the singularity at the center of a vortex is replaced by an out-of-plane magnetized core in order to reduce the exchange energy. Magnetic vortices are excited from the uniform ferromagnetic state with much higher energy than the magnonic twisted eigenmode. Topologically, a magnetic vortex is characterized by two essential features: the out-of-plane, nanometer-size vortex-core magnetization. This determines the vortex *polarity p* which can be up or down. The second feature is related to the in-plane spin configuration of the vortex (say with extension $r \gg 1$ in scaled units) described by $\mathbf{m}(r \gg 1, \phi) = \cos \Phi \hat{\mathbf{e}}_x + \sin \Phi \hat{\mathbf{e}}_y$ with $\Phi = q\phi + c\pi/2$. The topological *vorticity* is set by q indicating the winding number, where c is the vortex *chirality*. As shown in figure 4, the stable magnetization of YIG waveguides is simulated with different lengths L. The topology of the magnetic configuration is characterized by the skyrmion number $s = \sum_{\mathbf{r}} \chi_{\mathbf{r}}/L$, where $\chi_{\mathbf{r}} = \mathbf{m}_{\mathbf{r}} \cdot (\mathbf{m}_{\mathbf{r}+\mathbf{x}} \times \mathbf{m}_{\mathbf{r}+\mathbf{y}}) + \mathbf{m}_{\mathbf{r}} \cdot (\mathbf{m}_{\mathbf{r}-\mathbf{x}} \times \mathbf{m}_{\mathbf{r}-\mathbf{y}})$. For example, a vortex with a winding number q and core polarization p has a half-integer skyrmion number $s = qp/2$, while a skyrmion has integer $s = qp$ and ferromagnetic (FM) state has $s = 0$. Clearly, the demagnetizing field plays a crucial role in the formation of the magnetic configurations. The magnetic vortex states are stable only if the waveguide is compressed into a magnetic disc. Note that due to rotational symmetry of the magnetic vortex and the strong
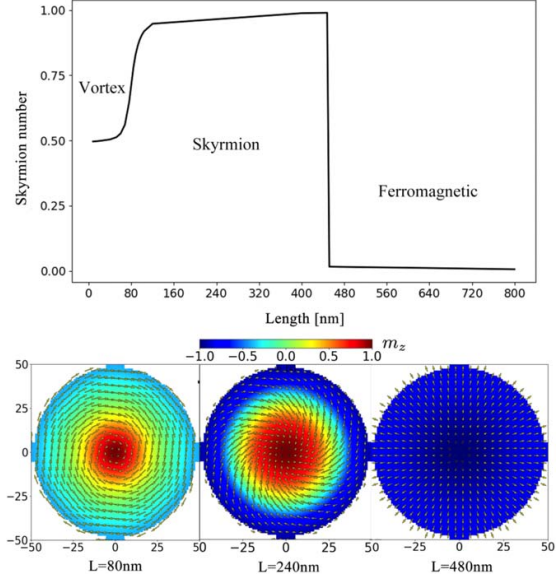

Figure 4. (Upper inset) The evolution of the magnetic configuration (as characterized by the skyrmion number) in YIG waveguides with varying length L and a fixed radius of $R = 200$ nm. (Lower inset) Slices showing the typical configurations of the stable magnetization state with increasing length L: a magnetic vortex, a magnetic skyrmion, and a ferromagnetic.

exchange interaction in ferromagnetic materials, a large energy barrier prevents changing easily the chirality of the vortices. For thicker magnetic disks, skyrmions are stabilized by the demagnetizing fields, whereas in the limit of long cylindrical wire the exchange interaction is dominant and leads to a stable ferromagnetic configuration.

Turning to the magnonic twisted eigenmode of the FM waveguide, the topological vorticity is given by the twisted beam OAM, $-\ell$. The skyrmion number is, however, nearly zero. The chirality is not fixed as well. It depends on the radius r, the time t, and/or the distance z, as demonstrated in figure 5. Furthermore, it is well-known that a magnetic vortex-antivortex pair is unstable: the pair with parallel polarization belongs to the same topological sector as a uniform FM ground state, meaning that we can deform the pair continuously into the ground state once the vortex-antivortex pair with parallel polarization was created; whereas, the vortex-antivortex pair with antiparallel polarization has a nontrivial topological number. Its annihilation is accompanied with the ejection of a magnetic monopole and spin waves. The magnonic twisted eigenmodes with $\pm\ell$ are degenerate states, they can be excited simultaneously and result in a right-handed superposition $|R\rangle = \xi_+|+\ell\rangle + \xi_-|-\ell\rangle$, which defines a new degree of freedom that we can refer to as the magnonic vorticity.

As for the interplay between the magnonic twisted beams and a magnetic vortex, it has been shown that a smooth
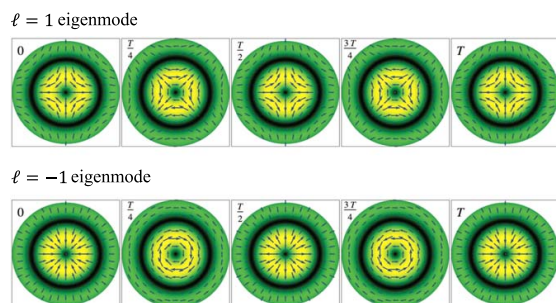
ℓ = 1 eigenmode

ℓ = −1 eigenmode

Figure 5. The dynamic spin configurations. Snapshots showing the topological difference between the magnetization vortex [29] and twisted magnons: the chirality of vortices is very robust by virtue of the rotational symmetry and strong exchange interaction. In contrast, the chirality of twisted beams varies with the radius and/or the time. Here, T is the period of magnetization precession. With the boundary conditions of vanishing magnetic fluctuations at the boundary and outside the magnetic sample, one can have a square wave oscillation of the chirality with time t and/or distance z.

background magnetic texture affects the dynamics of a spin-wave by changing the basic equation that rules the spin-wave behavior [30]. An O(2) vector potential and a scalar potential enter in the Schrödinger-like equation for the magnons. The SPP allows us to investigate the scattering of magnonic twisted beams by topologically nontrivial magnetic textures, including magnetic vortices, magnetic skyrmions, and magnetic Bloch points.

4. Summary

We discussed several aspects of magnonic beams carrying orbital angular momentum. We highlighted the characteristics of these topological excitations contrasting them with the well-known magnetic vortices. For generating OAM carrying magnonic beams, we proposed and realized numerically a magnonic spiral phase plate on the basis of the YIG/Py heterostructure. Fully-fledged numerical simulations using the heterostructure endorse the experimental feasibility of this type of helical magnonic beams.

ORCID iDs

Chenglong Jia ● https://orcid.org/0000-0003-2064-923X
Decheng Ma ● https://orcid.org/0000-0001-8955-1076
Alexander F Schäffer ● https://orcid.org/0000-0003-3228-2228
Jamal Berakdar ● https://orcid.org/0000-0001-8727-3981

References

[1] Allen L, Beijersbergen M W, Spreeuw R J C and Woerdman J P 1992 Orbital angular momentum of light and the transformation of Laguerre–Gaussian laser modes *Phys. Rev.* A **45** 8185
[2] Yao A M and Padgett M J 2011 Orbital angular momentum: origins, behavior and applications *Adv. Opt. Photon.* **3** 161
[3] Uchida M and Tonomura A 2010 Generation of electron beams carrying orbital angular momentum *Nature* **464** 737
[4] Verbeeck J, Tian H and Schattschneider P 2010 Production and application of electron vortex beams *Nature* **467** 301
[5] Clark C W *et al* 2015 Controlling neutron orbital angular momentum *Nature* **525** 504
[6] Bliokh K *et al* 2017 Theory and applications of free-electron vortex states *Phys. Rep.* **690** 1–70
  Lloyd S M, Babiker M, Thirunavukkarasu G and Yuan J 2017 Electron vortices: beams with orbital angular momentum *Rev. Mod. Phys.* **89** 035004
[7] Bliokh K Y and Nori F 2019 Spin and orbital angular momenta of acoustic beams *Phys. Rev.* B **99** 174310
[8] Khomeriki R *et al* 2016 Positive–negative birefringence in multiferroic layered metasurfaces *Nano Lett.* **16** 7290–4
[9] Landau L D and Lifshitz E M 1981 *Quantum Mechanics: Non-Relativistic Theory* (Burlington, MA: Butterworth-Heinemann)
[10] Chumak A V, Vasyuchka V I, Serga A A and Hillebrands B 2015 Magnon spintronics *Nat. Phys.* **11** 453
[11] Wang Q *et al* 2018 Reconfigurable nanoscale spin-wave directional coupler *Sci. Adv.* **4** e1701517
[12] Kruglyak V V, Demokritov S O and Grundler D 2010 Magnonics *J. Phys. D Appl. Phys.* **43** 264001
[13] Vogt K *et al* 2014 Realization of a spin-wave multiplexer *Nat. Commun.* **5** 3727
[14] Chumak A V, Serga A A and Hillebrands B 2014 Magnon transistor for all-magnon data processing *Nat. Commun.* **5** 4700
[15] Sadovnikov A V *et al* 2015 Directional multimode coupler for planar magnonics: side-coupled magnetic stripes *Appl. Phys. Lett.* **107** 202405
[16] Sadovnikov A V *et al* 2017 Toward nonlinear magnonics: intensity-dependent spin-wave switching in insulating side-coupled magnetic stripes *Phys. Rev.* B **96** 144428
[17] Sadovnikov A V *et al* 2018 Magnon straintronics: reconfigurable spin-wave routing in strain-controlled bilateral magnetic stripes *Phys. Rev. Lett.* **120** 257203
[18] Aharonov Y and Casher A 1984 Topological quantum effects for neutral particles *Phys. Rev. Lett.* **53** 319
[19] Nakata K, Klinovaja J and Loss D 2017 Magnonic quantum Hall effect and Wiedemann–Franz law *Phys. Rev.* B **95** 125429
[20] Onose Y *et al* 2010 Observation of the magnon hall effect *Science* **329** 297
[21] Jia C L, Ma D, Schäffer A F and Berakdar J 2019 Twisted magnon beams carrying orbital angular momentum *Nat. Commun.* **10** 2077
[22] Vansteenkiste A *et al* 2014 The design and verification of MuMax3 *AIP Adv.* **4** 107133

[23] Papp A, Porod W and Csaba G 2015 Hybrid yttrium iron garnet-ferromagnet structures for spin-wave devices *J. Appl. Phys.* **117** 17E101

[24] Wang X G, Chotorlishvili L, Guo G H and Berakdar J 2018 Electric field controlled spin waveguide phase shifter in YIG *J. Appl. Phys.* **124** 073903

[25] Coey J M D 2010 *Magnetism and Magnetic Materials* (Cambridge: Cambridge University Press)

[26] Wachowiak A *et al* 2002 Direct observation of internal spin structure of magnetic vortex cores *Science* **298** 577–80

[27] Shinjo T, Okuno T, Hassdorf R, Shigeto K and Ono T 2000 Magnetic vortex core observation in circular dots of permalloy *Science* **289** 930–2

[28] Van Waeyenberge B *et al* 2006 Magnetic vortex core reversal by excitation with short bursts of an alternating field *Nature* **444** 461–4

[29] Wintz S *et al* 2016 Magnetic vortex cores as tunable spin-wave emitters *Nat. Nanotechnol.* **11** 948–53

[30] Carvalho-Santos V L, Elías R G and Nunez A S 2015 Spin wave vortex from the scattering on Bloch point solitons *Ann. Phys.* **363** 364–70

Generation, electric detection, and orbital-angular momentum tunneling of twisted magnons

Min Chen,[1] Alexander F. Schäffer,[2] (iD) Jamal Berakdar,[2] (iD) and Chenglong Jia[1,a)] (iD)

AFFILIATIONS

[1]Key Laboratory for Magnetism and Magnetic Materials of the Ministry of Education, Lanzhou University, Lanzhou 730000, China
[2]Institut für Physik, Martin-Luther-Universität Halle-Wittenberg, 06099 Halle (Saale), Germany

[a)]Author to whom correspondence should be addressed: cljia@lzu.edu.cn

ABSTRACT

A scheme for generating twisted magnons that carry orbital angular momentum in ferromagnetic nanodisks is presented. The topological signature of these eigenmode excitations entails particular features in the associated spin pumping currents. The latter is electrically detectable and can be used to identify these magnons. Considering two disks coupled via the dipole interaction, angular momentum tunneling is demonstrated. The predictions are based on a transparent analytical model and are confirmed by full numerical simulations. As the orbital angular momentum of the magnon is robust to damping, the current findings endorse the potential of twisted magnons for two-dimensional planar integrated spin-wave circuits.

Published under license by AIP Publishing. https://doi.org/10.1063/5.0005764

Spin-waves (or their quanta magnons) are the low-energy collective excitations of ordered magnetic systems and are considered as a potential medium for information exchange with several advantages such as nanoscale integration and low energy consumption.[1–3] In recent years, spin-wave based devices such as logic gates,[4,5] filters,[6] waveguides,[7,8] diodes,[9] beamsplitters,[10,11] and multiplexors[12] have been proposed and designed. An important factor that affects the fidelity of information transmitted as magnonic signals is magnetic (Gilbert) damping that leads to a decaying magnon density. Recently, we pointed to additional types of twisted spin waves that carry a definite amount of orbital angular momentum.[13,14] This orbital angular momentum is measurable and protected against the damping, and, hence, it is worthwhile considering it as a carrier of information. In this Letter, we show that twisted spin-waves can be excited in ferromagnetic (FM) nanodisks. The nontrivial topology, i.e., the spatial and temporal configurations of spin-waves, can be electrically read out, exploiting spin pumping effects and the inverse spin Hall effect (ISHE). Another interesting issue is the tunneling of orbital angular momentum between two disks coupled through the dipole–dipole interaction, and the tunneling is evidenced by pumped DC/AC spin currents and spin accumulation.

Disk-shaped FM was studied intensely theoretically and experimentally in the past, for example, in the context of whispering gallery modes.[15] Here, we consider a disk with perpendicular magnetization **M** (this direction is taken as the z-axis), whose radius R is chosen to be

small enough so that the exchange interaction is more prominent than the dipole interaction. By introducing a dimensionless unit vector field $\mathbf{m} = \mathbf{M}/M_s$, with M_s being the saturation magnetization, the total Lagrangian density of the FM nanodisk reads

$$\mathcal{L} = -\mathcal{A}(\partial_\mu \mathbf{m})^2 + \mathcal{K}_z m_z^2, \tag{1}$$

where $\mathcal{A}$ is the exchange stiffness and $\mathcal{K}_z$ describes the uniaxial magnetic anisotropy. Linearizing Eq. (1), we arrive at the Euler–Lagrange equation that determines the spin-wave dynamics,

$$-\mathcal{A}\partial_\mu^2 \psi_m + \mathcal{K}_z \psi_m = 0, \tag{2}$$

with $\mu = x, y$ and $\psi_m = m_x - i m_y$. The above equation shows the non-diffractive Bessel solutions in cylindrical coordinates $\mathbf{r} \to (\rho, \phi)$ for spin-wave excitations,

$$\psi_m(\mathbf{r}, t) \propto J_\ell(k_{\ell,n}\rho) \exp(i\ell\phi - i\omega t), \tag{3}$$

where $\ell \in \mathbb{Z}$. $J_\ell(x)$ is the Bessel function of the first kind with order ℓ. $k_{\ell,n}$ is determined from the boundary condition and is the nth root of the Bessel prime function $dJ_\ell(\rho)/d\rho|_{\rho=R}$ under the Neumann boundary conditions. The eigenfrequency is $\omega = \mathcal{A}k_{\ell,n}^2 + \mathcal{K}_z$.

Similar to the twisted spin-waves in a FM nanowire, we define a pseudo Poynting-like vector as

$$\mathcal{P} := \mathcal{J}_\mu^z = \mathcal{A}\Im[\psi_m(\mathbf{r}, t)\partial_\mu \psi_m^\star(\mathbf{r}, t)] = -\mathcal{A}n_\ell \frac{\ell}{\rho}\mathbf{e}_\phi, \tag{4}$$

where $\mathcal{J}_\mu^z$ is the z-polarized (magnon) spin current along the μ spatial direction and n_ℓ is the spin-wave density. It is then straightforward to introduce a canonical orbital angular moment of the spin-waves as $\mathbf{L} = \mathbf{r} \times \mathcal{P}$. One finds that $\ell = \mathbf{e}_z \cdot \langle \mathbf{L} \rangle$ by averaging $\mathbf{L}$ over the whole disk. Thus, this ℓ can be identified as the topological charge of spin-waves, and it is an intrinsic damping-resistant parameter, as shown below. Furthermore, in terms of the ISHE, these topological spin-waves can be detected electrically by measuring the pumped spin currents. In general, here, we have two types of pumped spin currents ($\mathcal{I}_s \sim \mathbf{m} \times \partial_t \mathbf{m}$):[16] (i) the $x-$ and y-polarized AC spin currents are

$$\mathcal{I}_s^x \sim -\partial_t m_y \propto -\omega \cos(\omega t - \ell\phi), \qquad (5)$$

$$\mathcal{I}_s^y \sim \partial_t m_x \propto -\omega \sin(\omega t - \ell\phi), \qquad (6)$$

respectively. (ii) The z-polarized DC spin current is

$$\mathcal{I}_s^z \sim \Im\left[\psi_m \partial_t \psi_m^\star\right] \propto \omega. \qquad (7)$$

Clearly, the integral over the whole nanodisk implies $\mathcal{I}_s^x = \mathcal{I}_s^y \equiv 0$, and only $\mathcal{I}_s^z$ remains, which means that now both AC and DC signals do not depend on the internal (spatial) phase structure of the topological spin-waves (and hence, no dependence on ℓ is present). However, these spatial inhomogeneities can be detected by the angular-resolved ISHE. For example, given that $|\ell| = 1$, the left and right half-disks possess exactly opposite AC signals, as supported by the full-fledged numerical simulations presented below.

Considering the SO(2) rotational symmetry of the FM disk, we expect that the dipole interaction does not destroy the above eigenmode excitations but would lift the degeneracy between the $\pm\ell$ modes.[17]

To this end, we conduct micromagnetic simulation using the GPU-accelerated, open-source software package *mumax3*[20] for an experimentally realistic nanodisk made of ferromagnetic alloy FeB. In the simulations, a FeB disk with the diameter of 120 nm and a thickness of 2 nm is selected to have an exchange interaction that is stronger than the dipole interaction. The saturation magnetization is $M_s = 1.375 \times 10^6$ A/m, the exchange stiffness constant is $\mathcal{A} = 0.9 \times 10^{-11}$ J/m, the uniaxial magnetic anisotropy along the z direction is $\mathcal{K}_z = 1.05 \times 10^6$ J/m, and the Gilbert damping parameter is $\alpha = 0.005$.[17] For the following simulation results, a cell of $2 \times 2 \times 2$ nm^3 within the typical range of exchange interactions is used to discretize the FeB disk. To launch the desired spin-waves, we excite the nanodisk locally by applying a spatially inhomogeneous radio frequency (rf) magnetic field. As discussed in Refs. 17–19, different ℓ-eigenmodes can be excited by appropriate spatial configurations of the rf fields. In the present study, we focus on the topologically nontrivial $\ell = \pm 1$ eigenmodes for a clear demonstration.

First, a sinc function of the rf magnetic fields, $\mathbf{B}_y(t) = B(y)\text{sinc}(\omega t)\mathbf{e}_y$, with $\omega = 60$ GHz and $B(y) = \pm 1.5$ mT in the up (down) half-disk, is superimposed to launch spin-waves. As shown in Fig. 1, the $\ell = \pm 1$ eigenmodes are indeed excited in the FeB nanodisk and the dispersion relation of spin-waves, given by the two-dimensional fast Fourier transform (FFT) from the space-and-time domain (ρ, t) is split into many subbands because of the Neumann boundary condition used in the simulations. The twofold degeneracy of $\pm\ell$ eigenmodes is lifted by the dynamic dipole interaction. Using the discrete-time FFT, the ferromagnetic resonance spectra are obtained, in which the two lowest eigenfrequencies with the wavenumber $k_{\ell,n} = k_{\pm 1,0}$ are identified as $\omega_- = 3.61$ GHz and $\omega_+ = 3.79$ GHz, respectively.
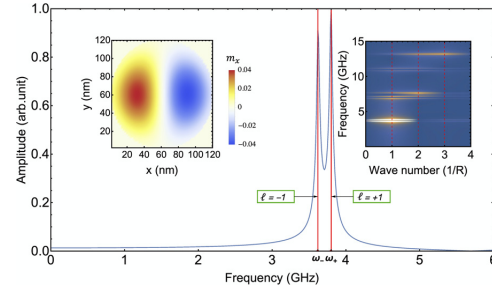

FIG. 1. FFT showing the excited ferromagnetic resonance spectra of the FeB nanodisk. Insets: (Left) snapshot of the m_x component of spin-wave eigenmodes with $\ell = \pm 1$. (Right) Dispersion relation of spin-waves, in which the dashed lines correspond to the eigen wavevector $k_{\pm 1,n}$.

Next, the same spatial configuration but with a single-frequency sinusoidal microwave, $\mathbf{B}_y^\pm(t) = B(y)\sin(\omega_\pm t)\mathbf{e}_y$, is applied to excite a single spin-wave eigenmode in the FeB nanodisk. Snapshots in Figs. 2(a) and 2(b) show excellent agreement with the theoretical formula, Eq. (3) of $\ell = \pm 1$ and $n = 0$. After turning off the externally applied microwave, the finite Gilbert damping leads to a time-decaying spin-wave density [Fig. 2(c)]. However, when evaluating the topological charge ℓ from numerically integrating orbital angular moment $\langle L \rangle$, we find that ℓ is damping resistant and is conserved during the spin-wave evolution [Fig. 2(d)].

To investigate the spin pumping effect, we take the lowest eigenfrequency (ω_-) excitations as a demonstration mode. As shown in Fig. 3(a), the numerical spin-wave density is well described by the Bessel function with $\ell = -1$. The numerically calculated z-polarized spin currents over both the left ($\langle \mathcal{I}_s^z \rangle_L$) and right ($\langle \mathcal{I}_s^z \rangle_R$) half-disks possess DC behavior [Fig. 3(b)]. The angular dependence of $\langle \mathcal{I}_s^z(\rho) \rangle$ in Figs. 3(c) and 3(d) is determined by the function $\cos 2\ell\phi$.
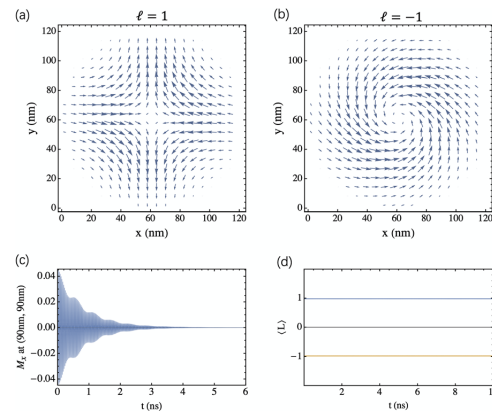

FIG. 2. (a) and (b) Snapshots of the in-plane nonequilibrium magnetization configuration of the $\ell = \pm 1$ eigenmodes. (c) and (d) Time resolved amplitude of m_x at the point (90, 90) nm and the averaged orbital angular moment $\langle L \rangle$, respectively.
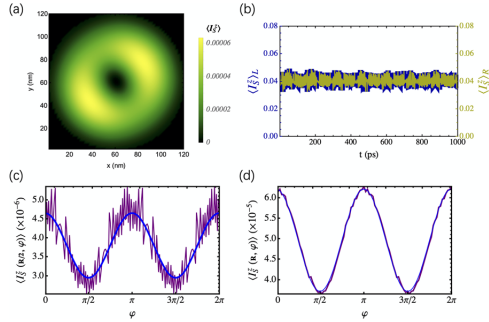
FIG. 3. (a) Snapshot of spin current density $\langle \mathcal{I}_s^z \rangle$ of $\ell = -1$ eigenmode. (b) The integral z-polarized spin density over the left and right half-disks, $\langle \mathcal{I}_s^z \rangle_L$ (dark blue line) and $\langle \mathcal{I}_s^z \rangle_R$ (dark yellow line), respectively. (c) and (d) Angular resolved $\langle \mathcal{I}_s^z \rangle$ along the circle with the radius $\rho = R$ and $\rho = R/2$ respectively.

Concerning the pumped AC spin current, $\langle \mathcal{I}_s^x \rangle$ and $\langle \mathcal{I}_s^y \rangle$ as depicted in Fig. 4, the integral over both the left and right half-disks shows a time-oscillating behavior with frequency ω_- but with a phase difference $\ell\pi$. Clearly, as expected, the topology (ℓ) of the spin-wave eigenmodes can be extracted using the spin-pumping method.

Another important issue is the transmission and interference of spin-waves in two coupled FM disks. It has been shown that the spin-wave coupling efficiency depends on both the geometry of magnonic structures and the characteristics of the spin-wave modes.[21–23] Here, we explicitly demonstrate these important effects by exciting only one
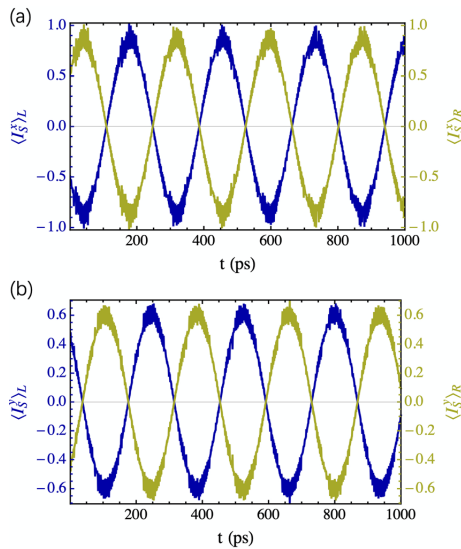
of the two point-adjacent FeB disks, meaning that disk I is exposed to the single-frequency microwave $\mathbf{B}_y^-(t)$. As depicted in Fig. 5(a), the Bessel eigenmode with topological charge $\ell = -1$ is excited in disk I and is then transmitted into disk II. Furthermore, as demonstrated in Fig. 5(b), the point-like inter-disk exchange interaction is ignorable and the transmission of spin waves is solely mediated by the inter-disk dipole interaction. However, the pumped spin current signals show that the amplitude of spin-waves in disk II is strongly reduced and there is a $\pi/2$ phase shift between two disks. Compared to the pumped spin currents of a single FeB disk in Figs. 3 and 4, we notice that the eigenfrequency of spin-waves is slightly modified by the dipole interaction and the z-polarized spin current $\langle \mathcal{I}_s^z \rangle$ becomes a DC + AC mixed signal with a doubled frequency of the x-polarized AC spin current.

In conclusion, we studied analytically and numerically the spin-wave excitations in ferromagnetic nanodisks. Using the micromagnetic simulation program *mumax3*, we showed that twisted spin-wave eigenmodes can be launched individually and can be detected based on the inverse spin Hall effect and methods sensing spin accumulations. The topological charge of spin-waves is protected against damping and has a well-defined signature in the DC/AC pumped spin current. Furthermore, the topological charge can be exchanged between two dipole-coupled nanodisks. We find, moreover that the topological charge of spin-waves is robust against reasonable disk shape variations that do not destroy the topology. For instance, the twisted magnons can be launched in ellipsoid, square, and rectangle structures as long as the spin-wave modes are dominated by the exchange interaction rather than the dipole interaction. Our results add an additional twist to the topological spin-wave and their use for information transfer and processing.
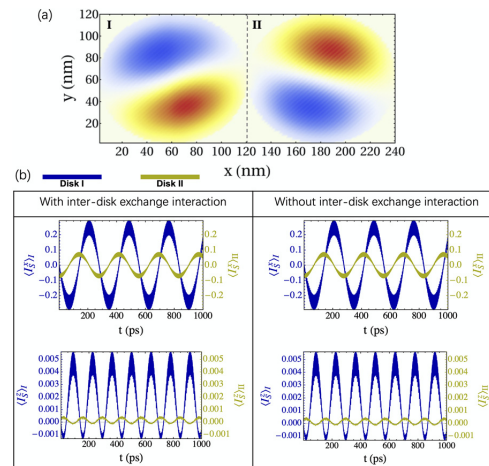

FIG. 4. The integral (a) x- and (b) y-polarized spin current density over the left (dark blue line) and right (dark yellow line) half-disks.

FIG. 5. Transmission of spin-waves between two coupled FeB disks. Note that only disk I is excited locally by the applied rf magnetic field $\mathbf{B}_y^-(t)$. (a) shows a snapshot of the y-component of magnetization m_y. (b) The integral x- and z-polarized spin density averaged over disk I (dark blue line) and disk II (dark yellow line) with or without point-like inter-disk exchange interaction.

The data that support the findings of this study are available from the corresponding author upon reasonable request.

REFERENCES

[1] S. O. Demokritov and A. N. Slavin, *Magnonics: From Fundamentals to Applications*, Topics in Applied Physics Vol. 125 (Springer, New York, 2013).

[2] A. V. Chumak, V. I. Vasyuchka, A. A. Serga, and B. Hillebrands, "Magnon spintronics," Nat. Phys. **11**, 453 (2015).

[3] A. V. Chumak and H. Schultheiss, "Magnonics: Spin waves connecting charges, spins and photons," J. Phys. D **50**, 300201 (2017).

[4] M. P. Kostylev, A. A. Serga, T. Schneider, B. Leven, and B. Hillebrands, "Spin-wave logical gates," Appl. Phys. Lett. **87**, 153501 (2005).

[5] T. Schneider, A. A. Serga, B. Leven, and B. Hillebrands, "Realization of spin-wave logic gates," Appl. Phys. Lett. **92**, 022505 (2008).

[6] S.-K. Kim, K.-S. Lee, and D.-S. Han, "A gigahertz-range spin-wave filter composed of width-modulated nanostrip magnonic-crystal waveguides," Appl. Phys. Lett. **95**, 082507 (2009).

[7] F. Garcia-Sanchez, P. Borys, R. Soucaille, J.-P. Adam, R. L. Stamps, and J.-V. Kim, "Narrow magnonic waveguides based on domain walls," Phys. Rev. Lett. **114**, 247206 (2015).

[8] K. Vogt, H. Schultheiss, S. Jain, J. E. Pearson, A. Hoffmann, S. D. Bader, and B. Hillebrands, "Spin waves turning a corner," Appl. Phys. Lett. **101**, 042410 (2012).

[9] J. Lan, W. Yu, R. Wu, and J. Xiao, "Spin-wave diode," Phys. Rev. X **5**, 041049 (2015).

[10] X. S. Wang, Y. Su, and X. R. Wang, Phys. Rev. B **95**, 014435 (2017).

[11] X. S. Wang, H. W. Zhang, and X. R. Wang, Phys. Rev. Appl. **9**, 024029 (2018).

[12] K. Vogt, F. Y. Fradin, J. E. Pearson, T. Sebastian, S. D. Bader, B. Hillebrands, A. Hoffmann, and H. Schultheiss, "Realization of a spin-wave multiplexer," Nat. Commun. **5**, 3727 (2014).

[13] C. Jia, D. Ma, A. F. Schäffer, and J. Berakdar, Nat. Commun. **10**, 2077 (2019).

[14] C. Jia, D. Ma, A. F. Schäffer, and J. Berakdar, J. Opt. **21**, 124001 (2019).

[15] K. Schultheiss, R. Verba, F. Wehrmann, K. Wagner, L. Körber, T. Hula, T. Hache, A. Kákay, A. A. Awad, V. Tiberkevich, A. N. Slavin, J. Fassbender, and H. Schultheiss, Phys. Rev. Lett. **122**, 097202 (2019).

[16] Y. Tserkovnyak, A. Brataas, and G. E. W. Bauer, Phys. Rev. Lett. **88**, 117601 (2002); Rev. Mod. Phys. **77**, 1375 (2005).

[17] J. Cho, S. Miwa, K. Yakushiji, S. Tamaru, H. Kubota, A. Fukushima, S. Fujimoto, E. Tamura, C.-Y. You, S. Yuasa, and Y. Suzuki, Phys. Rev. B **94**, 184411 (2016).

[18] S. Tamaru, H. Kubota, K. Yakushiji, M. Konoto, T. Nozaki, A. Fukushima, H. Imamura, T. Taniguchi, H. Arai, S. Tsunegi, S. Yuasa, and Y. Suzuki, J. Appl. Phys. **115**, 17C740 (2014).

[19] C. Jaehun, M. Shinji, Y. Kay, K. Hitoshi, F. Akio, Y. Chun-Yeol, Y. Shinji, and S. Yoshishige, Phys. Rev. Appl. **10**, 014033 (2018).

[20] A. Vansteenkiste, J. Leliaert, M. Dvornik, M. Helsen, F. Garcia-Sanchez, and B. Van Waeyenberge, AIP Adv. **4**, 107133 (2014).

[21] A. V. Sadovnikov, E. N. Beginin, S. E. Sheshukova, D. V. Romanenko, Y. P. Sharaevskii, and S. A. Nikitov, Appl. Phys. Lett. **107**, 202405 (2015).

[22] C. Behncke, C. F. Adolff, N. Lenzing, M. Hänze, B. Schulte, M. Weigand, G. Schütz, and G. Meier, Commun. Phys. **1**, 50 (2018).

[23] Q. Wang, P. Pirro, R. Verba, A. Slavin, B. Hillebrands, and A. V. Chumak, Sci. Adv. **4**, e1701517 (2018).

ARTICLE   OPEN

Chiral logic computing with twisted antiferromagnetic magnon modes

Chenglong Jia [1 ✉], Min Chen[1], Alexander F. Schäffer[2] and Jamal Berakdar [2 ✉]

Antiferromagnetic (AFM) materials offer an exciting platform for ultrafast information handling with low cross-talks and compatibility with existing technology. Particularly interesting for low-energy cost computing is the spin wave-based realization of logic gates, which has been demonstrated experimentally for ferromagnetic waveguides. Here, we predict chiral magnonic eigenmodes with a finite intrinsic, magnonic orbital angular momentum ℓ in AFM waveguides. ℓ is an unbounded integer determined by the spatial topology of the mode. We show how these chiral modes can serve for multiplex AFM magnonic computing by demonstrating the operation of several symmetry- and topology-protected logic gates. A Dzyaloshinskii–Moriya interaction may arise at the waveguide boundaries, allowing coupling to external electric fields and resulting in a Faraday effect. The uncovered aspects highlight the potential of AFM spintronics for swift data communication and handling with high fidelity and at a low-energy cost.

INTRODUCTION

Magnetic materials are essential elements in data storage, information processing, and sensory devices. Their low-energy excitations, the spin waves with magnons as quanta of excitations, can be utilized to transmit and process information at low-energy cost and without heat dissipation due to Ohmic losses[1–3]. Recent research on AFM[4–11] demonstrated their potential for the next generation of spintronics and optoelectronic devices. Experiments evidenced that the AFM ordering is switchable on THz time scale by charge current or THz pulses. Material-wise, AFM structures are well compatible with a variety of material classes and amenable to nanopatterning. For instance, synthetic AFM samples (SyAF) were fabricated out of two magnetic layers that are coupled antiferromagnetically[12–14]. SyAFs allow thus creating AFM/FM heterostructures. The field is further fuelled by the uncovered properties of van der Waals coupled 2D materials[15–19], which may be viewed (depending on their synthesis) as a type of FM, AFM or SyAF structure. Notably, ref. [20] demonstrated the excitation and the long-distance AFM magnon transport in the quasi-2D van der Waals AFM MnPS$_3$.

Generally, magnons in AFM[21,22] are qualitatively different from their FM counterpart: (1) FM magnons are always right-handed. In contrast, AFM have two degenerate spin wave eigenmodes of opposite chirality, referred to as right- and left-handed magnons depending on the precessional handedness of the AFM order parameter (the Néel vector, cf. Fig. 1). Combining these two polarizations, any polarization state can be produced, offering a way to encode information based on polarization-states. (2) AFM materials do not suffer from cross talks, as demagnetizing fields are minor, and hence signals carried by AFM excitation are robust to external magnetic perturbations. The small intrinsic magnetization which emerges upon a spatiotemporal variation of the AFM order parameter may be utilized to act on the dynamics of magnetic textures and spin currents. (3) Being much fast than FM magnons, AFM spin waves can be employed for swift data transfer.

Another feature of AFM magnons is demonstrated in this work: AFM waveguides support chiral magnonic eigenmodes that carry a well-defined amount ℓ of magnonic orbital angular momentum (OAM) (with respect to the propagation direction). ℓ is unbounded and associated with the spatial topology or the "twist" of the eigenmode extending over the whole waveguide. We demonstrate how the twisted modes serve for realizing a class of symmetry-protected logic gates and for multiplex data transfer[23–26]. The operation of the gates is robust, for the twisted beams are found as eigenmodes of the waveguide with a dispersion allowing for forming signals as fast as AFM magnonics. Waveguide boundaries can host a Dzyaloshinskii–Moriya[27,28] interaction (DMI) due to the break of inversion symmetry. We find DMI is useful for triggering and steering twisted modes. The analytic predictions are ubiquitous, meaning that twisted AFM magnons should appear in conventional AFM, SyAF, or van-der-Waals-AF cylindrical waveguides. We present a general theory and demonstrate with full-numerical simulations the character and the functionalization of twisted modes for a prototypical NiO AFM waveguide for a demonstration.

RESULTS AND DISCUSSION

Chiral antiferromagnetic magnons

As a magnonic waveguide we consider a cylindrical wire made of a G-type AFM[29] with an axis aligned along with the AFM easy ($\mathbf{e}_z$) direction (cf. Fig. 1). In practice, the waveguide can be deposited or imprinted on a substrate or be part of integrated magnonic circuits. For capturing the low-energy AFM dynamics, it is adequate to start from the Heisenberg Hamiltonian

$$\mathcal{H} = \frac{J}{2}\sum_{ij} \mathbf{S}_i \cdot \mathbf{S}_j - \frac{K_z}{2}\sum_i (\mathbf{S}_i \cdot \mathbf{e}_z)^2, \qquad (1)$$

where $J > 0$ stands for the strength of the (uniform) AFM exchange coupling between neighboring spins $\mathbf{S}_i$ localized at lattice sites i with a lattice distance a. The uniaxial anisotropy energy

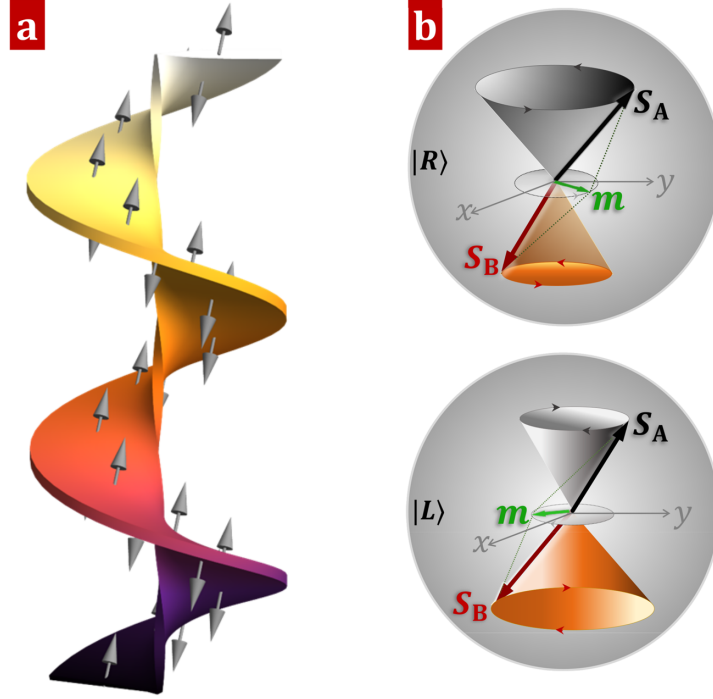**Fig. 1 Schematic representation of twisted magnon beams in AFM waveguide. a** Twisted magnon beams propagating along a cylindrical AFM waveguide with two magnetic sublattices A (up arrows) and B (down arrows). **b** Degenerate right- and left-handed spin wave modes, $|L\rangle$ and $|R\rangle$ dominated by the sublattice A and B, respectively. The small magnetization (green arrows) is defined as $\mathbf{m} = (\mathbf{S}_A + \mathbf{S}_B)/2S$.

contribution (with strength $\propto K_z > 0$) is large enough to suppress quantum fluctuations enforcing so a collinear (Néel) ground state aligned with the easy axis (cf. Fig. 1). The spin dynamics follows Heisenberg's equation of motion $d\mathbf{S}_i/dt = -i/\hbar[\mathbf{S}_i, \mathcal{H}] = \mathbf{S}_i \times (K_z \mathbf{S}_i^z - \sum_{j \in i} J \mathbf{S}_j)$. Low-energy excitations, meaning AFM spin waves are described[21] by introducing the classical dimensionless unit vector field $\mathbf{s}_i = \mathbf{S}_i/S$, where $|\mathbf{S}_i| = S$ for all sites. The spin waves are then transversal excitations propagating according to

$$i\hbar \frac{ds_i^-}{dt} = -\left(K_S s_i^z - \sum_{j \in i} J_S s_j^z\right)s_i^- - s_i^z \sum_{j \in i} J_S s_j^-, \tag{2}$$

with $s_i^\pm := s_i^x \pm i s_i^y$. $K_S = K_z S\hbar$, $J_S = JS\hbar$ are respectively the anisotropy and exchange energies. Using a plane-wave ansatz $s_i^-(t) \sim e^{i(\mathbf{k} \cdot \mathbf{r}_i - \omega_k t)}$, one infers the dispersion relation for spin waves as $E_k^2 = \hbar^2 \omega_k^2 = (K_S + \zeta J_S)^2 - (\zeta J_S \gamma_k)^2$ where ζ is the coordination number ($\zeta = 2, 4, 6$ for respectively one-dimensional spin chain, two-dimensional square lattice, and a three-dimensional cubic lattice). $\gamma_k = \sum_{j \in i} e^{i\mathbf{k} \cdot \mathbf{r}_{ij}}/\zeta$. The same dispersion follows from a Holstein–Primakoff approach[30,31].

AFM magnonic Dirac dynamics

The physics of AFM low-energy excitations is most transparent upon a mapping onto two sub-lattices[32–36] denoted A and B with antiparallel spins (cf. Fig. 1a). The ordering in each sublattice is FM but a translation by a lattice vector transforms $\mathbf{S}(\mathbf{r} + \mathbf{a}) \rightarrow -\mathbf{S}(\mathbf{r})$, meaning that the translational invariance is broken. Thus, the AFM Heisenberg system is mappable onto an antiferromagnetic (AFM) CP^1 model[36]. Note, the AFM Hamiltonian is still invariant under the combined time-reversal ($\mathcal{T}$) and sub-lattice exchange ($\mathcal{I}$), a fact underlying the degeneracy of the two chiral magnon modes.

Equation (1) is, in addition, invariant under global spin rotation around the z-axis, and thus the z-component of the total spin is a good quantum number. For a further insight, let us follow Haldane[32] (see also[33,35,36]) and consider small sublattice-dependent fluctuations around the one-dimensional Néel ground state[32]. To do so, one introduces $\mathbf{s}_i^A = (\mathbf{a}_i + \sqrt{1 - \mathbf{a}_i^2} \mathbf{e}_z)$ and $\mathbf{s}_i^B = (\mathbf{b}_i - \sqrt{1 - \mathbf{b}_i^2} \mathbf{e}_z)$, where $|\mathbf{a}_i| \ll 1$ and $|\mathbf{b}_i| \ll 1$. Linearizing Eq. (2) and noting that $\mathbf{a}_j = \mathbf{a}_i + (\mathbf{r}_{ij} \cdot \nabla)\mathbf{a}_i + \frac{1}{2}\mathbf{r}_{ij}^2 \nabla^2 \mathbf{a}_i + \dots$ (and proceeding similarly for $\mathbf{b}_i$), we arrive at the continuum Hamiltonian (valid up to the second-order derivatives)

$$i\hbar \frac{d\psi_i^+}{dt} = \mathcal{H}_D \psi_i^+, \tag{3}$$

where $\psi_i^+(z,t) = (a_i^+, b_i^+)^T$ is the two-component Dirac spinor, and $\tilde{\partial}_z := 2a \, \partial/\partial z$)

$$\mathcal{H}_D = \begin{bmatrix} K_S + 2J_S & 2J_S - J_S \tilde{\partial}_z + J_S \tilde{\partial}_z^2/2 \\ -2J_S - J_S \tilde{\partial}_z - J_S \tilde{\partial}_z^2/2 & -K_S - 2J_S \end{bmatrix}. \tag{4}$$

The first-order derivative ($\sim J_S \tilde{\partial}_z$) in $\mathcal{H}_D$ is a parity-breaking term and as such is not invariant under sublattice exchange ($A \leftrightarrow B$) in the G-type AFMs. This term introduces a finite precessional phase difference between the sublattice A and B. In the long-wavelength limit of plane-wave ansatz, the eigenenergies of the Dirac Hamiltonian Eq. (3) are $E_k = \pm \left[J_S^2 k_z^2 + K_S(K_S + 4J_S)\right]^{1/2}$ with the corresponding eigenmodes

$$\psi_L^+ = \begin{bmatrix} \cosh \frac{\vartheta}{2} \\ -e^{i\varphi} \sinh \frac{\vartheta}{2} \end{bmatrix} \text{ and } \psi_R^+ = \begin{bmatrix} -\sinh \frac{\vartheta}{2} \\ e^{i\varphi} \cosh \frac{\vartheta}{2} \end{bmatrix}, \tag{5}$$

where $\cosh \vartheta = (K_S + 2J_S)/|E_k|$ and $\tan \varphi = J_S k_z/(2J_S - J_S k_z^2/2)$[37].

ψ_L^+ (ψ_R^+) with eigenfrequency $\omega_k > 0$ ($\omega_k < 0$) describes the left-circularly (right-circularly) polarized modes dominated by the precession in A (B) sublattice, as illustrated in Fig. 1b. The opposite holds true for the complex conjugate $\psi_i^- = (a_i^-, b_i^-)^T$. In the following, we take the positive eigenfrequency modes, $|L\rangle \equiv \psi_L^+$ and $|R\rangle \equiv \psi_R^-$ as the chirally complete basis for AFM magnons. Although $\mathcal{H}_D$ is not Hermitian, the chiral basis can be easily normalized by applying a momentum-dependent factor, such that $\langle L|L\rangle / \mathcal{N}_k = \langle R|R\rangle / \mathcal{N}_k = 1$ with $\mathcal{N}_k = \cosh\vartheta$ and the averaged $\langle L|R\rangle_k = -\langle \sinh\vartheta \rangle_k \equiv 0$. Considering the spin precession around the z-axis, we define a chirality (chiral charge) as $C_L = \langle L|\sigma_z|L\rangle = 1$ and $C_R = \langle R|\sigma_z|R\rangle = -1$, clearly, $|L\rangle$ and $|R\rangle$ have particle-hole symmetry. Note, the AFM magnon chirality is intrinsic and independent of the propagation direction of magnons. Its origin stem from the symmetry of the AFM system. Hence, it is useful to employ the magnon chirality for a non-volatile encoding of information, as explicitly demonstrated below.

Magnonic Klein–Gordon dynamics
When applying Haldane's mapping procedure, no apparent parity-breaking exchange term appears in the continuum energy function. The parity-breaking term is important to correctly capture the intrinsic magnetization, as evident in the continuum limit of the free energy of AFM magnons. Let us employ the staggered field[35] $\mathbf{n} = (\mathbf{S}_A - \mathbf{S}_B)/(2S)$ and the intrinsic magnetization $\mathbf{m} = (\mathbf{S}_A + \mathbf{S}_B)/(2S)$. For large and isotropic AFM exchange $J \gg K_z$, the total Lagrangian density reads[32,33,35],

$$\mathcal{L} = \rho_s \mathbf{m} \cdot (\partial_t \mathbf{n} \times \mathbf{n}) - \frac{\mathbf{m}^2}{2\chi_m} - \frac{A}{2}(\partial_\mu \mathbf{n} \cdot \partial_\mu \mathbf{n})$$
$$- \xi_s \sum_\mu (\mathbf{m} \cdot \partial_\mu \mathbf{n}) + \frac{K_s}{2} n_z^2. \tag{6}$$

where $\rho_s = 2S$ is the magnitude of the staggered spin angular momentum per unit cell, χ_m is the magnetic susceptibility, $A = 2\zeta a^2 J S^2$ is the exchange stiffness, and $\xi_s = 2\zeta a J S^2$ signifies the amplitude of the parity-breaking term. In the absence of a strong external magnetic field, the spin density field $\mathbf{m}$ is a slave variable ($|\mathbf{m}| \ll 1$) that follows the temporal and spatial evolution of the staggered AFM order as[32,33,35]

$$\mathbf{m}/\chi_m = \rho_s (\partial_t \mathbf{n} \times \mathbf{n}) - \xi_s \partial_\mu \mathbf{n}. \tag{7}$$

Eliminating $\mathbf{m}$ we obtain the two-component Klein–Gordon equation for $|\psi_n\rangle = (n_x + i n_y, n_x - i n_y)^T$ as

$$\left(\partial_z^2 - \frac{1}{c^2} \partial_t^2 \right) |\psi_n\rangle = \mathcal{K}_z |\psi_n\rangle, \tag{8}$$

where $c = 2aJS/\hbar$ is the spin wave velocity, and $\mathcal{K}_z = K_S(K_S + 4J_S)/(4J_S^2 a^2)$ determines the spin wave gap. Obviously, ψ_n^+ (i.e., $n_x + i n_y$) and ψ_n^- (i.e., $n_x - i n_y$) are associated with the degenerate left- and right-handed chiral magnons, respectively. Conventional magnons without a spatial phase structure (i.e., without OAM) exhibit opposite intrinsic magnetization of the left- and right-handed modes. Upon time averaging, we find

$$\langle m_L^z \rangle \propto \Im[\psi_n^+ \partial_t (\psi_n^+)^\star] = +\omega_k \rho_n^+, \tag{9}$$

$$\langle m_R^z \rangle \propto \Im[(\psi_n^-)^\star \partial_t \psi_n^-] = -\omega_k \rho_n^-, \tag{10}$$

which clarifies the chiral character of the modes.

Now we show the existence of eigenmodes characterized (in addition to their chirality) by a definite amount of magnonic (meaning akin to the quasiparticles, magnons) OAM. We term these helical modes as twisted AFM magnons.

Twisted AFM magnons
In an extended cylindrical AFM tube and in cylindrical coordinates $\mathbf{r} \to (r, \phi, z)$, the above Klein–Gordon equation admits the non-diffractive Bessel solutions

$$\psi_n(\mathbf{r}, t) \propto J_\ell(k_\perp r) \exp(i\ell\phi + i k_z z) \exp(-i\omega t), \tag{11}$$

with $\ell = 0, \pm 1, \pm 2, \ldots$. $J_\ell(x)$ is the Bessel function of the first kind with order ℓ. For a cylindrical waveguide which is narrow compared to the magnon wavelength one may apply the paraxial approximation $\mathbf{k}^2 \gg (\mathbf{k}^2 - k_z^2)$, i.e., the transverse wave number $k_\perp$ is small. One finds then that $\partial_z^2 \simeq k^2 + 2ik\partial_z$ leading to the Schrödinger-type equation for the spin waves

$$i\frac{\partial \psi_n}{\partial \tilde{z}} = -\left[\frac{1}{r}\frac{\partial}{\partial r}\left(r\frac{\partial}{\partial r} \right) + \frac{1}{r^2}\frac{\partial^2}{\partial \phi^2} + k^2 \right]\psi_n, \tag{12}$$

where $\tilde{z} = z/2k$ can be interpreted as the independent "time-like" variable. We conclude that in the AFM waveguides the modes are transversely confined Laguerre-Gaussian (LG) beams

$$\psi_{\ell,\varsigma}^{LG} \propto \left(\frac{r}{w(z)} \right)^{|\ell|} L_\varsigma^{|\ell|}\left(\frac{2r^2}{w(z)^2} \right)$$
$$\times \exp\left(-\frac{r^2}{w(z)^2} + ik\frac{r^2}{2R(z)^2} \right) e^{i\ell\phi + ikz} e^{i(2\varsigma + |\ell| + 1)\eta(z)}, \tag{13}$$

where $L_\varsigma^{|\ell|}$ are the generalized Laguerre polynomials, $\ell = 0, \pm 1, \pm 2, \ldots$; $\varsigma = 0, 1, 2, \ldots$ is the radial quantum number, $w(z) = w_0\sqrt{1 + z^2/z_R^2}$ is the beam width depending on z due to diffraction, $R(z) = z(1 + z_R^2/z^2)$ is the radius of curvature of the wave fronts, and $\eta(z) = \arctan(z/z_R)$. The last exponential factor $(2\varsigma + |\ell| + 1)\eta(z)$ is related to the Gouy phase yielding an additional phase delay on the beam propagation. LG modes have well-defined azimuthal and radial wavefront distributions (quantified by ℓ and ς, respectively) and they form an orthogonal and complete basis in terms of which an arbitrary function can be represented. The existence and utility of twisted modes for various systems ranging from electrons and neutron to acoustic waves are documented[25,38–42]. In AFM the underlying symmetries, free-energy density and the generic equations of motions are different from known cases, yet twisted AFM modes carrying OAM do exist under appropriate setting. To inspect the properties of the canonical OAM, we consider the continuity equation for spin angular momentum transfer in AFMs[35], $\rho_s \partial_t \mathbf{m} + \sum_\mu \partial_\mu \mathcal{J}_\mathbf{m}^\mu = \mathbf{0}$. The spin current along the μ spatial direction reads

$$\mathcal{J}_\mathbf{m}^\mu = -\frac{\rho_s \xi_s}{\chi_m}\partial_t \mathbf{n} - \mathcal{A}(\mathbf{n} \times \partial_\mu \mathbf{n}). \tag{14}$$

The first temporal term on the r. h. s. is determined by the precession of the staggered field $\mathbf{n}$ and thus carries the magnon chirality of any type of magnon beams. The second term is intimately related to the spatial topology of the (helical) magnon wave. In particular, the spatial phase modulations of the spin wave whose twist is characterize by the integer ℓ is decisive. For example, in terms of the left-handed Bessel/LG beams, one finds the conserved z-component of the magnonic spin current

$$\mathcal{J}_{m_z}^\mu = \mathcal{A}\Im[\psi_n^+ \partial_\mu (\psi_n^+)^\star] = -\mathcal{A}\rho_\ell^+(r)\left(\frac{\ell}{r}\mathbf{e}_\phi + k_z \mathbf{e}_z \right), \tag{15}$$

where ρ_ℓ^+ is the magnon density of twisted, left-hand chiral magnons. ℓ characterizes the z-component of the intrinsic OAM of the respective mode, $L_z \sim \hbar\ell$ that is independent on the choice of the coordinate origin[25] and different ℓ correspond to different modes, implying that these modes may serve as multiplex information channels. We note that ℓ is unbounded and akin to the geometry and topology of the waveguide, presenting an additional twist that is independent of the magnon chirality. Due to (Gilbert) damping of magnetization precession, the magnon density is a time-decaying function. OAM ℓ however, is robust to damping, meaning when functionalized ℓ for information transmission, the signal becomes weaker with time but the information content is preserved. Further micromagentic

simulations show that ℓ is a global property of the waveguide and is less affected by reasonable variations of deformation in the shape.

DMI coupling, Faraday effects, and electric field control

For controlling twisted AFM magnons with electric means, the electric-field-tunable interfacial DMI can be used to realize twisted spin wave computing. The break of the inversion symmetry at the cylindrical surface along the radial direction $\mathbf{e}_r$ allows for a DMI of the following form, $\mathcal{H}_{\text{DM}} = -\mathbf{D}_{ij} \cdot (\mathbf{S}_i \times \mathbf{S}_j)$. The DMI vector reads $\mathbf{D}_{ij} = D(\mathbf{e}_r \times \mathbf{r}_{ij})$. The DMI adds to the Lagrangian density as $\mathcal{L}_{\text{DM}} = D_S[\mathbf{n} \cdot (\tilde{\nabla} \times \mathbf{n}) + \tilde{\nabla} \cdot (\mathbf{n} \times \mathbf{m}) - \mathbf{m} \cdot (\tilde{\nabla} \times \mathbf{m})]$. where $D_S = DS^2$ and $\tilde{\nabla} = (\mathbf{e}_r \times \nabla_{\mathbf{r}_{ij}})$. The second term on the r. h. s. is a parity-breaking term and has the structure of a total derivative. Hence, it does not affect the local dynamics. Dropping the small last higher-order term on the r. h. s. ($\mathbf{m} \ll 1$), we arrive at the in-plane DMI density (note, $\mathbf{r}_{ij} \in xy$-plane)

$$\mathcal{L}_{\text{DM}}^{xy} = -D_S/r(n_x \partial_\phi n_y - n_y \partial_\phi n_x). \qquad (16)$$

Otherwise, $\mathbf{r}_{ij} \| \mathbf{e}_z$ results in the longitudinal DMI density

$$\mathcal{L}_{\text{DM}}^z = -D_S \mathbf{n} \cdot \partial_z [n_z \cos\phi, n_z \sin\phi, -(n_x \cos\phi + n_y \sin\phi)]. \qquad (17)$$

Up to the second order in the transversal fluctuations around the equilibrium of $\mathbf{n}$, $\mathcal{L}_{\text{DM}}^z$ does not affect the magnon dynamics but pins Walker-type domain walls to the right-Néel type.

The Euler–Lagrange dynamics for the staggered field, Eq. (6) is augmented by an additional term in the presence of DMI. To a leading order in the density $\mathcal{L}_{\text{DM}}^z$, the magnon dynamics is governed by

$$\left[\partial_\mu^2 - \frac{1}{c^2} \partial_t^2 + i\sigma_z \mathcal{D} \partial_\phi \right] |\psi_n\rangle = \mathcal{K}_z |\psi_n\rangle, \qquad (18)$$

where $\mathcal{D} = \frac{D_S}{AR}$ with R being the radius of the AFM tube. Note, the thickness scaling as r/R of the interface-induced DMI (i.e., $D_S \sim r/R$) has been used to derive Eq. (18). In the absence of DMI ($\mathcal{D} = 0$), the topological charge ℓ is independent of the helicity of spin waves and the left-handed ($\psi_{\ell,\varsigma}^+$) and right-handed ($\psi_{\ell,\varsigma}^-$) chiral modes with arbitrary topological charges ℓ are degenerate. This infinite degeneracy is however lifted by the introduction of $\mathcal{L}_{\text{DM}}^{xy}$ which behaves as a fictitious electric field that couples to the magnons via the Aharanov–Casher effect. For Bessel/LG modes as solutions for Eq. (18) we infer the modified dispersion relation of the chiral magnons

$$\omega_\pm^2 = c^2 (k_z^2 + k_\perp^2 \pm \mathcal{D}\ell + \mathcal{K}_z). \qquad (19)$$

The energy dispersion is now dependent on the topological charge ℓ. The spin wave gap is softened by the DMI, meaning that even below the AFM resonance point at $\omega_R = c\sqrt{\mathcal{K}_z}$, twisted magnons can be excited. Equation (19) indicates that the chiral degeneracy of left- and right-handed magnons ($\psi_{\ell,\varsigma}^\pm$) with same topological charge ℓ is lifted, however, the twofold topological $\pm\ell$ degeneracy survives in the presence of interfacial DMI. These degenerate twisted beams with opposite topological charge are decoupled from each other. The OAM-balanced superposition $|\chi_\phi\rangle$ is thus robust to the surface-induced DMI. The Bloch circles and the interference patterns are rotated during propagation along the waveguide resulting in a Faraday effect (cf. Fig. 2)[43–45]. In the paraxial approximation with relatively small transverse kinetic energy, the allowed wave numbers are approximated as $k_\pm^z \simeq k + \delta k_\pm^z$ with $\delta k_\pm^z = \pm \mathcal{D}\ell/(2k) + \mathcal{K}_z/(2k)$. The DMI modifies the longitudinal wave vector resulting in an additional phase difference $\delta\varphi(z) \propto (\mathcal{D}\ell z/k)$. Let l be the length of the AFM tube, then $\delta\varphi(l) = \pi$ can be realized since arbitrarily large values of ℓ are possible allowing so for any desired phase shift even at very weak DMI and the twisted magnon beams exhibit so a rich magneto-electric interference pattern. It is worth noting that such electrical control of the flow of OAM-carrying magnon beams can be
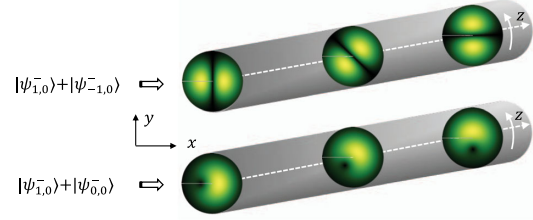

Fig. 2 Faraday effects. Propagation of the interference patterns of the OAM-balanced ($|\psi_{1,0}^-\rangle + |\psi_{-1,0}^-\rangle$) and OAM-unbalanced ($|\psi_{1,0}^-\rangle + |\psi_{0,0}^-\rangle$) superpositions along a AFM waveguide with the interfacial-induced DMI.
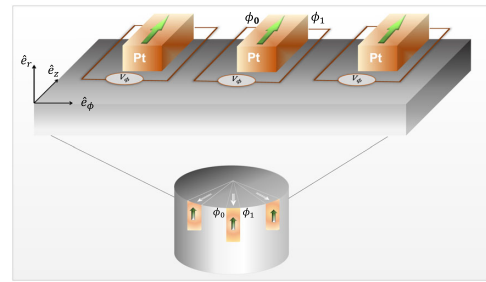

Fig. 3 Angular resolved ISHE measurement. Detections of the pumped spin density $\mathcal{I}_s^z$ of the state $\cos\vartheta_\ell|R\rangle$ by the ϕ-resolved ISHE. At the waveguide end, the z-polarized spins (green arrows) radially pumped into a narrow Pt layers result in an inverse spin Hall voltage $V_\phi \sim \cos^2\vartheta_\ell$ with $\vartheta_\ell \approx \ell(\phi_0 + \phi_1)/2$.

directly realized by applying an external electric field through the Aharonov–Casher (AC) effect[25].

OAM-based information coding and AFM logic gates

A conventional way to read/detect the magnonically encoded data is to convert the signal back to electronic signals via the combination of two physical effects: spin pumping and the inverse spin Hall effect (ISHE). In terms of the staggered AFM order parameter $\mathbf{n}$, there are two types of pumping effect generated by the spin current: the pumped spin density ($\mathcal{I}_s \sim \mathbf{n} \times \partial_t \mathbf{n}$) and the staggered spin pumping ($\mathcal{I}_{ss} \sim \partial_\mu[\mathbf{n} \times \partial_t \mathbf{n}]$) representing the imbalance between the spin current carried by the two sublattices[46]. Averaging over time only the $\mathcal{I}_s^z$ and $\mathcal{I}_{ss}^z$ contribute to the DC pumped spin density, in contrast to the x-and y-components of $\mathcal{I}_s$ (and $\mathcal{I}_{ss}$ as well). Integrating further over the cross section we find that $\langle \mathcal{I}_s^z \rangle$ and $\langle \mathcal{I}_{ss}^z \rangle$ do not depend on the internal phase (spatial) structure of the modes (and hence no dependence on ℓ is present). However, a ϕ-resolved analysis evidences a spatial distribution of pumped spin density. For instance, the state $\cos\vartheta_\ell|R\rangle$ (with $\vartheta_\ell = \ell\phi$) gives rise to

$$\mathcal{I}_s^z \propto \omega_k \cos^2\vartheta_\ell \quad \text{and} \quad \mathcal{I}_{ss}^z \propto -\frac{\ell}{r}\omega_k \sin 2\vartheta_\ell. \qquad (20)$$

These inhomogeneous spin densities can be detected by the ϕ-resolved ISHE, as demonstrated in Fig. 3.

With this we arrive at a key result: The helical or twisted chiral magnons propagating along the same direction in an AFM waveguide are exploitable for realizing parallel logic gates[47]. For a demonstration we recall that $\cos\vartheta_\ell|R\rangle$, $\sin\vartheta_\ell|R\rangle$, $\cos\vartheta_\ell|L\rangle$, and
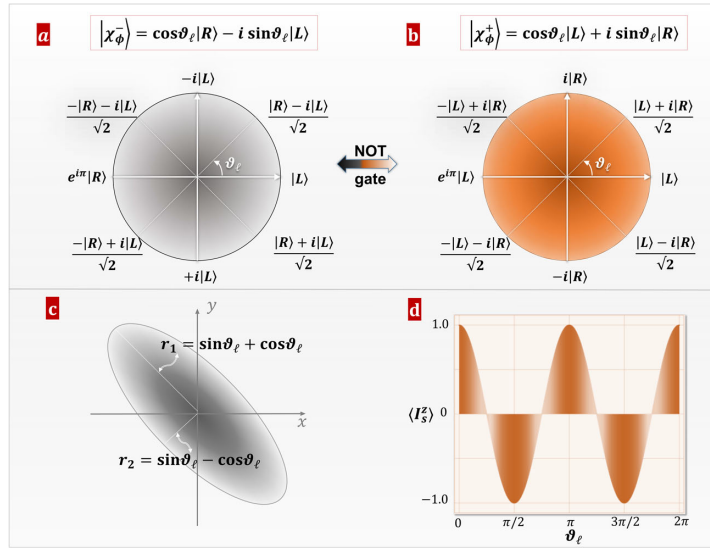
Fig. 4 OAM-based AFM logic gates. a and **b** Logic gates realized by the OAM-balanced twisted AFM chiral magnon states with opposite topological charge ℓ. **c** Corresponding elliptical precession orbit of the chiral magnon state $|\chi_\phi^-\rangle$ in the x–y plane. **d** Pumped spin accumulation for which the DC component is given by the area of the ellipse: $\langle \mathcal{I}_s^z \rangle = \langle \partial_t \mathbf{n} \times \mathbf{n} \rangle \sim \cos 2\vartheta_\ell$.

$\sin \vartheta_\ell |L\rangle$ are four-fold degenerate states. Our logic gates are realized then as follows:

(i) **Phase shift (R_ϕ) gates** with OAM-unbalanced superposition of two chiral magnon beams with topological charge 0 and ℓ,

$$|\chi_\phi\rangle = |R\rangle + e^{i\vartheta_\ell}|L\rangle. \tag{21}$$

Some special examples are: *T-gate* with $\vartheta_\ell = \pi/4$, *S-gate* with $\vartheta_\ell = \pi/2$, and the *phase-flip Pauli-Z gate* with $\vartheta_\ell = \pi$.

(ii) **Hadamard (H) gate** with OAM-balanced superposition of two chiral magnon eigenmodes with opposite topological charges $\pm \ell$, meaning

$$\begin{aligned}|\chi_\phi\rangle &= e^{i\vartheta_\ell}|R\rangle + e^{-i\vartheta_\ell}|L\rangle \\ &= \cos \vartheta_\ell (|R\rangle + |L\rangle) + i \sin \vartheta_\ell (|R\rangle - |L\rangle).\end{aligned} \tag{22}$$

We may rewrite the above superposition into two Bloch circles as, $|\chi_\phi\rangle = |\chi_\phi^+\rangle + |\chi_\phi^-\rangle$ with

$$|\chi_\phi^-\rangle = \cos \vartheta_\ell |R\rangle - i \sin \vartheta_\ell |L\rangle, \tag{23}$$

$$|\chi_\phi^+\rangle = \cos \vartheta_\ell |L\rangle + i \sin \vartheta_\ell |R\rangle. \tag{24}$$

We have then the *NOT (Pauli-X)* connecting $|\chi_\phi^\pm\rangle$, the *Pauli-Y gates* with $|R\rangle \to i|L\rangle$ and $|L\rangle \to -i|R\rangle$, and *the square root of NOT gates* with $|R\rangle \to [(1+i)|R\rangle + (1-i)|L\rangle]/2$ and $|L\rangle \to [(1-i)|R\rangle + (1+i)|L\rangle]/2$, as demonstrated in Fig. 4a, b.

Without breaking the time-reversal $\mathcal{T}$ and/or sublattice exchange $\mathcal{I}$ symmetries, the parallel manipulations of magnon chiralities are thus fully realized in the AFM waveguides with an additional degree of freedom, the topological charge ℓ. Such particular chiral magnon state $|\chi_\phi\rangle$ can be electrically read out by virtue of spin pumping[46] (cf. Figs. 3 and 4 c/d).

Simulations for experimental realization

The preceding derivations are fully general. To confirm the robustness of the predictions when accounting for material and geometry specific effects that are important for an experimental realization, it is instructive to perform full-fledged numerical simulations for a specific waveguide. To this end, let us consider the G-type AFM waveguide made of NiO with material parameters determined by the previous experimental and theoretical studies. For conducting micromagnetic simulations we discretized the waveguide into boxes with a size of the atomic lattice constant of 0.418 nm[348]. Based on previous investigations and our own initial calculations for a cylindrical model system, we estimate the relevant frequency regime to be around $f \sim 0.5$ THz. In the following we use a 0.5 THz frequency for the exciting field and investigate different setups with a special focus on the impact of different topological charges and helicities of the spin waves. Details on the spin dynamics simulations including the spatial and temporal profile of the applied field can be found in the Supplementary Methods.

Twisted wave packet propagation

To demonstrate the twisted wave packets propagation, we consider a waveguide with $100 \times 100 \times 300$ unit cells (u. c.) excited at one end by a twisted magnetic field. For the frequency of 0.5 THz, the wavelength of the plane-wave mode is $\lambda \approx 30.5$ nm. The boundaries are modeled such that they absorb most of the incoming magnons by introducing an exponentially increasing damping parameter in a tube shell with a 20 u. c. thickness. This helps avoiding reflection effects in order to focus on the core features of twisted magnon beams. Because of the discrete rotational symmetry characterized by the OAM, twisted magnon modes are protected against perturbations including defects and finite size effects as discussed for the case of a FM wave guide in ref.[49]. An example of a few-cycle wave packet propagating along the NiO wire is shown in Fig. 5a.

For further insight, let us continue with different wave packets propagating along the wire, especially focusing on the group velocity, broadening, and signal decay.

In Fig. 5b, few-cycle twisted AFM pulses are propagated along the wire, and the position of maximum magnon density is tracked. For this calculation, only one line of magnetic moments parallel to the z-axis is analyzed. The offset to the center is 25 u. c. (≈ 10 nm).
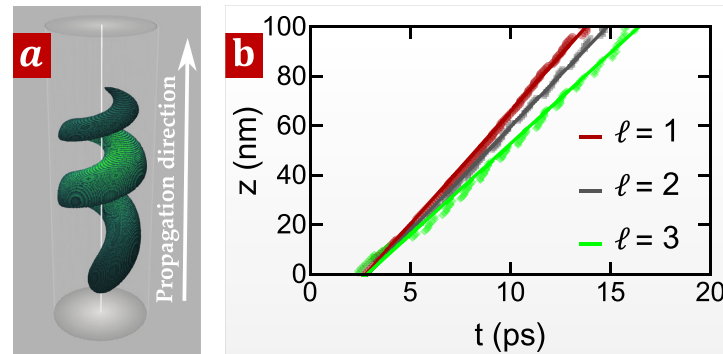
Fig. 5 Propagation of a twisted magnon wave pulse in an AFM waveguide. a A snapshot of the twisted AFM magnonic pulse with $\ell = 1$ taken 10 ps after being triggered with the magnetic field of a THz pulse focused on one end of the waveguide. n_x component of the staggered field is shown. **b** Speed comparison for few-cycle twisted magnonic wave packets carrying different OAM.
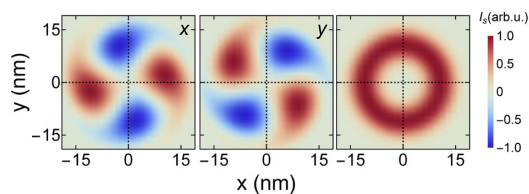

Fig. 6 Cross section of the ISHE signal. The spin accumulation due to a twisted magnon wave packet with $\ell = 2$ and left-handed (clockwise) chirality is calculated according to the ISHE via $\mathcal{I}_s \sim \mathbf{n} \times \partial_t \mathbf{n}$. The three panels display the different components of the induced spin-current showing that only the z-component delivers a non-zero value after integration over the whole cross section. The staggered magnetization is obtained from full-numerical spin dynamics simulations.

The group velocities are different for different winding numbers ℓ. The linear regressions give velocities of $v_{\ell=1} = 9.09$ km s^{-1}, $v_{\ell=2} = 8.36$ km s^{-1} and $v_{\ell=3} = 7.35$ km s^{-1}. Also, the signal amplitude decays more rapidly when increasing the topological number.

Spin dynamics induced by twisted AFM beams

In addition to the propagation of AFM twisted magnon beams, the induced electronic spin density at the surface of the tube can be calculated from the spin dynamics calculations. This we do by calculating the staggered magnetization from the full G-type AFM lattice and subsequently calculate the ISHE via $\mathcal{I}_s \sim \mathbf{n} \times \partial_t \mathbf{n}$ for a cross section of the NiO wire. The resulting patterns of the three Cartesian components of pumped spin density $\mathcal{I}_s$ for a beam with $\ell = 2$ are shown in Fig. 6. All signals are normalized with respect to the maximum value for each component. As predicted, only the z-component has a completely positive signal, delivering a finite signal when integrating over time. In contrast to that, the x- and y-components possess a twofold distribution with alternating positive and negative areas eventually summing up to a total induced spin density of zero.

The characteristic features of the z-component for different chiralities and topological charges are presented in Fig. 7 for a transversal profile through the center of the wire. Generally, the maximum pumped spin density can be found in the region where the highest magnon amplitudes are expected. This also means that for higher topological charges ℓ, the maximum intensity distance increases (cf. dark red and bright green markers). The diminished intensity is explainable by the higher damping of the magnon amplitudes, which is proportional to the magnon density.
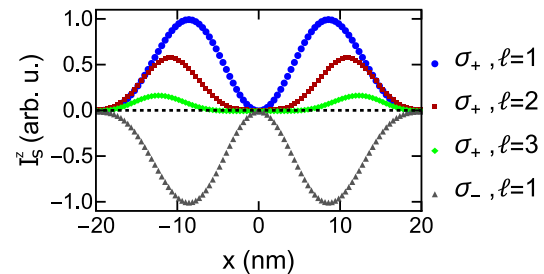
Fig. 7 Spatial profile of the time-integrated out-of-plane ISHE signal. Twisted magnon waves for different topological charges and chiralities are generated in the NiO waveguide. The resulting z-component of the spin accumulation according to the ISHE is calculated via $\mathcal{I}_s \sim \mathbf{n} \times \partial_t \mathbf{n}$.

In addition, the sign of the pumped spin density is determined by the chirality of the magnon polarization, meaning that a change from left-handed to right-handed magnons exclusively changes the sign of the signal and not its distribution. Thus, the pumped spin current due to the ISHE delivers a fingerprint for different twisted magnon modes determined by both the chirality and the topological charge of the spin wave. Current efforts are focused on utilizing the twisted beam for driving AFM structures[50–52] where we expect the topology of these beams to add an additional twist on existing AFM magnonics.

Superposed beams—proof of gate operations

In principle, the spin current density profiles shown in Figs. 6 and 7, generated by different types of magnon modes indicate the possibility of an OAM specific detection of signals. In order to close the gap between these results and the concept of parallel information transport and logic gate operations, we now proceed with numerical simulations of superpositions of different magnon modes. We perform spin dynamics calculations as before, but the cylindrical system is now excited with superimposed magnetic fields, each exciting an individual twisted magnon mode.

As an example, the superposition of beams with $\ell = \pm 1$ and positive helicity are excited in the same NiO cylinder as before. The time resolved pumped spin density is shown in Fig. 8 with the reference signal for a single $\ell = 1$ magnon in Fig. 8a. All results have in common, that the excited beams need a finite time to reach the measurement slice at 150 u.c. distance, therefore
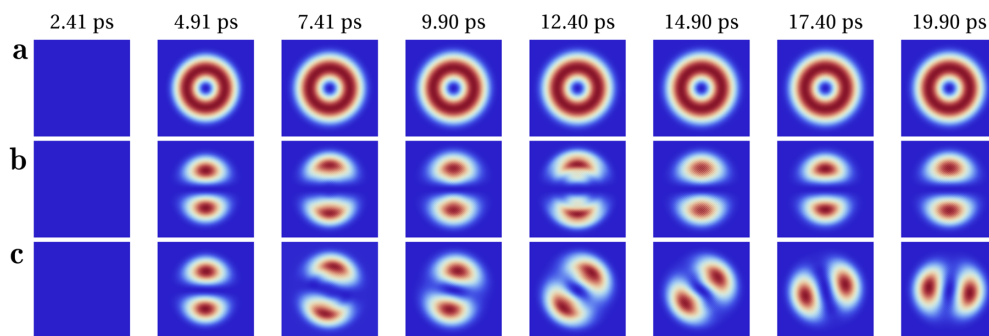
Fig. 8 Time evolution of the out-of-plane ISHE signal. Twisted magnon waves with different compositions are generated in the NiO waveguide. **a** Shows the reference signal, which is the *z*-component of the spin accumulation according to the ISHE is calculated via $\mathcal{I}_s \sim \mathbf{n} \times \partial_t \mathbf{n}$. **b** Shows the superposition of two twisted modes of opposite topological charge $\ell = \pm 1$ and (**c**) the same combination of beams but for a small difference in the frequencies: $f_1 = 0.5$ THz, $f_2 = 1.1 f_1$. The resulting pattern rotates with the beating frequency.

showing no spin accumulation at the first snapshot after 2.41ps. Next, let's consider two monochromatic beams (b, $f_1 = f_2 = 0.5$ THz) and slightly detuned beams (c, $f_1 = f_2/1.1 = 0.5$ THz). Because of the fixed phase difference in case of the monochromatic beam composition, a steady pattern in the ISHE signal is present in Fig. 8b, showing the areas of constructive and destructive interference of the spin waves in contrast to the radially symmetric result in Fig. 8a. The 10% detuned beams exhibit a time dependent phase relation, hence the whole interference pattern rotates over time with a frequency significantly lower than the excitation frequency. Ideally, the beating frequency is $f_B = 0.5|f_2 - f_1| = 0.05f_1 = 25$ GHz. Therefore, it can be utilized to overcome limitations in the time resolution of the ISHE measurement.

METHODS

Spin dynamics simulations

The predictions are generic. For a material-specific demonstration we used NiO with a material parameters as determined experimentally. For the numerical realizations to assess the analytical predictions and provide experimental guidance, we used the open-source, GPU-accelerated software package mumax3[53] for the micromagnetic simulations. Input data and more detailes are provided in the Supplementary Methods.

DATA AVAILABILITY

All data needed to reach the conclusions in the paper are present in the paper and/or the Supplementary Methods and may be requested from the authors.

CODE AVAILABILITY

The codes developed in this study are available from the authors upon reasonable request. The open-source software package mumax3 is freely available.

REFERENCES

1. Chumak, A. V., Vasyuchka, V. I., Serga, A. A. & Hillebrands, B. Magnon spintronics. *Nat. Phys.* **11**, 453–461 (2015).
2. Wang, Q. et al. A magnonic directional coupler for integrated magnonic half-adders. *Nat. Electron* **3**, 765–774 (2020).
3. Dieny, B. et al. Opportunities and challenges for spintronics in the microelectronics industry. *Nat. Electron* **3**, 446–459 (2020).
4. Kampfrath, T. Coherent Terahertz Control of Antiferromagnetic Spin Waves. *Nat. Photonics* **5**, 31–34 (2011).
5. Jungwirth, T., Martí, X., Wadley, P. & Wunderlich, J. Antiferromagnetic spintronics. *Nat. Nanotechnol.* **11**, 231–241 (2016).
6. Gomonay, O., Baltz, V., Brataas, A. & Tserkovnyak, Y. Antiferromagnetic spin textures and dynamics. *Nat. Phys.* **14**, 213–216 (2018).
7. Gomonay, E. V. & Loktev, V. M. Spintronics of antiferromagnetic systems (Review Article). *Low. Temp. Phys.* **40**, 17–35 (2014).
8. Šmejkal, L., Mokrousov, Y., Yan, B. & MacDonald, A. H. Topological antiferromagnetic spintronics. *Nat. Phys.* **14**, 242–251 (2018).
9. Jungwirth, T. et al. The multiple directions of antiferromagnetic spintronics. *Nat. Phys.* **14**, 200–203 (2018).
10. Baltz, V. Antiferromagnetic spintronics. *Rev. Mod. Phys.* **90**, 015005 (2018).
11. Fukami, S., Lorenz, V. O. & Gomonay, O. Antiferromagnetic spintronics. *J. Appl. Phys.* **128**, 070401 (2020).
12. Duine, R. A., Lee, K.-J., Parkin, S. S. P. & Stiles, M. D. Synthetic antiferromagnetic spintronics. *Nat. Phys.* **14**, 217 (2018).
13. Lavrijsen, R. et al. Magnetic ratchet for three-dimensional spintronic memory and logic. *Nature* **493**, 647 (2013).
14. Yang, S.-H., Ryu, K.-S. & Parkin, S. S. P. Domain-wall velocities of up to 750 m s^{-1} driven by exchange-coupling torque in synthetic antiferromagnets. *Nat. Nanotechnol.* **10**, 221 (2015).
15. Huang, B. Layer-dependent ferromagnetism in a van der Waals crystal down to the monolayer limit. *Nature* **546**, 270 (2017).
16. Gong, C. Discovery of intrinsic ferromagnetism in two-dimensional van der Waals crystals. *Nature* **546**, 265 (2017).
17. Xing, W. Electric field effect in multilayer $Cr_2Ge_2Te_6$: a ferromagnetic 2D material. *2D Mater.* **4**, 024009 (2017).
18. Wang, X. Raman spectroscopy of atomically thin two-dimensional magnetic iron phosphorus trisulfide ($FePS_3$) crystals. *2D Mater.* **3**, 031009 (2016).
19. Lee, J.-U. Ising-Type Magnetic Ordering in Atomically Thin $FePS_3$. *Nano Lett.* **16**, 7433 (2016).
20. Xing, W. Magnon Transport in Quasi-Two-Dimensional van der Waals Antiferromagnets. *Phys. Rev. X* **9**, 011026 (2019).
21. Kittel, C. Theory of Antiferromagnetic Resonance. *Phys. Rev.* **82**, 565 (1951).
22. Keffer, F. & Kittel, C. Theory of Antiferromagnetic Resonance. *Phys. Rev.* **85**, 329 (1952).
23. Willner, A. E. Optical communications using orbital angular momentum beams. *Adv. Opt. Photon.* **7**, 66 (2015).
24. Bozinovic, N. Terabit-Scale Orbital Angular Momentum Mode Division Multiplexing in Fibers. *Science* **340**, 1545 (2013).
25. Jia, C. L., Ma, D. C., Schäffer, A. F. & Berakdar, J. Twisted magnon beams carrying orbital angular momentum. *Nat. Commun.* **10**, 2077 (2019).
26. Chen, M., Schäffer, A. F., Berakdar, J. & Jia, C. L. Generation, electric detection, and orbital-angular momentum tunneling of twisted magnons. *Appl. Phys. Lett.* **116**, 172403 (2020).
27. Dzyaloshinsky, I. A thermodynamic theory of "weak" ferromagnetism of antiferromagnetics. *J. Phys. Chem. Solids* **4**, 241 (1958).
28. Moriya, T. Anisotropic Superexchange Interaction and Weak Ferromagnetism. *Phys. Rev.* **120**, 91 (1960).
29. Liu, Y., Sellmyer, D. J. & Shindo, D. *Handbook of Advanced Magnetic Materials* (Springer, 2006).
30. Auerbach, A. *Interacting Electrons and Quantum Magnetism* (Springer-Verlag, Inc. 1994).

31. Nakata, K., Kim, S. K., Klinovaja, J. & Loss, D. Magnonic topological insulators in antiferromagnets. *Phys. Rev. B* **96**, 224414 (2017).

32. Haldane, F. D. M. Nonlinear Field Theory of Large-Spin Heisenberg Antiferromagnets: semiclassically Quantized Solitons of the One-Dimensional Easy-Axis Néel State. *Phys. Rev. Lett.* **50**, 1153–1156 (1983).

33. Ivanov, B. A. & Kolezhuk, A. K. Solitons with Internal Degrees of Freedom in 1D Heisenberg Antiferromagnets. *Phys. Rev. Lett.* **74**, 1859 (1995).

34. Ivanov, B. A. Spin dynamics of antiferromagnets under action of femtosecond laser pulses (Review Article). *Low. Temp. Phys.* **40**, 91–105 (2014).

35. Tveten, E. G., Müller, T., Linder, J. & Brataas, A. Intrinsic magnetization of antiferromagnetic textures. *Phys. Rev. B* **93**, 104408 (2016).

36. Delfino, F., Pelissetto, A. & Vicari, E. Three-dimensional antiferromagnetic CPN-1 models. *Phys. Rev. E* **91**, 052109 (2015).

37. Cheng, R., Okamoto, S. & Xiao, D. Spin Nernst Effect of Magnons in Collinear Antiferromagnets. *Phys. Rev. Lett.* **117**, 217202 (2016).

38. Allen, L., Beijersbergen, M. W., Spreeuw, R. J. C. & Woerdman, J. P. Orbital angular momentum of light and the transformation of Laguerre-Gaussian laser modes. *Phys. Rev. A* **45**, 8185 (1992).

39. Yao, A. M. & Padgett, M. J. Orbital angular momentum: origins, behavior and applications. *Adv. Opt. Photon.* **3**, 161 (2011).

40. Uchida, M. & Tonomura, A. Generation of electron beams carrying orbital angular momentum. *Nature* **464**, 737 (2010).

41. Verbeeck, J., Tian, H. & Schattschneider, P. Production and application of electron vortex beams. *Nature* **467**, 301 (2010).

42. Clark, C. W. Controlling Neutron Orbital Angular Momentum. *Nature* **525**, 504 (2015).

43. Greenshields, C., Stamps, R. L. & Franke-Arnold, S. Vacuum Faraday effect for electrons. *N. J. Phys.* **14**, 103040 (2012).

44. Tveten, E. G., Qaiumzadeh, A. & Brataas, A. Antiferromagnetic Domain Wall Motion Induced by Spin Waves. *Phys. Rev. Lett.* **112**, 147204 (2014).

45. Tadic, M., Nikolic, D., Panjan, M. & Blake, G. R. Magnetic properties of NiO (nickel oxide) nanoparticles: blocking temperature and Neel temperature. *J. All. Comp.* **647**, 1061 - 1068 (2015).

46. Cheng, R., Xiao, J., Niu, Q. & Brataas, A. Spin Pumping and Spin-Transfer Torques in Antiferromagnets. *Phys. Rev. Lett.* **113**, 057601 (2014).

47. Nielsen, M. A. & Chuang I. L. *Quantum Computation and Quantum Information* (Cambridge University Press, 2010).

48. Coey, J. M. D. *Magnetism and magnetic materials* (Cambridge University Press, 2010).

49. Jia, C., Ma, D., Schäffer, A. F. & Berakdar, J. Twisting and tweezing the spin wave: on vortices, skyrmions, helical waves, and the magnonic spiral phase plate. *J. Opt.* **21**, 124001 (2019).

50. Cheng, R., Daniels, M. W., Zhu, J.-G. & Xiao, D. Antiferromagnetic Spin Wave Field-Effect Transistor. *Sci. Rep.* **6**, 24223 (2016).

51. Lan, J., Yu, W. & Xiao, J. Antiferromagnetic domain wall as spin wave polarizer and retarder. *Nat. Commun.* **8**, 178 (2017).

52. Qaiumzadeh, A., Kristiansen, L. A. & Brataas, A. Controlling chiral domain walls in antiferromagnets using spin-wave helicity. *Phys. Rev. B* **97**, 020402(R) (2018).

53. Vansteenkiste, A. et al. The design and verification of MuMax3. *AIP Adv.* **4**, 107133 (2014).

ADDITIONAL INFORMATION

Supplementary information The online version contains supplementary material available at https://doi.org/10.1038/s41524-021-00570-0.

Correspondence and requests for materials should be addressed to C.J. or J.B.

Reprints and permission information is available at http://www.nature.com/reprints

Publisher's note Springer Nature remains neutral with regard to jurisdictional claims in published maps and institutional affiliations.

CHAPTER 5

CONCLUSION AND OUTLOOK

The aim has been to pursue new concepts in the field of topologically non-trivial spin excitations. Using inspirational experimental and theoretical accomplishments, essential new insights to this rapidly evolving research field could be contributed.

Regarding the ultrafast manipulation of magnetic textures, it was shown that by combining sophisticated experimental techniques, like optoelectrical SOT generation, deterministic switching processes can be triggered by excitation durations on the scale of only a few picoseconds (AFS2, AFS4). In combination with the mentioned manipulation concept, a skyrmionium-based racetrack device is proposed that avoids the obstructive skyrmion Hall effect by employing a chiral quasiparticle with a vanishing total topological charge. In contrast to these two approaches based on focused electron or laser beams, a fundamentally different draft for a magnetic shift register was developed (AFS9). The necessity of global fields or currents could completely be relinquished. Instead, a local rotating edge-field is applied to wind or unwind arbitrarily mixed bit chains of skyrmions and DWs. The propulsion of the chain of information itself is driven by the repulsive interaction of the involved quasiparticles. This interaction is also the main driving mechanism for the presented results on skyrmion ensembles in confined geometries at elevated temperatures (AFS5). Two different time scales of pattern formation were identified when tracking the magnetization of such nanoislands. These characteristic times affect time-integrating experimental techniques like SP-STM measurements and push forward the branch of probabilistic and reservoir computing. These concepts offer new approaches towards brain-inspired computation like neural networks that do not rely on binary logic calculations.

The second part of the presented works brings a new *twist* to the flourishing field of magnonics, in which spin waves are utilized for computation and information transfer. Based on the developed analytical model, the existence of spin wave modes with helical wavefronts that are characterized by their topological charge was predicted (AFS6). This

additional degree of freedom allows for multiplexing signals via magnonic waveguides because of the orthogonal basis set of eigenmodes. Hence not only the frequency of a spin wave but its OAM can be used to encode information. As it was also shown that the OAM itself is robust against damping and perturbations, information can be transferred without loss. Different excitation and transformation concepts were adopted from the field of optics and their transferability to twisted spin waves was shown by large-scale micromagnetic simulations (AFS6,AFS7,AFS8). The possibility of transferring a twisted spin wave between separate waveguides via dipolar interactions was studied, which enables logic gate operations in future studies and technological applications. As a possible way to detect the outcome of a three-dimensional magnonic device, the pumped spin current at the end of a waveguide was analyzed, exhibiting characteristic fingerprints of modes with different spin wave polarizations and topological charges. Finally, the existence and usability of twisted magnon modes in AFM materials are predicted(AFS10). By this extension, not only the operating frequency reaches values up to THz, but also an additional degree of freedom opens up due to the fully controllable choice of polarization. In consequence, parallel, wave-based, topologically protected logic operations are achievable that can be detected via the ISHE.

In summary, the results on skyrmionic systems and twisted spin waves pave the way for fascinating future studies and applications in information and communication technology. Both systems offer the possibility to extend existing on-chip concepts into the third dimension. This fascinating opportunity still demands plenty of theoretical and experimental work to lead to the next era of information technology.

LIST OF PUBLICATIONS

[AFS1]   A. F. Schäffer, J. Wätzel, J. Berakdar
          Optomagnetism and ultrafast spintronics via optical vortices
          Spintronics IX **9931**, 99311B (2016)

[AFS2]   A. F. Schäffer, H. A. Dürr, J. Berakdar
          Ultrafast imprinting of topologically protected magnetic textures via pulsed
          electrons
          Appl. Phys. Lett. **111**, 3, 032403 (2017)

[AFS3]   A. F. Schäffer, L. Chotorlishvili, I. V. Maznichenko, A. Ernst, K. Dörr, I. Mer-
          tig, J. Berakdar
          Element specific hysteresis of $La_{0.7}Sr_{0.3}MnO_3$-$SrRuO_3$ (LSMO-SRO) het-
          erostructures
          APL Materials **6**, 7, 076103 (2018)

[AFS4]   B. Göbel*, A. F. Schäffer*, J. Berakdar, I. Mertig, S. S. P. Parkin
          Electrical writing, deleting, reading, and moving of magnetic skyrmioniums in
          a racetrack device
          Sci. Rep. **9**, 12119 (2019)

[AFS5]   A. F. Schäffer, L. Rózsa, J. Berakdar, E. Y. Vedmedenko, R. Wiesendanger
          Stochastic dynamics and pattern formation of geometrically confined
          skyrmions
          Commun. Phys. **2**, 1, 72 (2019)

[AFS6]   C. Jia, D. Ma, A. F. Schäffer, J. Berakdar
          Twisted magnon beams carrying orbital angular momentum
          Nat. Commun. **10**, 2077 (2019)

[AFS7]   C. Jia, D. Ma, A. F. Schäffer, J. Berakdar
          Twisting and tweezing the spin wave: on vortices, skyrmions, helical waves,
          and the magnonic spiral phase plate
          J. Opt. **21**, 124001 (2019)

[AFS8]   M. Chen, A. F. Schäffer, J. Berakdar, C. Jia

Generation, electric detection, and orbital-angular momentum tunneling of twisted magnons
Appl. Phys. Lett. **116**, 17, 172403 (2019)

[AFS9] A. F. Schäffer, P. Siegl, M. Stier, T. Posske, J. Berakdar, M. Thorwart, R. Wiesendanger, E. Y. Vedmedenko
Rotating edge-field driven processing of chiral spin textures in racetrack devices
Sci. Rep. **10**, 20400 (2020)

[AFS10] C. Jia, M. Chen, A. F. Schäffer, J. Berakdar
Chiral logic computing with twisted antiferromagnetic magnon modes
npj Comput. Mat. **7**:101 (2021)

* These authors contributed equally.

COPYRIGHT

APPENDIX

Supplementary Materials: Ultrafast imprinting of topologically protected magnetic textures via pulsed electrons

A. F. Schäffer[1], H. A. Dürr[2], J. Berakdar[1]

[1]*Institut für Physik, Martin-Luther-Universität Halle-Wittenberg,*

06099 Halle (Saale), Germany and

[2]*Stanford Institute for Materials and Energy Sciences,*

SLAC National Accelerator Laboratory,

2575 Sand Hill Road, Menlo Park, California 94025, USA

(Dated: May 27, 2017)

I. ELECTRON PULSE DRIVEN PRECESSIONAL SWITCHING OF FERRO-MAGNETIC FILMS

A. Analytical Model

To substantiate both, the experimental and numerical results, a straightforward analytical ansatz is established. Here we model the system behavior using a mono-domain, macrospin picture in the presence of spatially structured magnetic field. The moment's dynamics is governed by the Landau-Lifshitz-Gilbert equation[2, 3]

$$\frac{d\mathbf{m}}{dt} = -\frac{\gamma}{1+\alpha^2}[\mathbf{m} \times \mathbf{B}(\mathbf{r}, t)] - \frac{\alpha\gamma}{1+\alpha^2}[\mathbf{m} \times [\mathbf{m} \times \mathbf{B}(\mathbf{r}, t)]] \qquad (S1)$$

which captures the (low-energy) precessional and damped part of the spin motion. During the pulse we neglect the influence of the internal fields for simplicity. As we are dealing with only one single spin driven by the oersted-field of the electron bunch, we can simplify and separate the equations of motion for the components of $\mathbf{m}$. The generated magnetic fields of a classical electron-beam propagating in the z direction has a B_φ component only, as inferred from Biot-Savart's law in cylindrical coordinates. For the switching behavior, mainly the z component of the magnetization is relevant. Therefore, the sign of m_z after the pulse is in the focus of interest. The pulses temporal profile can, for example, be approximated by a $\sin^2$ envelope $B(t) = B_0 \sin^2(\frac{\sqrt{\pi}t}{2\delta})$ where δ denotes the pulses duration. The factor $\sqrt{\pi}/2$ is introduced for normalization reasons. The measured damping in the granular sample amounts a quite large value for the Gilbert damping-parameter $\alpha = 0.3$ the magnetization relaxes rapidly towards one of the two possible easy directions of anisotropy. The time-dependence of m_z during the pulse can be deduced to be

$$m_z(t) = \cos\left[c_1 B_0 \left(t - \tilde{\delta}\sin(t/\tilde{\delta})\right)\right] / \cosh\left[\alpha c_1 B_0 \left(t - \tilde{\delta}\sin(t/\tilde{\delta})\right)\right] , \qquad (S2)$$

with $\tilde{\delta} = \delta/\sqrt{2}$ and $c_1 = \frac{\gamma}{2(1+\alpha^2)}$ Following this result, one can compute m_z at the end of the pulse as a function of the external field value. The value $m_z(\delta)$ depending on the pulse duration and the strength of the magnetic pulse is displayed in fig. S1. As expected an alternating pattern with decreasing amplitude can be seen. Examining an ideal parameter-regime in which a switching occurs reliably, the region around $(5\,\mathrm{T}, 2\,\mathrm{ps})$ seems to be preferable because of the broad dark area. This means that the spin flip takes place even if there are small fluctuations in the pulse duration or the magnetic field amplitude.

As the Oersted-fields decay typically as $\sim \rho^{-1}$, the experimental data can be reproduced by the calculations of the final spin-orientation for the spatially varying $B_0 = B_\varphi(\rho) = B_{\mathrm{max}}/(\rho + \epsilon)$. In this part of the presented work, the focus is set on extended systems with a size ranging in the order of several hundred microns. Therefore the calculations incorporate the pulse's far field only. In order to prevent the magnetic field from a divergent behavior at the origin, a small length $\epsilon = 20\,\mathrm{nm}$ is added to the distance. In the far field this does not affect the results. Due to the radial symmetry the results can be extended by a rotation so that two-dimensional systems are modeled. The results are shown together with the numerical and experimental in the main text (Fig.1).
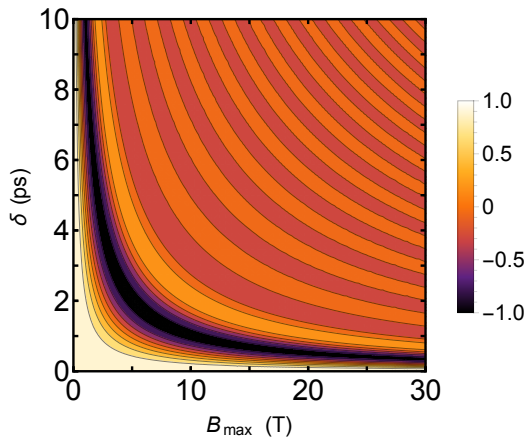

FIG. S1: Spin orientation after the magnetic pulse, depending on the amplitude B_{max} and the duration δ.

II. FULL NUMERICAL SIMULATIONS

In addition to the analytical approach, micromagnetic simulations are carried out. The material specific parameters are chosen to be equal to the measured ones ([1]), meaning a saturation magnetization $M_{\mathrm{sat}} = 517.25\,\mathrm{kA/m}$, the uniaxial anisotropy $K_{\mathrm{u}} = 156.98\,\mathrm{kJ/m^3}$ and the Gilbert damping parameter $\alpha = 0.3$.

Similar to the experimental work, we also consider a thin film of CoCrPt and a size of $150\,\mu\mathrm{m} \times 150\,\mu\mathrm{m} \times 14\,\mathrm{nm}$. As the included Co-atoms lead to a granular structure, with

decoupled magnetic grains with a size of $20.6 \pm 4\,\text{nm}$, we can model the system with discrete cells with a dimension of $(41.2 \times 41.2 \times 14)\,\text{nm}^3$. To cover the desired area we need 3640^2 cells.

In the described discretization, each simulation cell is associated with a magnetization $\mathbf{m}_i = \mathbf{M}_i/M_S$ normalized to the saturation magnetization M_S. The magnetization dynamics is governed by the Landau-Lifshitz-Gilbert equation [2, 3]

$$\dot{\mathbf{m}}_i = -\frac{\gamma}{1+\alpha^2}\left\{\mathbf{m}_i \times \mathbf{B}_i^{\text{eff}}(t) + \alpha\left[\mathbf{m}_i \times \left(\mathbf{m}_i \times \mathbf{B}_i^{\text{eff}}(t)\right)\right]\right\} \tag{S3}$$

where $\gamma = 1.76 \cdot 10^{11}\,\text{1/(Ts)}$ denotes the gyromagnetic ratio and α is the dimensionless Gilbert damping parameter. The local effective magnetic field $\mathbf{B}_i^{\text{eff}}(t)$ can be calculated following the equation $\mathbf{B}_i^{\text{eff}}(t) = -1/M_S \delta F/(\delta \mathbf{m}_i)$ and is therefore a functional of the system total free energy $F = F_{\text{EXCH}} + F_{\text{MCA}} + F_{\text{DMF}} + F_{\text{ZMN}}$. This quantity is influenced by the exchange interaction of adjacent magnetic moments $F_{\text{EXCH}} = -A/c^2 \sum_{<ij>} \mathbf{m}_i \cdot \mathbf{m}_j$, the magnetocrystalline anisotropy F_{MCA}, the demagnetizing fields F_{DMF}, and the Zeeman-energy F_{ZMN}. The MCA is typically uniaxial in nature for magnetic storage media, in the case of CoCrPt-alloys as well, with an easy axis in out-of-plane direction, which coincides with the cylindrical z-axis. Further details on the single contributions can be found for example in ref.[4]. In order to simulate the magnetization dynamics an adaptive Heun solver method has been used. As the excitation of the system takes place in a very short time scale the time step is fixed to $1\,\text{fs}$ during the time evolution, which is calculated for an elapsed time of $300\,\delta$. Afterwards the new configuration is relaxed. This means that the precessional term of the LLG is disregarded for the purpose of a fast approach towards the final stable magnetic configuration.

Full GPU-based micromagnetic simulations using the simulation package `mumax3`[5] were employed to account for the effect of demagnetizing fields efficiently. Just like in the analytical approach, the electron beam is considered as a pulsed magnetic field in φ-direction, acting on the initially homogeneously magnetized ($\mathbf{m}_i = \hat{e}_z$) sample. To account for the influence of the DMF two results are shown in Fig.1(b,c) of the main text. The first neglects the DMFs and the second accounting for them. Both have in common that in a radius-range of about $10\,\mu\text{m}$ a dark area similar to the experimental results arises, which signals a magnetization reversal in this region. The usual effect of the DMF favoring an in-plane magnetization can be seen but still the actual in-plane orientation should be investigated further, hence the

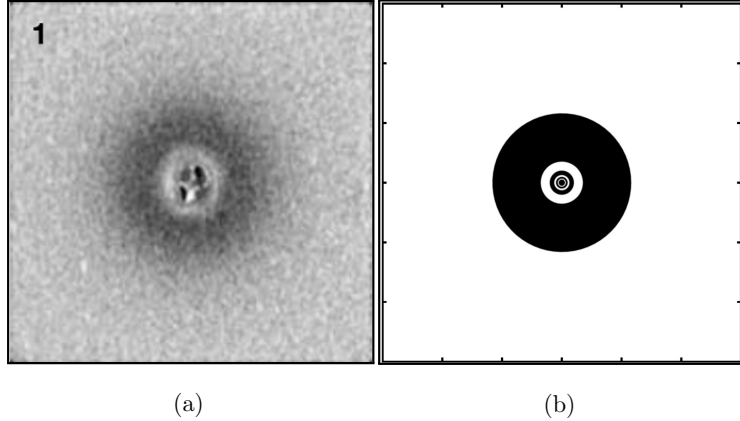measurements could only unveil the m_z component of the magnetic structure.

(a)   (b)

FIG. S2: Comparison between experimental (a) and analytical (b) results. Figures correspond to an area of $150 \times 150 \, \mu\mathrm{m}^2$. The brightness stands for the z component of the magnetization with white meaning $m_z = +\hat{e}_z$ and black $m_z = -\hat{e}_z$.

In the shown approaches the analytical and the numerical calculations are in line with each others and match well the experimental results. The simple analytical treatment neglects all kinds of effects arising due to collective phenomena. But already in this reduced picture, the ring-like domain-pattern can qualitatively be reproduced, taking into account the motion of a single spin, in the presence of the magnetic pulse. The large damping parameter was adapted from the previous works, which has been justified by arguments of spin fluctuations[1]. Nevertheless, the size of α does only affect the time needed by the system to relax towards either the spin up or down orientation. The sign of m_z after the pulse is essentially dictated by the strength of the magnetic field and its duration.

III.   MAGNETIC NEAR FIELD

Up to now, only the magnetic far field of a localized electric current has been considered. For the investigated nano disc system the finite beam size becomes important, as it is

5

currently on the same size as the nanostructures. Therefore the calculation of the magnetic near field is indispensable. Here we assume again a pulse of electrons with a Gaussian envelope in space in time. The current density in cylindrical coordinates (r, φ and z) reads as

$$j_z(r, \varphi, z) = \frac{N_e e v}{(2\pi)^{3/2} \sigma_{xy}^2 \sigma_z} \exp\left[-\frac{1}{2}(r/\sigma_{xy})^2 - \frac{1}{2}((z - tv)/\sigma_z)^2 \right] . \quad \text{(S4)}$$

Here N_e corresponds to the number of electrons, e is the electron charge, v the average velocity and σ_{xy} and σ_z are the standard deviations in the related directions. The field's profile resulting from Biot-Savart's law

$$\mathbf{B}(\mathbf{r}) = \frac{\mu_0}{4\pi} \int_V \mathbf{j}(\mathbf{r'}) \times \frac{\mathbf{r} - \mathbf{r'}}{|\mathbf{r} - \mathbf{r'}|^3} dV' \quad \text{(S5)}$$

is shown in fig. S3 for two different sets of parameters. The curves shapes are almost the same, as in both cases the radial extension of the beam is much smaller than the standard deviation in the propagation direction. If this is changed the profiles do change as well. The peak field strength for the $30\,\mu$m beam is ten times smaller than the other pulse. This can be deduced from the number of electrons being a hundred times larger, but contrary the beam width is a thousand times wider, which leads to a resulting factor of 10.
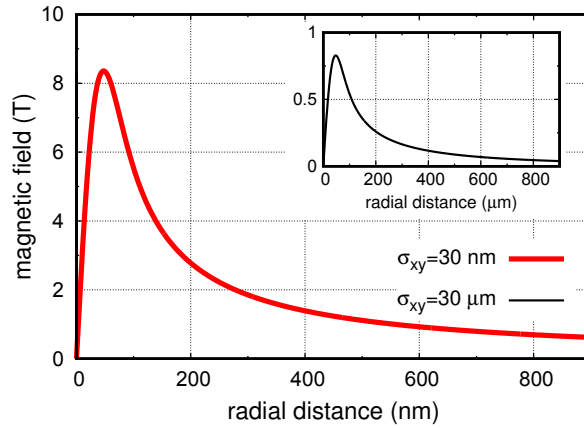

FIG. S3: Radial dependence of the peak magnetic field for a pulse duration of $\sigma_t = 2.3\,$ps. The red curve corresponds to $\sigma_{xy} = 30\,$nm and $N_e = 10^8$, whereas the black line relates to $\sigma_{xy} = 30\,\mu$m and $N_e = 10^{10}$.

[1] I. Tudosa, C. Stamm, A.B. Kashuba, F. King, H.C. Siegmann, J. Stöhr, G. Ju, B. Lu, and D. Weller, Nature **428**, 6985 (2004).

[2] L.D. Landau and E.M. Lifshitz, Phys. Z. Sowietunion **8**, 135 (1935).

[3] T.L. Gilbert, Physical Review **100**, 1243 (1955).

[4] A. Sukhov, P.P. Horley, J. Berakdar, A. Terwey, R. Meckenstock, and M. Farle, IEEE Transactions on Magnetics **50**, 12 (2014).

[5] A. Vansteenkiste, J. Leliaert, M. Dvornik, M. Helsen, F. Garcia-Sanchez, and B. Van Waeyenberge, AIP Advances **4**, 107133 (2014).

Electrical writing, deleting, reading, and moving of magnetic skyrmioniums in a racetrack device — Supplementary information —

Börge Göbel,[1] Alexander F. Schäffer,[2] Jamal Berakdar,[2] Ingrid Mertig,[1,2] and Stuart S. P. Parkin[1]

[1]*Max-Planck-Institut für Mikrostrukturphysik, D-06120 Halle (Saale), Germany*
[2]*Institut für Physik, Martin-Luther-Universität Halle-Wittenberg, D-06099 Halle (Saale), Germany*

In this Supplementary information we show five additional figures which were mentioned in the main paper. In Supplementary Fig. 1 we show the skyrmionium-skyrmionium interaction potential. In Supplementary Fig. 2 the current dependence of the skyrmionium velocity is analyzed. Supplementary Fig. 3 visualizes an optoelectrically generated skyrmionium at room temperature. In Supplementary Fig. 4 we analyze the skyrmionium generation process for different writing parameters. Finally, in Supplementary Fig. 5 the skyrmionium stability and current-driven motion are shown for different DMI constants. More information is given in the caption of the respective figure.
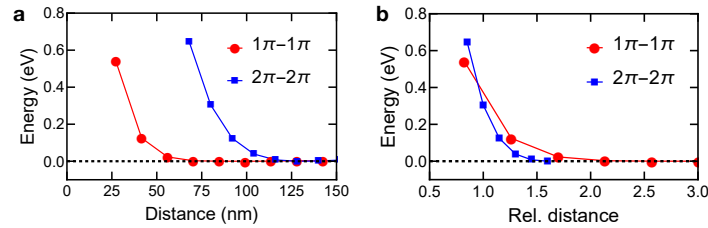

Supplementary Fig. 1: **Repulsive potential energies between magnetic quasiparticles.** The skyrmion-skyrmion ($1\pi-1\pi$) and skyrmionium-skyrmionium ($2\pi-2\pi$) interaction energies have been extracted from micromagnetic simulations of an unconfined system (periodic boundary conditions in the plane). The distance dependence is obtained from pinning the centers of the two interacting quasiparticles at different distances and subsequent relaxation of the magnetization configuration. **a** For both objects, the potential decays rapidly for distances larger than the intrinsic size of the objects (skyrmion: $\approx 33\,$nm; skyrmionium: $\approx 80\,$nm). **b** As panel a but the distance is normalized by the size of the respective particles.
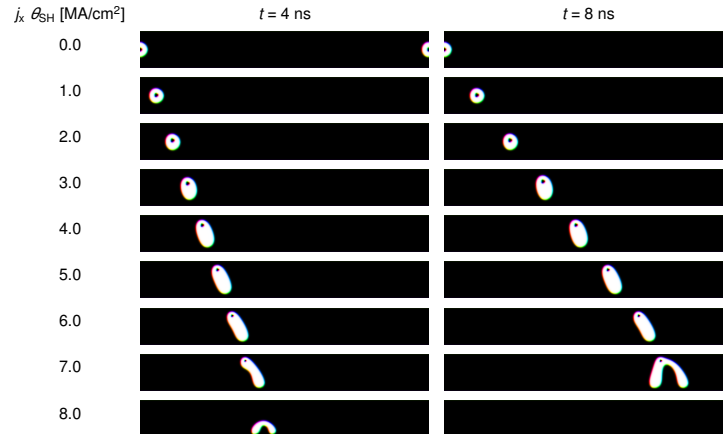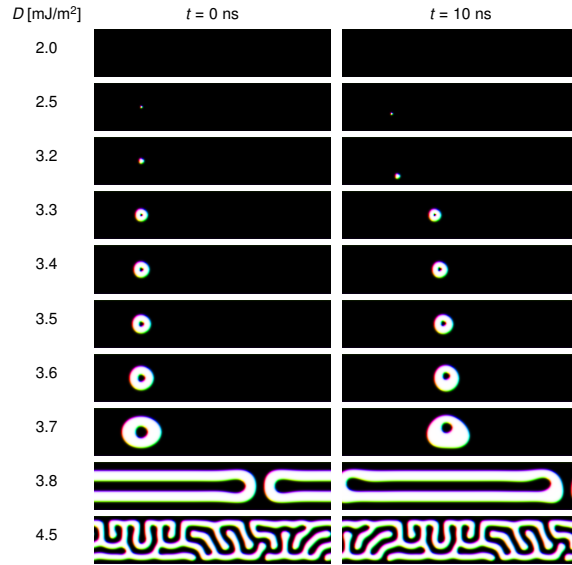

Supplementary Fig. 2: **Current dependence of skyrmionium velocity.** The left column indicates the simulated configuration after $4\,$ns and the right column after $8\,$ns of propagation time. The applied current density increases linearly from the top to the bottom row. The skyrmionium velocity increases nearly linearly until an effective current density $j_x\theta_{\mathrm{SH}}$ of around $6\,\mathrm{MA/cm}^2$ is reached. The skyrmionium velocity is approximately $140\,$m/s in this case. For higher values the skyrmionium strongly deforms, transitions to a skyrmion and annihilates. A utilization in the context of a racetrack storage is not possible anymore. The simulated racetrack has the dimensions $1600\,\mathrm{nm} \times 200\,\mathrm{nm} \times 1\,\mathrm{nm}$ with periodic boundary conditions along the racetrack direction.
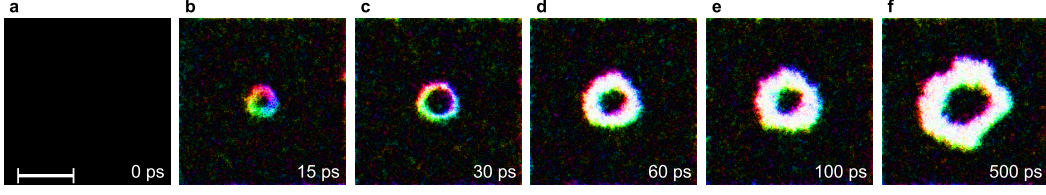
Supplementary Fig. 3: **Skyrmionium generation at room temperature.** Similar to Fig. 2 of the paper but for $T = 300\,$K. The system size is increased to an area of $300\,$nm $\times\,300\,$nm $\times\,1\,$nm to show the stability of the skyrmionium without an additional stabilization by the boundary. All other parameters are equal to the ones used in the main text. The scale bar corresponds to $100\,$nm.
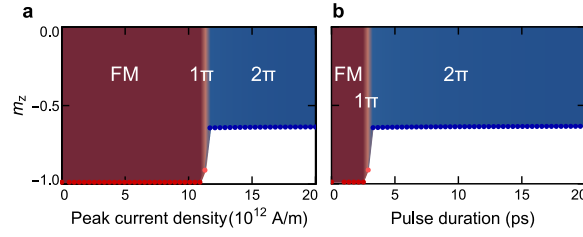
Supplementary Fig. 4: **Analysis of the writing parameters.** Resulting spin configuration in dependence of **a** the peak current density and **b** the pulse duration. The final state is characterized by the averaged z component of the magnetization, indicating a collinear ferromagnetic state (FM), a skyrmion (1π) or a skyrmionium (2π). Due to the different sizes of skyrmion and skyrmionium, the net magnetization allows to distinguish them. For both writing parameters a threshold needs to be overcome to reliably create skyrmioniums. For **a** the FWHM pulse duration is fixed to $9\,$ps, **b** assumes a fixed peak current density of $2 \times 10^{13}\,$A m^{-1}. Both values correspond to the parameters used in the paper.

Supplementary Fig. 5: **DMI dependence of skyrmionium stability and current-driven motion.** The left column shows the relaxed texture and the right column shows the texture after a propagation for $10\,$ns under the influence of an effective current density of $j_x\theta_{\mathrm{SH}} = 1\,$MA/cm^2. The DMI constant D increases from the top to the bottom row as indicated. The skyrmionium is stable for D between $3.3\,$mJ/m^2 and $3.7\,$mJ/m^2. The simulated racetrack has the dimensions $1000\,$nm $\times\,200\,$nm $\times\,1\,$nm with periodic boundary conditions along the racetrack direction.

Supplementary material: Rotating edge-field driven processing of chiral spin textures in racetrack devices

Alexander F. Schäffer,[1,2] Pia Siegl,[3] Martin Stier,[3] Thore Posske,[3] Jamal Berakdar,[1] Michael Thorwart,[3] Roland Wiesendanger,[2] and Elena Y. Vedmedenko[2]

[1]*Institute of Physics, Martin-Luther-Universität Halle-Wittenberg, D-06120 Halle (Saale), Germany*

[2]*Department of Physics, Universität Hamburg, D-20355 Hamburg, Germany*

[3]*I. Institute for Theoretical Physics, Universität Hamburg, D-20355 Hamburg, Germany*

A. ATOMISTIC SIMULATIONS ON A MONOLAYER WITH AN HCP(111) STACKING

For the systems, discussed in the main text, we have used a discretization into cubic simulation cells. However, ultrathin films such as the Pd/Fe bilayer on Ir(111) typically grow in hexagonal close-packed (hcp) stacking. Here, we strictly use the hcp structure of magnetic adatoms and show the applicability of the presented writing and deleting mechanism also to these cases. Additionally, the skyrmions are stabilized by a combination of the DMI and the geometric confinement entering as fixed boundary conditions. This represents another example of nanometer sized skyrmions in the absence of global magnetic fields.

For the atomistic simulations, classical Heisenberg magnetic moments $\mathbf{S_i} = (S_i{}^x, S_i{}^y, S_i{}^z)$ of unit length $\boldsymbol{\mu}_i/\mu_{\mathrm{s}}$ are placed at each lattice point. The energy of the system is given by the Hamiltonian

$$\mathcal{H} = -J\sum_{\langle ij\rangle} \mathbf{S}_i \cdot \mathbf{S}_j - \sum_{\langle ij\rangle} \mathbf{D}_{ij} \cdot (\mathbf{S}_i \times \mathbf{S}_j) - B_z \sum_i S_z - \sum_i \mathbf{B}_i(t) \cdot \mathbf{S}_i - K_z \sum_i (S_i^z)^2, \quad (1)$$

where $J > 0$ is the ferromagnetic exchange coupling between nearest neighbors, $\mathbf{D}_{ij}$ is the DMI vector, B_z is a global magnetic field, K_z is the perpendicular magnetic anisotropy and $\mathbf{B}_i(t)$ is a local space- and time-dependent magnetic field. The material parameters were set to $K_z = 0.05\,J$, $D = 0.07\,J$ and the magnetic moments at the edges are fixed to $\mathbf{S} = \hat{\mathbf{e}}_z$ to stabilize skyrmions in the absence of an additional external field. The spins at $x = 0$ were rotated parametrically. The time scale in these calculations can be expressed by $dt = \tau\mu_s/\gamma J$ with the reduced time step τ and the gyromagnetic ratio γ. For $\mu_s = 2\mu_B$, $J = 5.72$ meV and $\tau = 0.01$ a simulation step corresponds to the time span of $\approx 10^{-14}$ s. The frequency of rotation at the edge of the stripe was varied between 1 and 10 GHz. The propagation velocities were similar to those found in micromagnetic simulations.

The dynamics of the free spins is determined by the LLG equation

$$\dot{\mathbf{m}}_i(t) = -\frac{\gamma}{1+\alpha^2} \left[\mathbf{m}_i \times \mathbf{B}_i^{\mathrm{eff}} + \alpha\mathbf{m}_i \times \left(\mathbf{m}_i \times \mathbf{B}_i^{\mathrm{eff}}\right) \right] \ , \tag{2}$$

with the effective magnetic field

$$\mathbf{B}_i^{\mathrm{eff}} = -\frac{\partial\mathcal{H}}{\mu_s \partial\mathbf{S}_i} \ . \tag{3}$$

Fig. S1 shows a sequence of snapshots of the creation and deletion of magnetic skyrmions using atomistic LLG simulations on a triangular lattice with 8×100 spins. The excited

line of magnetic moments is visualized by the gray screw, also indicating the rotational sense. As shown in the micromagnetic simulations presented in the main text, skyrmions can be injected into the sample. In Fig. S2 the spins along the screw are rotated in opposite direction. Particularly interesting is that the rotation against the DMI chirality destroys skyrmions only on one side of the excited line as can be seen in time steps t_3 to t_6 of Fig. S2. In conclusion, this shows that skyrmions stabilized by DMI and fixed boundary conditions can be created and annihilated similar to the open systems discussed in the main text. Furthermore, the hexagonal lattice has no fundamental impact on the proposed control mechanism.
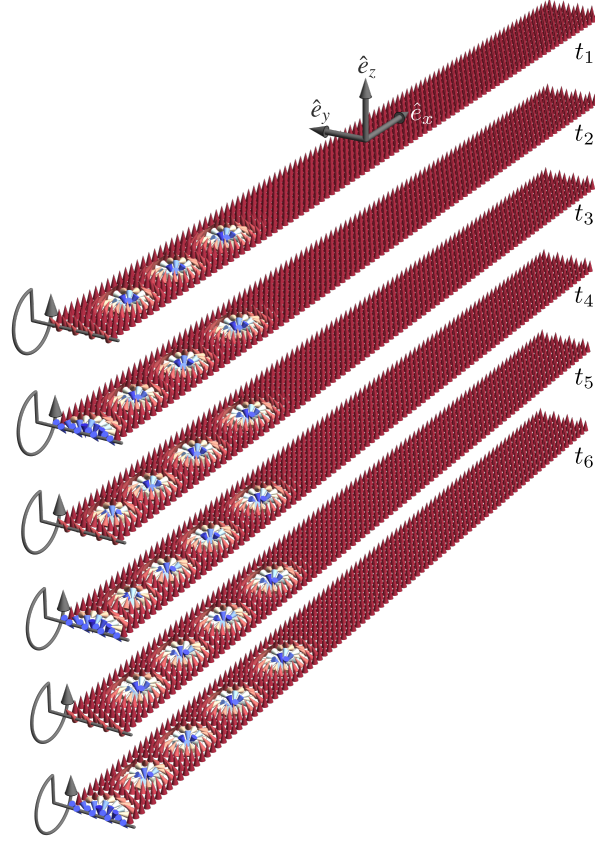
Fig. S1. Skyrmion creation in a magnetic stripe from atomistic simulations. Snapshots corresponding to the writing of individual skyrmions by a local rotating edge-field following the chirality of Dzyaloshinskii-Moriya interaction.
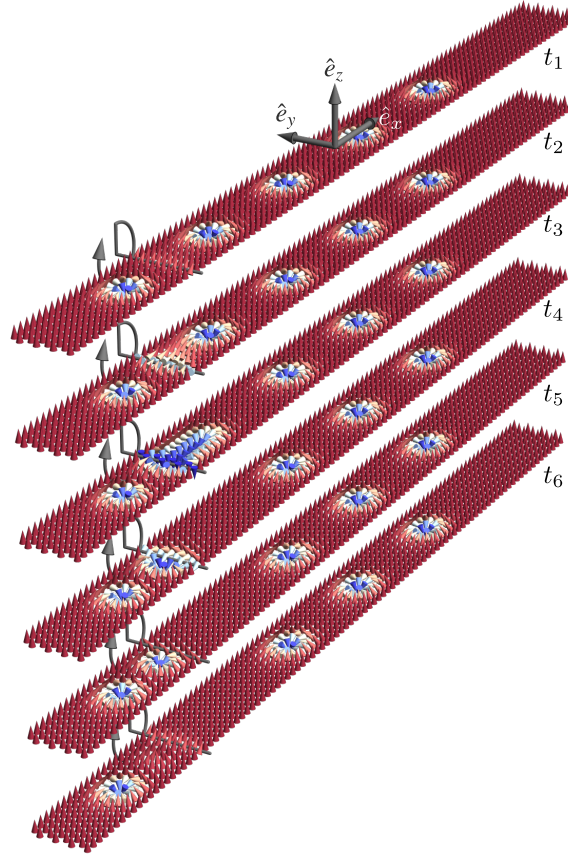
4

Fig. S 2. Skyrmion deletion in a magnetic stripe from atomistic simulations. Local rotating edge-field opposite to the rotational sense in Fig. S1 leads to the deletion of a skyrmion in $+x$ direction.

B. PHASE DIAGRAM OF SKYRMION CREATION FOR GAUSSIAN ROTATION

The creation processes of either domain walls or skyrmions discussed in the main paper have been modeled by a simplified rotation scheme, namely a uniform rotation of a distinct number of involved edge magnetic moments due to a rotating magnetic field. While for domain walls this intuitively is the optimal scheme, a rotation respecting the intrinsic circular form of skyrmions is a more adequate skyrmion creation process. As we will show in the following, such a tailored rotation allows for higher creation rates, which in the context of information technologies is a desirable goal.

We study the general properties of the skyrmion creation and compare different rotation schemes of a model system. To this end, we consider a square lattice of 128 x 128 lattice sites with ferromagnetic boundary conditions and system parameters of $A_{\mathrm{exch}} = 0.69$ pJ m^{-1}, $D = 0.267$ mJ m^{-2} and $B = 0.0864$ T. Here, the ground state is the ferromagnetic state, with all magnetic moments pointing in $+z$-direction. Furthermore, we directly rotate the magnetic moments at the edge of the sample at $x = 0$ which reflects the limits of sufficiently large magnetic fields. Considering the uniform rotation of all involved boundary moments, the maximum rotation frequency resulting in a stable skyrmion depends on the number of rotated edge moments, see Fig. S3(b). An optimum is found for 20 to 60 rotated moments where a rotation with maximum frequency of $\nu = 12.5$ GHz can create a stable skyrmion.

A skyrmion creation by a uniform rotation is only possible due to the directional sense of the DMI inclining the outer moments towards the outside, such that a circular structure is formed. The creation speed is therefore determined by this process. However, it can be increased if the inclination of the moments is itself induced by the rotation. A significant improvement is achieved by a tailor-made rotation which we call the Gauss rotation. The name and rotation protocol are motivated by the z-component of the normalized magnetization m_z of the cross section of a skyrmion which can approximately be fitted by a shifted Gauss function, i.e.

$$m_z(y) = -2 \exp\left[-\left(\frac{y - y_0}{\sigma}\right)^2\right] + 1. \tag{4}$$

Here σ is a measure of the width of the Gauss distribution, y refers to the position of the magnetic moment and y_0 to the center of the skyrmion, coinciding in the following with the center of the edge. Fig. S3(a) illustrates the scheme of the Gauss rotation. The moments

(black arrows) rotate around the spatially dependent rotation axis (red arrow) and are depicted in their initial state (dashed line) and after half a rotation (continuous line). The angle φ between $\mathbf{m}(t = 0)$ and $\mathbf{m}(t = \frac{T}{2})$, T being the period of the rotation, depends on the Gauss function in equation 5, namely

$$\cos(\varphi(y)) = -2 \exp\left[-\left(\frac{y - y_0}{\sigma}\right)^2\right] + 1. \tag{5}$$

Using this rotation, we find the creation diagram of the Gauss rotation, see Fig. S3(c). The Gauss rotation yields the possibility of skyrmion creation at significantly higher frequencies up to 20.8 GHz, i.e., a creation of a skyrmion within 50 ps, for an optimal Gauss width $\sigma = 20$. This underlines the increased efficiency of the rotation, if it adequately forms the skyrmion shape.
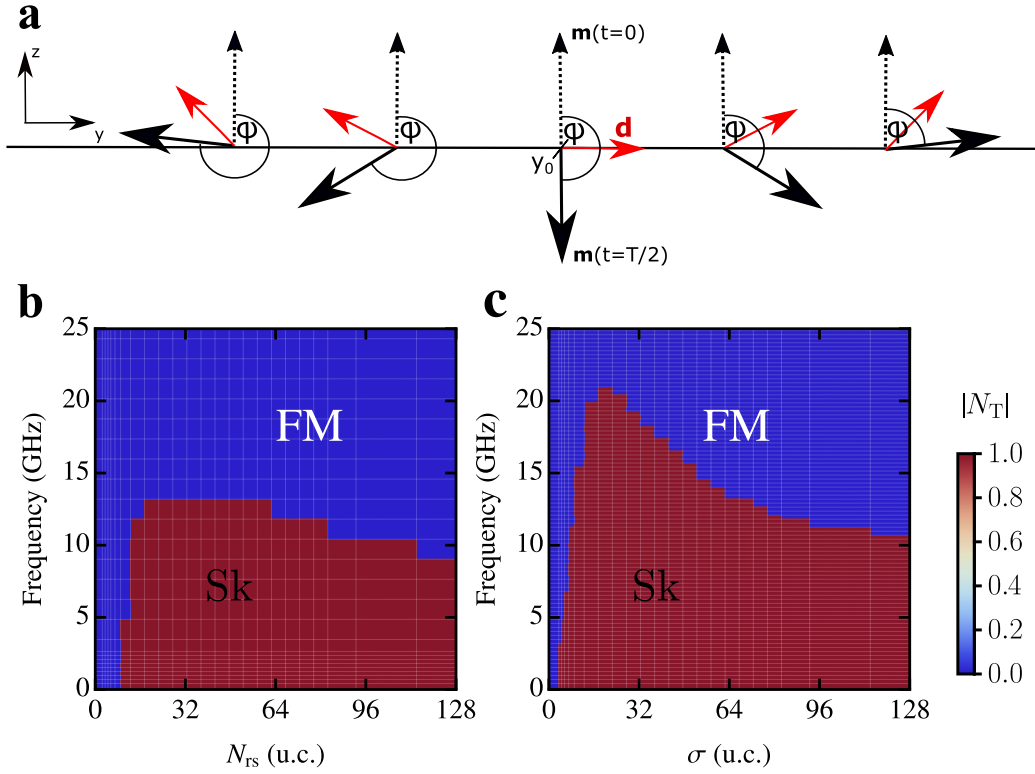
Fig. S 3. (a) Scheme of the Gauss rotation. The magnetization **m** is depicted for the initial state (black dashed arrow) and after half a rotation (black arrow) around the spatially dependent rotation axis (red arrow). (b,c) Phase diagrams of the creation of a single skyrmion by either the uniform (b) rotation or the Gauss rotation (c). Depicted is the absolute value of the topological charge in dependence of the number of the rotated magnetic moments N_{rs} (uniform rotation) or the Gaussian width σ (Gauss rotation) and the rotation frequency ν. The skyrmion is created at the end of a complete rotation, but as some will annihilate, the diagram depicts the stable solution after a sufficiently large time after the rotation.

C. DESCRIPTIONS OF THE VIDEOS

Supplementary Video 1: Skyrmion and domain wall creation in a Pd/Fe/Ir(111) stripe. Real-space dynamics of the skyrmion and DW creation. For the skyrmion the field is applied to two thirds of the width of the stripe. In the case of the DW, the full edge is affected by the field. The lower panel of the animation shows the out-of-plane component of the magnetization along the x-direction. System size: $100 \times 30 \times 1c^3$, $c = 0.233$ nm, with material parameters for Pd/Fe/Ir(111); $\nu = 2$ GHz, $B = 10$ T.

Supplementary Video 2: Continuous skyrmion creation in a Pd/Fe/Ir(111) stripe. Real-space magnetization dynamics steered by a continuously rotating effective field at the left edge of the stripe. The skyrmion density increases until the sample is saturated and no further skyrmions can be induced without destroying previously generated quasiparticles. System size: $100 \times 30 \times 1c^3$, $c = 0.233$ nm, with material parameters for Pd/Fe/Ir(111); $\nu = 2$ GHz, $B = 2.5$ T.

Supplementary Video 3: Creation of a mixed sequence of DWs and skyrmions in a Pd/Fe/Ir(111) stripe. Starting from a field-polarized state, multiple different field operations are performed to generate a mixed sequence of skyrmions and DWs. The only parameter varied to create either a skyrmion or a DW is the field amplitude with $B_{\mathrm{Sk}} = 2.5$ T and $B_{\mathrm{DW}} = 3.5$ T according to (Fig. 1(e)) of the main text. System size: $100 \times 30 \times 1c^3$, $c = 0.233$ nm, with material parameters for Pd/Fe/Ir(111); $\nu = 2$ GHz.

Supplementary Video 4: Skyrmion creation and annihilation in a Pd/Fe/Ir(111) stripe. Starting from a field-polarized state, two writing operations and one deletion with reversed rotational sense of the external field are performed. System size: $60 \times 30 \times 1c^3$, $c = 0.233$ nm, with material parameters for Pd/Fe/Ir(111); $\nu = 2$ GHz, $B = 2.5$ T

# Supplementary information: Stochastic dynamics and pattern formation of geometrically confined skyrmions

(Dated: May 28, 2019)

SUPPLEMENTARY METHODS

Calculation of the skyrmion-skyrmion and skyrmion-boundary interaction potentials. For the calculation of the potential, the total energy of a stripe-shaped model system ($75 \times 30 \times 0.4\,\text{nm}^3$) was investigated with micromagnetic simulations for two different cases. In the first case, Neumann boundary conditions were used along the long side, and a homogeneous magnetization was relaxed leading to a canted rim. Afterwards a skyrmion was added to the system at a certain distance from the boundary. Because of the repulsive nature of the interaction, a standard relaxation of the skyrmion position was not suitable for determining the distance dependence. Instead, we fixed the central magnetic moments in the skyrmion (in a circular region of $0.9\,\text{nm}$ diameter) at a specific position and relaxed the magnetic texture in the other cells. Analogously, in the second case the skyrmion-skyrmion interaction was calculated by fixing one skyrmion and changing the position of the other skyrmion, using periodic boundary conditions along both directions in the plane. From the obtained total energies we subtracted a reference spectrum for a homogeneously magnetized periodic surrounding around the skyrmion fixed at different positions in the mesh. Small deviations arising due to the finite mesh are mostly canceled out by this procedure.

The results for the interaction strengths are shown in Supplementary Fig. 1. A smooth energy function rapidly decaying with increasing distance between skyrmion and boundary is obtained. For small distances between the boundary and a skyrmion or between two skyrmions, a deformation of the quasiparticles is visible in the micromagnetic simulations, also leading to a bending of the potential in Supplementary Fig. 1. During the construction of the quasiparticle model it is assumed that the thermal energy $k_\text{B}T$ is lower than the energy value where the potential function starts to bend, which is around $5\,\text{meV}$ ($60\,\text{K}$) for the skyrmion-skyrmion interaction potential in Supplementary Fig. 1. In this regime it can be assumed that for sufficiently short simulation times the strong deformation of the skyrmions due to the interactions becomes exceedingly rare, and the basic spin structure is maintained. This temperature regime is in reasonable qualitative agreement with the range where the escape, collapse or creation of skyrmions may also be excluded, discussed in detail in Fig. 3 of the main text. It was shown in Ref.[1] that the interaction potentials in this regime may be approximated

by the exponential model function $E(r) = a\exp(-r/b)$. This is confirmed by the simulation results in Supplementary Fig. 1, with the fitted model parameters $a = 0.211\,\text{meV}$,
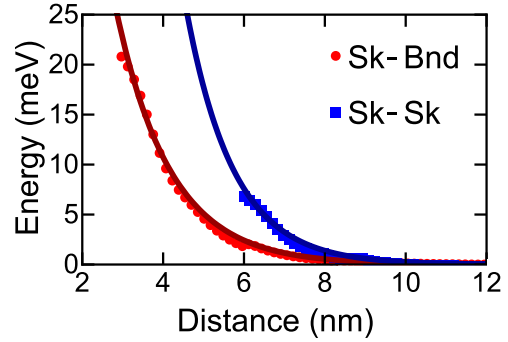
Supplementary Fig. 1. **Potential energy depending on the skyrmion-skyrmion and skyrmion-boundary distance.** Micromagnetic interaction energies between skyrmion and skyrmion (blue squares), and between skyrmion and boundary (red circles) on a finite nanoisland. Solid lines display exponential fits based on the model function $E(r) = ae^{-r/b}$; the fitting parameters are skyrmion-boundary (Sk-Bnd): $a = 0.211\,\text{meV}$, $b = 1.343\,\text{nm}$; skyrmion-skyrmion (Sk-Sk): $a = 1.246\,\text{meV}$, $b = 1.176\,\text{nm}$.

$b = 1.343\,\text{nm}$ for skyrmion-boundary (Sk-Bnd) repulsion and $a = 1.246\,\text{meV}$, $b = 1.176\,\text{nm}$ for skyrmion-skyrmion (Sk-Sk) interaction. The similar characteristic length scales b between the two cases support that the same physical mechanism is responsible for the interactions, namely the formation of chiral noncollinear spin structures due to the DMI as discussed in the main text. The different values of the parameter a can be reformulated as a shift of the exponential function along the r axis. While this distance is measured between two magnetization cells pointing oppositely to the homogeneous background in the case of two skyrmions, in the case of the skyrmion-boundary repulsion it is measured between the center of the skyrmion and the magnetization at the edge which is only slightly tilted from the homogeneous background, meaning that the same interaction strength is reached at a smaller distance in the latter scenario.

─────────────────────────────────

Supplementary references

[1] Lin, S.-Z., Reichhardt, C., Batista, C. D. & Saxena, A. Particle model for skyrmions in metallic chiral magnets: Dynamics, pin-ning, and creep. *Phys. Rev. B* **87**, 214419 (2013).

Supplementary Information: Chiral logic computing with twisted antiferromagnetic magnon modes

Chenglong Jia,[1, *] Min Chen,[1] Alexander F. Schäffer,[2] and Jamal Berakdar[2, †]

[1]*Key Laboratory for Magnetism and Magnetic Materials of the Ministry of Education &*
Lanzhou Center for Theoretical Physics, Lanzhou University, Lanzhou 730000, China
[2]*Institut für Physik, Martin-Luther-Universität Halle-Wittenberg, 06099 Halle (Saale), Germany*

SUPPLEMENTARY METHODS

For the micromagnetic calculations the GPU-accelerated, open-source software package `mumax3` [3] is used to solve the Landau-Lifhshitz-Gilbert equation

$$\dot{\mathbf{S}}_i(t) = -\frac{\gamma}{1+\alpha^2}\left[\mathbf{S}_i \times \mathbf{B}_i^{\mathrm{eff}} + \alpha\mathbf{S}_i \times \left(\mathbf{S}_i \times \mathbf{B}_i^{\mathrm{eff}}\right)\right] \ , \tag{1}$$

for every simulation cell $\mathbf{S}_i$ of the discretized vector field of the magnetization. Here, $\gamma_0 = 1.76\times10^{11}(\mathrm{T}^{-1}\mathrm{s}^{-1})$ denotes the gyromagnetic ratio of an electron, α is the Gilbert damping parameter. The time- and space-dependent effective magnetic field,

$$\mathbf{B}_i^{\mathrm{eff}}(t) = \mathbf{B}_i^{\mathrm{ext}} + \mathbf{B}_i^{\mathrm{ex}} + \mathbf{B}_i^{\mathrm{a}} \ , \tag{2}$$

is composed of the external field $\mathbf{B}_i^{\mathrm{ext}}$; exchange interaction field $\mathbf{B}_i^{\mathrm{exch}} = 2A_{\mathrm{ex}}/M_{\mathrm{s}}\Delta\mathbf{S}_i$, with A_{ex} the exchange stiffness and M_{s} the saturation magnetization; uniaxial magnetocrystalline anisotropy field $\mathbf{B}_i^{\mathrm{a}} = 2K_{\mathrm{u}}/M_s m_z\mathbf{e}_z$, with K_{u} the anisotropy constant. The spatial profile of the excitation field applied at the $z = 20$ u.c. layer reads $\mathbf{B}_\ell(\rho, \phi, t) = \Re\left\{\hat{\mathbf{e}}B_{\mathrm{max}}(\frac{\rho}{w_0})^{|\ell|}\exp\left[\frac{|\ell|}{2}\left(1-\frac{\rho^2}{w_0^2}\right)\right]\exp\left[-i(t\omega_{\mathrm{B}}+\ell\phi)\right]\right\}$. The waist parameter w_0 denotes the distance of maximum field strength B_{max}, $\hat{e}$ corresponds to the polarization vector, $w_0 = 14$ nm, $B_{\mathrm{max}} = 10$ mT. For the few cycle wave packets the magnetic field has a $\sin^2$ envelope covering N cycles of period T: $\tilde{\mathbf{B}}_\ell = \sin^2\left(\omega_{\mathrm{B}}t/(NT)\right)\mathbf{B}_\ell(\rho, \phi, t)$. We note, that such structured fields are now available in integrated photonics [5–9] . The used material parameters read: $M_{\mathrm{s}} = 125$ kA/m, $A_{\mathrm{ex}} = -0.5$ pJ/m [1], $\alpha = 2.1\times10^{-4}$ [4], $K_{\mathrm{u}} = 8$ kJ/m³ [2].

The micromagnetic simulations involve the full dynamics of both sublattices. In order to extract significant information, it is expedient to return to the picture of staggered AFM order parameter $\mathbf{n}$. We calculate $\mathbf{n}$ on the cubic simulation grid at each lattice site

$$\begin{aligned}\mathbf{n}_{\mathrm{ijk}} = \frac{(-1)^{i+j+k}}{2S}\Big[&\mathbf{S}_{\mathrm{ijk}} - \frac{1}{6}(\mathbf{S}_{\mathrm{ijk+1}} + \mathbf{S}_{\mathrm{ijk-1}}\\ &+\mathbf{S}_{\mathrm{ij+1,k}} + \mathbf{S}_{\mathrm{ij-1,k}} + \mathbf{S}_{\mathrm{i+1,jk}} + \mathbf{S}_{\mathrm{i-1,jk}})\Big]\ . \end{aligned} \tag{3}$$

Subsequently, the ISHE can be evaluated following $\mathcal{I}_{\mathrm{s}} \sim \mathbf{n} \times \partial_{\mathrm{t}}\mathbf{n}$.

---

[1] Tveten, E. G., Qaiumzadeh, A. & Brataas, A. Antiferromagnetic Domain Wall Motion Induced by Spin Waves. *Phys. Rev. Lett.* **112**, 147204 (2014).

[2] Tadic, M., Nikolic, D., Panjan, M., & Blake, G. R. Magnetic properties of NiO (nickel oxide) nanoparticles: Blocking temperature and Neel temperature. *J. All. Comp.* **647**, 1061 - 1068 (2015).

[3] Vansteenkiste, A. *et al.* The design and verification of MuMax3. *AIP Advances* **4**, 107133 (2014).

[4] Kampfrath, T. *et al.* Coherent Terahertz Control of Antiferromagnetic Spin Waves. *Nat. Phot.* **5**, 31-34 (2011).

[5] Strain, M. J. *et al.* Fast electrical switching of orbital angular momentum modes using ultra-compact integrated vortex emitters. *Nat. Commun.* **5**, 4856 (2014).

---

* cljia@lzu.edu.cn

† jamal.berakdar@physik.uni-halle.de

[6] Zhang, J. *et al.* An InP-based vortex beam emitter with monolithically integrated laser. *Nat. Commun.* **9**, 2652 (2018).

[7] Cai, X. *et al.* Integrated compact optical vortex beam emitters. *Science* **33**, 363-366 (2012).

[8] Li, H. *et al.* Orbital angular momentum vertical-cavity surface-emitting lasers. *Optica* **2**, 547-552 (2015).

[9] Liu, J. *et al.* Direct fiber vector eigenmode multiplexing transmission seeded by integrated optical vortex emitters. *Light: Science & Applications* **7**, 17148 (2018)

BIBLIOGRAPHY

[1] C. Abert et al. "A fast finite-difference method for micromagnetics using the magnetic scalar potential". In: *IEEE Trans. Magn.* 48.3 (2011), pp. 1105–1109.

[2] Y. Aharonov and A. Casher. "Topological quantum effects for neutral particles". In: *Phys. Rev. Lett.* 53.4 (1984), p. 319.

[3] L. Allen et al. "Orbital angular momentum of light and the transformation of Laguerre-Gaussian laser modes". In: *Phys. Rev. A* 45.11 (1992), p. 8185.

[4] M. N. Baibich et al. "Giant magnetoresistance of (001) Fe/(001) Cr magnetic superlattices". In: *Phys. Rev. Lett.* 61.21 (1988), p. 2472.

[5] M. Beg et al. "Ground state search, hysteretic behaviour, and reversal mechanism of skyrmionic textures in confined helimagnetic nanostructures". In: *Sci. Rep.* 5 (2015).

[6] L. Berger. "Low-field magnetoresistance and domain drag in ferromagnets". In: *J. Appl. Phys.* 49.3 (1978), pp. 2156–2161.

[7] M. V. Berry. "Quantal phase factors accompanying adiabatic changes". In: *Proc. R. Soc. A* 392.1802 (1984), pp. 45–57.

[8] P. F. Bessarab et al. "Lifetime of racetrack skyrmions". In: *Sci. Rep.* 8.1 (2018), pp. 1–10.

[9] G. Binasch et al. "Enhanced magnetoresistance in layered magnetic structures with antiferromagnetic interlayer exchange". In: *Phys. Rev. B* 39.7 (1989), p. 4828.

[10] F. Bloch. "Zur theorie des austauschproblems und der remanenzerscheinung der ferromagnetika". In: *Zur Theorie des Austauschproblems und der Remanenzerscheinung der Ferromagnetika*. Springer, 1932, pp. 295–335.

[11] P. Błoński and J. Hafner. "Density-functional theory of the magnetic anisotropy of nanostructures: an assessment of different approximations". In: *J. Condens. Matter Phys.* 21.42 (2009), p. 426001.

[12] A. Bogdanov and A Hubert. "Thermodynamically stable magnetic vortex states in magnetic crystals". In: *J. Magn. Magn. Mater.* 138.3 (1994), pp. 255–269.

[13]   A. N. Bogdanov and U. Rößler. "Chiral symmetry breaking in magnetic thin films and multilayers". In: *Phys. Rev. Lett.* 87.3 (2001), p. 037203.

[14]   A. N. Bogdanov and D. Yablonskii. "Thermodynamically stable "vortices" in magnetically ordered crystals. The mixed state of magnets". In: *Zh. Eksp. Teor. Fiz* 95 (1989), pp. 178–182.

[15]   W. F. Brown. *Magnetoelastic interactions*. Vol. 9. Springer, 1966.

[16]   W. F. Brown. *Micromagnetics*. 18. interscience publishers, 1963.

[17]   W. F. Brown Jr. "Thermal fluctuations of a single-domain particle". In: *Phys. Rev.* 130.5 (1963), p. 1677.

[18]   H. Brune and P. Gambardella. "Magnetism of individual atoms adsorbed on surfaces". In: *Surf. Sci.* 603.10-12 (2009), pp. 1812–1830.

[19]   F. Büttner et al. "Field-free deterministic ultrafast creation of magnetic skyrmions by spin–orbit torques". In: *Nat. Nanotechnol.* 12.11 (2017), p. 1040.

[20]   E. Callen and H. B. Callen. "Magnetostriction, forced magnetostriction, and anomalous thermal expansion in ferromagnets". In: *Phys. Rev.* 139.2A (1965), A455.

[21]   Y. Chen et al. "Mapping twisted light into and out of a photonic chip". In: *Phys. Rev. Lett.* 121.23 (2018), p. 233602.

[22]   C. W. Clark et al. "Controlling neutron orbital angular momentum". In: *Nature* 525.7570 (2015), pp. 504–506.

[23]   J. M. Coey. *Magnetism and magnetic materials*. Cambridge university press, 2010.

[24]   F. Den Broeder, W Hoving, and P. Bloemen. "Magnetic anisotropy of multilayers". In: *J. Magn. Magn. Mater.* 93 (1991), pp. 562–570.

[25]   M. J. Donahue and M. Donahue. *OOMMF user's guide, version 1.0*. US Department of Commerce, National Institute of Standards and Technology, 1999.

[26]   M. I. Dyakonov and V. Perel. "Current-induced spin orientation of electrons in semiconductors". In: *Phys. Lett. A* 35.6 (1971), pp. 459–460.

[27]   M. I. D'Yakonov and V. Perel. "Possibility of orienting electron spins with current". In: *JETPL* 13 (1971), p. 467.

[28]   I. Dzyaloshinsky. "A thermodynamic theory of "weak" ferromagnetism of antiferromagnetics". In: *J. Phys. Chem. Sol.* 4.4 (1958), pp. 241–255.

[29]   P. Ehrenfest. "Bemerkung über die angenäherte Gültigkeit der klassischen Mechanik innerhalb der Quantenmechanik". In: *Zeitschrift für Physik* 45.7-8 (1927), pp. 455–457.

[30]   R. F. L. Evans et al. "Stochastic form of the Landau-Lifshitz-Bloch equation". In: *Phys. Rev. B* 85.1 (2012), p. 014433.

[31]   M. Farle. "Ferromagnetic resonance of ultrathin metallic layers". In: *Rep. Prog. Phys.* 61.7 (1998), p. 755.

[32]   A. Fert, V. Cros, and J. Sampaio. "Skyrmions on the track". In: *Nat. Nanotechnol.* 8.3 (2013), pp. 152–156.

[33]   A. Fert and P. M. Levy. "Role of anisotropic exchange interactions in determining the properties of spin-glasses". In: *Phys. Rev. Lett.* 44.23 (1980), p. 1538.

[34]   M. Fiebig et al. "The evolution of multiferroics". In: *Nat. Rev. Mater.* 1.8 (2016), pp. 1–14.

[35]   L. Fu, C. L. Kane, and E. J. Mele. "Topological insulators in three dimensions". In: *Phys. Rev. Lett.* 98.10 (2007), p. 106803.

[36]   D. A. Garanin. "Fokker-Planck and Landau-Lifshitz-Bloch equations for classical ferromagnets". In: *Phys. Rev. B* 55.5 (1997), p. 3050.

[37]   T. Gerhardt. "Micromagnetic simulations of ferromagnetic domain walls in nanowires". PhD thesis. Universität Hamburg, 2014.

[38]   M. Getzlaff. *Fundamentals of magnetism*. Springer Science & Business Media, 2007.

[39]   T. L. Gilbert. "A phenomenological theory of damping in ferromagnetic materials". In: *IEEE Trans. Magn.* 40.6 (2004), pp. 3443–3449.

[40]   T. Gilbert. "A Lagrangian formulation of the gyromagnetic equation of the magnetization field". In: *Phys. Rev.* 100 (1955), p. 1243.

[41]   E. K. Gross and R. M. Dreizler. *Density functional theory*. Vol. 337. Springer Science & Business Media, 2013.

[42]   F. D. M. Haldane. "Fractional quantization of the Hall effect: a hierarchy of incompressible quantum fluid states". In: *Phys. Rev. Lett.* 51.7 (1983), p. 605.

[43]   F. D. M. Haldane. "Model for a quantum Hall effect without Landau levels: Condensed-matter realization of the "parity anomaly"". In: *Phys. Rev. Lett.* 61.18 (1988), p. 2015.

[44]   E. H. Hall et al. "On a new action of the magnet on electric currents". In: *Am. J. Math.* 2.3 (1879), pp. 287–292.

[45]   S. Heinze et al. "Spontaneous atomic-scale magnetic skyrmion lattice in two dimensions". In: *Nat. Phys.* 7.9 (2011), pp. 713–718.

[46] D. Hsieh et al. "A topological Dirac insulator in a quantum spin Hall phase". In: *Nature* 452.7190 (2008), pp. 970–974.

[47] J. D. Jackson and R. F. Fox. *Classical electrodynamics*. Vol. 67. 9. American Association of Physics Teachers, 1999, pp. 841–842.

[48] H. Jansen. "Magnetic anisotropy in density-functional theory". In: *Phys. Rev. B* 59.7 (1999), p. 4699.

[49] W. Jiang et al. "Blowing magnetic skyrmion bubbles". In: *Science* 349.6245 (2015), pp. 283–286.

[50] W. Jiang et al. "Direct observation of the skyrmion Hall effect". In: *Nat. Phys.* 13.2 (2017), pp. 162–169.

[51] N. Jones. "How to stop data centres from gobbling up the world's electricity." In: *Nature* 561.7722 (2018), pp. 163–167.

[52] C. L. Kane and E. J. Mele. "Quantum spin Hall effect in graphene". In: *Phys. Rev. Lett.* 95.22 (2005), p. 226801.

[53] T. Kasuya. "Effects of s-d Interaction on Transport Phenomena". In: *Prog. Theor. Phys.* 22.2 (1959), pp. 227–246.

[54] C. Kittel. "On the theory of ferromagnetic resonance absorption". In: *Phys. Rev.* 73.2 (1948), p. 155.

[55] E. F. Kneller and R. Hawig. "The exchange-spring magnet: a new material principle for permanent magnets". In: *IEEE Trans. Magn.* 27.4 (1991), pp. 3588–3560.

[56] M. König et al. "Quantum spin Hall insulator state in HgTe quantum wells". In: *Science* 318.5851 (2007), pp. 766–770.

[57] J. M. Kosterlitz and D. J. Thouless. "Ordering, metastability and phase transitions in two-dimensional systems". In: *J. Phys. C: Solid State Phys.* 6.7 (1973), p. 1181.

[58] G. Kresse and J. Furthmüller. "Efficient iterative schemes for ab initio total-energy calculations using a plane-wave basis set". In: *Phys. Rev. B* 54.16 (1996), p. 11169.

[59] S. V. Kusminskiy. *Quantum Magnetism, Spin Waves, and Optical Cavities*. Springer, 2019.

[60] L. Landau and E. Lifshitz. "On the theory of the dispersion of magnetic permeability in ferromagnetic bodies". In: *Phys. Z. Sowjetunion* 8.153 (1935), pp. 101–114.

[61] D. C. Langreth and J. W. Wilkins. "Theory of spin resonance in dilute magnetic alloys". In: *Phys. Rev. B* 6.9 (1972), p. 3189.

[62]   K. Litzius et al. "Skyrmion Hall effect revealed by direct time-resolved X-ray microscopy". In: *Nat. Phys.* 13.2 (2017), pp. 170–175.

[63]   R. P. McNeil et al. "Localized magnetic fields in arbitrary directions using patterned nanomagnets". In: *Nano Lett.* 10.5 (2010), pp. 1549–1553.

[64]   A. Mook et al. "Topological Magnon Materials and Transverse Magnon Transport". PhD thesis. Martin-Luther-Universität Halle-Wittenberg, 2017.

[65]   G. E. Moore et al. *Cramming more components onto integrated circuits*. 1965.

[66]   J. E. Moore. "The birth of topological insulators". In: *Nature* 464.7286 (2010), pp. 194–198.

[67]   T. Moriya. "Anisotropic superexchange interaction and weak ferromagnetism". In: *Phys. Rev.* 120.1 (1960), pp. 91–98.

[68]   M. Mostovoy. "Ferroelectricity in spiral magnets". In: *Phys. Rev. Lett.* 96.6 (2006), p. 067601.

[69]   S Mühlbauer et al. "Skyrmion lattice in a chiral magnet". In: *Science* 323.5916 (2009), pp. 915–919.

[70]   J. Müller, A. Rosch, and M. Garst. "Edge instabilities and skyrmion creation in magnetic layers". In: *New J. Phys.* 18.6 (2016), p. 065006.

[71]   N. Nagaosa and Y. Tokura. "Topological properties and dynamics of magnetic skyrmions". In: *Nat. Nanotechnol.* 8.12 (2013), pp. 899–911.

[72]   P. B. Ndiaye, C. A. Akosa, and A. Manchon. "Topological Hall and spin Hall effects in disordered skyrmionic textures". In: *Phys. Rev. B* 95.6 (2017), p. 064426.

[73]   W. Nolting and A. Ramakanth. *Quantum theory of magnetism*. Springer Science & Business Media, 2009.

[74]   J. Osborn. "Demagnetizing factors of the general ellipsoid". In: *Phys. Rev.* 67.11-12 (1945), p. 351.

[75]   S. S. Parkin. *Shiftable magnetic shift register and method of using the same*. US Patent 6,834,005. 2004.

[76]   S. S. Parkin, M. Hayashi, and L. Thomas. "Magnetic domain-wall racetrack memory". In: *Science* 320.5873 (2008), pp. 190–194.

[77]   D. Pinna et al. "Skyrmion gas manipulation for probabilistic computing". In: *Phys. Rev. Appl.* 9.6 (2018), p. 064018.

[78]   D. Prychynenko et al. "Magnetic skyrmion as a nonlinear resistive element: a potential building block for reservoir computing". In: *Phys. Rev. Appl.* 9.1 (2018), p. 014034.

[79] G. F. Quinteiro and J Berakdar. "Electric currents induced by twisted light in quantum rings". In: *Opt. Express* 17.22 (2009), pp. 20465–20475.

[80] D. C. Ralph and M. D. Stiles. "Spin transfer torques". In: *J. Magn. Magn. Mater.* 320.7 (2008), pp. 1190–1216.

[81] C. Reig, S. Cardoso, and S. C. Mukhopadhyay. *Giant magnetoresistance (GMR) sensors*. Vol. 1. Springer, 2013, pp. 157–80.

[82] N. Romming et al. "Writing and deleting single magnetic skyrmions". In: *Science* 341.6146 (2013), pp. 636–639.

[83] L. Rózsa et al. "Complex magnetic phase diagram and skyrmion lifetime in an ultrathin film from atomistic simulations". In: *Phys. Rev. B* 93 (2 2016), p. 024417.

[84] S. Sankar, M. Shaw, and K. Vaid. "Impact of temperature on hard disk drive reliability in large datacenters". In: *2011 IEEE/IFIP 41st international conference on dependable systems & networks (DSN)*. IEEE. 2011, pp. 530–537.

[85] J. Shibata, G. Tatara, and H. Kohno. "A brief review of field-and current-driven domain-wall motion". In: *J. Phys. D: Appl. Phys* 44.38 (2011), p. 384004.

[86] T Shinjo et al. "Magnetic vortex core observation in circular dots of permalloy". In: *Science* 289.5481 (2000), pp. 930–932.

[87] T. Skyrme. "Particle states of a quantized meson field". In: *Proc. R. Soc. A* 262.1309 (1961), pp. 237–245.

[88] T. H. R. Skyrme. "A unified field theory of mesons and baryons". In: *Nucl. Phys.* 31 (1962), pp. 556–569.

[89] J. C. Slonczewski. "Current-driven excitation of magnetic multilayers". In: *J. Magn. Magn. Mater.* 159.1-2 (1996), pp. L1–L7.

[90] C. Song et al. "Spin-orbit torques: Materials, mechanisms, performances, and potential applications". In: *Prog. Mater. Sci.* (2020), p. 100761.

[91] J Stöhr. "Exploring the microscopic origin of magnetic anisotropies with X-ray magnetic circular dichroism (XMCD) spectroscopy". In: *J. Magn. Magn. Mater.* 200.1-3 (1999), pp. 470–497.

[92] E. C. Stoner. "Collective electron ferromagnetism II. Energy and specific heat". In: *Proc. R. Soc. A* 169.938 (1939), pp. 339–371.

[93] A. A. Thiele. "Steady-State Motion of Magnetic Domains". In: *Phys. Rev. Lett.* 30 (6 1973), pp. 230–233.

[94] D. J. Thouless et al. "Quantized Hall conductance in a two-dimensional periodic potential". In: *Phys. Rev. Lett.* 49.6 (1982), p. 405.

[95] I. Tudosa et al. "The ultimate speed of magnetic switching in granular recording media". In: *Nature* 428.6985 (2004), pp. 831–833.

[96] K. Uchida et al. "Observation of the spin Seebeck effect". In: *Nature* 455.7214 (2008), pp. 778–781.

[97] M. Uchida and A. Tonomura. "Generation of electron beams carrying orbital angular momentum". In: *Nature* 464.7289 (2010), pp. 737–739.

[98] V. M. Uzdin et al. "The effect of confinement and defects on the thermal stability of skyrmions". In: *Physica B: Condens. Mat.* 549 (2018), pp. 6–9.

[99] A. Vansteenkiste et al. "The design and verification of MuMax3". In: *AIP Advances* 4.10 (2014), p. 107133.

[100] E. Y. Vedmedenko and D Altwein. "Topologically protected magnetic helix for all-spin-based applications". In: *Phys. Rev. Lett.* 112.1 (2014), p. 017206.

[101] J. Verbeeck, H. Tian, and P. Schattschneider. "Production and application of electron vortex beams". In: *Nature* 467.7313 (2010), pp. 301–304.

[102] A. Wachowiak et al. "Direct observation of internal spin structure of magnetic vortex cores". In: *Science* 298.5593 (2002), pp. 577–580.

[103] J. Wätzel, A. Moskalenko, and J Berakdar. "Photovoltaic effect of light carrying orbital angular momentum on a semiconducting stripe". In: *Opt. Express* 20.25 (2012), pp. 27792–27799.

[104] J. Wätzel et al. "Optical vortex driven charge current loop and optomagnetism in fullerenes". In: *Carbon* 99 (2016), pp. 439–443.

[105] Y. Yang et al. "Ultrafast magnetization reversal by picosecond electrical pulses". In: *Science Advances* 3.11 (2017), e1603117.

[106] A. M. Yao and M. J. Padgett. "Orbital angular momentum: origins, behavior and applications". In: *Advances in Optics and Photonics* 3.2 (2011), pp. 161–204.

[107] G. Yin et al. "Topological spin Hall effect resulting from magnetic skyrmions". In: *Phys. Rev. B* 92.2 (2015), p. 024411.

[108] D. Yu et al. "Nondestructive ultrafast steering of a magnetic vortex by terahertz pulses". In: *NPG Asia Materials* 12.1 (2020), pp. 1–8.

[109] X. Yu et al. "Real-space observation of a two-dimensional skyrmion crystal". In: *Nature* 465.7300 (2010), pp. 901–904.

[110] J. Zang et al. "Dynamics of skyrmion crystals in metallic thin films". In: *Phys. Rev. Lett.* 107.13 (2011), p. 136804.

[111] S. Zhang et al. "Real-Space Observation of Skyrmionium in a Ferromagnet-Magnetic Topological Insulator Heterostructure". In: *Nano Lett.* 18.2 (2018), pp. 1057–1063.

[112] S. Zhang and Z Li. "Roles of nonequilibrium conduction electrons on the magnetization dynamics of ferromagnets". In: *Phys. Rev. Lett.* 93.12 (2004), p. 127204.

[113] X. Zhang et al. "Ultrafast oscillating-magnetic-field generation based on electronic-current dynamics". In: *Phys. Rev. A* 99.1 (2019), p. 013414.

[114] X. Zhang et al. "Control and manipulation of a magnetic skyrmionium in nanostructures". In: *Phys. Rev. B* 94.9 (2016), p. 094420.

ACKNOWLEDGEMENTS

Finally, I do also thank the attentive reader of this work and close with the words of Douglas Adams:

So Long, and Thanks for All the Fish.

CURRICULUM VITAE

Personal Data

Name	Alexander Frederic Schäffer
Date of birth	03.10.1991
Place of birth	Hannover, Germany

Education

Since July 2017	Member of the International Max Planck Research School for Science and Technology of Nano-Systems
Since April 2017	Ph.D. studies at the Martin-Luther-Universität (MLU) Halle-Wittenberg
2014-2017	M.Sc. in Physics ($\varnothing$1.2) at the MLU Halle-Wittenberg, Thesis: *Nicht-lineare Magnetisierungsdynamik in ferromagnetischen Nanowürfeln*
2011-2014	B.Sc. in Medical Physics ($\varnothing$1.8) at the MLU Halle-Wittenberg, Thesis: *Erzeugung lokalisierter Ströme in Nanostrukturen*
2003-2011	Allgemeine Hochschulreife (*A-levels*, $\varnothing$1.1) Gymnasium der Stadt Rahden, Rahden, Germany
1998-2003	Grundschule (elementary school) Westrup, Stemwede, Germany

Academic work experience

Since January 2018	Regular research stays in the group *Scanning Probe Methods* led by Prof. Roland Wiesendanger at the University of Hamburg
Since January 2017	Research assistant, MLU Halle-Wittenberg

Halle (Saale), June 30, 2021, Alexander Frederic Schäffer

EIDESSTATTLICHE ERKLÄRUNG

Hiermit erkläre ich, Alexander Frederic Schäffer, die vorliegende Arbeit *Control of topologically non-trivial spin excitations* selbständig und ohne fremde Hilfe verfasst zu haben. Es wurden keine anderen als die von mir angegebenen Quellen und Hilfsmittel benutzt. Die den benutzten Werken wörtlich oder inhaltlich entnommenen Stellen sind als solche kenntlich gemacht worden. Ich erkläre, die Angaben wahrheitsgemäß gemacht, keine vergeblichen Promotionsversuche unternommen und keine Dissertation an einer anderen wissenschaftlichen Einrichtung zur Erlangung eines akademischen Grades eingereicht zu haben. Ich bin weder vorbestraft noch sind gegen mich Ermittlungsverfahren anhängig.

Alexander Frederic Schäffer

Halle (Saale), den 30. Juni 2021